

Development of Magnetic Resonance Methodologies for Battery Investigation



By

CLAIRE LINDA DOSWELL

A thesis submitted to the University of Birmingham for the

degree of

DOCTOR OF PHILOSOPHY

School of Chemistry

College of Engineering and Physical Sciences

University of Birmingham

September 2021

UNIVERSITY OF
BIRMINGHAM

University of Birmingham Research Archive

e-theses repository

This unpublished thesis/dissertation is copyright of the author and/or third parties. The intellectual property rights of the author or third parties in respect of this work are as defined by The Copyright Designs and Patents Act 1988 or as modified by any successor legislation.

Any use made of information contained in this thesis/dissertation must be in accordance with that legislation and must be properly acknowledged. Further distribution or reproduction in any format is prohibited without the permission of the copyright holder.

Abstract

In this thesis, magnetic resonance (MR) methods are developed to examine battery chemistries. A method to increase the signal-to-noise ratio (SNR) without increasing experimental time is developed.

Furthermore, sodium and lithium batteries are investigated using nuclear magnetic resonance (NMR) spectroscopy and magnetic resonance imaging (MRI). Additionally, the speciation in electrolytes for aluminium batteries is investigated using NMR spectroscopy.

In Chapter 3, MRI methodology is developed to increase the SNR to enable quantitative T_1 relaxation time maps without an increase in acquisition time. The increased SNR allows the visualisation of water ingress into an ionic liquid (IL) containing a zinc salt, Zn(TfO) in 1-ethyl-3-methylimidazolium triflate ($C_2C_1\text{imTfO}$) over time. A change in the zinc speciation is determined from a plot of ^{19}F T_1 NMR relaxation time versus water concentration.

In Chapter 4, *operando* ^{23}Na NMR and MRI methodology is developed to visualise battery chemistry. ^{23}Na NMR spectroscopy is used to establish changes in the sodium species present during the formation cycle of a cell. This is applied to a sodium metal cell, where the speciation changes in the electrolyte are observed, and a sodium full cell, where the development of quasimetallic nanoparticles and a metallic species are

observed during the formation cycle for the first time. This methodology is used in Chapter 5 with ^7Li NMR spectroscopy and MRI to observe the changes in the lithium metal electrode and electrolyte species in a lithium metal cell during the formation cycle.

In Chapter 6, aluminium battery chemistries are explored using ^1H and ^{27}Al NMR spectroscopy. The speciation and molecular interactions in an aluminium IL, 1-butyl-3-methylimidazolium chloride ($\text{C}_4\text{C}_1\text{imCl}$) containing AlCl_3 and water, is investigated. ^{27}Al NMR spectroscopy is used to investigate the speciation changes in the IL with respect to AlCl_3 concentration. ^1H NMR spectroscopy, combined with ^{27}Al NMR spectroscopy is used to suggest hydrogen bonding interactions within the IL. ^1H T_1 and T_2 NMR relaxation times with respect to AlCl_3 concentration are explored, demonstrating possible utility as MRI contrast. The intermolecular interactions and relaxation times of ^{27}Al and ^1H species are investigated in a potential aqueous aluminium battery electrolyte, AlCl_3 in saltwater. The ^1H T_1 NMR relaxation time is shown to provide suitable contrast for MRI of AlCl_3 in saltwater.

The methods developed in this thesis are applicable across multiple nuclei and address some of the issues surrounding poor SNR in the use of NMR active nuclei with low gyromagnetic ratios and rapid NMR relaxation times. This thesis demonstrates how data from NMR spectroscopy and

MRI can be combined to develop a more holistic understanding of battery chemistry.

Acknowledgements

I would like to acknowledge my supervisor, Melanie Britton, for support throughout this project and numerous opportunities. Additional thanks go to Cécile Le Duff and Bridget Tang for their technical support, and to my numerous collaborators for their help and guidance along the way.

This project would have been considerably duller without the wonderful people in the office along the way. Thanks to Yasmeeen AlZahrani, Gabriele Cimmarusti, Joseph Okeke, Giulia Molinaro, Pooja Kumari, and Joshua Bray. Specific thanks to Emma Thompson for her help during my early work and continued support, and Helen Abbott for bringing joy. Thanks also go to Joseph Hamill, Oliver Irving, Nashwa Awais, and Christopher Weaver for welcome distractions and office parties. Special thanks to Adrian Fortuin, for constant entertainment and encouragement.

Thanks to my summer student, Colombe Ténieres, for all your hard work and being a delight to supervise. Also, to all the undergraduate students whom I have taught for reminding me of the joy of discovery.

Mostly, I would like to thank my partner, Joseph Benford-Ward, for his unwavering support.

List of Abbreviations

1D.....	One-dimensional
2D.....	Two-dimensional
3D.....	Three-dimensional
AFM.....	Atomic force microscopy
AlB.....	Aluminium ion battery
ALFA.....	Aluminium anode, lid, film, air cathode
C ₂ C ₁ imCl.....	1-ethyl-3-methylimidazolium chloride
C ₂ C ₁ imTfO.....	1-ethyl-3-methylimidazolium triflate
C ₄ C ₁ imCl.....	1-butyl-3-methylimidazolium chloride
CE.....	Counter electrode
CPMG.....	Carr-Purcell-Meiboom-Gill
CSI.....	Chemical shift imaging
DEC.....	Diethyl carbonate
DFT.....	Density functional theory
DMC.....	Dimethyl carbonate
dOp.....	Derivative operando
EC.....	Ethylene carbonate
EMC.....	Ethyl methyl carbonate
EPR.....	Electron paramagnetic resonance
FID.....	Free induction decay
FOV.....	Field of view
FWHM.....	Full width at half maximum

HPLC.....High pressure liquid chromatography
 IL.....Ionic liquid
 IR.....Inversion recovery
 LIB.....Lithium ion battery
 LTR.....Linear transmit/receive
 MAS.....Magic angle spinning
 Micro-CT.....X-ray micro-computed tomography
 MOF.....Metal-organic framework
 MOLLI.....Modified Look-Locker inversion recovery
 MR.....Magnetic resonance
 MRI.....Magnetic resonance imaging
 MSME.....Multi-slice-multi-(spin) echo
 NIB.....Sodium ion battery
 NMC811..... $\text{LiNi}_{0.8}\text{Mn}_{0.1}\text{Co}_{0.1}\text{O}_2$
 NMR.....Nuclear magnetic resonance
 PDF.....Atomic pair distribution function
 PEEK.....Polyether ether ketone
 PGSE.....Pulsed gradient spin echo
 PGSTE.....Pulsed gradient stimulated echo
 PTFE.....Polytetrafluorethene
 QTR.....Quadrature transmit/receive
 RARE.....Rapid acquisition with relaxation enhancement
 RF.....Radiofrequency

RTIL.....Room temperature ionic liquid

SAPPHIRE.....
.....Saturation pulse prepared heart rate independent inversion recovery

SASHA.....Saturation recovery single-shot acquisition

SECCM.....Scanning electrochemical cell microscopy

SEI.....Solid electrolyte interphase

SEM.....Scanning electron microscopy

ShMOLLI.....Shortened modified Look-Locker inversion recovery

SNR.....Signal-to-noise ratio

SR.....Saturation recovery

SSNMR.....Solid state nuclear magnetic resonance

WE.....Working electrode

XAS.....X-ray absorption spectroscopy

XRD.....X-ray diffraction

ZIB.....Zinc ion battery

Table of Contents

1. Introduction.....	1
1.1 Lithium Ion Batteries.	1
1.1.1 Metal Cells.....	3
1.1.2 Full Cells.....	4
1.2 Beyond Lithium Ion Batteries.....	4
1.2.1 Sodium Ion Batteries.....	6
1.2.2 Zinc Ion Batteries.....	8
1.2.2.1 Aqueous Zinc Ion Batteries.....	8
1.2.2.2 Ionic Liquid Zinc Ion Batteries.....	9
1.2.3 Aluminium Ion Batteries.....	10
1.2.3.1 Aqueous Aluminium Ion Batteries.....	11
1.2.3.2 Ionic Liquid Aluminium Ion Batteries.....	12
1.3 Characterisation Techniques.....	14
1.3.1 X-Ray Techniques.....	14
1.3.1.1 X-ray Diffraction.....	15
1.3.1.2 X-ray Scattering Techniques.....	15
1.3.1.3 X-ray Micro-Computed Tomography.....	16
1.3.2 Surface Microscopy Techniques.....	16
1.3.2.1 Scanning Electron Microscopy.....	17
1.3.2.2 Atomic Force Microscopy.....	17
1.3.2.3 Scanning Electrochemical Cell Microscopy.....	18
1.3.3 Magnetic Resonance Techniques.....	18

1.3.3.1	Nuclear Magnetic Resonance Spectroscopy....	19
1.3.3.2	Magnetic Resonance Imaging.....	21
1.4	References.....	24
2.	Experimental Techniques.....	34
2.1	Magnetic Resonance Techniques.....	34
2.1.1	Nuclear Magnetic Resonance Spectroscopy.....	34
2.1.1.1	Radio Frequency Radiation.....	34
2.1.1.2	Chemical Shift.....	36
2.1.1.3	NMR Relaxation.....	37
2.1.1.4	NMR Relaxation Mechanisms.....	37
2.1.1.5	Measuring T_1 NMR Relaxation Times.....	40
2.1.1.6	Measuring T_2 NMR Relaxation Times.....	43
2.1.1.7	NMR Signal Intensity.....	46
2.1.1.8	Spatial Encoding.....	47
2.1.1.9	Diffusion Spectroscopy.....	49
2.1.2	Magnetic Resonance Imaging.....	52
2.1.2.1	k Space.....	52
2.1.2.2	Slice Selection.....	55
2.1.2.3	Spin-Echo Imaging.....	55
2.1.2.4	Multi-Slice-Multi-(Spin) Echo Imaging....	57
2.1.2.4	Rapid Acquisition with Relaxation Enhancement Imaging.....	57
2.1.2.5	NMR Relaxation Time Imaging.....	58

2.1.1.6 Image Artefacts.....	59
2.1.1.7 Experimental Conditions.....	60
2.2 Electrochemical Techniques.....	61
2.2.1 Charge Cycling.....	61
2.2.2 Considerations with Magnetic Resonance Techniques.....	63
2.3 References.....	66
 3. Quantitative T_1 Magnetic Resonance Imaging for Battery Characterisation.....	69
3.1 Introduction.....	69
3.2 Experimental.....	76
3.3 Quantifying the Effects of Summing Echo Images on the Measured T_1 NMR Relaxation Time.....	81
3.3.1 Results.....	81
3.3.2 Discussion.....	86
3.4 Application of Signal-To-Noise Ratio Improvement Methodology to Water Ingress in an Ionic Liquid.....	88
3.4.1 Results.....	88
3.4.2 Discussion.....	93
3.5 Conclusion.....	95
3.6 References.....	96
 4. Magnetic Resonance Imaging of Sodium Ion Batteries.....	100

4.1 Introduction.....	100
4.2 Experimental.....	103
4.3 Results and Discussion.....	109
4.3.1 Distribution and Evolution of Sodium Species in a Sodium Metal Cell.....	109
4.3.2 Distribution and Evolution of Sodium Species in a Sodium Full Cell.....	113
4.3.3 Metallic Sodium Formation in a Sodium Metal Cell.....	115
4.3.4 Metallic Sodium Formation in a Sodium Full Cell.....	119
4.4 Conclusion.....	129
4.5 References.....	131
5. Magnetic Resonance Studies on a Lithium Metal Cell.....	133
5.1 Introduction.....	133
5.2 Experimental.....	136
5.3 Results and Discussion.....	139
5.3.1 Pristine Cell Before Cycling.....	139
5.3.2 Formation Cycle.....	144
5.4 Conclusion.....	154
5.5 References.....	156
6. Magnetic Resonance Investigations of Aluminium Battery Electrolytes	158

6.1 Introduction.....	158
6.2 Experimental.....	161
6.3 Results and Discussion.....	164
6.3.1 C ₄ C ₁ imCl: AlCl ₃ Ionic Liquid Electrolyte.....	164
6.3.2 AlCl ₃ in Brine Electrolyte.....	178
6.4 Conclusion.....	183
6.5 References.....	186
7. Conclusions and Further Work.....	189
7.1 References.....	194
8. Appendices.....	195
Appendix 1.....	195
Appendix 2.....	236
Appendix 3.....	239
Appendix 4.....	241

1 Introduction

Energy storage is one of the largest challenges facing society today. With an increasing demand for devices requiring battery power,¹ such as smartphones and electric vehicles. These devices need to be lightweight and have higher energy capacities; hence, there is increasing interest in new battery technologies.² In addition to consumer demand, there is an increasing need for battery materials to be sustainably sourced. The current market leader in rechargeable (secondary) batteries is lithium ion due to its early success, low weight and high charge density; however alternative battery chemistries, such as sodium,³ zinc,⁴ and aluminium,⁵ offer an opportunity for decreased environmental impact, in addition to an increase in theoretical capacity for zinc and aluminium based batteries.^{4, 5}

1.1 Lithium Ion Batteries

Lithium ion batteries (LIBs) are currently the most successful battery chemistry, with the founding scientists receiving the 2019 Nobel Prize in Chemistry.⁶ These LIBs **batteries operate using a 'rocking chair' model**, where lithium is removed from one electrode, transferred across an electrolyte, and incorporated into the other upon charging and discharging (Figure 1.1).

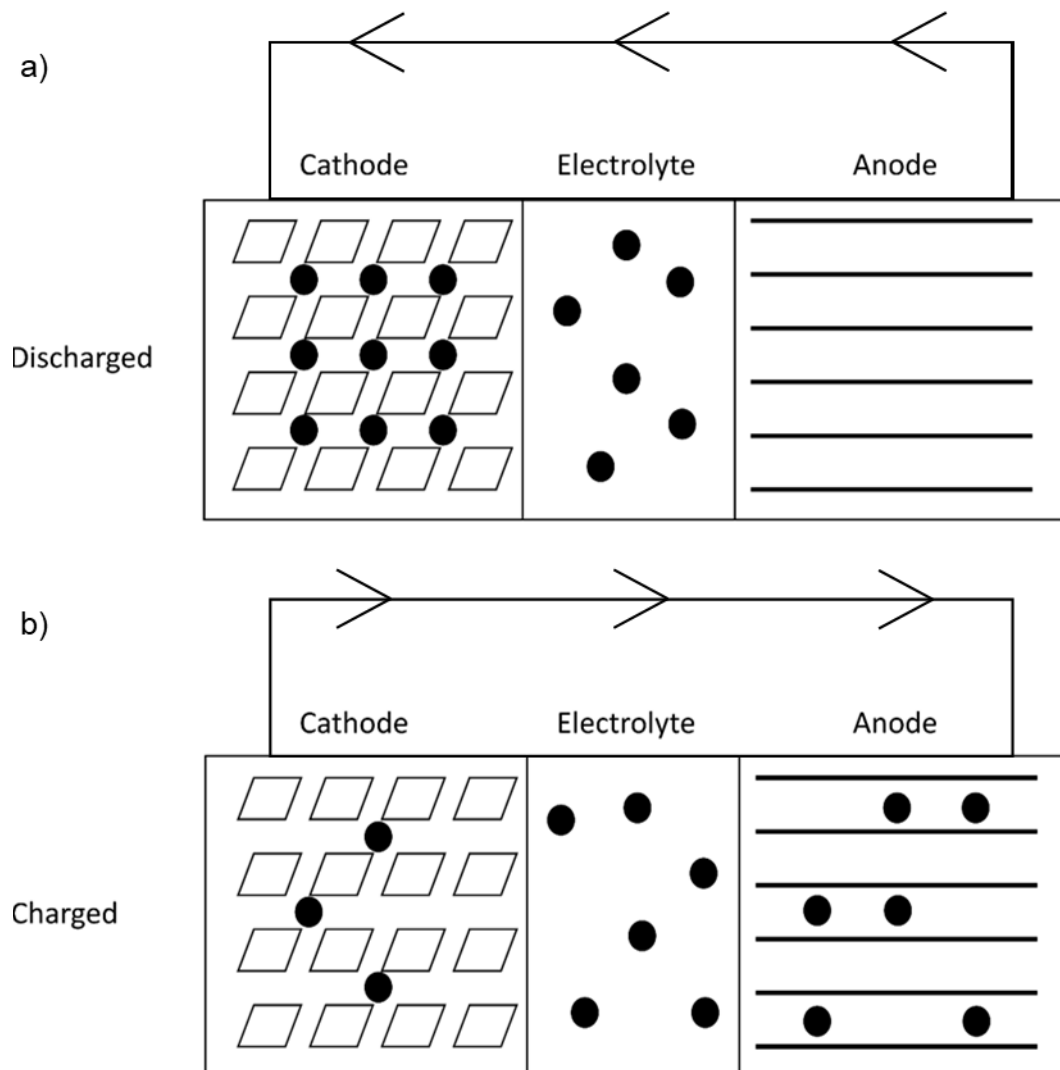


Figure 1.1: Schematic diagram showing the location of electroactive ions in a) discharged and b) charged state in a lithium ion full cell. The cathode is a layered oxide material, illustrated with layers of parallelograms. Arrows indicate electron flow during a) discharging and b) charging. The anode is graphite, with the carbon layers shown as black lines. The lithium ions are shown as circles.

Studies into battery chemistry can be performed on several types of cells.

Metal cell (half cell) configurations have one metal electrode, such as lithium metal in a lithium battery, and another electrode that is either metal oxide or carbon based, such as graphite or hard carbon.^{7, 8} Metal cells are used to establish the behaviour of the non-metal battery electrode. After the chemistry of the non-metal electrode has been

characterised, material compatibility with electrolytes can be tested in a full cell configuration with both a metal oxide cathode and a carbon-based anode, which more resembles a commercial battery.

1.1.1 Metal Cells

Ideally, to get the highest volumetric and gravimetric capacities, a lithium metal electrode would be used. However, due to the high reactivity of lithium metal with air, water, common organic solvents, as well as the propensity to form dendrites, lithium metal batteries pose a high safety risk.^{9, 10} The issue of electrode reactivity with the electrolyte solvent is complex: some reactivity with the solvent is necessary, as this forms the solid electrolyte interphase (SEI) which is essential for battery performance and has been extensively reported in the literature.¹¹⁻¹⁴ The SEI protects the electrode from further reaction, and thus degradation, with the electrolyte but allows the diffusion of the electroactive species through its structure enabling the battery to function. The structure of the SEI affects its ability to allow diffusion of the electroactive species; if the electroactive species is trapped, battery capacity is decreased.¹⁵

Dendrites are metallic microstructures that form on an electrode and can extend toward the other electrode. Dendrites present several problems in battery function including an increase in surface area of metal in the cell, the potential creation of dead lithium metal detached from an electrode,

and short-circuiting of the battery. Increasing the electrode surface area is an issue that will increase the amount of SEI formed, which in turn will trap more of the electroactive species and decrease the battery capacity.¹⁵ Furthermore, dead lithium is formed when lithium microstructures break away from the main metal electrode;¹⁶⁻¹⁸ this lithium is not electroactive, cannot be used to store charge and can move around in the electrolyte and make contact with the electrodes. Both dead lithium and dendrites can contribute to short-circuiting hazards.

1.1.2 Full Cells

Due to its flammability, commercial lithium batteries do not contain lithium metal and typically have a metal oxide cathode and a graphite anode. The formation of the SEI is critical for function in these cells with various strategies for controlling the formation such as electrolyte additives¹⁹ and SEI precursor coatings²⁰ being employed. Advantageously, lithium ion full cells are less susceptible to the growth of dendrites as only intercalation, and not plating, occurs during cycling and the lithium content can be better balanced to reduce the likelihood of overlithiation.²¹

1.2 Beyond Lithium Ion Batteries

Whilst LIBs are a commercial success, they alone cannot support the future demand for energy storage. Lithium is not naturally abundant and

is often found in areas in the world that are difficult to access which makes it expensive. Furthermore, other critical materials, such as cobalt, are required in the battery electrode materials. Lithium is highly reactive which has caused numerous safety concerns associated with thermal runaway in battery packs over the past decade,²² such as the recent **battery fire in Tesla's lithium ion** battery bank in Victoria, Australia. To address the issues of cost and safety, new materials for current lithium batteries need to be found, in addition to different battery chemistries to ensure sustainable energy storage. Non-lithium battery chemistries, such as sodium,³ zinc,⁴ and aluminium⁵ are advantageous because they are based on naturally abundant materials. The natural abundance helps to avoid supply issues and reduce the cost. Furthermore, batteries using elements with the potential for multielectron redox chemistry, such as aluminium and zinc, have higher theoretical capacities than lithium batteries, and so offer a more efficient method of charge storage.^{4, 5}

The challenges with non-lithium batteries are primarily associated with the materials required. In the case of intercalation processes, such as in sodium ion batteries (NIBs), the difference in ionic radius between lithium and sodium is enough to prevent the direct translation of lithium battery materials to sodium.²³ Furthermore, sodium ion batteries are susceptible to dendrite formation³ and so electrolyte development to inhibit dendrite growth is required. For multielectron redox chemistries, the ions tend not

to intercalate and instead the batteries function using electroplating. The reliance on electroplating means that the morphology of the plated metal is of importance to prevent the growth of dendrites and so new electrolytes are required.

1.2.1 Sodium Ion Batteries

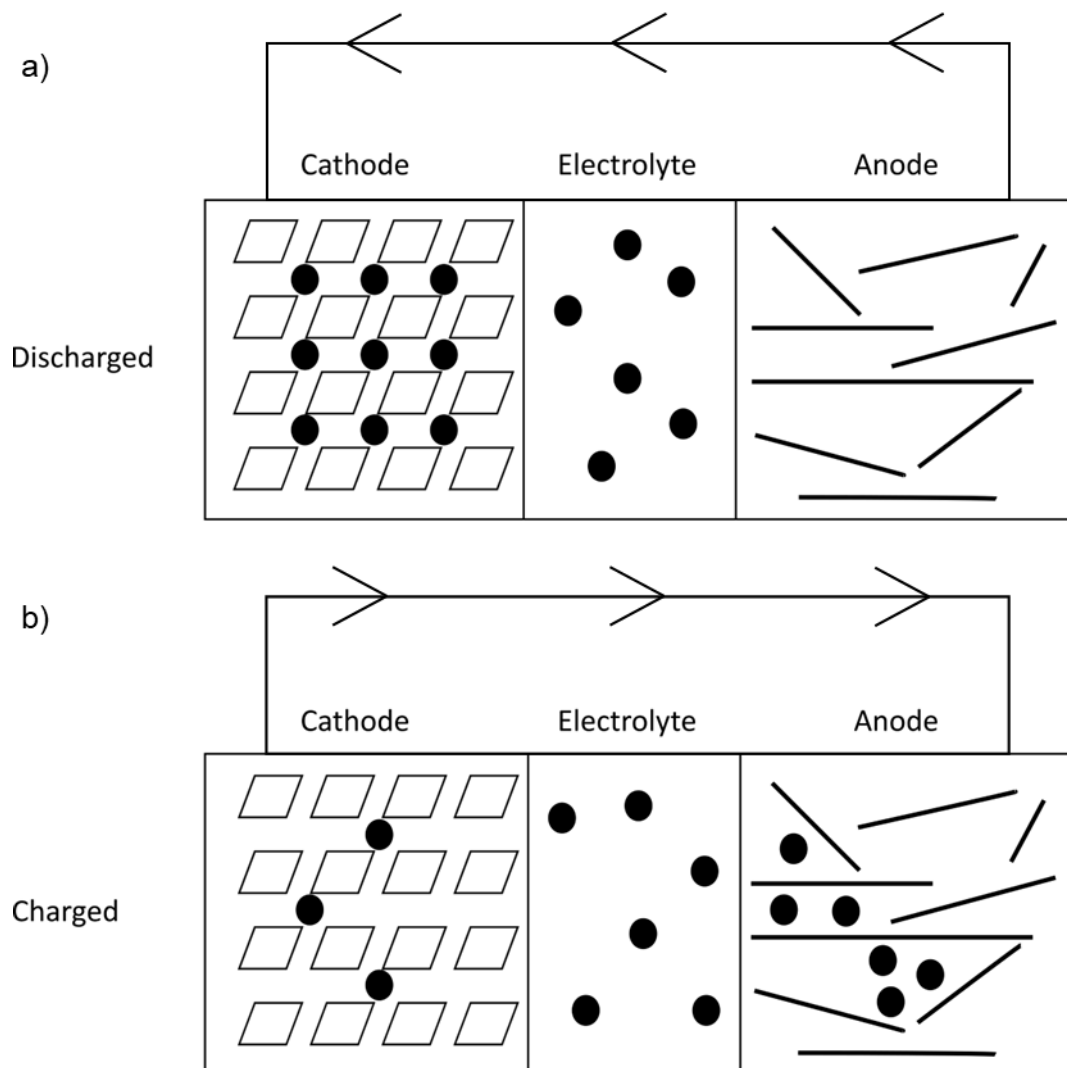


Figure 1.2: Schematic diagram showing the location of electroactive ions in a) discharged and b) charged states in a sodium ion full cell. The cathode is a layered oxide material, illustrated with layers of parallelograms. Arrows indicate electron flow during a) discharging and b) charging. The anode is a disordered carbon, with the carbon layers shown as black lines. The sodium ions are shown as circles.

Sodium metal batteries have many of the same issues as lithium metal batteries such as the tendency to grow dendrites and electrode reactivity with the electrolyte, air, and water. Furthermore, the popular LIB anode, graphite, cannot be used in a NIB as sodium is unable to intercalate due to the small interlayer spacing between the graphitic planes.^{23, 24} The size mis-match between sodium ions and graphite interlayer spacing has led to more disordered carbon structures, such as hard carbons, being used instead.

Using a more disordered anode means that the incorporation of sodium ions into the structure is more complex than that in LIBs (Figure 1.2). Studies conducted on sodium metal cells have proposed that as the cell is charged, the sodium intercalates into the turbostratic (parallel) planes within the hard carbon during the sloping region.²⁵ The potential slope is followed by a potential plateau, during which sodium pools within the larger pores within the carbon.²⁶ Sodiation of hard carbon electrodes has been investigated further using solid state NMR (SSNMR), X-ray total scattering studies, and density functional theory (DFT) calculations to suggest that the sodium first binds to defect sites within the carbon layers and on the pore surfaces during the sloping region of the charge curve.²⁵ Quasimetallic nanoparticles are clusters of metal atoms in the nanometre size range that have partially metallic character. The formation of sodium quasimetallic nanoparticles takes place only when a potential plateau is

observed and the pores of the carbon begin to fill.²⁵ This two-stage mechanism of intercalation is supported by the observation of quasimetallic nanoparticle formation by *operando* nuclear magnetic resonance (NMR) spectroscopy.²⁷

1.2.2 Zinc Ion Batteries

Zinc ion batteries (ZIBs) are an alternative to LIBs due to the low cost, lower environmental impact, and high power and energy densities.⁴ ZIBs typically have a zinc metal electrode, an intercalation or other electrode for zinc plating, and an electrolyte. The reliance on zinc plating makes zinc batteries susceptible to dendrite formation, although many methods have been used to reduce this possibility as described in the following sections 1.2.2.1 and 1.2.2.2.²⁸

1.2.2.1 Aqueous Zinc Ion Batteries

Aqueous ZIBs use a zinc metal electrode and an intercalation electrode. The strong interaction of Zn^{2+} with the intercalation material makes the development of an intercalation electrode difficult as the energy to remove the Zn^{2+} from the structure is high. Furthermore, the intercalation electrode materials have low conductivity which reduces the rate of the electrode intercalation of Zn^{2+} , and the transition metal-containing intercalation electrode can dissolve, diminishing the battery lifetime.²⁹

Often a Mn_2O_4 or V_2O_5 material is used as the intercalation electrode;³⁰⁻³² however, organic materials, such as methylene blue have been tested for ultrafast, long lifetime devices³³ in addition to a combination approach using metal-organic frameworks (MOFs) with organic coatings,³⁴ and interphase modification.³⁵ Despite these advances in materials, the aqueous ZIB has not yet been commercialised due to the lack of suitable electrode materials.

1.2.2.2 Ionic Liquid Zinc Ion Batteries

Non-aqueous ZIBs, using ionic liquid (IL) electrolytes, can store charge via zinc intercalation into a material and instead use zinc electroplating and stripping, but most commonly through stripping.⁴ ILs have shown promise in this area and are defined as liquids that contain only charged components but are liquid below 100 °C,³⁶ the branch of ILs that are liquid at room temperature are termed room-temperature ILs (RTILs).³⁷ These liquids have a variety of advantages over standard electrolytes, such as non-flammability, wide electrochemical potential windows, high conductivity, and non-aqueous chemistry,³⁸ all of which promise increased device safety. One such RTIL that shows promise in ZIBs is 1-ethyl-3-methylimidazolium triflate ($\text{C}_2\text{C}_1\text{imTfO}$) due to its stability in air.³⁹ The morphology of the electroplated zinc deposit is important for the minimisation of dendrite growth. It has been shown in metal surface finishing research that the density and morphology of zinc deposit can be

controlled by changing the anion and the IL, and so the performance of the ionic liquid can be tuned to provide a smooth and dense deposit.⁴⁰⁻⁴²

One limitation with ILs is their high viscosity which decreases their conductivity which can be altered by the incorporation of additives.³⁶ It has been shown that incorporating additives in the IL system changes the morphology of the zinc deposit³⁹ and so the use of additives must be thoroughly investigated. A common additive is water as it provides the necessary decrease in viscosity, however, this has been shown to decrease the electrochemical potential window and adversely affect the deposition of zinc.⁴³

1.2.3 Aluminium Ion Batteries

Initial research into aluminium ion batteries (AIBs) began alongside LIB research until the rapid success of LIBs.⁵ Aluminium is the third most abundant element in **the Earth's crust**⁴⁴ as well as the most abundant metal, and hence is a cost-effective, renewable alternative to lithium. Furthermore, the three-electron redox means AIBs have high theoretical volumetric and gravimetric energy densities,⁵ and is less reactive than lithium due to the passivation layer on aluminium,⁴⁵ making AIBs safer and easier to handle.

Aluminium batteries have yet to be commercialised. One of the main problems is the difficulty in developing intercalating electrodes as aluminium is difficult to intercalate as Al^{3+} due to the high charge density. Furthermore, it is not clear whether Al^{3+} is intercalated as Al^{3+} or as $[\text{AlCl}_4]^-$ which is a large structure to intercalate⁴⁶ and may cause cracking associated with electrode expansion.⁴⁷ Therefore, batteries based on electroplating aluminium metal have been explored.

1.2.3.1 Aqueous Aluminium Ion Batteries

Aqueous AIBs have a similar configuration to early LIBs, with a bulk metal electrode and a carbon electrode surrounding an alkaline electrolyte such as a KOH solution. The primary issue with alkaline AIBs is corrosion of the aluminium electrode by the formation of $\text{Al}(\text{OH})_3$.⁴⁸ Hence, to have a functioning aqueous AIB, the electrolyte must contain inhibitors to allow the electrodeposition of aluminium metal on the positive electrode^{49, 50} or an intermediary material is required.⁵¹ Early development of aqueous aluminium batteries included a cell based on aluminium and sea water for use under the sea, although this cell was unsuitable for use due to the evolution of hydrogen.⁵² Mori *et al.* have demonstrated where an aqueous AIB rechargeable battery based on an AlCl_3 in brine electrolyte.^{51, 53} Further work has addressed issues such as byproduct, such as $\text{Al}(\text{OH})_3$, accumulation,^{54, 55} and capacity recovery.⁵⁶

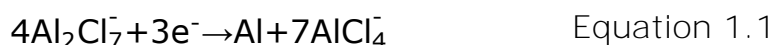
To increase the theoretical energy and power density of aluminium batteries, an air electrode has been proposed. Aluminium is a more suitable metal to lithium for use in an air battery as it is less reactive and can be exposed to oxygen and water, forming a passivating layer of Al_2O_3 , preventing violent reaction.⁴⁵ Aluminium air batteries operate using alkaline electrolytes due to the high solubility of the charge carrier $\text{Al}(\text{OH})_3$, but have similar corrosion issues as aqueous AIBs. Furthermore, other components in an aluminium electrode, for example silicon, can accelerate the self-corrosion⁵⁷ and so a high-purity aluminium electrode is required, increasing the battery cost. In some cases, the reaction is not completely reversible leading to a semi-rechargeable battery that could be recharged by replacing the aluminium electrode.⁵⁸

1.2.3.2 Ionic Liquid Aluminium Ion Batteries

Solving the corrosion issue in AIBs would enable improved cycling due to reduced build-up of reaction products. There are two ways to approach the issue: develop new electrodes^{59, 60} and develop new electrolytes. Electrolytes should cause controlled electrode passivation, have high conductivity, and have tuneable qualities for specific battery applications; hence ILs are a suitable electrolyte.⁶¹

Alkylimidazolium chloride ILs with additions of AlCl_3 , in particular 1-ethyl-3-methyl imidazolium chloride ($\text{C}_2\text{C}_1\text{imCl}$), have been studied in

aluminium electroplating and batteries.⁶² Addition of AlCl_3 to $\text{C}_2\text{C}_1\text{imCl}$ forms several new ionic species, whose identity is determined by the molar ratio of AlCl_3 added.⁶³ If the molar ratio is less than 1, it produces a Lewis basic solution with $\text{C}_2\text{C}_1\text{im}^+$, $[\text{AlCl}_4]^-$, and Cl^- species. A neutral solution is formed with a molar ratio of 1:1 where the only species are $\text{C}_2\text{C}_1\text{im}^+$ and $[\text{AlCl}_4]^-$. If the molar ratio of AlCl_3 is greater than 1, a Lewis acidic solution is formed where $\text{C}_2\text{C}_1\text{im}^+$ and $[\text{AlCl}_4]^-$ are present, along with $[\text{Al}_2\text{Cl}_7]^-$ and potentially $[\text{Al}_3\text{Cl}_{10}]^-$. Electroplating aluminium requires the Lewis acidic IL due to the plating reaction shown in Equation 1.1, which demonstrates why electroplating is not possible from the $[\text{AlCl}_4]^-$ species.⁶⁴



The morphology of the electroplated aluminium from an alkyimidazolium chloride IL has been shown to be controllable and dense deposits can be formed.^{64, 65} Dense electrodeposits are desirable in aluminium batteries to reduce dendrite growth. The formation of dendrites in such systems is a known issue,⁶⁶ however, the formation can be reduced through small external changes to the system, such as temperature,⁶⁵ or by using a different IL,⁶⁷ Small quantities of impurities, such as nickel, iron, and copper, have been shown to decrease the quality of the deposit,⁶⁸ hence the required smooth electrodeposit is only achievable with a high purity IL, which increases production cost. The alkyimidazolium ILs are highly hygroscopic and the incorporation of water into the system may alter the

electrodeposition of aluminium, although little research has been performed in the area. Instead, more hydrophobic ILs are being investigated to reduce water ingress into the IL such as those with the bis(trifluoromethylsulfonyl)imide (Tf₂N) counterion,⁶⁷ and use of a deep eutectic solvent with Vaseline and water.⁶⁹

1.3 Characterisation Techniques

Due to the complexity of battery chemistry and the breadth of materials required, there are a variety of characterisation techniques that are used to deduce the processes occurring within a battery at multiple length scales. When combined, the data from these techniques can provide a more comprehensive understanding of battery chemistry.

1.3.1 X-ray Techniques

X-ray techniques are often used to understand the local structure and identification of a material on the micro- or atomic scale. X-ray techniques can be used on crystalline samples and the wavelength can be tuned to study an element of interest. Furthermore, some X-ray techniques can be used on amorphous samples to study local order.

1.3.1.1 X-ray Diffraction

X-ray diffraction (XRD) is extensively used to characterise crystalline electrode materials at different stages in battery cycling due to its ease of execution and availability. XRD has been used to determine material purity,³⁰ changes in d-spacing during intercalation,⁷⁰ and structural changes in the cathode during cycling.⁷¹ However, samples must have crystalline ordering to be examined using XRD which may result in amorphous sample changes being overlooked.

1.3.1.2 X-ray Scattering Techniques

Atomic pair distribution function (PDF) analysis is a total scattering X-ray technique that can determine short and long range order in an amorphous material.⁷² It is not as commonplace as XRD, due to the need for synchrotron radiation and difficulty in data analysis. Insight into sodium incorporation mechanisms has been provided by PDF,^{27, 73} in addition to lithium insertion that results in disordered structure formation.⁷⁴

X-ray absorption spectroscopy (XAS) is similar to PDF in that it is able to provide information on the local atomic structure of quasi-crystalline and amorphous materials, but uses a specific wavelength that is tuned to the absorption edge of the chosen element and thus is element specific.⁷⁵ As with PDF, XAS requires synchrotron radiation which limits use of the

technique. XAS has been used to determine Cl-C bonding on a graphite electrode,⁷⁶ provide information on the behaviour of a sulfur electrode in a lithium sulfur battery,⁷⁷ and deduce structural changes in a mixed oxide lithium cathode.⁷⁸

1.3.1.3 X-ray Micro-Computed Tomography

X-ray micro-computed tomography (micro-CT) provides three-dimensional (3D) structural information about a sample on the micrometre scale.⁷⁹ Image contrast is obtained by X-ray attenuation of the sample and acquisition time is on the order of minutes to hours.⁷⁹ Micro-CT is often performed using synchrotron radiation, and, as with other synchrotron radiation techniques, this restricts the accessibility which is further limited by the use of a specific sample holder for the battery.⁸⁰ The structural information provided has enabled investigation into electrode degradation,⁸¹ dendrite growth in solid-state batteries,⁸² and changes in electrode porosity.⁸³

1.3.2 Surface Microscopy Techniques

Surface microscopy experiments interrogate the chemistry that occurs within a small segment of material. Resolution can be down to the molecular and atomic scale and in 3D for some techniques.⁸⁴ The high resolution can aid with characterisation of processes that occur in

materials with defects and investigate the impact of defects, such as cracks, can be targeted for characterisation.

1.3.2.1 Scanning Electron Microscopy

Scanning electron microscopy (SEM) is an imaging technique that has been used to characterise dendrite formation,^{82, 85} monitor the decomposition of NaO₂ crystals in a Na-O₂ battery,⁸⁶ and visualise morphological transitions on metal anodes.⁸⁷ SEM is an invasive technique as it requires a specific cell to be constructed, hence the structures recorded may not be representative of what is present in the battery during cycling.

1.3.2.2 Atomic Force Microscopy

Atomic force microscopy (AFM) has been used to characterise the surface of a material and provide spatially resolved chemical information. It requires an open cell geometry and is therefore not necessarily representative of a full battery system. Recently, the AFM cantilever has been incorporated as an active component to control the battery process on a microscale enabling the characterisation of surface changes, such as the growth of the SEI, with greater detail.⁸⁸ Furthermore, AFM has been used to determine the diffusion coefficient of lithium in a single active

material particle⁸⁹ and confirm the nucleation and growth mechanism of an anion-derived SEI.⁹⁰

1.3.2.3 Scanning Electrochemical Cell Microscopy

Scanning electrochemical cell microscopy (SECCM) moves a droplet of electrolyte and the electrode across a surface and performs electrochemistry in the electrolyte droplet, thus characterising the electrochemistry in two-dimensions (2D) at a specified position on the electrode surface.⁹¹ The resolution is on the order of 10s of micrometres and the level of detection can be improved to less than 10 nm.⁹¹ SECCM measures either current or potential and is performed in a different electrochemical setup than a typical battery, thus it is an invasive technique. However, SECCM can provide information on the electrochemistry that occurs on a single particle. SECCM has been used to monitor the electrochemical performance of a particle,⁹² visualise inhomogeneities in current distribution,⁹³ and provide information on the diffusion coefficient on a thin-film electrode.⁹⁴

1.3.3 Magnetic Resonance Techniques

Magnetic resonance (MR) methodologies can provide a wealth of information with respect to chemical speciation and interaction, and, in

the case of magnetic resonance imaging (MRI), these properties can be spatially resolved.⁹⁵

1.3.3.1 Nuclear Magnetic Resonance Spectroscopy

NMR spectroscopy has been used extensively to study battery chemistry in electrolytes and electrodes using many electroactive nuclei, for example ^1H , ^{19}F , $^6,^7\text{Li}$ and ^{23}Na .⁹⁶⁻⁹⁸ However, as the radio frequency radiation is not able to penetrate metals beyond a skin-depth ($\sim 10^{-5}$ m),⁹⁹ it is essential that magnetic resonance studies employ cells that are not encased in metal;¹⁰⁰ a variety of plastic, NMR compatible battery designs have been reported in the literature to overcome this issue.^{97, 100-105} The implementation of MR techniques for *in situ* and *operando* battery investigations is discussed further in Chapter 2.2.

In LIBs and NIBs, electroactive species can be detected directly across both electrolytic and metallic environments in both the electrolyte and battery electrodes.^{98, 106, 107} In LIBs, ^6Li and ^7Li NMR spectroscopy has been used to investigate the growth of lithium dendrite structures.^{105, 107} Furthermore, properties of the electrolyte, such as diffusion and transport number,^{97, 108-111} have been studied using ^7Li NMR spectroscopy and degradation products elucidated using ^{13}C and ^1H NMR spectroscopy.¹¹² Additional studies have investigated SEI chemistry, probing its growth^{113, 114} and structure.¹¹⁵⁻¹¹⁷ To fully understand the processes that occur

during battery cycling, *operando* techniques have been employed.¹¹⁸

Operando techniques have provided information on lithium full cell function,¹¹⁹ microstructure formation,¹⁰⁵ and of overcharging mechanisms in both LIBs and NIBs.¹²⁰

In the case of NIBs, NMR studies have largely relied on *in situ* and *ex situ* ²³Na NMR spectroscopy.¹²¹⁻¹²³ *Ex situ* studies are performed on battery components after the electrochemistry has been performed and the cell disassembled whilst *in situ* studies are performed on the battery before disassembly, typically whilst maintaining a cell potential. *Ex situ* ²³Na NMR spectroscopy has been used to investigate cluster sizes of quasimetallic species formed inside different hard carbon materials.¹²³ *Ex situ* ²³Na NMR spectroscopy, combined with *in situ* XRD mapping and electron paramagnetic resonance (EPR) techniques, has been used to study the sodiation mechanism of hard carbon in a sodium metal cell.⁷⁰ Recently, *in situ* ²³Na NMR spectroscopy has been used to investigate the formation of high surface area mossy and dendritic sodium microstructures during cell cycling,¹²¹ identify different sodium crystallographic sites^{71, 124} and sodium states in hard carbon materials.¹²² Furthermore, ²³Na NMR spectroscopy has previously been used to investigate sodium metal deposition during cell cycling¹²¹ and identify different sodium environments in electrode materials.^{71, 122, 124} *Operando* ²³Na NMR spectroscopy has been used with

ex situ SSNMR and PDF to provide insight into the insertion of sodium into hard carbon.²⁷

1.3.3.2 Magnetic Resonance Imaging

Magnetic resonance imaging (MRI) is non-invasive and able to provide spatially-resolved physical and chemical information. Furthermore, MRI is complementary to other imaging techniques by providing combined information on multiple battery components such as electrode materials, electrolyte materials, and charge carrying ions in both the electrode and electrolyte.^{95, 98, 113, 125, 126} MRI has the advantage of being able to detect magnetic resonance active nuclei within the electrodes and electrolyte, enabling a more holistic view of battery behaviour.^{125, 127} In addition to changes in the construction of the cell, the switching of radio frequency (RF) and magnetic field gradient pulses, which can induce Eddy currents, can cause variations in RF (B_1) and magnetic field (B_0) fields, leading to image artefacts.^{100, 128, 129} Hence, it is necessary to align metallic components, such as current collectors and electrodes, with respect to both B_1 and B_0 fields.¹⁶ The challenges of performing MRI on batteries is discussed further in Chapter 2.2.2.

Dendrites have been visualised directly using ^7Li MRI^{130, 131} and indirectly, by generating negative images, using signal from the ^1H in the electrolyte.¹²⁶ Both 2D and 3D ^7Li MRI of dendrites have been

performed.¹³¹ ^7Li MRI has been used to study dendrite growth mechanisms. Chang *et al.* correlate depletion in lithium in the electrolyte with dendrite growth at high charge rates and not at low charge rates.¹⁰⁶ Additionally, this study also observed the formation of mossy lithium microstructures before dendrite growth.¹⁰⁶

Furthermore, mass transport and cell polarisation have been monitored *in situ* using a combination of indirect detection, by ^1H and ^{19}F MRI, or direct detection of the charge carrier, by ^7Li MRI.^{97, 132-135} The magnetic field around a battery has also been observed to change and ^1H MRI of water surrounding a lithium battery has shown to be sensitive to the state of charge of a cell.¹³⁶ Other battery chemistries have been investigated using indirect detection of the electrolyte, where the electroactive species is either not MR active or its MR properties are inhibitive to its use. For example, ^1H MRI has been used to investigate the distribution of zinc species during the operation of a zinc-air cell.¹³⁷

While ^{23}Na NMR spectroscopy has proved useful for identifying species during charge cycling, the use of ^{23}Na MRI to directly visualise the distribution of electroactive species comes with additional difficulties. ^{23}Na has a lower receptivity, due to its low gyromagnetic ratio, compared to ^1H ,¹³⁸ resulting in a lower signal-to-noise ratio (SNR) and greater signal averaging. Moreover, as ^{23}Na is quadrupolar, it typically has significantly

shorter relaxation times than ^1H and even ^7Li . Despite the challenges, NIB chemistry has been monitored directly by MRI, using the ^{23}Na MR signal of the electroactive species,^{98, 139} or indirectly, using the ^1H or ^{19}F MR signal of the electrolyte.^{96, 97, 126} Sodium dendrites have been visualised in sodium metal cells directly, using signal from metallic ^{23}Na ,^{82, 139} and indirectly, using ^1H signal from the electrolyte.⁹⁸ Dendrites have also been imaged in a solid-state battery using T_2 relaxation time weighted ^{23}Na MRI in combination with micro-CT and SEM.⁸² The use of T_2 weighted images allows for a dendrite that is smaller than the MRI resolution to be observed. Furthermore, the ^{23}Na T_2 NMR relaxation time of the dendrite was found to be longer than that of the bulk metal electrode as was associated with increased sodium dynamics in the dendrite.⁸²

This thesis will expand on current MR methodologies in the study of various battery chemistries. Methodology will be developed to enable the visualisation of water ingress in an IL containing zinc for use in ZIBs using T_1 relaxation time mapping. The intercalation mechanism in NIBs will then be investigated using *operando* ^{23}Na NMR spectroscopy. This methodology is implemented using *operando* ^7Li NMR spectroscopy to examine the evolution of lithium species in a LIB. Finally, the speciation of aluminium in ionic liquid and aqueous electrolytes for AIBs will be investigated using ^{27}Al and ^1H NMR spectroscopy.

1.4 References

1. M. M. Thackeray, C. Wolverton and E. D. Isaacs, *Energy Environ. Sci.*, 2012, 5.
2. J. B. Goodenough and K. S. Park, *J. Am. Chem. Soc.*, 2013, 135, 1167-1176.
3. J. Y. Hwang, S. T. Myung and Y. K. Sun, *Chem. Soc. Rev.*, 2017, 46, 3529-3614.
4. N. Zhang, X. Chen, M. Yu, Z. Niu, F. Cheng and J. Chen, *Chem. Soc. Rev.*, 2020, 49, 4203-4219.
5. S. K. Das, S. Mahapatra and H. Lahan, *J. Mater. Chem. A*, 2017, 5, 6347-6367.
6. A. K. Padhi, K. S. Nanjundaswamy and J. B. Goodenough, *J. Electrochem. Soc.*, 1997, 144, 1184-1194.
7. X. Su, F. Dogan, J. Ilavsky, V. A. Maroni, D. J. Gosztola and W. Lu, *Chem. Mater.*, 2017, 29, 6205-6213.
8. S. Doubaji, B. Philippe, I. Saadoun, M. Gorgoi, T. Gustafsson, A. Solhy, M. Valvo, H. Rensmo and K. Edstrom, *ChemSusChem*, 2016, 9, 97-108.
9. X. B. Cheng, R. Zhang, C. Z. Zhao and Q. Zhang, *Chem. Rev.*, 2017, 117, 10403-10473.
10. P. B. Balbuena, *AIP Conference Proceedings*, 2014, 1597, 82-97.
11. S. J. An, J. Li, C. Daniel, D. Mohanty, S. Nagpure and D. L. Wood, *Carbon*, 2016, 105, 52-76.
12. L. Cabo-Fernandez, F. Mueller, S. Passerini and L. J. Hardwick, *Chem. Commun.*, 2016, 52, 3970-3973.
13. R. Dugas, A. Ponrouch, G. Gachot, R. David, M. R. Palacin and J. M. Tarascon, *J. Electrochem. Soc.*, 2016, 163, A2333-A2339.
14. M. A. Hope, B. L. D. Rinkel, A. B. Gunnarsdottir, K. Marker, S. Menkin, S. Paul, I. V. Sergeyev and C. P. Grey, *Nat. Commun.*, 2020, 11, 2224.

15. A. Patil, V. Patil, D. Wook Shin, J.-W. Choi, D.-S. Paik and S.-J. Yoon, *Mater. Res. Bull.*, 2008, 43, 1913-1942.
16. A. B. Gunnarsdottir, C. V. Amanchukwu, S. Menkin and C. P. Grey, *J. Am. Chem. Soc.*, 2020, 142, **20814–20827**.
17. J. Steiger, D. Kramer and R. Mönig, *Electrochim. Acta*, 2014, 136, 529-536.
18. I. Yoshimatsu, T. Hirai and J.-i. Yamaki, *J. Electrochem. Soc.*, 1988, 135, 2422-2427.
19. A. D. Pathak, K. Samanta, K. K. Sahu and S. Pati, *J. Appl. Electrochem.*, 2020, 51, 143-154.
20. S. Heng, X. Shan, W. Wang, Y. Wang, G. Zhu, Q. Qu and H. Zheng, *Carbon*, 2020, 159, 390-400.
21. K. J. Griffith, Y. Harada, S. Egusa, R. M. Ribas, R. S. Monteiro, R. B. Von Dreele, A. K. Cheetham, R. J. Cava, C. P. Grey and J. B. Goodenough, *Chem. Mater.*, 2020, 33, 4-18.
22. Y. Chen, Y. Kang, Y. Zhao, L. Wang, J. Liu, Y. Li, Z. Liang, X. He, X. Li, N. Tavajohi and B. Li, *J. Energy Chem.*, 2021, 59, 83-99.
23. E. Irisarri, A. Ponrouch and M. R. Palacin, *J. Electrochem. Soc.*, 2015, 162, A2476-A2482.
24. A. Vyalikh, V. O. Koroteev, W. Munchgesang, T. Kohler, C. Roder, E. Brendler, A. V. Okotrub, L. G. Bulusheva and D. C. Meyer, *ACS Appl. Mater. Interfaces*, 2019, 11, 9291-9300.
25. **H. Au, H. Alptekin, A. C. S. Jensen, E. Olsson, C. A. O’Keefe, T. Smith, M. Crespo-Ribadeneyra, T. F. Headen, C. P. Grey, Q. Cai, A. J. Drew and M.-M. Titirici, *Energy Environ. Sci.*, 2020, 13, 3469-3479.**
26. J. S. Weaving, A. Lim, J. Millichamp, T. P. Neville, D. Ledwoch, E. Kendrick, P. F. McMillan, P. R. Shearing, C. A. Howard and D. J. L. Brett, *ACS Appl. Energy Mater.*, 2020, 3, 7474-7484.
27. J. M. Stratford, P. K. Allan, O. Pecher, P. A. Chater and C. P. Grey, *Chem. Commun.*, 2016, 52, 12430-12433.

28. K. Bass, P. J. Mitchell, G. D. Wilcox and J. Smith, *J. Power Sources*, 1991, 35, 333-351.
29. N. Liu, B. Li, Z. He, L. Dai, H. Wang and L. Wang, *J. Energy Chem.*, 2021, 59, 134-159.
30. T. H. Wu and W. Y. Liang, *ACS Appl. Mater. Interfaces*, 2021, 13, 23822-23832.
31. D. Kundu, B. D. Adams, V. Duffort, S. H. Vajargah and L. F. Nazar, *Nat. Energy*, 2016, 1.
32. D. Batyrbekuly, B. Laïk, J.-P. Pereira-Ramos, Z. Bakenov and R. Baddour-Hadjean, *J. Energy Chem.*, 2021, 61, 459-468.
33. M. Tang, Q. Zhu, P. Hu, L. Jiang, R. Liu, J. Wang, L. Cheng, X. Zhang, W. Chen and H. Wang, *Adv. Funct. Mater.*, 2021.
34. B. Zhao, S. Wang, Q. Yu, Q. Wang, M. Wang, T. Ni, L. Ruan and W. Zeng, *J. Power Sources*, 2021, 504.
35. L. Cao, D. Li, T. Pollard, T. Deng, B. Zhang, C. Yang, L. Chen, J. Vatamanu, E. Hu, M. J. Hourwitz, L. Ma, M. Ding, Q. Li, S. Hou, K. Gaskell, J. T. Fourkas, X. Q. Yang, K. Xu, O. Borodin and C. Wang, *Nat. Nanotechnol.*, 2021, 16, 902-910.
36. A. P. Abbott, G. Frisch and K. S. Ryder, *Annu. Rev. Mater. Res.*, 2013, 43, 335-358.
37. J. L. Anderson, D. W. Armstrong and G.-T. Wei, *Anal. Chem.*, 2006, 78, 2893-2902.
38. A. P. Abbott and K. J. McKenzie, *Phys. Chem. Chem. Phys.*, 2006, 8, 4265-4279.
39. Z. Liu, S. Zein El Abedin, N. Borisenko and F. Endres, *ChemElectroChem*, 2015, 2, 1159-1163.
40. Z. Liu, T. Cui, T. Lu, M. Shapouri Ghazvini and F. Endres, *J. Phys. Chem. C*, 2016, 120, 20224-20231.
41. Z. Liu, G. Li, T. Cui, A. Lahiri, A. Borodin and F. Endres, *Phys. Chem. Chem. Phys.*, 2017, 19, 25989-25995.
42. Z. Liu, G. Pulletikurthi, A. Lahiri, T. Cui and F. Endres, *Dalton Trans.*, 2016, 45, 8089-8098.

43. Z. Liu, S. Z. E. Abedin and F. Endres, *Electrochim. Acta*, 2013, 89, 635-643.
44. N. N. Greenwood and A. Earnshaw, *Chemistry of the Elements*, Butterworth-Heinemann, Oxford, 2 edn., 1997.
45. J. Wysocka, M. Cieslik, S. Krakowiak and J. Ryl, *Electrochim. Acta*, 2018, 289, 175-192.
46. P. Bhauriyal, A. Mahata and B. Pathak, *Phys. Chem. Chem. Phys.*, 2017, 19, 7980-7989.
47. R. D. McKerracher, A. Holland, A. Cruden and R. G. A. Wills, *Carbon*, 2019, 144, 333-341.
48. S. I. Pyun and S. M. Moon, *J. Solid State Electrochem.*, 2000, 4, 267-272.
49. A. Mukherjee and I. N. Basumallick, *J. Power Sources*, 1996, 58, 183-187.
50. A. Mukherjee and I. N. Basumallick, *J. Power Sources*, 1992, 37, 411-414.
51. R. Mori, *RSC Adv.*, 2013, 3, 11547-11551.
52. P. K. Shen, A. C. C. Tseung and C. Kuo, *J. Power Sources*, 1994, 47, 119-127.
53. R. Mori, *RSC Adv.*, 2014, 4, 1982-1987.
54. R. Mori, *Sustain. Energ. Fuels*, 2017, 1, 1082-1089.
55. R. Mori, *ECS Trans.*, 2017, 80, 377-393.
56. R. Mori, *J. Appl. Electrochem.*, 2015, 45, 821-829.
57. A. A. Mahazar, S. T. Arab and E. A. Noor, *Bull. Electrochem.*, 2001, 17, 449-458.
58. R. Mori, *J. Electron. Mater.*, 2016, 45, 3375-3382.
59. J. R. González, F. Nacimiento, M. Cabello, R. Alcántara, P. Lavela and J. L. Tirado, *RSC Adv.*, 2016, 6, 62157-62164.
60. A. Holland, R. D. McKerracher, A. Cruden and R. G. A. Wills, *J. Appl. Electrochem.*, 2018, 48, 243-250.
61. P. Wasserscheid and T. Welton, *Ionic Liquids in Synthesis*, Wiley VCH, Weinheim, 2003.

62. F. M. Donahue, S. E. Mancini and L. Simonsen, *J. Appl. Electrochem.*, 1992, 22, 230-234.
63. P. C. Trulove and R. A. Osteryoung, *Inorg. Chem.*, 1992, 31, 3980-3985.
64. T. Jiang, M. J. Chollier Brym, G. Dubé, A. Lasia and G. M. Brisard, *Surf. Coat. Technol.*, 2006, 201, 1-9.
65. E. Berretti, A. Giaccherini, S. M. Martinuzzi, M. Innocenti, T. J. S. Schubert, F. M. Stiemke and S. Caporali, *Materials*, 2016, 9, 719-733.
66. L. D. Reed and E. Menke, *J. Electrochem. Soc.*, 2013, 160, A915-A917.
67. S. Zein El Abedin, E. M. Moustafa, R. Hempelmann, H. Natter and F. Endres, *ChemPhysChem*, 2006, 7, 1535-1543.
68. S. Caporali, S. M. Martinuzzi, P. Von Czarnecki, T. J. S. Schubert and U. Bardi, *J. Mater. Eng. Perform.*, 2017, 26, 685-691.
69. R. Mori, *RSC Adv.*, 2019, 9, 22220-22226.
70. S. Qiu, L. F. Xiao, M. L. Sushko, K. S. Han, Y. Y. Shao, M. Y. Yan, X. M. Liang, L. Q. Mai, J. W. Feng, Y. L. Cao, X. P. Ai, H. X. Yang and J. Liu, *Adv. Energy Mater.*, 2017, 7, 1700403.
71. Q. Li, Z. Liu, F. Zheng, R. Liu, J. Lee, G. L. Xu, G. Zhong, X. Hou, R. Fu, Z. Chen, K. Amine, J. Mi, S. Wu, C. P. Grey and Y. Yang, *Angew. Chem. Int. Ed.*, 2018, 57, 11918-11923.
72. Y. Ren and X. Zuo, *Small Methods*, 2018, 2, 1800064.
73. J. M. Stratford, M. Mayo, P. K. Allan, O. Pecher, O. J. Borkiewicz, K. M. Wiaderek, K. W. Chapman, C. J. Pickard, A. J. Morris and C. P. Grey, *J. Am. Chem. Soc.*, 2017, 139, 7273-7286.
74. D. Dambournet, K. W. Chapman, M. Duttine, O. Borkiewicz, P. J. Chupas and H. Groult, *ChemistryOpen*, 2015, 4, 443-447.
75. G. Cibir, D. Gianolio, S. A. Parry, T. Schoonjans, O. Moore, R. Draper, L. A. Miller, A. Thoma, C. L. Doswell and A. Graham, *Radiat. Phys. Chem.*, 2020, 175, 108479.

76. D. Y. Wang, C. Y. Wei, M. C. Lin, C. J. Pan, H. L. Chou, H. A. Chen, M. Gong, Y. Wu, C. Yuan, M. Angell, Y. J. Hsieh, Y. H. Chen, C. Y. Wen, C. W. Chen, B. J. Hwang, C. C. Chen and H. Dai, *Nat. Commun.*, 2017, 8, 14283.
77. M. U. Patel, I. Arcon, G. Aquilanti, L. Stievano, G. Mali and R. Dominko, *ChemPhysChem*, 2014, 15, 894-904.
78. T. Kim, B. Song, A. J. G. Lunt, G. Cibir, A. J. Dent, L. Lu and A. M. Korsunsky, *Mater. Des.*, 2016, 98, 231-242.
79. A. du Plessis, C. Broeckhoven, A. Guelpa and S. G. le Roux, *Gigascience*, 2017, 6, 1-11.
80. C. Tan, S. R. Daemi, O. O. Taiwo, T. M. M. Heenan, D. J. L. Brett and P. R. Shearing, *Materials*, 2018, 11.
81. P. Trogadas, O. O. Taiwo, B. Tjaden, T. P. Neville, S. Yun, J. Parrondo, V. Ramani, M.-O. Coppens, D. J. L. Brett and P. R. Shearing, *Electrochem. Commun.*, 2014, 48, 155-159.
82. G. J. Rees, D. Spencer Jolly, Z. Ning, T. J. Marrow, G. E. Pavlovskaya and P. G. Bruce, *Angew. Chem. Int. Ed.*, 2021, 60, 2110-2115.
83. F. R. Brushett, L. Trahey, X. Xiao and J. T. Vaughey, *ACS Appl. Mater. Interfaces*, 2014, 6, 4524-4534.
84. A. F. Raigoza, J. W. Dugger and L. J. Webb, *ACS Appl. Mater. Interfaces*, 2013, 5, 9249-9261.
85. M. Golozar, P. Hovington, A. Paoletta, S. Bessette, M. Lagace, P. Bouchard, H. Demers, R. Gauvin and K. Zaghib, *Nano. Lett.*, 2018, 18, 7583-7589.
86. T. Liu, G. Kim, M. T. Casford and C. P. Grey, *J. Phys. Chem. Lett.*, 2016, 7, 4841-4846.
87. C. M. López, J. T. Vaughey and D. W. Dees, *J. Electrochem. Soc.*, 2009, 156, 726-729.
88. W. J. Legerstee, M. Boekel, S. Boonstra and E. M. Kelder, *Front. Chem.*, 2021, 9, 505876.

89. D. Renz, M. Cronau and B. Roling, *J. Phys. Chem. C*, 2021, 125, 2230-2239.
90. C. Yan, L. L. Jiang, Y. X. Yao, Y. Lu, J. Q. Huang and Q. Zhang, *Angew. Chem. Int. Ed.*, 2021, 60, 8521-8525.
91. O. J. Wahab, M. Kang and P. R. Unwin, *Curr. Opin. Electrochem.*, 2020, 22, 120-128.
92. B. Tao, L. C. Yule, E. Daviddi, C. L. Bentley and P. R. Unwin, *Angew. Chem. Int. Ed.*, 2019, 58, 4606-4611.
93. H. Inomata, Y. Takahashi, D. Takamatsu, A. Kumatani, H. Ida, H. Shiku and T. Matsue, *Chem. Commun.*, 2019, 55, 545-548.
94. Y. Takahashi, T. Yamashita, D. Takamatsu, A. Kumatani and T. Fukuma, *Chem. Commun.*, 2020, 56, 9324-9327.
95. M. M. Britton, *Chem. Soc. Rev.*, 2010, 39, 4036-4043.
96. J. M. Bray, A. J. Davenport, K. S. Ryder and M. M. Britton, *Angew. Chem. Int. Ed.*, 2016, 55, 9394-9397.
97. S. A. Krachkovskiy, J. D. Bazak, P. Werhun, B. J. Balcom, I. C. Halalay and G. R. Goward, *J. Am. Chem. Soc.*, 2016, 138, 7992-7999.
98. J. M. Bray, C. L. Doswell, G. E. Pavlovskaya, L. Chen, B. Kishore, H. Au, H. Alptekin, E. Kendrick, M. M. Titirici, T. Meersmann and M. M. Britton, *Nat. Commun.*, 2020, 11, 2083.
99. A. J. Illott, S. Chandrashekar, A. Klockner, H. J. Chang, N. M. Trease, C. P. Grey, L. Greengard and A. Jerschow, *J. Magn. Reson.*, 2014, 245, 143-149.
100. M. M. Britton, *ChemPhysChem*, 2014, 15, 1731-1736.
101. S. Wiemers-Meyer, M. Winter and S. Nowak, *Phys. Chem. Chem. Phys.*, 2017, 19, 4962-4966.
102. Z.-R. Ni, X.-H. Cui, S.-H. Cao and Z. Chen, *AIP Adv.*, 2017, 7, 085205.
103. S. Benders, B. F. Gomes, M. Carmo, L. A. Colnago and B. Blumich, *J. Magn. Reson.*, 2020, 312, 106692.

104. J. D. Bazak, S. A. Krachkovskiy and G. R. Goward, *J. Phys. Chem. C*, 2017, 121, 20704-20713.
105. S. A. Kayser, A. Mester, A. Mertens, P. Jakes, R. A. Eichel and J. Granwehr, *Phys. Chem. Chem. Phys.*, 2018, 20, 13765-13776.
106. H. J. Chang, A. J. Illott, N. M. Trease, M. Mohammadi, A. Jerschow and C. P. Grey, *J. Am. Chem. Soc.*, 2015, 137, 15209-15216.
107. H. J. Chang, N. M. Trease, A. J. Illott, D. Zeng, L.-S. Du, A. Jerschow and C. P. Grey, *J. Phys. Chem. C*, 2015, 119, 16443-16451.
108. Alexander C. Forse, John M. Griffin, C. Merlet, J. Carretero-Gonzalez, A.-Rahman O. Raji, Nicole M. Trease and Clare P. Grey, *Nat. Energy*, 2017, 2, 16216.
109. J. D. Bazak, J. P. Allen, S. A. Krachkovskiy and G. R. Goward, *J. Electrochem. Soc.*, 2020, 167.
110. A. D. Pauric, I. C. Halalay and G. R. Goward, *Phys. Chem. Chem. Phys.*, 2016, 18, 6657-6667.
111. A. K. Sethurajan, S. A. Krachkovskiy, I. C. Halalay, G. R. Goward and B. Protas, *J. Phys. Chem. B*, 2015, 119, 12238-12248.
112. Y. Jin, N. H. Kneusels and C. P. Grey, *J. Phys. Chem. Lett.*, 2019, 10, 6345-6350.
113. A. J. Illott and A. Jerschow, *J. Phys. Chem. C*, 2018, 122, 12598-12604.
114. A. I. Freytag, A. D. Pauric, S. A. Krachkovskiy and G. R. Goward, *J. Am. Chem. Soc.*, 2019, 141, 13758-13761.
115. Y. Jin, N. H. Kneusels, P. Magusin, G. Kim, E. Castillo-Martinez, L. E. Marbella, R. N. Kerber, D. J. Howe, S. Paul, T. Liu and C. P. Grey, *J. Am. Chem. Soc.*, 2017, 139, 14992-15004.
116. Y. Jin, N. H. Kneusels, L. E. Marbella, E. Castillo-Martinez, P. Magusin, R. S. Weatherup, E. Jonsson, T. Liu, S. Paul and C. P. Grey, *J. Am. Chem. Soc.*, 2018, 140, 9854-9867.
117. M. Leskes, G. Kim, T. Liu, A. L. Michan, F. Aussenac, P. Dorffer, S. Paul and C. P. Grey, *J. Phys. Chem. Lett.*, 2017, 8, 1078-1085.

118. M. Mohammadi and A. Jerschow, *J. Magn. Reson.*, 2019, 308, 106600.
119. K. Marker, C. Xu and C. P. Grey, *J. Am. Chem. Soc.*, 2020, 142, 17447-17456.
120. K. Gotoh, T. Yamakami, I. Nishimura, H. Kometani, H. Ando, K. Hashi, T. Shimizu and H. Ishida, *J. Mater. Chem. A*, 2020, 8, 14472-14481.
121. P. M. Bayley, N. M. Trease and C. P. Grey, *J. Am. Chem. Soc.*, 2016, 138, 1955-1961.
122. R. Morita, K. Gotoh, M. Fukunishi, K. Kubota, S. Komaba, N. Nishimura, T. Yumura, K. Deguchi, S. Ohki, T. Shimizu and H. Ishida, *J. Mater. Chem. A*, 2016, 4, 13183-13193.
123. R. Morita, K. Gotoh, K. Kubota, S. Komaba, K. Hashi, T. Shimizu and H. Ishida, *Carbon*, 2019, 145, 712-715.
124. D. L. Smiley, D. Carlier and G. R. Goward, *Solid State Nucl. Magn. Reson.*, 2019, 103, 1-8.
125. M. M. Britton, *Prog. Nucl. Magn. Reson. Spectrosc.*, 2017, 101, 51-70.
126. A. J. Illott, M. Mohammadi, H. J. Chang, C. P. Grey and A. Jerschow, *Proc. Natl. Acad. Sci. U. S. A.*, 2016, 113, 10779-10784.
127. O. Pecher, J. Carretero-González, K. J. Griffith and C. P. Grey, *Chem. Mater.*, 2017, 29, 213-242.
128. H. Graf, G. Steidle, P. Martirosian, U. A. Lauer and F. Schick, *Med. Phys.*, 2006, 33, 124-127.
129. S. Vashaei, F. Goora, M. M. Britton, B. Newling and B. J. Balcom, *J. Magn. Reson.*, 2015, 250, 17-24.
130. L. E. Marbella, S. Zekoll, J. Kasemchainan, S. P. Emge, P. G. Bruce and C. P. Grey, *Chem. Mater.*, 2019, 31, 2762-2769.
131. S. Chandrashekar, N. M. Trease, H. J. Chang, L. S. Du, C. P. Grey and A. Jerschow, *Nat. Mater.*, 2012, 11, 311-315.

132. M. Klett, M. Giesecke, A. Nyman, F. Hallberg, R. W. Lindstrom, G. Lindbergh and I. Furo, *J. Am. Chem. Soc.*, 2012, 134, 14654-14657.
133. S. Chandrashekar, O. Oparaji, G. Yang and D. Hallinan, *J. Electrochem. Soc.*, 2016, 163, A2988-A2990.
134. P. H. Chien, X. Feng, M. Tang, J. T. Rosenberg, S. O'Neill, J. Zheng, S. C. Grant and Y. Y. Hu, *J. Phys. Chem. Lett.*, 2018, 9, 1990-1998.
135. S. Klamor, K. Zick, T. Oerther, F. M. Schappacher, M. Winter and G. Brunklaus, *Phys. Chem. Chem. Phys.*, 2015, 17, 4458-4465.
136. A. J. Ilott, M. Mohammadi, C. M. Schauerman, M. J. Ganter and A. Jerschow, *Nat. Commun.*, 2018, 9, 1776.
137. M. M. Britton, P. M. Bayley, P. C. Howlett, A. J. Davenport and M. Forsyth, *J. Phys. Chem. Lett.*, 2013, 4, 3019-3023.
138. G. Madelin, J. S. Lee, R. R. Regatte and A. Jerschow, *Prog. Nucl. Magn. Reson. Spectrosc.*, 2014, 79, 14-47.
139. Y. Xiang, G. Zheng, Z. Liang, Y. Jin, X. Liu, S. Chen, K. Zhou, J. Zhu, M. Lin, H. He, J. Wan, S. Yu, G. Zhong, R. Fu, Y. Li and Y. Yang, *Nat. Nanotechnol.*, 2020, 15, 883-890.

2 Experimental Techniques

The combination of magnetic resonance (MR) and electrochemical techniques facilitates the holistic observation of battery chemistry. This chapter will provide a brief overview of the MR and electrochemical techniques used in this thesis.

2.1 Magnetic Resonance Techniques

2.1.1 Nuclear Magnetic Resonance Spectroscopy

Nuclear magnetic resonance (NMR) spectroscopy is a commonly used non-destructive technique to aid in compound identification and the understanding of intermolecular interactions.

2.1.1.1 Radio Frequency Radiation

NMR uses radio frequency (RF) radiation pulses at the Larmor frequency to manipulate the orientation of net magnetisation, M_0 , in a rotating frame of reference by changing the distribution of the nuclear spins across the energy levels available.¹ The tip angle, θ , of M_0 is dictated by the pulse power, B_1 , pulse duration, t_p , and the gyromagnetic ratio of the nucleus, γ (Equation 2.1).^{1, 2}

$$\theta = \frac{360\gamma}{2\pi} B_1 t_p \quad \text{Equation 2.1}$$

A 90° pulse will flip M_0 into the transverse plane resulting in equal populations of the spin-up and spin-down nuclei. The precession of M_0 at the Larmor frequency, whilst in the transverse plane, induces an oscillating voltage in the RF coil; the oscillating voltage produces the free induction decay (FID) which can be Fourier transformed to produce an NMR spectrum.² The amplitude of the oscillating voltage decreases over time due to the return of the nuclear spins to equilibrium via NMR relaxation processes.² Most NMR experiments use a hard pulse with a short duration to excite a range of frequencies, resulting in additional side lobes of excited frequencies (Figure 2.1a).² If a narrow range of frequency excitation is required a soft RF pulse can be used (Figure 2.1b), with a longer duration, producing a selective excitation profile.²

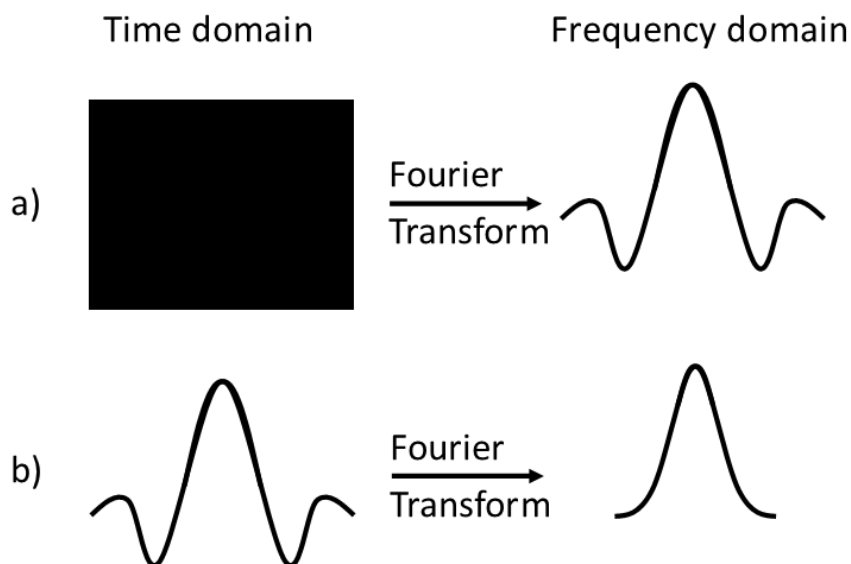


Figure 2.1: Excitation diagram showing the Fourier relationship between the time and frequency domains for a) a hard RF pulse and b) a soft RF pulse.

2.1.1.2 Chemical Shift

The precession rate of NMR active nuclei is dependent upon their chemical environment within a molecule due to magnetic field inhomogeneities created by electron distribution.³ The application of an external magnetic field, B_0 , causes the electrons to move in the molecule and results in a local magnetic field thus changing the magnetic field experienced by different nuclei in the molecule.³ This variation in nuclear precession frequency results in different peaks in the NMR spectrum after Fourier transformation of the FID. Further shifts in frequency precession occur in materials with conducting electrons. These conducting electrons are magnetised and result in a large change in the local magnetic field experienced by the nucleus, known as the Knight shift.⁴ For example, the chemical shift of metallic lithium is ~ 250 ppm,⁵ and metallic sodium is ~ 1010 ppm.^{6, 7} Additionally, the orientation of the metal with respect to B_0 influences the chemical shift observed.^{5, 6}

NMR environments are not always observed as discrete peaks in an NMR spectrum; due to the proximity of frequency and the lifetime of the spin excited state, these peaks can overlap. Overlapping NMR peaks can hinder data interpretation, and so peak deconvolution can be used. The deconvolution performed in this thesis used the minimum number of environments required to accurately reproduce the experimental NMR spectrum. The fitted peaks were a combination of Gaussian and

Lorentzian lineshapes depending on the model fit to the spectrum. NMR signals are typically Lorentzian,² however Gaussian lineshapes can result from a Gaussian distribution of NMR environments. The optimisation algorithm employed compares the model spectrum and the experimental spectrum and uses the quadratic distance between the two to evaluate the spectral fit, and aims to minimise the differences between the model and experimental spectra by incrementally altering the starting model.⁸ More detail on the fitting procedure can be found in reference 8.

2.1.1.3 NMR Relaxation

The rate at which nuclear spins return to thermal equilibrium after excitation by a RF pulse is determined by NMR relaxation processes, T_1 and T_2 .² Longitudinal relaxation, T_1 , is related to the time taken for the distribution of spin-up and spin-down nuclei to return to equilibrium, whilst transverse relaxation, T_2 , is related to the time taken for the nuclear spin to lose phase coherence in the transverse plane.²

2.1.1.4 NMR Relaxation Mechanisms

Both T_1 and T_2 relaxation are caused by oscillations in the local magnetic field, only T_1 relaxation requires oscillations to be at the Larmor frequency.⁹ The local magnetic field can be influenced by molecular motion, dipolar coupling which can be affected by the presence of paramagnetic species, chemical shift anisotropy, and quadrupolar

relaxation.² Dipolar coupling, the coupling of spins through the interaction of the magnetic field, is dependent upon the distance between the spins and the angle of the vector between the spins relative to B_0 .² Unpaired electrons on paramagnetic species influence relaxation due to the large magnetic moment, for example the dipolar coupling in water is increased by the presence of paramagnetic ions. Quadrupolar relaxation is experienced only by nuclei with spin, I , greater than $1/2$, such as ^{23}Na ($I = 3/2$), ^7Li ($I = 1$), and ^{27}Al ($I = 5/2$), and is caused by electric field gradients at the nucleus.^{10, 11} Quadrupolar nuclei have a magnetic dipole moment and an electric quadrupole moment as the charge surrounding the nucleus is not symmetrical.² Hence, electric field gradients, and not symmetrical electric fields, in the vicinity of the nucleus can influence the quadrupole moment.² As the molecule rotates and moves in solution the electric field gradient changes which, if it occurs at the correct frequency, promotes nucleus flipping and stimulates relaxation.² For quadrupolar nuclei, quadrupolar relaxation is often the dominant relaxation mechanism.

The local magnetic field experienced by the spins changes over time due to the tumbling of the molecules.² The rotational correlation time, τ_c , is the average time taken for a molecule to rotate by one radian and is related to the molecular tumbling.² The spectral density, $J(\omega)$, is the

frequency distribution of magnetic fields related to τ_c and is given by Equation 2.2.²

$$J(\omega) = \frac{2\tau_c}{1 + \omega^2\tau_c^2} \quad \text{Equation 2.2}$$

T_1 relaxation occurs when the magnetic field experienced by spins oscillates at or near the Larmor frequency, therefore the T_1 relaxation time is shorter where there is a greater density of the magnetic field oscillation.² Maximum T_1 relaxation will occur when the molecular motion is the same as the Larmor frequency. Figure 2.2 shows the relationship between rotational correlation time and MR relaxation time. Short rotational correlation times, and hence rapid molecular motion, result in a greater range of frequencies, thus decreasing the probability of oscillations at the Larmor frequency and increasing the T_1 relaxation time.² Long rotational correlation times and slow molecular motion will also result in a greater range of frequencies and increase the T_1 relaxation time. Rapid T_1 relaxation occurs at the point where there is the greatest frequency density of oscillations at the Larmor frequency.^{1, 2} T_2 relaxation requires the magnetic fields to oscillate at the Larmor frequency and is also stimulated by non-oscillating local magnetic fields.² Hence, T_2 relaxation increases with respect to molecular tumbling and is more sensitive to magnetic susceptibility, viscosity, and temperature.^{2, 12}

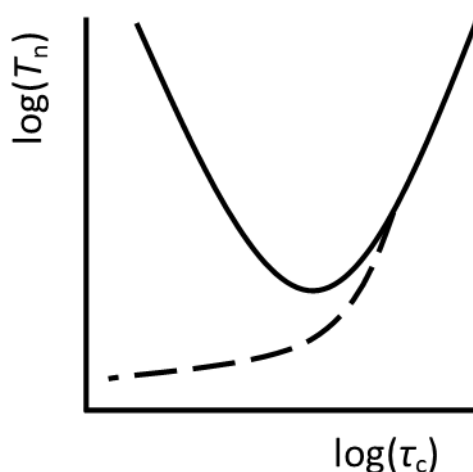


Figure 2.2: A graph showing the relationship between rotational correlation time (τ_c) and MR relaxation times (T_n) for T_1 (solid line) and T_2 (dashed line).

2.1.1.5 Measuring T_1 NMR Relaxation Times

T_1 relaxation time is measured using either an inversion recovery (IR) or saturation recovery (SR) pulse sequence.¹³ Both experiments allow the nuclei to return to their equilibrium state after excitation, but the initial preparation of the magnetisation differs.

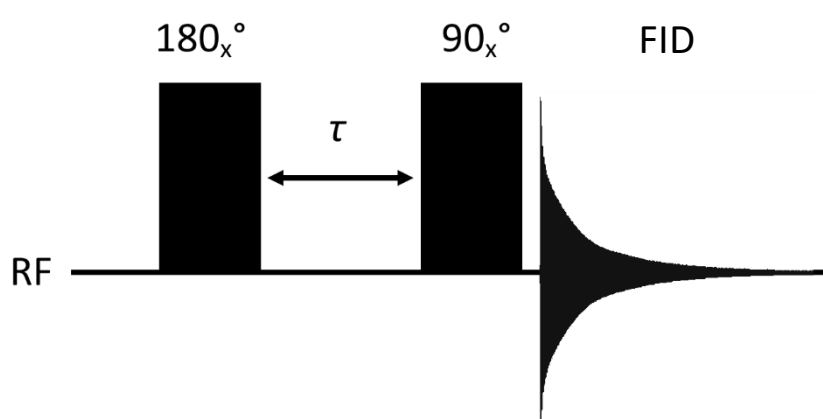


Figure 2.3: A schematic diagram of an IR pulse sequence.

Figure 2.3 is a schematic diagram of an IR pulse sequence. The net magnetisation M_0 is first inverted along the $-z$ axis before a recovery time, τ , a 90° excitation pulse, and signal acquisition. The experiment is repeated with a range of recovery delays. The integral of the NMR signal is then plotted against the recovery delay time, resulting in a graph of signal intensities (Figure 2.4).² The recovery curve is fit using Equation 2.3.² Fitting IR data may involve the calculation of an offset, c , due to inaccuracies in the 180° pulse. The resulting T_1 relaxation time is dependent upon the accurate determination of the offset.

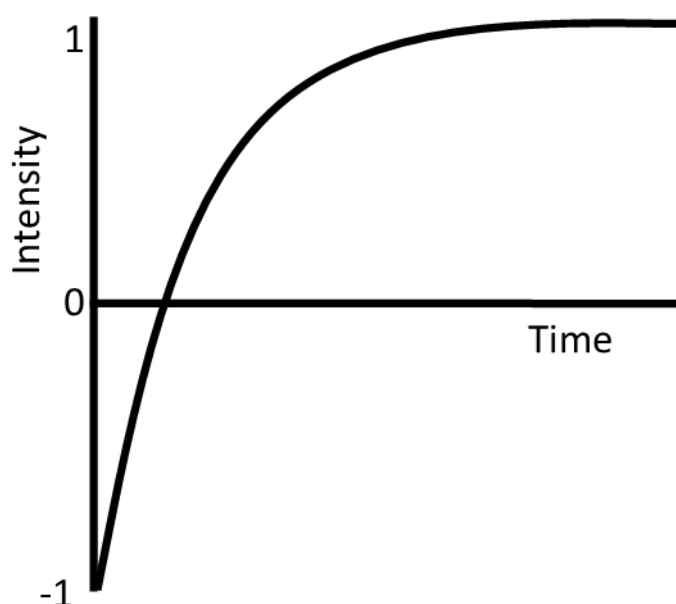


Figure 2.4: An example graph of signal intensity versus time for an IR pulse sequence

$$M_z(t) = M_z \left(1 - 2e^{\frac{-t}{T_1}} \right) + c \quad \text{Equation 2.3}$$

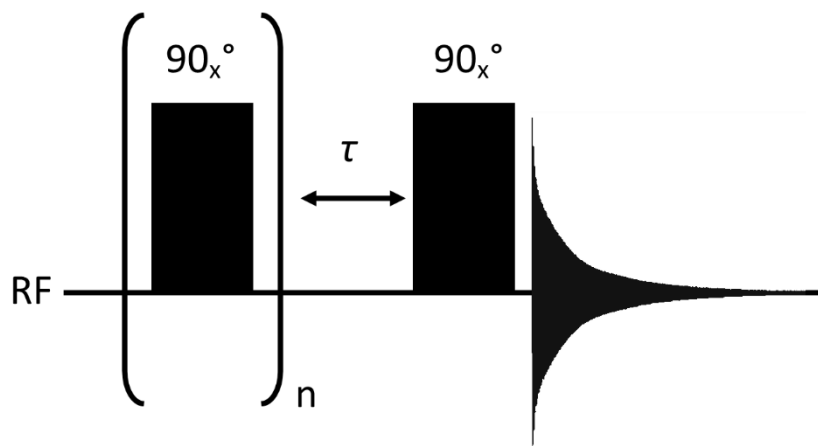


Figure 2.5: A schematic diagram of a SR pulse sequence.

SR differs from IR in that the net magnetisation is first destroyed by the application of numerous 90° pulses or spoiler gradients.¹³ The recovery time, τ , is varied and acquisition of the final signal is the same as in IR (Figure 2.5). The recovery curve (Figure 2.6), starting from zero intensity, is fit using Equation 2.4. No offset is required as the magnetisation is always destroyed at the start of the experiment and so the fitted curve always passes through zero.

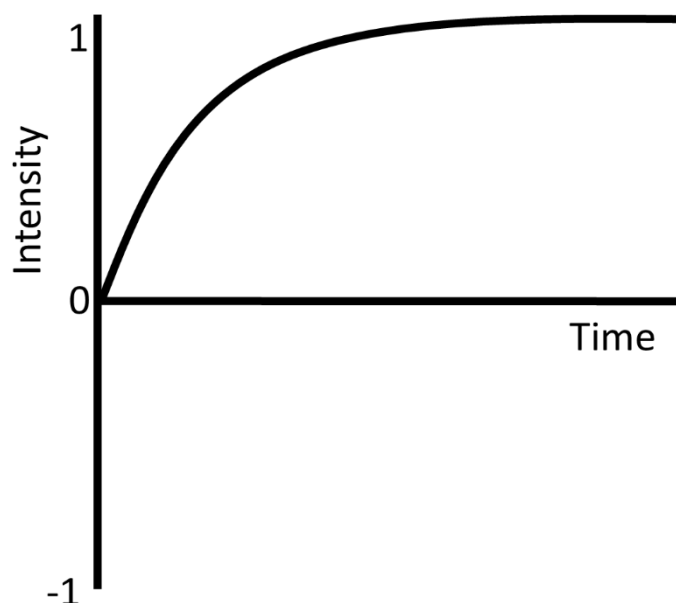


Figure 2.6: An example graph of signal intensity versus time for a SR pulse.

$$M_z(t) = M_z(1 - e^{-\frac{t}{T_1}}) \quad \text{Equation 2.4}$$

2.1.1.6 Measuring T_2 NMR Relaxation Times

Whilst in the transverse plane, T_2 relaxation causes spins to lose phase coherence, reducing the signal to zero over time.¹ Phase coherence loss is caused by both the inhomogeneity in \mathbf{B}_0 , $T_{2(\Delta B_0)}$, and variations in the local magnetic field, T_2 ; the sum of these factors is represented by T_2^* (Equation 2.5).²

$$\frac{1}{T_2^*} = \frac{1}{T_2} + \frac{1}{T_{2(\Delta B_0)}} \quad \text{Equation 2.5}$$

T_2^* is inversely related to the full width at half maximum (FWHM), $\nu_{1/2}$, of peaks in NMR spectra (Equation 2.6).

$$\nu_{1/2} = \frac{1}{\pi T_2^*} \quad \text{Equation 2.6}$$

T_2 relaxation can be measured using a spin-echo pulse sequence (Figure 2.7) where the nuclear spins are first excited by a 90° pulse into the transverse plane and phase coherence is lost during time τ due to inhomogeneity in \mathbf{B}_0 , $T_{2(\Delta B_0)}$. The spins are then refocussed by a 180° pulse; spins that dephased during τ will not be fully refocussed causing signal attenuation, whereas spins that maintained phase coherence will be fully refocussed. The NMR signal is recorded after a second τ duration. The attenuation of the NMR signal in the spin-echo pulse sequence is susceptible to diffusion as the location of the nucleus changes during τ and may experience a variation in \mathbf{B}_0 .

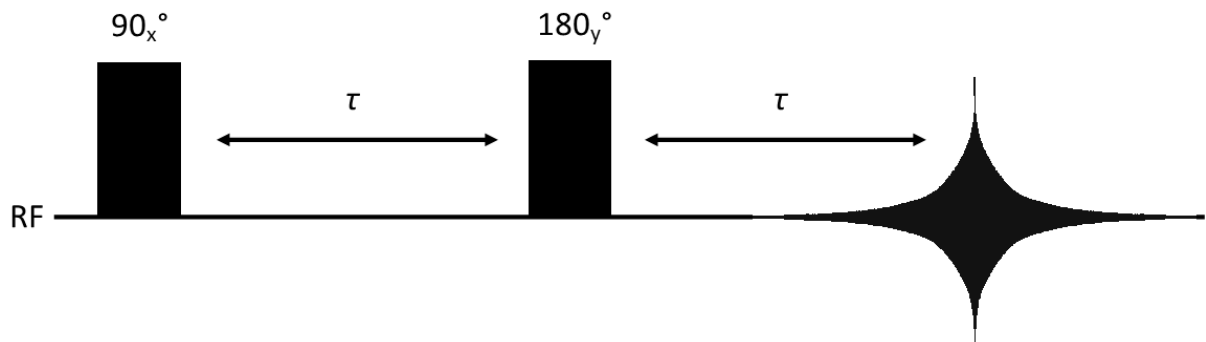


Figure 2.7: A schematic diagram of a spin-echo pulse sequence.

To reduce the effects of diffusion observed in a spin-echo pulse sequence,¹⁴⁻¹⁶ the true T_2 relaxation time can be measured using a Carr-Purcell-Meiboom-Gill (CPMG) pulse sequence; a 90° pulse puts the magnetisation into the transverse plane and is repeatedly refocused by a

180° pulse, with an echo time, τ , after which the FID is acquired (Figure 2.8).² The experiment is repeated with different values of n , resulting in a signal intensity plot (Figure 2.9). The T_2 relaxation time is obtained from a fit of this signal intensity data using Equation 2.7.²

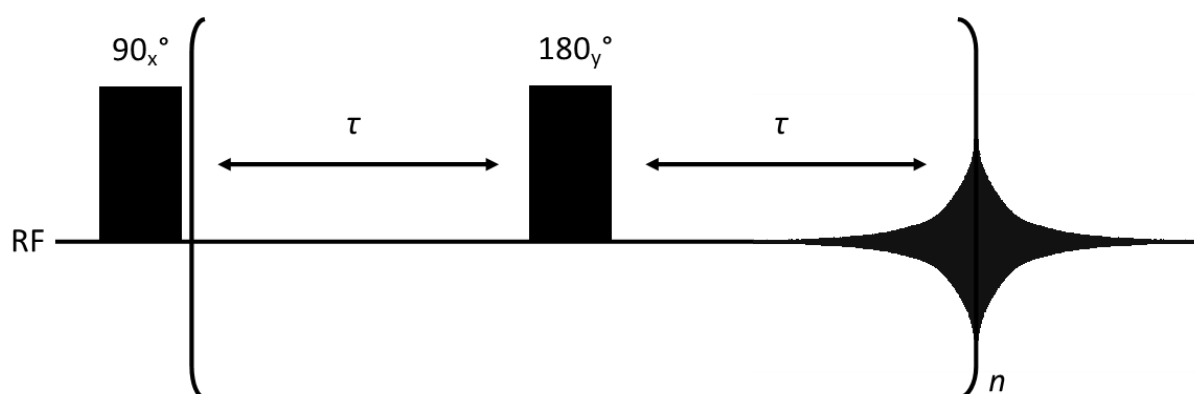


Figure 2.8: A schematic diagram of a CPMG pulse sequence.

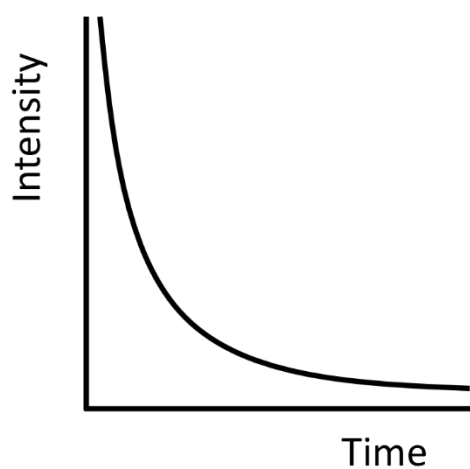


Figure 2.9: An example graph of signal intensity versus time for a CPMG pulse sequence

$$M_z = M_0 e^{\frac{-2\tau}{T_2}} \quad \text{Equation 2.7}$$

2.1.1.7 NMR Signal Intensity

The intensity of the NMR signal in an experiment is affected by the gyromagnetic ratio of the nucleus, the magnetic field strength, temperature, the quantity of excited spins, the number of signal averages, and the NMR relaxation times. The gyromagnetic ratio is a constant assigned to a nucleus and is a measure of how sensitive NMR techniques are to observing that nucleus.² The magnetic field strength influences the Boltzmann distribution of spins in differing energy levels.² A large magnetic field strength will increase the energy difference between energy levels and so will increase the difference in spin energy level populations. Temperature also affects the NMR signal intensity by influencing the difference in spin energy level population; by decreasing the temperature, the amount of energy available in the system decreases and so fewer spins will have sufficient energy to exist in a higher energy state.² Signal averaging is a common method to increase NMR signal intensity and improve the signal-to-noise ratio (SNR). As the NMR signal is coherent and the noise adds incoherently, the SNR scales with the number of averages, N_s (Equation 2.8).

$$SNR = \sqrt{N_s} \quad \text{Equation 2.8}$$

NMR relaxation affects the SNR due to the loss of net magnetisation over time. As the manipulation of nuclear spin and acquisition of the NMR signal takes place over time and the spins are subject to NMR relaxation

from the moment they are excited, signal is lost before acquisition occurs, reducing the SNR.

2.1.1.8 Spatial Encoding

The NMR signal can be spatially encoded by the application of a linear magnetic field gradient so that the precessional frequency of the nucleus is spatially dependent.² The spatial encoding is described by Equation 2.9, where G is the magnetic field gradient strength and r is the position of the nucleus in the direction that G is applied.¹²

$$\omega(r) = \gamma B_0 + \gamma Gr \quad \text{Equation 2.9}$$

The linear variation in gradient strength generates a helix of phase (Figure 2.10), where the orientation of M_0 for each spin is dependent upon its spatial location.² A full phase shift of 360° defines a reciprocal space vector, k , which is dependent upon the gradient strength, G , and duration, t (Equation 2.10).¹²

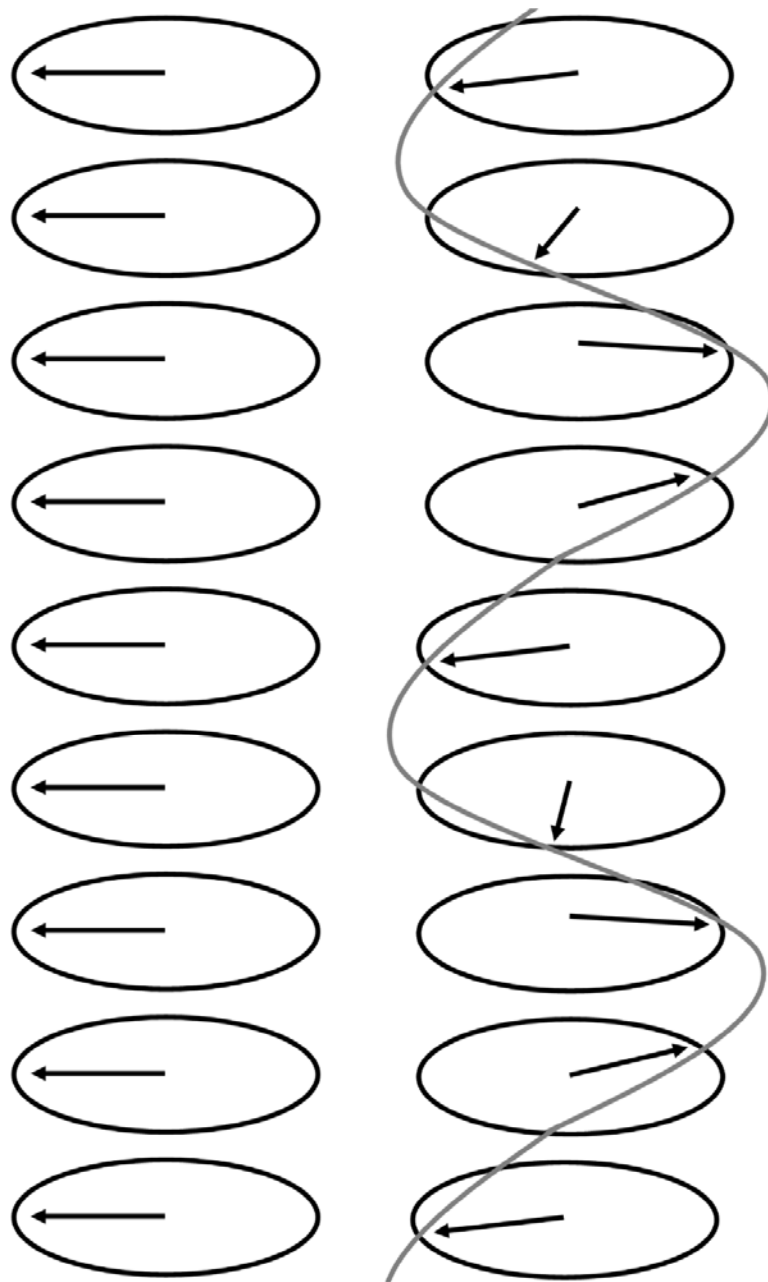


Figure 2.10: A diagram demonstrating the creation of the helix of phase (grey) in spin orientation.

$$k = \frac{\gamma G t}{2\pi} = \lambda^{-1}$$

Equation 2.10

2.1.1.9 Diffusion Spectroscopy

Using the helix of phase to spatially locate molecules, the change in position of nuclei over time can be determined.² The self-diffusion coefficient relates to the shape and size of the molecule (Equation 2.11). and is a measure of the random translational motion of the molecule as mean-squared displacement.²

$$D = \frac{k_b T}{6\pi\eta r_s} \quad \text{Equation 2.11}$$

The self-diffusion coefficient can be measured using a pulsed gradient spin-echo (PGSE) pulse sequence (Figure 2.10). The magnetisation is excited onto the transverse plane by a 90° pulse, after which a magnetic field gradient of magnitude G **and duration δ is applied to wind a helix of** phase, encoding the spin location at that point in time. The spins are then inverted by a 180° pulse, and hence the helix of phase is unwound by the application of a magnetic field gradient with the same magnitude and duration as before. The time between the application of the magnetic field **gradients is Δ and** the time between the 90° and 180° pulses and signal acquisition is τ . By repeating the PGSE experiment with different gradient strengths, a plot with a Gaussian decay is obtained (Figure 2.12).² The plot can be fitted to the Stejskal-Tanner Equation (Equation 2.12) to obtain the self-diffusion coefficient.¹⁷ Inaccuracies in the measurement of the self-diffusion coefficient using the PGSE pulse sequence can result

from the spins being subject to T_2 relaxation, in addition to diffusion, whilst in the transverse plane.

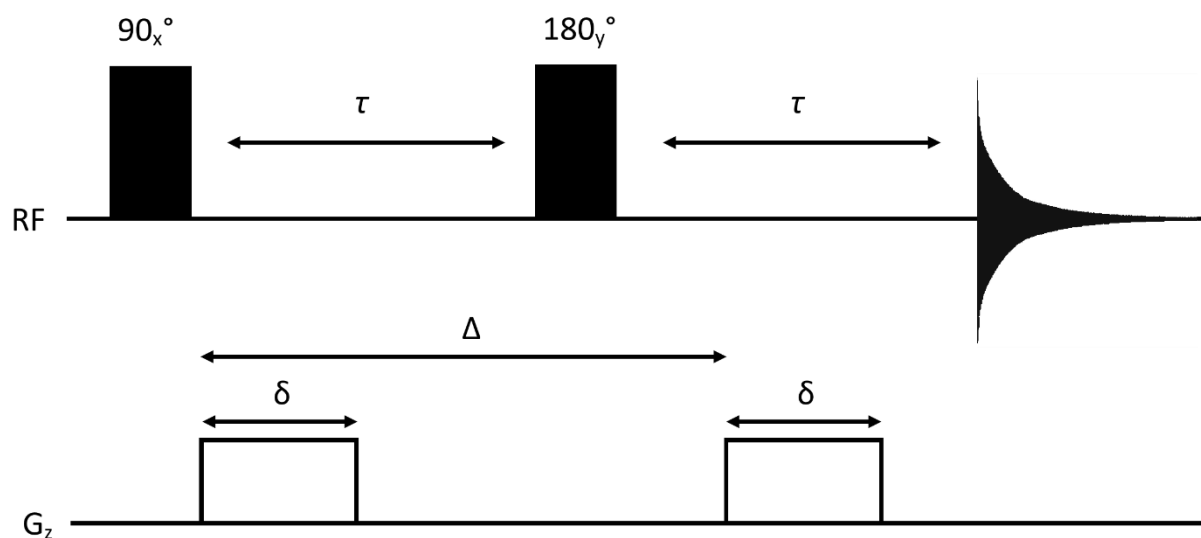


Figure 2.11: A schematic diagram of a PGSE pulse program.

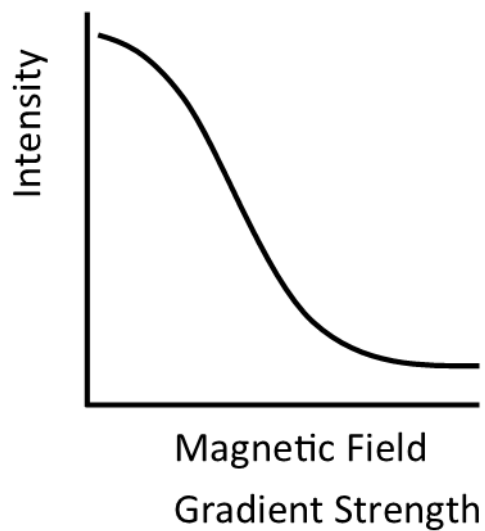


Figure 2.12: An example graph of signal intensity versus time for a PGSE pulse sequence.

$$\frac{S}{S_0} = e^{(-\gamma^2 \delta^2 G^2 D (\Delta - \frac{\delta}{3}))} \quad \text{Equation 2.12}$$

To avoid issues associated with T_2 relaxation during a diffusion measurement, a pulsed gradient stimulated echo (PGSTE) experiment is used (Figure 2.13).^{2, 18} After the initial excitation pulse, the positions of the spins are spatially encoded by a gradient pulse of duration δ . Diffusion during the gradient pulse can be neglected providing that the observation time, Δ , is sufficiently larger than the gradient pulse duration. This is followed by another 90° pulse which returns the magnetisation onto the z axis, thus minimising any T_2 relaxation occurring during the observation time.² A 90° pulse returns the magnetisation into the transverse plane, after which a gradient pulse of the same magnitude and duration as the initial gradient pulse is applied, followed by acquisition of the FID. The experiment is repeated with varying gradient strengths, producing a Gaussian plot of signal intensities which can be fit using Equation 2.12.

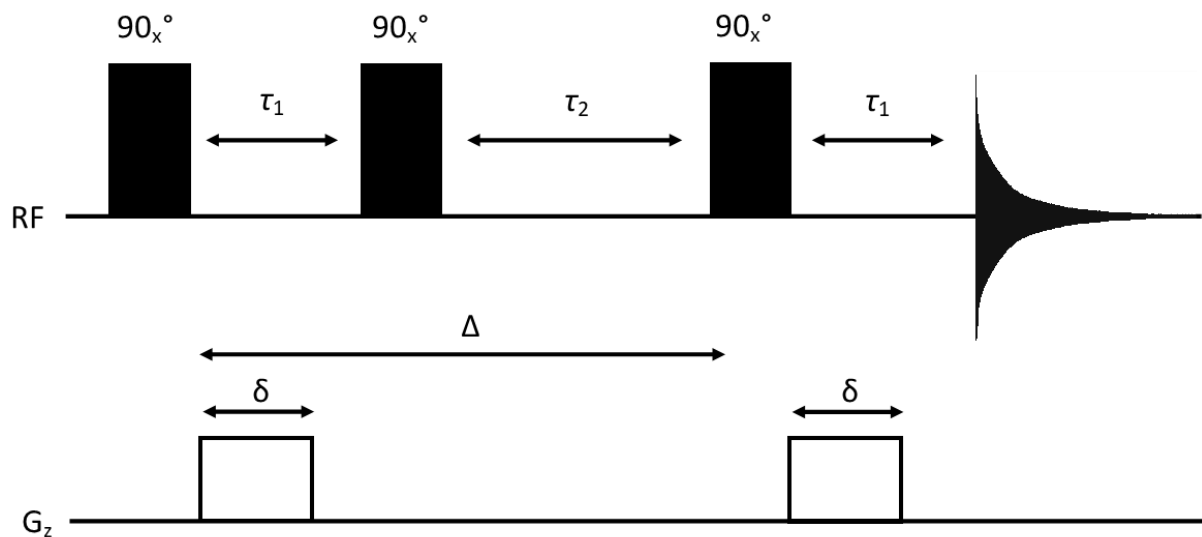


Figure 2.13: A schematic diagram of a PGSTE sequence.

2.1.2 Magnetic Resonance Imaging

Magnetic resonance imaging (MRI)^{19, 20} uses magnetic field gradients to alter the phase of nuclei enabling spatial location. Different types of contrast, such as relaxation time and spin density, can be acquired by varying the acquisition parameters across a set of experiments.

2.1.2.1 k Space

MRI uses the Fourier relationship between the NMR signal, collected under the influence of a magnetic field gradient, and nuclear spin density to acquire a k space raster. The k space raster can be Fourier transformed into an MR image. A k space raster can be traversed by varying the gradient pulse strength and duration (phase encoding) and acquiring data during the application of a magnetic field gradient (frequency encoding) following a 90 ° excitation pulse (Figure 2.14).²¹ Frequency encoding is performed by collecting the NMR signal during the application of a gradient pulse, whilst for phase encoding the NMR signal is collected after a gradient pulse has been applied and the helix of phase has been formed. To obtain a one-dimensional (1D) projection of all spin intensity on to one axis, frequency encoding can be used in isolation. If further dimensions are required, phase encoding is used in addition to frequency encoding. Phase encoding is achieved by applying a magnetic field gradient to generate a helix of phase, spatially locating the spins, before signal acquisition. In the frequency encoding direction of the k space

raster, a negative gradient in the frequency encoding direction (read gradient precursor) prior to the positive gradient, can be applied to traverse negative values of k space. In phase encoding, the relative location in k space is determined by the application of magnetic field gradients with different amplitudes. An MR image is obtained after Fourier transformation of the k space data and is a projection of all spins in a given direction unless slice selection is used.

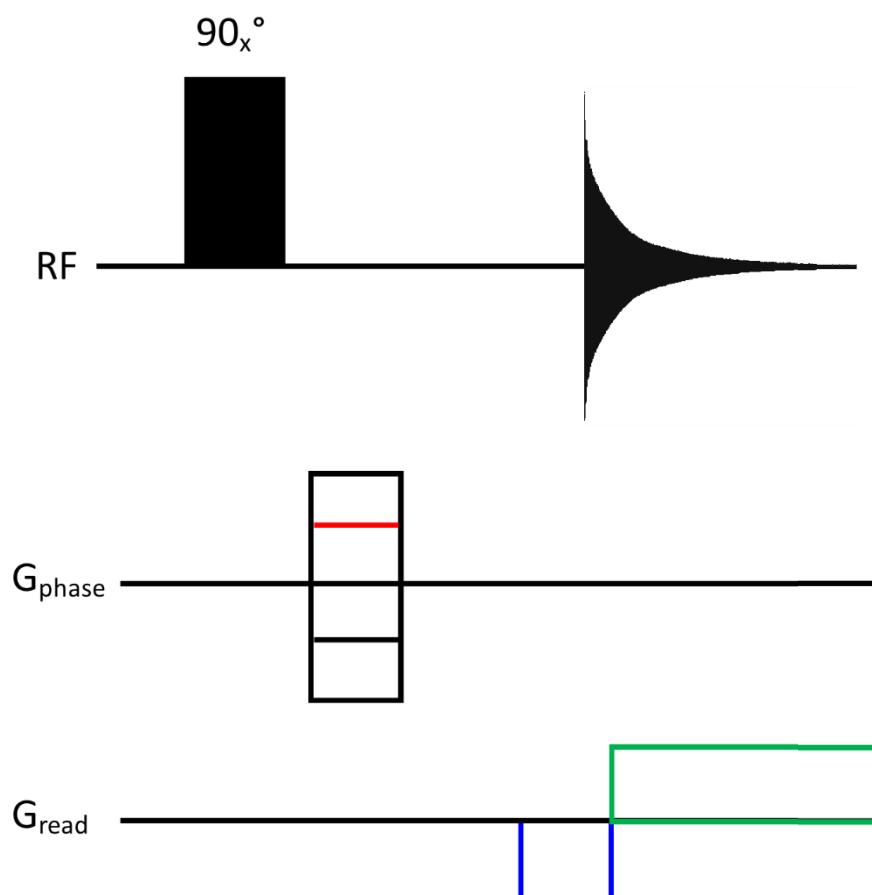
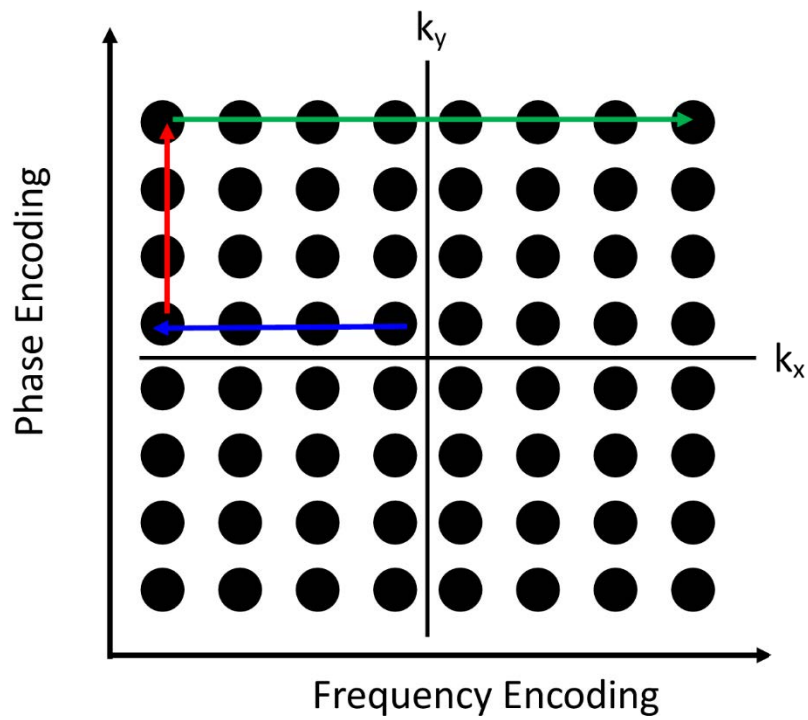


Figure 2.14: A schematic diagram of a \mathbf{k} space raster with an MR imaging pulse sequence, illustrating how the raster is traversed in the read and phase encoding directions.

2.1.2.2 Slice Selection

Slice selection is performed by applying a magnetic field gradient perpendicular to the desired slice and frequency encoding the spin location; this is followed by the application of a soft RF pulse to excite spins with a specific frequency, discussed in Section 2.1.1.1.^{12, 21} The frequency range excited is determined by the length of the soft pulse: as the pulse duration increases, the range of frequencies selected decreases and thus the slice thickness decreases. Therefore, the spins in the position with the same frequency of the soft pulse will be excited.

2.1.2.3 Spin-Echo Imaging

Imaging using a spin-echo pulse sequence is achieved using phase and frequency encoding of the spins in a selected slice. This is shown in Figure 2.15, the application of a soft pulse during a magnetic gradient pulse followed by a phase encoding gradient to wind the helix of phase. A refocusing 180° hard pulse is then applied and the signal acquisition occurs during the read encoding gradient. The time taken between the centre of the soft pulse and the end of signal acquisition is the repetition time, T_R , and the time between the centre of the soft pulse and the centre of the signal echo is the echo time, T_E . The total image acquisition time is dependent on the repetition time, the number of signal averages, and the number of pixels in the phase encoding direction (Equation 2.13), where

N_{ph} is the number of points in the phase encoding direction, N_s is the number of signal averages, and T_R is the repetition time.

$$T_{EXP} = N_{ph} \times N_s \times T_R \quad \text{Equation 2.13}$$

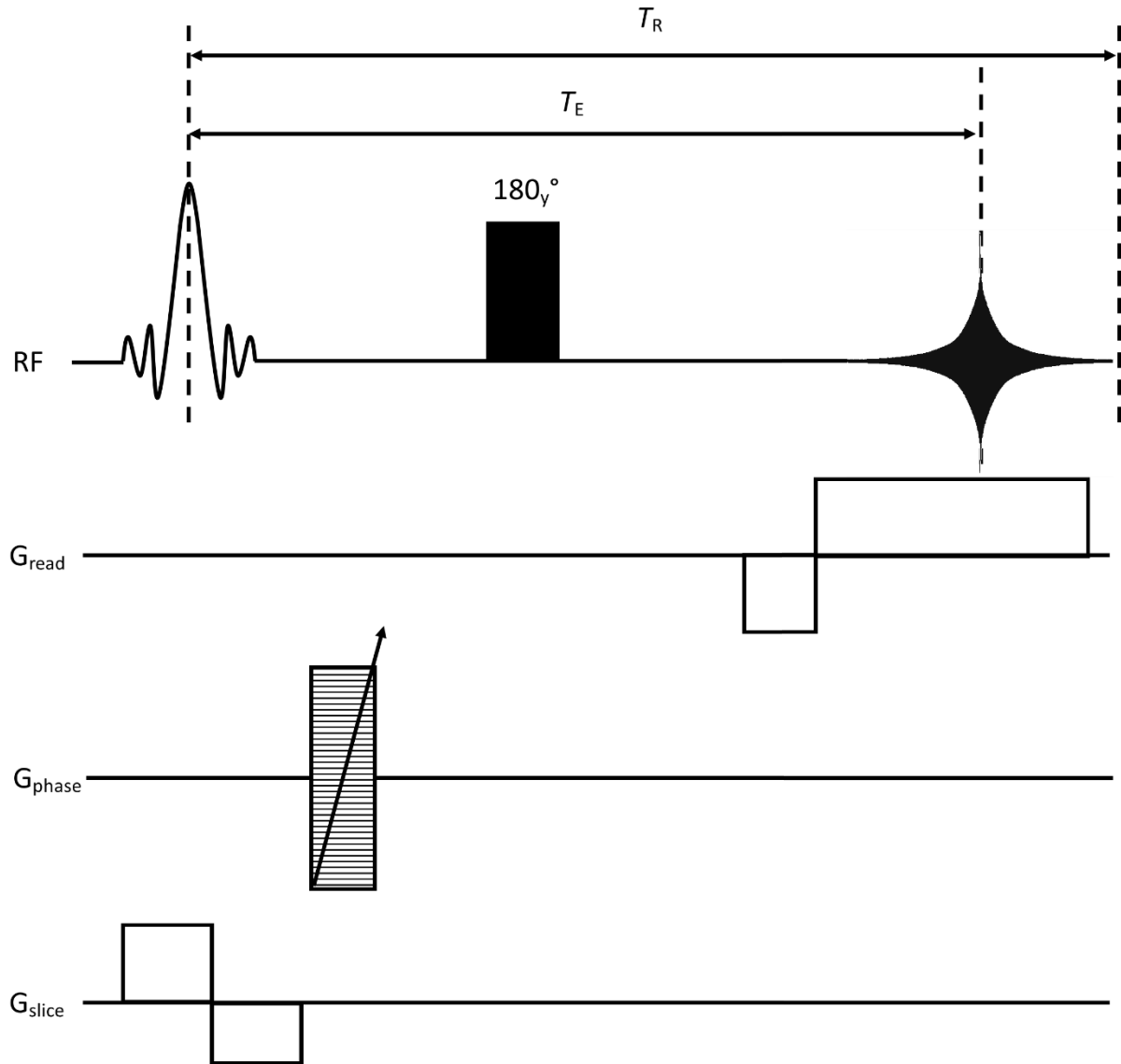


Figure 2.15: A schematic diagram of a spin-echo imaging pulse sequence.

2.1.2.4 Multi-Slice-Multi-(Spin) Echo Imaging

Multi-slice-multi-(spin) echo (MSME) imaging enables multiple slice images of the same sample to be acquired in the same time as the acquisition of one slice image.¹² The spin echo pulse program is used and repeated for each different slice position required. The excitation and acquisition for all slice positions occurs within the repetition time.

2.1.2.4 Rapid Acquisition with Relaxation Enhancement Imaging

Rapid Acquisition with Relaxation Enhancement (RARE) imaging is a type of spin-echo imaging, using phase and frequency encoding for a selected slice, that decreases the experiment time in comparison with a standard spin-echo imaging pulse program.²² In RARE imaging, multiple echoes are acquired in each excitation (Figure 2.16), acquiring successive lines of k space with the signal intensity dependent upon spin density and influenced by the T_2 relaxation time. The number of lines of k space acquired per excitation is known as the RARE factor, n , and acquiring more lines of k space shortens the experiment time, T_{EXP} (Equation 2.14). Increasing the RARE factor increases the time between individual excitations, and thus induces T_2 contrast in the image.¹²

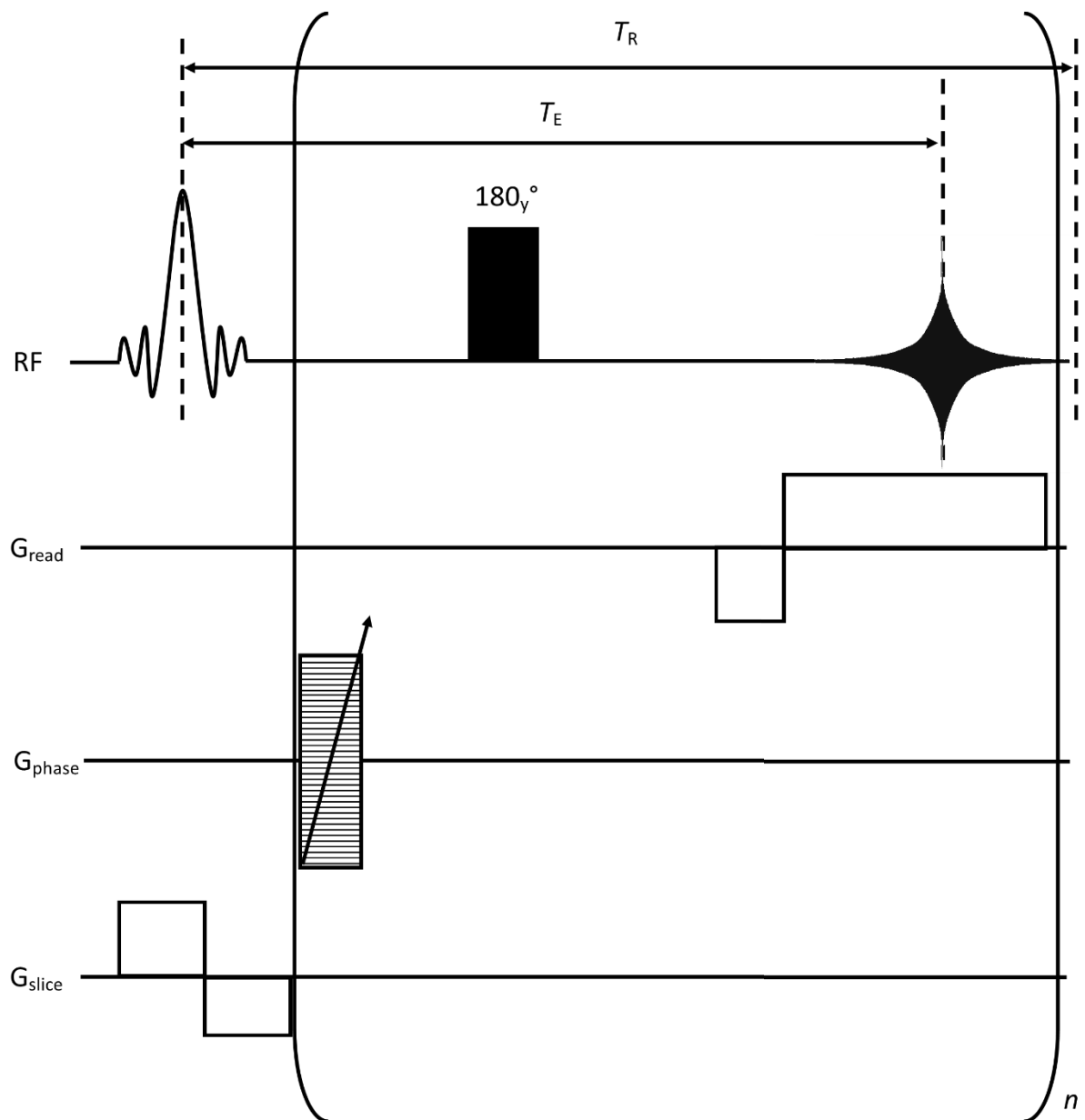


Figure 2.16: A schematic diagram of a RARE pulse sequence

$$T_{EXP} = \frac{N_{ph}}{n} \times N_s \times T_r \quad \text{Equation 2.14}$$

2.1.2.5 NMR Relaxation Time Imaging

T_1 and T_2 NMR relaxation times can be measured as quantitative image contrast. Quantitative relaxation time maps must be acquired with a

repetition time greater than $5T_1$ to ensure the nuclear spins return to thermal equilibrium before the next excitation, and a short echo time to reduce the effects of T_2 relaxation. T_1 relaxation time maps can be acquired using either IR or SR methodologies, outlined in Section 2.1.1.5, combined with a RARE image acquisition sequence. A RARE factor may be used and does not influence the measured T_1 value. T_2 relaxation time maps can be acquired using a RARE pulse sequence by collecting echo images. Due to the application of magnetic field gradients, the measured T_2 value is altered due to the diffusive attenuation that occurs during the echo time. Therefore, acquisition parameters must be the same for T_2 relaxation time maps to be compared. In this thesis, T_1 relaxation time maps will be acquired using both IR and SR methodologies with a RARE pulse sequence.

2.1.2.6 Image Artefacts

Image artefacts are signal intensity in an MR image that is not present in the original sample and are caused by misregistration of the NMR signal location, leading to image distortion. Artefacts due to metal present in the sample can occur at the interface of the metal due to a change in magnetic susceptibility between the metal and the surrounding material, such as an electrolyte. The change in magnetic susceptibility induces a local magnetic field, changing their precession frequency, causing signal misregistration.^{23, 24} Metal artefacts are more pronounced at sharp, right-

angled corners in the frequency encoding direction, and when the difference in magnetic susceptibility is increased.^{25, 26} The artefacts can be reduced by orientating the metal parallel to B_0 and altering the frequency encoding direction.^{23, 25} Further artefacts around metals occur due to the generation of eddy currents in the metal by RF pulses which alter the strength of the RF.^{24, 27} The variation in the RF pulse strength results in changes in signal intensity. Image distortions can also occur due to differences in chemical shift of different spin environments in a molecule.²³ If the chemical shift range of the spins in a molecule is larger than the frequency range of a voxel in the image, intensity from a molecule in one voxel may appear in another.

2.1.2.7 Experimental Conditions

In this thesis, experimental measurements are performed in multiple states: at equilibrium, *in situ*, and *in operando*. A measurement at equilibrium is taken with no expected changes to the sample during the measurement. *In situ* measurements are defined as occurring during approximately stationary external input, such as a cell at constant voltage. Stationary external input does not mean that no changes to the sample will occur during measurement, only that the system is not under standard operating conditions. For example, a battery will observe a drop in current during a constant potential hold or an ionic liquid may passively absorb water from the atmosphere during an *in situ* measurement. An

operando measurement is where system is under operating conditions during experimental acquisition; for example data is collected during the charging or discharging of a battery.

2.2 Electrochemical Techniques

2.2.1 Charge Cycling

Galvanostatic, constant current, cycling is commonly used to charge and discharge an electrochemical cell. In this thesis, two electrode cells have been used consisting of either a metal counter electrode (CE) and a carbon-based working electrode (WE) or a transition metal oxide cathode and a carbon-based anode. In galvanostatic plating, a constant current is applied to the cell and the cell potential measured.²⁸ A cycle consists of the application of current for a set duration, or until a desired cell potential is reached, and then the reverse current applied for a set duration or until a set potential.²⁹ The direction of initial current application depends on the constituents of the cell itself. The first cycle of a cell is termed the formation cycle, as this is the cycle where the solid-electrolyte interphase (SEI) is formed. As a metal cell with a graphite WE and a full cell are used in this thesis, only the electrochemistry pertaining to these will be discussed.

It is often helpful to characterise battery materials in terms of their energy densities, and so specific capacities, in mA h g⁻¹ or mA h cm⁻², are used. The specific capacity of a battery is defined as the amount of charge that can be accumulated during one cycle per unit weight or surface area of the material of choice.³⁰ The specific capacity is calculated using the current of the battery, I , the time that the current was applied for, t , and the weight of the active material, M_w , or the electrode area, M_A , as shown in Equations 2.15 and 2.16.

$$\text{Specific Capacity} = \frac{It}{M_w} \quad \text{Equation 2.15}$$

$$\text{Specific Capacity} = \frac{It}{M_A} \quad \text{Equation 2.16}$$

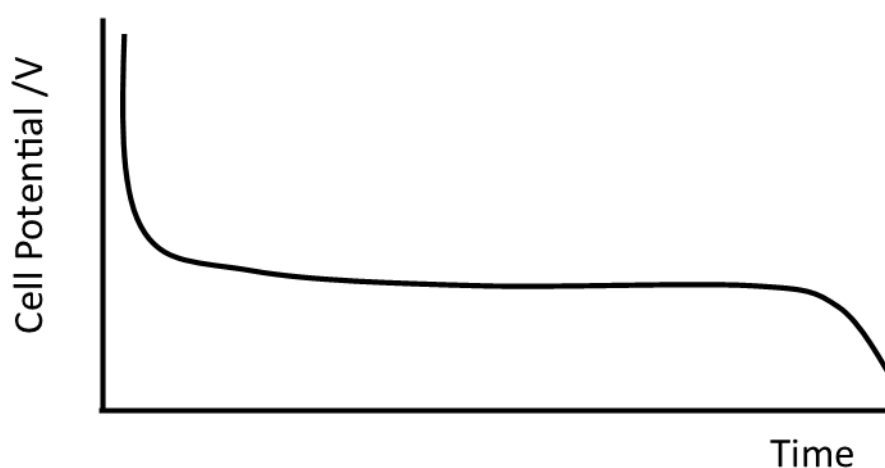


Figure 2.17: An example of a galvanostatic discharge curve for a cell with a metal electrode and a graphite electrode.

Figure 2.17 shows an example of an electrochemical discharge profile during the application of a constant negative current for a lithium metal

cell with a graphite electrode. The reduction in cell potential over time corresponds to the successive formation of more concentrated LiC_x where x decreases over time.³¹

An example of an electrochemical charge curve for a sodium full cell, with a metal oxide electrode and a hard carbon electrode is shown in Figure 2.18. The initial increase in cell potential is associated with the incorporation of sodium into the layers, defect sites, and pore surfaces of the hard carbon electrode.³² The potential increase is followed by a potential plateau and a further increase, during which sodium pools in the pores of the hard carbon.⁶

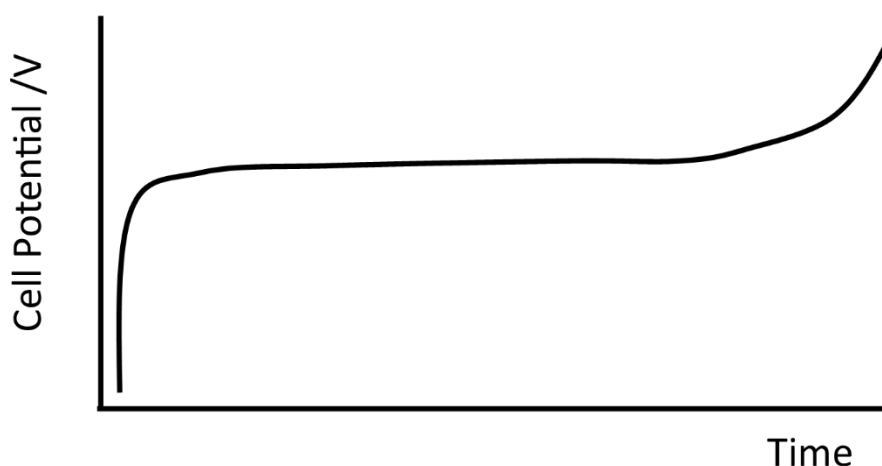


Figure 2.18: An example of a galvanostatic charge curve for a cell with a metal oxide electrode and a hard carbon electrode.

2.2.2 Considerations with Magnetic Resonance Techniques

The combination of electrochemistry with MR techniques poses a few issues which must be addressed to ensure accurate measurements can be

taken. RF radiation is not able to penetrate metals beyond a skin depth (Equation 2.17)³³ where δ is the RF skin depth penetration, ρ is the conductor resistivity, μ_0 is the permeability of a vacuum, μ_r is the conductor relative permeability, and ν_0 is the Larmor frequency; therefore *operando* MR studies on batteries must use a cell constructed from an MR compatible material.^{6, 24, 34-37} Furthermore, eddy currents can be induced by the switching of RF pulses and magnetic field gradients, creating variations in B_1 and B_0 which cause image artefacts. The artefacts are mitigated by aligning metallic components in the cell with respect to B_1 and B_0 .^{24, 38, 39}

$$\delta = \sqrt{\frac{\rho}{\pi\mu_0\mu_r\nu_0}} \quad \text{Equation 2.17}$$

For the electrochemistry, the use of a copper plate and earthing reduces the noise generated from the RF and magnetic gradient pulses to enable sufficient electrochemical control.²⁵ The addition of a lowpass filter²⁵ further aids noise reduction. The presence of the large magnetic field necessitates the use of low magnetic susceptibility coaxial cables to connect the lowpass filter box with the electrochemical cell.²⁵ A diagram of the experimental setup required is shown in Figures 2.19.

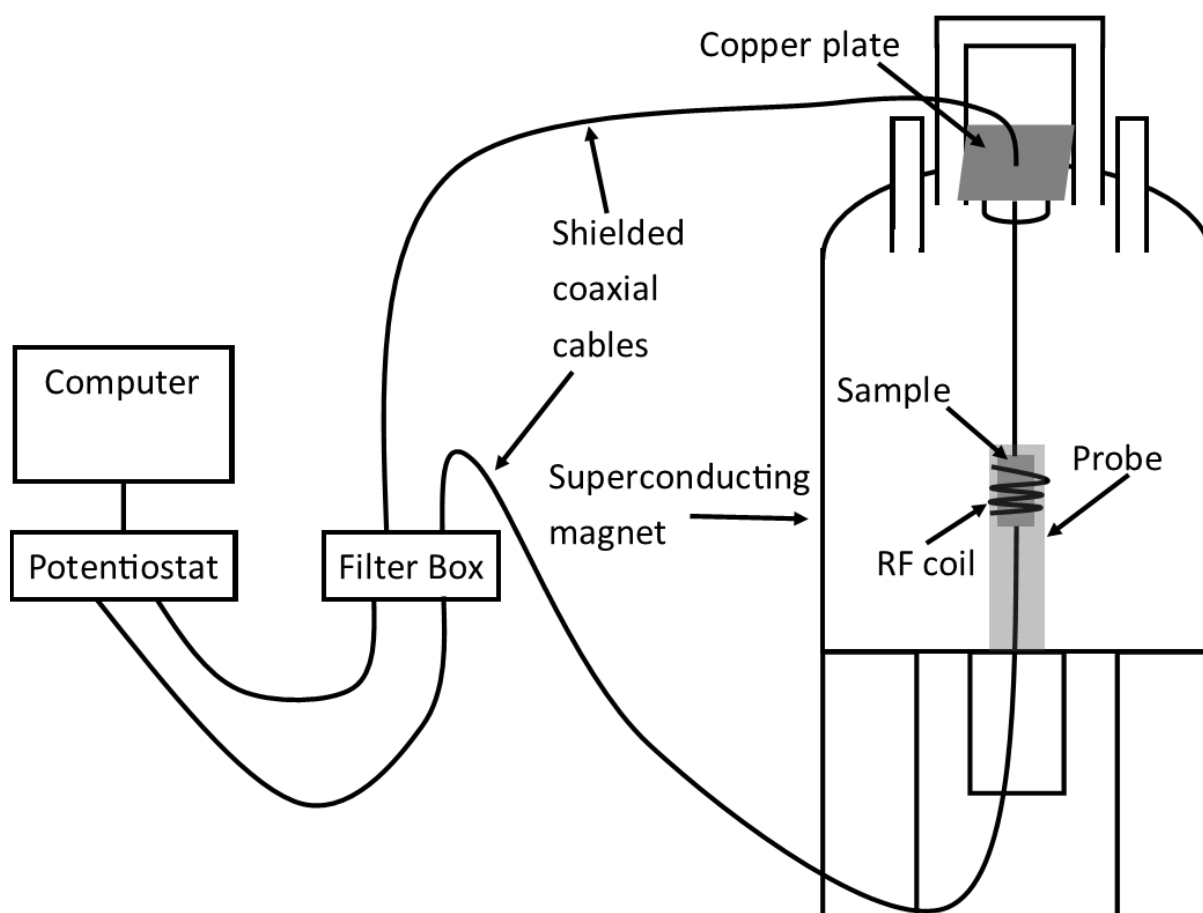


Figure 2.19: Labelled schematic diagram showing a standard set up for *operando* magnetic resonance experiments during electrochemistry.

2.3 References

1. P. J. Hore, *Nuclear Magnetic Resonance*, Oxford University Press, Oxford, 1995.
2. T. Claridge, *High-Resolution NMR Techniques in Organic Chemistry*, 3 edn., 2016.
3. M. H. Levitt, *Spin Dynamics: Basics of Nuclear Magnetic Resonance*, John Wiley and Sons, New York, 2002.
4. W. D. Knight, *Phys. Rev.*, 1949, 76, 1259-1260.
5. R. Bhattacharyya, B. Key, H. Chen, A. S. Best, A. F. Hollenkamp and C. P. Grey, *Nat. Mater.*, 2010, 9, 504-510.
6. J. M. Bray, C. L. Doswell, G. E. Pavlovskaya, L. Chen, B. Kishore, H. Au, H. Alptekin, E. Kendrick, M. M. Titirici, T. Meersmann and M. M. Britton, *Nat. Commun.*, 2020, 11, 2083.
7. Y. Xiang, G. Zheng, Z. Liang, Y. Jin, X. Liu, S. Chen, K. Zhou, J. Zhu, M. Lin, H. He, J. Wan, S. Yu, G. Zhong, R. Fu, Y. Li and Y. Yang, *Nat. Nanotechnol.*, 2020, 15, 883-890.
8. D. Massiot, F. Fayon, M. Capron, I. King, S. Le Calvé, B. Alonso, J. - O. Durand, B. Bujoli, Z. Gan and G. Hoatson, *Magn. Reson. Chem.*, 2002, 40, 70-76.
9. J. Keeler, *Understanding NMR Spectroscopy*, John Wiley & Sons, Chichester, 2010.
10. C. E. Keller and W. R. Carper, *Inorganica Chim. Acta*, 1993, 210, 203-208.
11. M. Haouas, F. Taulelle and C. Martineau, *Prog. Nucl. Magn. Reson. Spectrosc.*, 2016, 94-95, 11-36.
12. P. T. Callaghan, *Principles of Nuclear Magnetic Resonance Microscopy*, Oxford University Press, 1993.
13. P. B. Kingsley, *Concepts Magn. Reson.*, 1999, 11, 243-276.
14. E. L. Hahn, *Phys. Rev.*, 1950, 80, 580-594.
15. H. Y. Carr and E. M. Purcell, *Phys. Rev.*, 1954, 94, 630-638.
16. S. Meiboom and D. Gill, *Rev. Sci. Instrum.*, 1958, 29, 688-691.

17. J. E. Tanner and E. O. Stejskal, *J. Chem. Phys.*, 1968, 49, 1768-1777.
18. J. E. Tanner, *J. Chem. Phys.*, 1970, 52, 2523-2526.
19. P. C. Lauterbur, *Nature*, 1973, 242, 190-191.
20. P. Mansfield and P. K. Grannell, *J. Phys. Chem. C*, 1973, 6, L422-L426.
21. M. M. Britton, *Chem. Soc. Rev.*, 2010, 39, 4036-4043.
22. J. Hennig, A. Nauerth and H. Friedburg, *Magn. Reson. Med.*, 1986, 3, 823-833.
23. L. J. Erasmus, D. Hurter, M. Naudé, H. G. Kritzing and S. Acho, *S. Afr. J. Radiol.*, 2004, 8, 13-17.
24. M. M. Britton, *ChemPhysChem*, 2014, 15, 1731-1736.
25. J. M. Bray, A. J. Davenport, K. S. Ryder and M. M. Britton, *Angew. Chem. Int. Ed.*, 2016, 55, 9394-9397.
26. H. Imai, Y. Tanaka, N. Nomura, Y. Tsutsumi, H. Doi, Z. Kanno, K. Ohno, T. Ono and T. Hanawa, *Acta Biomater.*, 2013, 9, 8433-8439.
27. I. Sersa and U. Mikac, *J. Magn. Reson.*, 2018, 294, 7-15.
28. A. A. Pasa and M. L. Munford, in *Encyclopedia of Chemical Processing*, ed. S. Lee, Taylor & Francis, New York, 2006, vol. 1.
29. K. Marker, C. Xu and C. P. Grey, *J. Am. Chem. Soc.*, 2020, 142, 17447-17456.
30. A. Kirchev, in *Electrochemical Energy Storage for Renewable Sources and Grid Balancing*, 2015, pp. 411-435.
31. X. Han, X. Feng, M. Ouyang, L. Lu, J. Li, Y. Zheng and Z. Li, *Automot. Innov.*, 2019, 2, 263-275.
32. **H. Au, H. Alptekin, A. C. S. Jensen, E. Olsson, C. A. O'Keefe, T. Smith, M. Crespo-Ribadeneyra, T. F. Headen, C. P. Grey, Q. Cai, A. J. Drew and M.-M. Titirici**, *Energy Environ. Sci.*, 2020, 13, 3469-3479.
33. M. Mohammadi and A. Jerschow, *J. Magn. Reson.*, 2019, 308, 106600.

34. S. Wiemers-Meyer, M. Winter and S. Nowak, *Phys. Chem. Chem. Phys.*, 2017, 19, 4962-4966.
35. Z.-R. Ni, X.-H. Cui, S.-H. Cao and Z. Chen, *AIP Adv.*, 2017, 7, 085205.
36. S. Benders, B. F. Gomes, M. Carmo, L. A. Colnago and B. Blumich, *J. Magn. Reson.*, 2020, 312, 106692.
37. J. D. Bazak, S. A. Krachkovskiy and G. R. Goward, *J. Phys. Chem. C*, 2017, 121, 20704-20713.
38. H. Graf, G. Steidle, P. Martirosian, U. A. Lauer and F. Schick, *Med. Phys.*, 2006, 33, 124-127.
39. S. Vashaei, F. Goora, M. M. Britton, B. Newling and B. J. Balcom, *J. Magn. Reson.*, 2015, 250, 17-24.

3 Quantitative T_1 Magnetic Resonance Imaging for Battery

Characterisation

3.1 Introduction

The need for new battery chemistries which go beyond lithium ion batteries (LIBs),¹ such as sodium,^{2, 3} aluminium^{4, 5} and zinc⁶ require the development of new electrode materials and electrolytes, such as ionic liquids (ILs).⁷ ILs are promising battery electrolytes due to their tuneability, low volatility, high conductivity, and wide electrochemical potential window. Furthermore, ILs show promise in surface finishing⁸ with zinc due to the corrosion resistant properties of a zinc surface.⁹ However, ILs are also highly viscous and hygroscopic¹⁰ which means that water may be present in an IL without intentional addition. The presence of water in IL electrolytes has the advantage of reducing the viscosity, which may be favourable as it increases the conductivity.^{9, 11} Despite the effect of water in ILs having been characterised in the cases of cation and anion diffusion coefficients,¹² electrochemical potential limits,¹³ and morphology of the metal deposit,¹⁴ the overall influence of additives remains poorly understood.

One IL that has been used in zinc electroplating is 1-ethyl-3-methylimidazolium triflate ($C_2C_1\text{imTfO}$) with $\text{Zn}(\text{TfO})_2$.^{9, 15} $C_2C_1\text{imTfO}$ with $\text{Zn}(\text{TfO})_2$ is a promising electrolyte for zinc ion batteries (ZIBs) that do

not intercalate zinc, but its conductivity is limited by its viscosity and so water is a potential additive to improve the conductivity.⁹

The use of water as an additive has been found to adversely affect the quality of zinc deposit which may increase the likelihood of dendrite formation in a ZIB containing C₂C₁imTfO with Zn(TfO)₂.¹⁵ To fully understand the effects of water in the electrolyte, the chemical speciation of the Zn²⁺ with respect to water concentration must be known. It has been suggested that an IL sample with between 20–30% water is an IL-in-water;¹⁶ this is the point at which the interactions between the cations and anions in the IL are significantly reduced. Furthermore, intermolecular interactions in the C₂C₁imTfO with Zn(TfO)₂ IL both with and without water have been hypothesised (Figure 3.1) from Raman and infra-red spectroscopy data.¹⁷ The speciation shown in Figure 3.1 is further supported in the literature from far infra-red spectroscopy measurements¹⁸ and nuclear magnetic resonance (NMR) spectroscopy.¹⁹

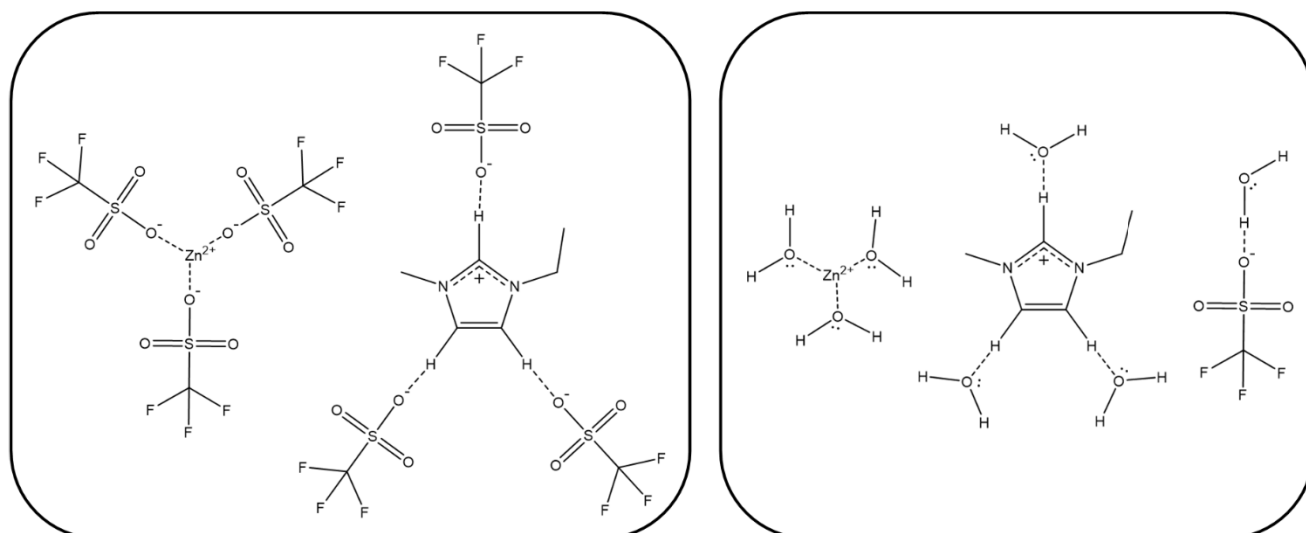


Figure 3.1: Expected speciation in $\text{Zn}(\text{TfO})_2$ in $\text{C}_2\text{C}_1\text{imTfO}$ a) without and b) with water as suggested in by Lui *et al.* in reference 16.

Typical methods of water determination, such as Karl-Fischer titration²⁰ and cyclic voltammetry,²¹ require a reaction to occur with the water in an IL which is invasive. However, NMR spectroscopy enables quantitative determination of the water content by integration of the signal from the water in the NMR spectrum without the need for a reaction with water. Furthermore, NMR spectroscopy provides insight into intermolecular interactions which can elucidate chemical speciation.¹⁹ ^1H NMR spectroscopy has been used in the literature to suggest that water in an IL exists in pockets within the larger IL lattice.²² Saihara *et al.*²² measured the self-diffusion coefficient for IL cations was an order of magnitude slower, at approximately $7 \times 10^{-11} \text{ m}^2 \text{ s}^{-1}$, than that for water within the system, at $4 \times 10^{-10} \text{ m}^2 \text{ s}^{-1}$, which indicates that the water and IL ions are in different environments. Investigating the change in intermolecular interactions in the IL between the IL-in-water and water-in-IL regimes is complicated by the cost of ILs, and thus the cost to synthesise samples

with sufficiently low water content due to the accuracy of the water volume required. Hence, the changes in molecular speciation in an IL at <10 mol% water have yet to be investigated.

Magnetic resonance imaging (MRI) is able to visualise opaque systems non-invasively,²³ and so can be used to visualise battery chemistry *in situ*.²⁴⁻²⁹ It is often useful to map the distribution of components directly for NMR active nuclei with favourable parameters. However, direct observation is not always possible due to the low sensitivity of MRI to such nuclei and fast magnetic resonance (MR) relaxation times of the nucleus. As a solution, the charge carrier can be indirectly visualised using the MR relaxation times of the ^1H or ^{19}F in the electrolyte.^{27, 30}

There are two commonly used methodologies to acquire T_1 relaxation time maps: inversion recovery (IR) and saturation recovery (SR). IR fully **inverts the magnetisation onto the $-z$ axis** before signal excitation and acquisition, whereas SR crushes the magnetisation before signal excitation and acquisition. More discussion on these methods can be found in Chapter 2.1.1.5. Other methods of measuring the T_1 relaxation time have been employed in medical imaging, where quantitative determination of MR relaxation time could enable improved diagnoses.³¹⁻
³³ Sequences such as saturation pulse prepared heart rate independent inversion recovery (SAPPHIRE),³⁴ saturation recovery single-shot

acquisition (SASHA),³⁵ modified Look-Locker inversion recovery (MOLLI),³⁶ and shortened MOLLI (ShMOLLI)³⁷ have been developed to reduce the time taken to measure the T_1 relaxation time. However, the reduction in experimental time is at the cost of reduced precision in the measurement of the MR T_1 relaxation time.³⁸ Hence, the medical imaging methods are not suitable for quantitative determination of MR relaxation time.

Previously, ^1H NMR T_1 relaxation time of water has been used to study *in situ* the concentration of Cu ions in solution during electrodissoolution.³⁰ Cu^{2+} is paramagnetic and so a small ion concentration change has a large effect on the ^1H NMR relaxation time of the water. However, if the dissolved ion is diamagnetic, a small change in ion concentration will have a significantly smaller effect on the NMR relaxation time and mapping the change in species distribution becomes challenging. Hence, it is important to decrease the standard deviation in the measured NMR relaxation time of water, for a specific ion concentration, by increasing the signal-to-noise ratio (SNR) of the images acquired.

Signal averaging is commonly used to improve the SNR; this method requires repetition of the experiment and sums the acquisitions resulting in an increase in the SNR. The increase occurs as the signal adds coherently whilst the noise sums incoherently, giving rise to a SNR

increase proportional to the square root of the number of signal averages (Equation 3.1), where N_s is the number of signal averages. Further information can be found in Chapter 2.1.1.7. Due to the repetition of the experiment, the time taken to acquire the data is increased by the number of signals averaged, which reduces temporal resolution for *in situ* and *operando* experiments.

$$SNR = \sqrt{N_s} \quad \text{Equation 3.1}$$

Further reduction in SNR is caused by T_2 relaxation during signal acquisition. After excitation, the nuclear spins are subject to T_2 relaxation in the transverse plane and as the spins dephase, the magnitude of the signal acquired decreases. Further discussion can be found in Chapter 2.1.1.7. The effect on the SNR of the signal dephasing is observed in RARE imaging where the signal is repeatedly refocused to acquire more lines of k space; hence, with each new line of k space acquired, the SNR is reduced.

Previously, summing echo images has been used to increase the SNR of both NMR spectra and MRI of low sensitivity nuclei.³⁹⁻⁴³ Additionally, the NMR T_1 relaxation time resulting from each set of echo images can be calculated computationally and the effect of averaging these calculated relaxation times has demonstrated a reduction in noise of up to 40% in T_1

relaxation time images.⁴⁴ Summing echo images has yet to be applied to increase the SNR of NMR T_1 relaxation time measurements.

In this chapter, echo image summation methodology is first explored using eight concentrations of aqueous CuSO_4 to establish the effect of experimental method and summing echo images and signal averaging on the measured T_1 relaxation time and its standard deviation. Summing echo images is then used to reduce the SNR of T_1 relaxation time maps of water absorbing into the 0.08 M $\text{Zn}(\text{TfO})_2$ in $\text{C}_2\text{C}_1\text{imTfO}$ IL from the atmosphere. Collection of the relaxation time maps of water ingress removes the requirement for production of large sample volumes of expensive IL to investigate the relationship between T_1 relaxation time and water concentration at low amounts of water. T_1 relaxation time measurements of 0.08 M $\text{Zn}(\text{TfO})_2$ in $\text{C}_2\text{C}_1\text{imTfO}$ with a known amount of water in both the water-in-IL and IL-in-water regimes are acquired using NMR spectroscopy. From the T_1 relaxation time maps of the ^{19}F in 0.08 M $\text{Zn}(\text{TfO})_2$ in $\text{C}_2\text{C}_1\text{imTfO}$ and the T_1 relaxation time measurements from NMR spectroscopy, and the relationship between the ^{19}F T_1 relaxation time and water concentration is established. The collection of ^{19}F T_1 relaxation time values at low water concentration allows for further insight into the speciation changes at low water concentration in the 0.08 M $\text{Zn}(\text{TfO})_2$ in $\text{C}_2\text{C}_1\text{imTfO}$ IL.

3.2 Experimental

0.08 M and 0.15 M $\text{Zn}(\text{TfO})_2$ in $\text{C}_2\text{C}_1\text{imTfO}$ samples were synthesised and the NMR spectroscopy data were collected by Yasmeen AlZahrani.

A phantom comprising eight solutions of CuSO_4 , between 0.5–10 mM prepared in ultrapure water (MilliQ, $18.2 \text{ M}\Omega \text{ l}^{-1}$).

0.08 M and 0.15 M $\text{Zn}(\text{TfO})_2$ (98%, Sigma Aldrich) in $\text{C}_2\text{C}_1\text{imTfO}$ (98% Iolitec) was prepared from dry $\text{C}_2\text{C}_1\text{imTfO}$ and $\text{Zn}(\text{TfO})_2$. $\text{C}_2\text{C}_1\text{imTfO}$ was dried under reduced pressure (1×10^{-3} mbar, 120°C) for 24 h before transferring into an argon-filled glove box (Saffron <25 ppm O_2).

$\text{Zn}(\text{TfO})_2$ was dried under reduced pressure (1 mbar, 120°C) for 18 h before transferring into an argon-filled glove box. The dried $\text{Zn}(\text{TfO})_2$ and $\text{C}_2\text{C}_1\text{imTfO}$ were combined in the glove box at desired concentrations in a vial, which was sealed with a lid and parafilm and removed from the glove box. The sample was then sonicated at 30 min intervals over a 6 h period at 60°C . Full dissolution occurred after 3 d and a clear, viscous, light brown liquid was formed. For ^{19}F T_1 NMR spectroscopy measurements of 0.08 M and 0.15 M $\text{Zn}(\text{TfO})_2$ in $\text{C}_2\text{C}_1\text{imTfO}$, ultrapure water was added to provide samples with 0.00–0.25 mole fraction of water.

All data were acquired on a Bruker AVANCE III HD spectrometer equipped with a 7 T vertical wide-bore superconducting magnet, using a Bruker diff30 probe equipped with either a 10 mm ^1H , for aqueous CuSO_4 samples, or 10 mm ^{19}F coils, for IL samples, for NMR spectroscopy. The RF pulses were calibrated for each sample, (21–23 μs at 10 W for ^1H and 39–45 μs at 3 W for ^{19}F). Data were acquired at 293 ± 0.3 K, maintained by the water-cooled gradient coils. ^1H T_1 NMR data were collected using inversion recovery (IR) and saturation recovery (SR) pulse sequences. ^{19}F T_1 NMR data were acquired using IR experiments only. IR experiments were performed using a minimum of seven time points logarithmically spaced from 5×10^{-6} s to $5T_1$. SR experiments were performed using a minimum of seven time points, logarithmically spaced from 0.01 s to $5T_1$. ^1H NMR diffusion data of the 0.15 M $\text{Zn}(\text{TfO})_2$ in $\text{C}_2\text{C}_1\text{imTfO}$ were collected using a pulsed gradient stimulated echo pulse sequence with 16 logarithmically spaced gradient steps up to 300 G m^{-1} , $\Delta = 0.06 \text{ s}$ and $\delta = 0.002 \text{ s}$. Data were analysed using *Prospa*⁴⁵ and the integrals fit using *KaleidaGraph*⁴⁶ as described in Chapter 2.

MRI data were acquired using a WB40 microimaging probe equipped with either 25 mm quadrature transmit/receive (QTR) ^1H or ^{19}F linear transmit/receive (LTR) coils. The RF pulses were automatically calibrated for each sample.

^1H MR images of a phantom containing eight CuSO_4 solutions were acquired with a 1 mm slice thickness and a 128×128 pixel matrix, with a pixel size of $195 \mu\text{m} \times 195 \mu\text{m}$. Images were acquired using a RARE pulse sequence.⁴⁷ Both SR and IR methods were used to acquire T_1 maps from a series of 9 images. For the IR experiments, a repetition time of $T_R > 5T_1$ was used with inversion delays logarithmically spaced from 55 ms to $5T_1$ and a RARE factor of both 1 and 4 was used. For the SR experiments, the repetition times were logarithmically spaced from 55 ms to $5T_1$, with a RARE factor of 1. For both IR and SR experiments, images were collected where the number of echo images varied from 1 to 16, and averages from 2 to 16 were acquired as shown in Table 3.1. T_1 maps were generated using *Prospa* and the standard deviation and SNR determined.

Table 3.1: All ^1H T_1 MRI experiments of $\text{CuSO}_4(\text{aq})$ acquired using inversion and saturation methodology, showing the RARE factor, number of signal averages, and number of echo images acquired.

IR				SR	
RARE factor 1		RARE factor 4		RARE factor 1	
Signal Averages	Echo Images	Signal Averages	Echo Images	Signal Averages	Echo Images
2	1	2	1	2	1
2	2	2	2	2	2
2	4	2	4	2	4
2	8	2	8	2	8
2	16	2	16	2	16
4	1	4	1	4	1
4	2	4	2	4	2
4	4	4	4	4	4
4	8	4	8	4	8
4	16	4	16	4	16
8	1	8	1	8	1
8	2	8	2	8	2
8	4	8	4	8	4
8	8	8	8	8	8
8	16	8	16	8	16
16	1	16	1	16	1
16	2	16	2	16	2
16	4	16	4	16	4
16	8	16	8	16	8
16	16	16	16	16	16

Vertical ^{19}F images of the 0.08 M $\text{Zn}(\text{TfO})_2$ in $\text{C}_2\text{C}_1\text{imTfO}$ were acquired with a 1 mm slice thickness and a 128×64 pixel matrix, with an isotropic pixel size of 234 μm . Images were acquired as for the ^1H T_1 maps of aqueous CuSO_4 except IR experiments were only performed with a RARE factor of 4.

$$P_z = \frac{1}{4\pi Dt} \left(e^{-\frac{z^2}{4Dt}} \right) \quad \text{Equation 3.2}$$

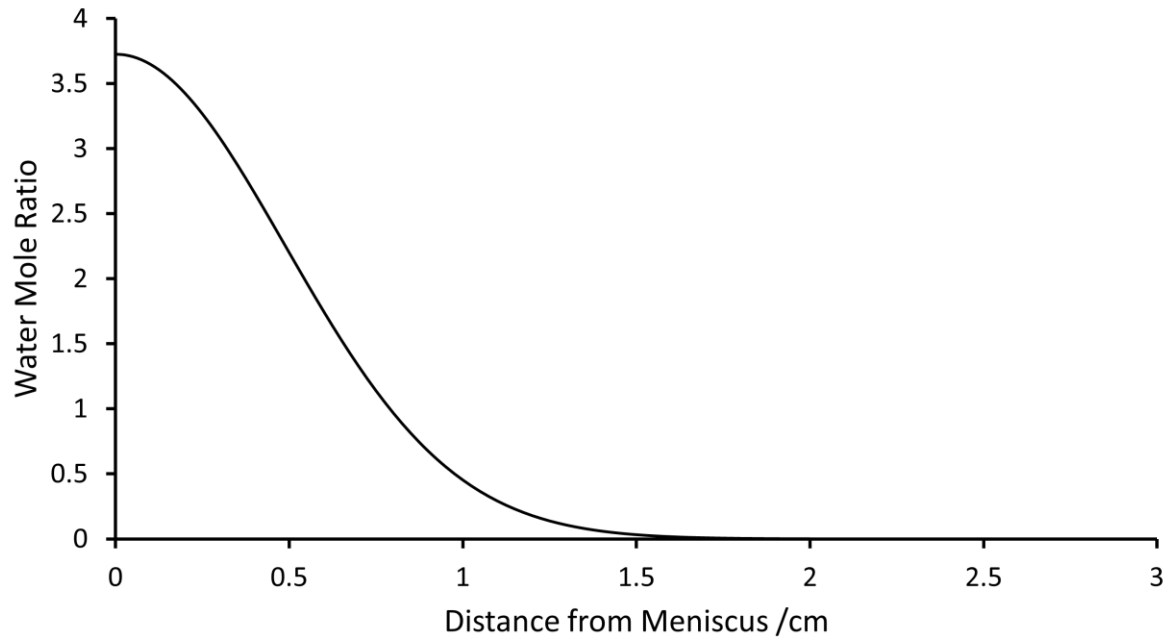


Figure 3.2: Plot of the simulated Gaussian water ingress at $t = 33.3$ h using a diffusion coefficient of $9.9 \times 10^{-11} \text{ m}^2 \text{ s}^{-1}$.

A simulated Gaussian distribution of the expected water content of the sample at the final time point (Figure 3.2) was generated using Equation 3.2, using Gaussian ingress, P_z , at a distance, z , at a known time point, t , with a diffusion coefficient, $D = 9.9 \times 10^{-11} \text{ m}^2 \text{ s}^{-1}$.

3.3 Quantifying the Effect of Summing Echo Images on the Measured T_1 NMR Relaxation Time

3.3.1 Results

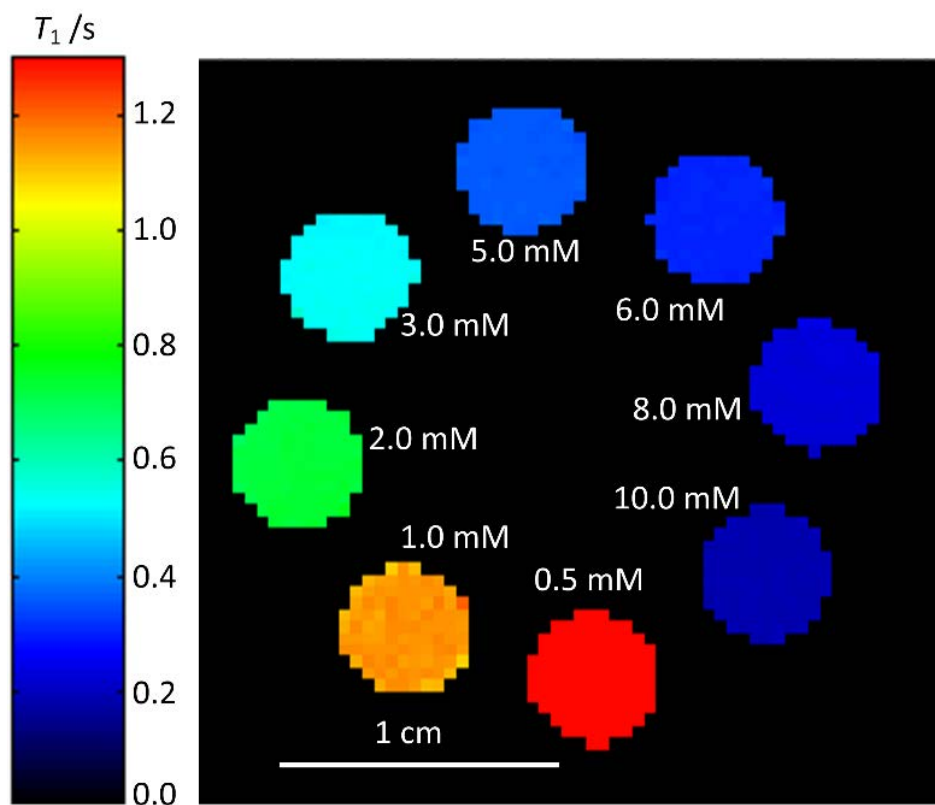


Figure 3.3: A ^1H T_1 MR relaxation time map of a phantom of aqueous CuSO_4 over a range of concentrations acquired using SR methodology with 16 summed echo images.

Figure 3.3 shows a ^1H T_1 relaxation time map acquired of a phantom containing different concentrations of aqueous CuSO_4 . The concentrations were chosen to provide a range of T_1 relaxation times that match the T_1 relaxation times of 0.08 M $\text{Zn}(\text{TfO})_2$ in $\text{C}_2\text{C}_{1\text{im}}\text{TfO}$ to evaluate the impact of summing echo images. Examples presented are for 0.5 mM CuSO_4 , data for other concentrations are found in the Appendix. The effect of

summing echo images on the T_1 relaxation time was investigated and compared to the effects of signal averaging.

Table 3.2: Values for the ^1H T_1 relaxation time of 0.5 mM CuSO_4 and standard deviation in seconds and as a percentage for both saturation and IR methodologies for each number of echoes images summed.

Echoes summed	SR			IR		
	T_1 /s	Standard deviation /s	Standard deviation /%	T_1 /s	Standard deviation /s	Standard deviation /%
1	1.680	0.014	0.840	1.690	0.014	0.800
2	1.670	0.012	0.690	1.690	0.008	0.500
4	1.650	0.011	0.640	1.690	0.010	0.570
8	1.650	0.009	0.570	1.690	0.009	0.540
16	1.640	0.008	0.510	1.690	0.009	0.510

Table 3.2 shows the T_1 relaxation time values for 0.5 mM CuSO_4 obtained using both SR and IR methods and different numbers of summed echo images used to generate relaxation time maps. For the SR experiments, there was a change in the T_1 relaxation time measured of 0.04 s across the experiments where between 1 and 16 echo images are summed, which was not significant. There was a reduction in the standard deviation as the number of echo images included in image analysis increased. For the IR experiments, there was no shift in the T_1 relaxation time as more echo imaged were summed, and the reduction in standard deviation was comparable to what was observed with the SR experiments. However, with an IR measurement there may be an offset in the signal intensity

curve, which must be calculated to accurately fit the IR data points and measure the T_1 relaxation time, as detailed in Chapter 2.1.1.4.⁴⁸

The change in the distribution of T_1 relaxation time due to signal averaging for 0.5 mM CuSO₄ is illustrated by Figure 3.4. The figure shows that the average distribution of relaxation times decreased with respect to the number of signal averages. Furthermore, there was no change in the measured T_1 relaxation time.

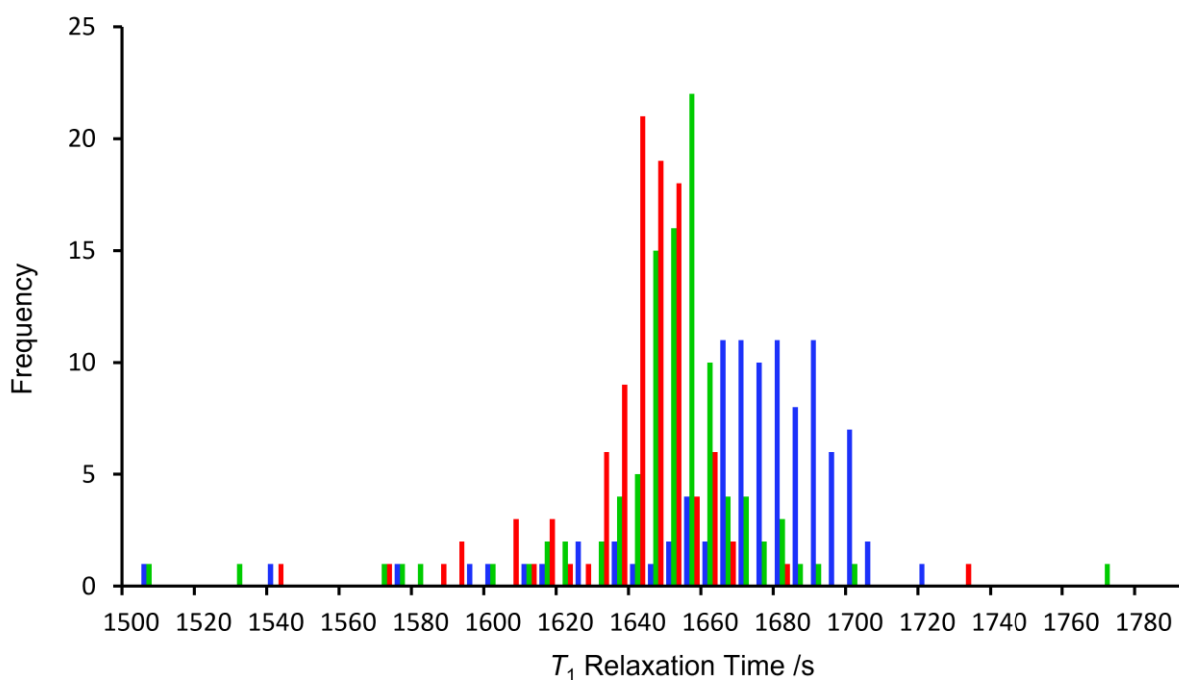


Figure 3.4: A histogram of the ^1H T_1 relaxation times observed for 0.5 mM CuSO₄ in relaxation time maps acquired with 2 (blue), 4 (green), 8 (red), and 16 (orange) signal averages. Histogram generated from MR image found in Appendix 1.

Figure 3.5 shows the change in the range of T_1 relaxation times measured of 0.5 mM CuSO₄ for 2, 4, 8, and 16 summed echo images. Here, the spread of T_1 relaxation times narrowed with an increase in the summed

echoes. Additionally, the average relaxation time reduced by 0.04 s, which was not significant.

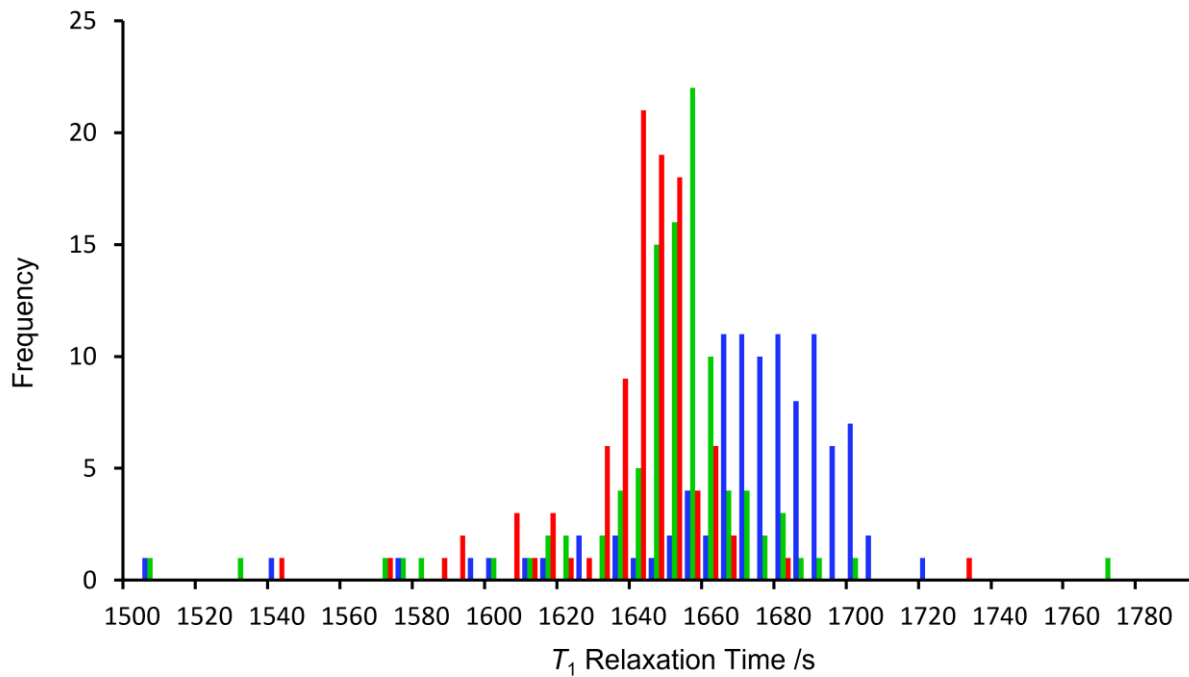


Figure 3.5: A histogram of the ^1H T_1 relaxation times observed for 0.5 mM CuSO_4 in relaxation time maps acquired with 1 (blue), 4 (green), and 16 (red) summed echo images.

It is well known that the increase in SNR from signal averaging is related to the square root of the number of averages acquired.⁴⁸ However, the relationship was different for echo images as not every echo image acquired had the same SNR due to T_2 relaxation. The effect on SNR was demonstrated in Figure 3.6 where the improvement in SNR decreased with respect to each echo summed. Data for IR experiments and additional IR experiments where a RARE factor of 4 was used can be found in Appendix 1. The reduced improvement with each echo image

suggested that there is a maximum increase in SNR that can be obtained by summing the echo images.

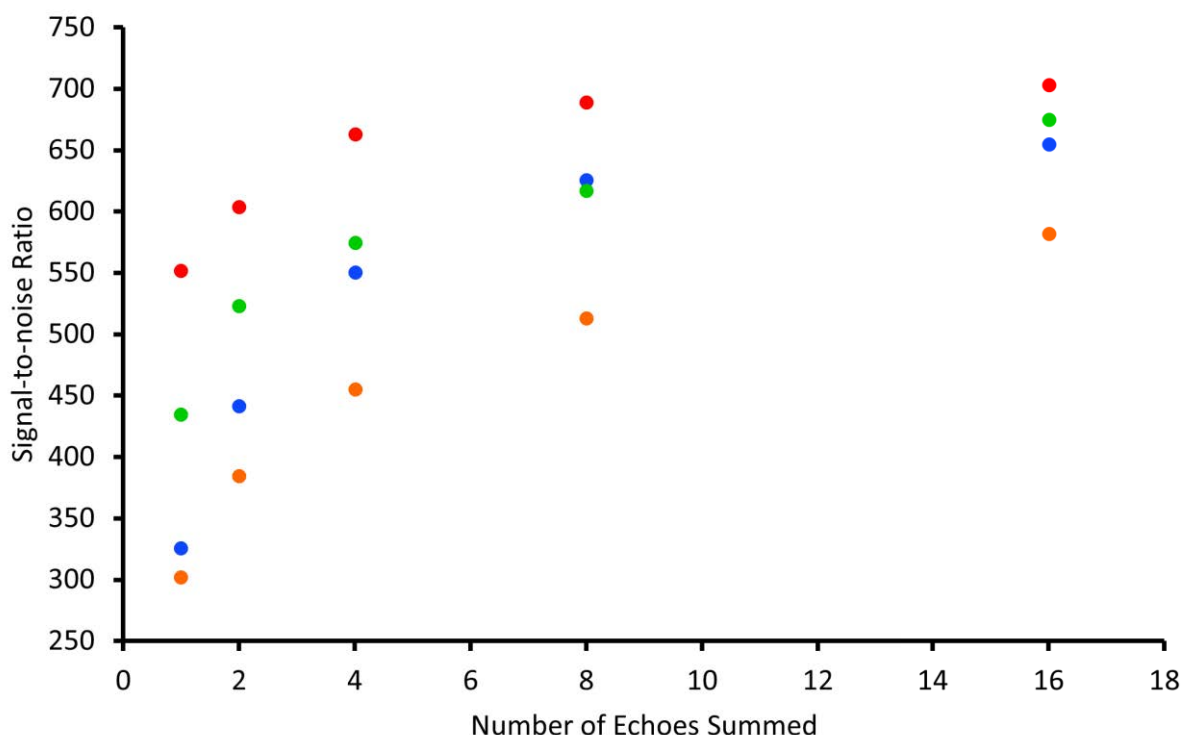


Figure 3.6: Plot of the signal-to-noise ratio and the number of echoes summed for 2 (orange), 4 (blue), 8 (green) and 16 (red) signal averages.

The effect of CuSO_4 concentration on the reduction in T_1 relaxation time standard deviation due to echo image summation is shown in Figure 3.7. The sample with the lowest CuSO_4 concentration, 0.5 mM (blue), showed a more gradual decrease in the standard deviation of the relaxation time when compared to the more concentrated 3 mM (green) and 10 mM (red) CuSO_4 samples. Plots showing SNR data for all CuSO_4 concentrations can be found in Appendix 1. The SNR for the samples with higher CuSO_4 concentrations appear to reach a plateau in the improvement of standard deviation after 8 echo images have been summed, whereas with a less

concentrated sample (0.5 mM CuSO₄), improvement of the standard deviation was still observed at 16 summed echo images.

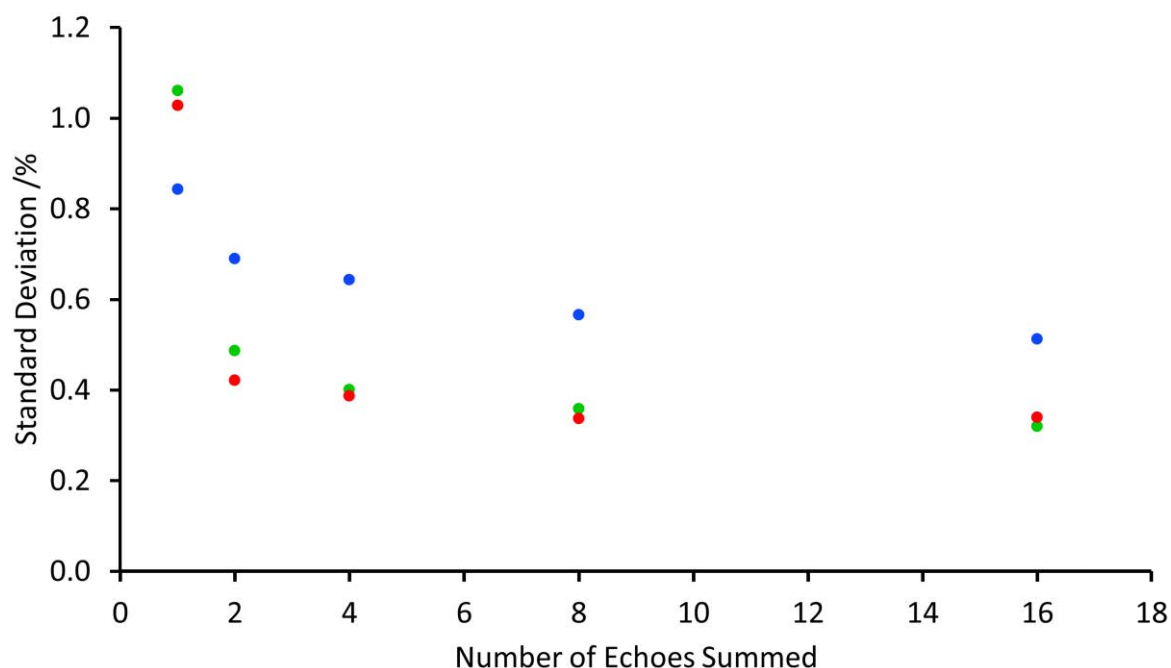


Figure 3.7: Plot of standard deviation in ¹H T₁ relaxation time as a percentage and the number of summed echoes for 0.5 mM (blue), 3 mM (green), and 10 mM (red) CuSO₄ solutions.

3.3.2 Discussion

Table 3.1 shows that the NMR relaxation time had a small variation, less than 1%, as more echo images are summed. Furthermore, the standard deviation decreased as more echoes were summed. A histogram of T₁ relaxation times acquired using signal averaging (Figure 3.4) shows the same decrease in T₁ relaxation time accompanied by a reduction in the spread of the T₁ relaxation time values. The consistency in T₁ relaxation time measurement suggested that summing echo images could accurately

determine the T_1 relaxation time and reduce the amount of time required to obtain data with improved standard deviation.

When compared to the improvement in SNR obtained by standard signal averaging, it can be seen in Figure 3.6 that a similar SNR was obtained for either 16 signal averages with 1 echo image (red), or 2 signal averages with 16 summed echo images (orange). By summing the echo images, an 8-fold decrease in experimental acquisition time was achieved whilst maintaining the accuracy of the measurement.

The limitation with summing echo images is that the improvement in standard deviation is dependent upon the T_2 relaxation time. The influence of T_2 relaxation time can be seen in Figure 3.7, where changes in the standard deviation of the measurement were not observed above 8 summed echo images for the samples with short T_2 relaxation times, 3 mM and 10 mM CuSO₄. Reduced standard deviation was observed for the sample with the longer T_2 relaxation time, 0.5 mM CuSO₄, through to 16 summed echo images.

3.4 Application of Signal-To-Noise Ratio Improvement Methodology to Water Ingress in an Ionic Liquid

3.4.1 Results

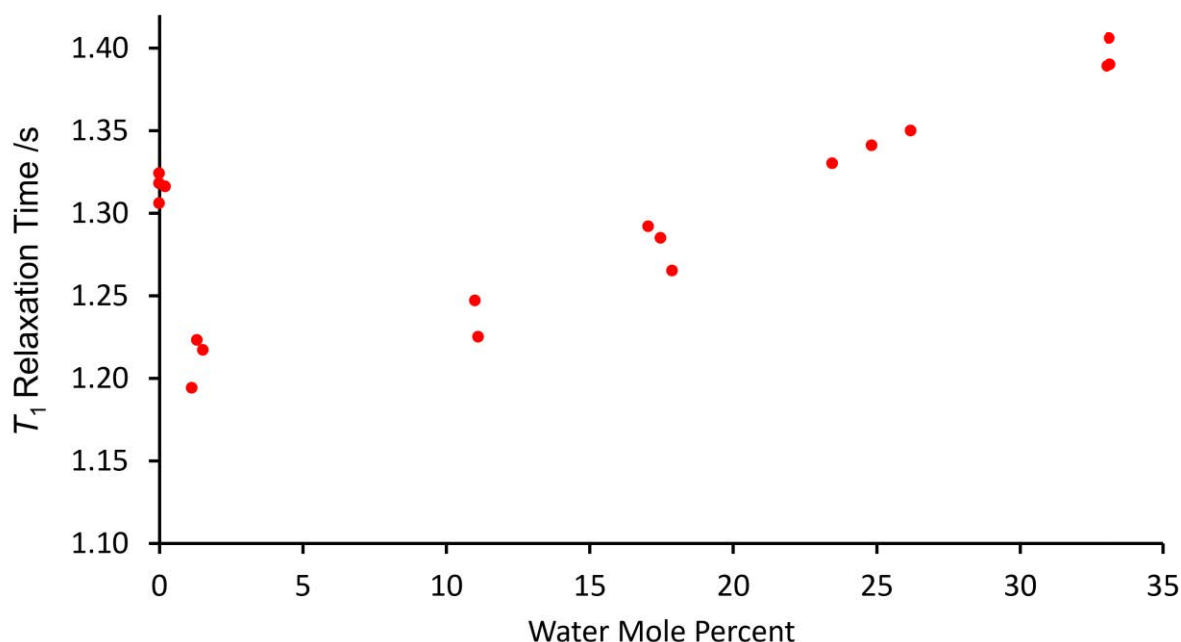


Figure 3.8: ^{19}F T_1 relaxation time measurements of 0.08 M $\text{Zn}(\text{TfO})_2$ in $\text{C}_2\text{C}_{11}\text{imTfO}$ obtained using bulk NMR spectroscopy IR experiments. Data acquired by Yasmeen AlZahrani.

The ^{19}F T_1 relaxation times acquired from samples of 0.08 M $\text{Zn}(\text{TfO})_2$ in $\text{C}_2\text{C}_{11}\text{imTfO}$ made with a known water concentration are shown in Figure 3.8. There is a clear differentiation between two regimes: the initial decrease in T_1 relaxation time following the addition of a low amount of water, up to approximately 3 mol%, and the linear increase in T_1 relaxation time at greater water concentrations, above 3 mol%. The low-water regime is difficult to characterise further using samples that are prepared via manual addition of a known water concentration due to the cost implications of the required sample size. However, the low-water

regime is a region of interest where the speciation in the IL begins to change and so NMR T_1 relaxation time maps of water ingress into 0.08 M $\text{Zn}(\text{TfO})_2$ in $\text{C}_2\text{C}_1\text{imTfO}$ over time were acquired to enable the acquisition of T_1 relaxation times at lower water concentrations.

Figure 3.9 shows the T_1 relaxation time maps, with no summed echo images, of the IL at various times after exposing to the atmosphere to allow water ingress. In these T_1 relaxation time maps, there was a change in T_1 relaxation time in the tube from top to bottom. However, the one-dimensional profiles from these maps have a low SNR and so it was impossible to generate any meaningful interpretation from these data. By summing echo images, the SNR was improved without an increase in experimental duration and thus no reduction in temporal resolution. The improvement in standard deviation can be seen in Figure 3.10, where the change in T_1 relaxation time of the IL over time is observable when compared with Figure 3.9.

To establish the relationship between T_1 relaxation time and water content, the amount of water at each point within the tube must be simulated. Simulation of the water content was achieved by assuming Fickian motion of the water molecules in 0.08 M $\text{Zn}(\text{TfO})_2$ in $\text{C}_2\text{C}_1\text{imTfO}$. Assuming Fickian motion allowed the use of a Gaussian profile of water ingress that was generated using a diffusion coefficient of

$9.9 \times 10^{-11} \text{ m}^2 \text{ s}^{-1}$, taken as the average diffusion coefficient of water in 0.15 M $\text{Zn}(\text{TfO})_2$ in $\text{C}_2\text{C}_1\text{imTfO}$. The horizontal average of the longest time point, at 33.3 h, was chosen to match with the Gaussian profile. The maximum water concentration for the tube at 33.3 h was found by performing a linear fit to the bulk T_1 data and correlating with the relaxation time close to the meniscus found in the final time point. The data from the relaxation time maps were plotted with the T_1 relaxation time measurements from NMR spectroscopy and demonstrate a non-linear relationship between T_1 relaxation time and water content at low amounts of water (Figure 3.11).

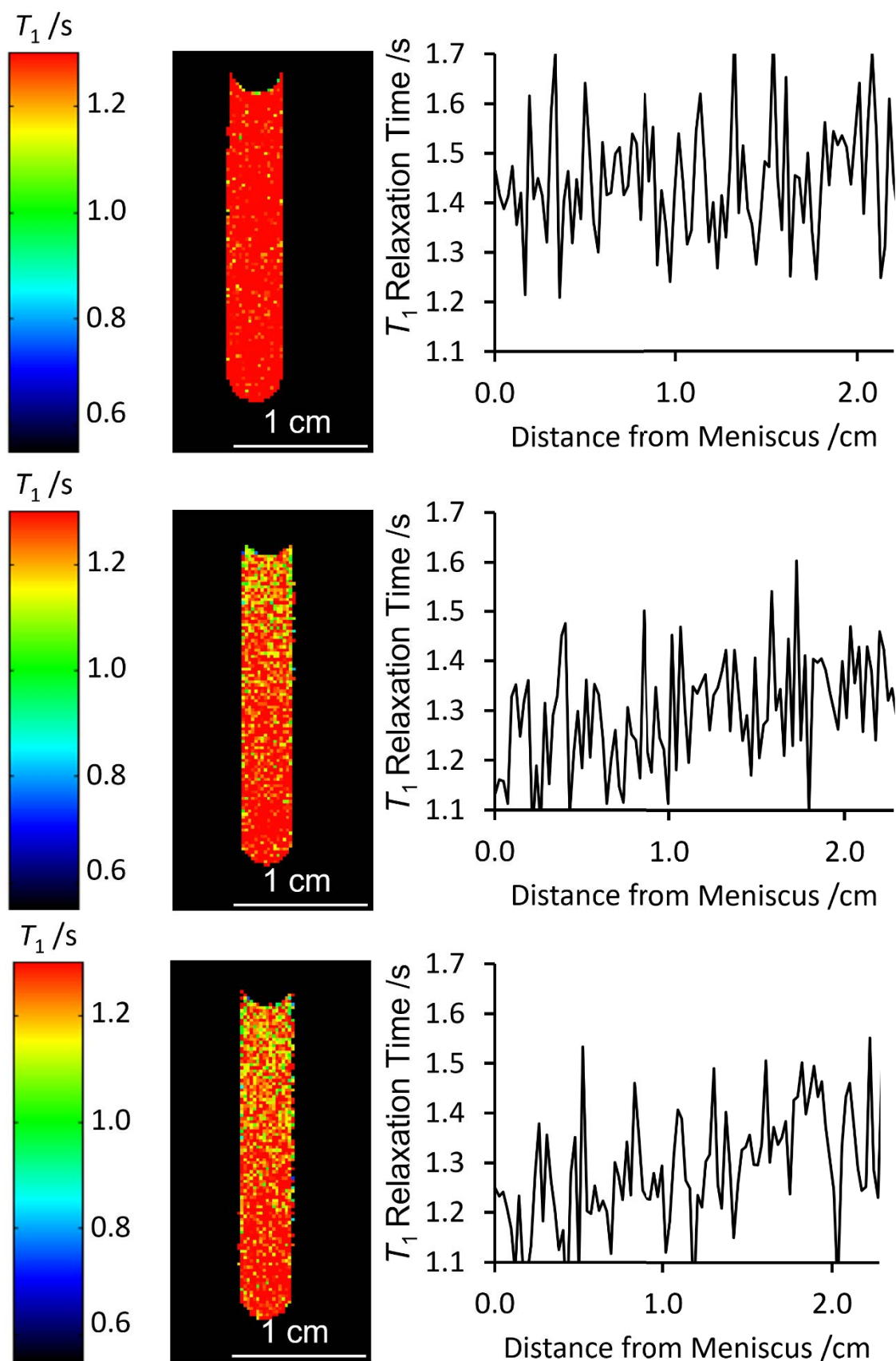


Figure 3.9: ^{19}F T_1 relaxation time maps of 0.08 M $\text{Zn}(\text{TfO})_2$ in $\text{C}_2\text{C}_1\text{imTfO}$ at 0 h, 22.5 h, and 33.3 h of water ingress from the atmosphere obtained without summing echo images.

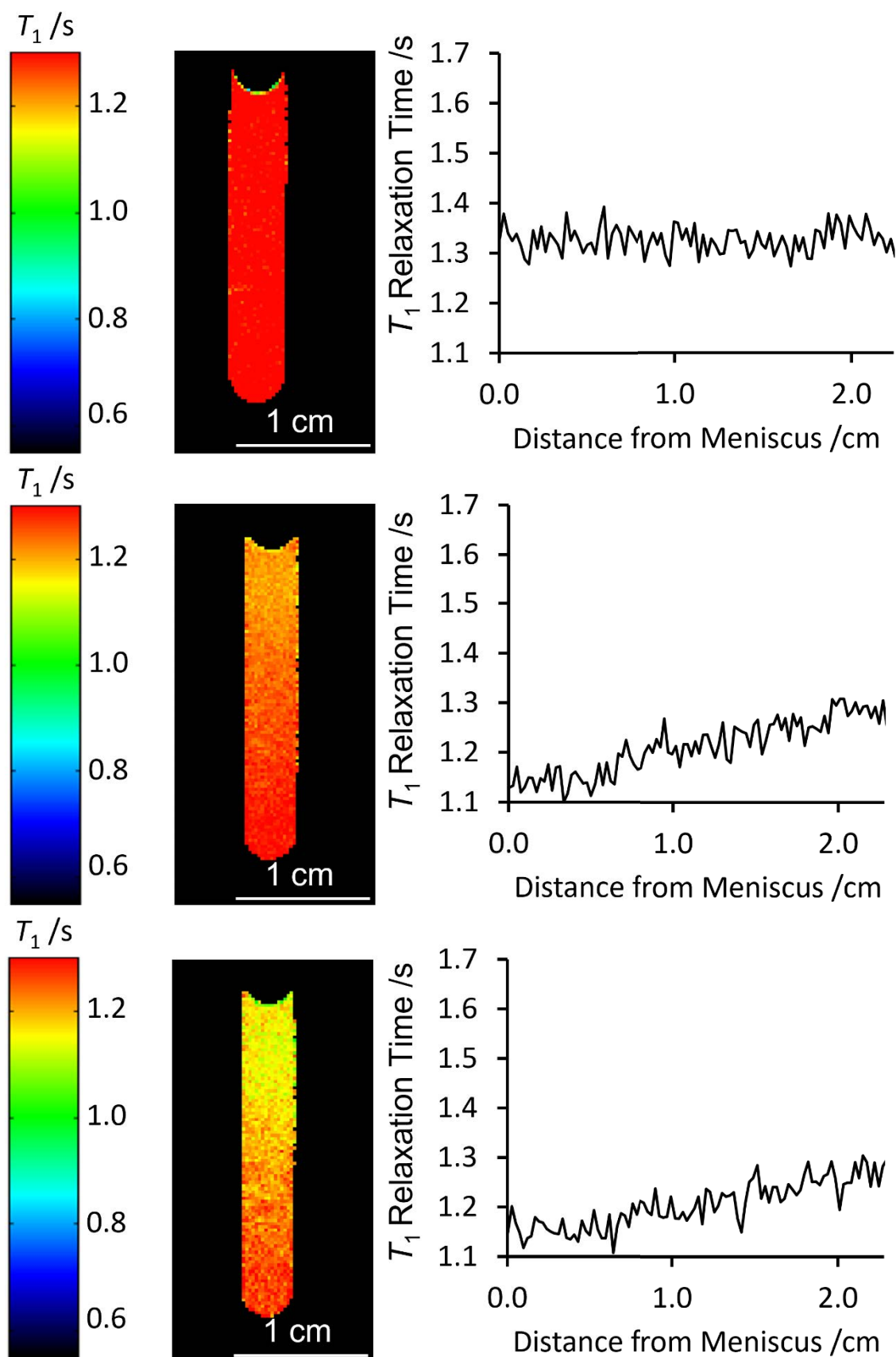


Figure 3.10: ^{19}F T_1 relaxation time maps of 0.08 M $\text{Zn}(\text{TfO})_2$ in $\text{C}_2\text{C}_{1\text{im}}\text{TfO}$ at 0 h, 22.5 h, and 33.3 h of water ingress from the atmosphere obtained by summing 16 echo images.

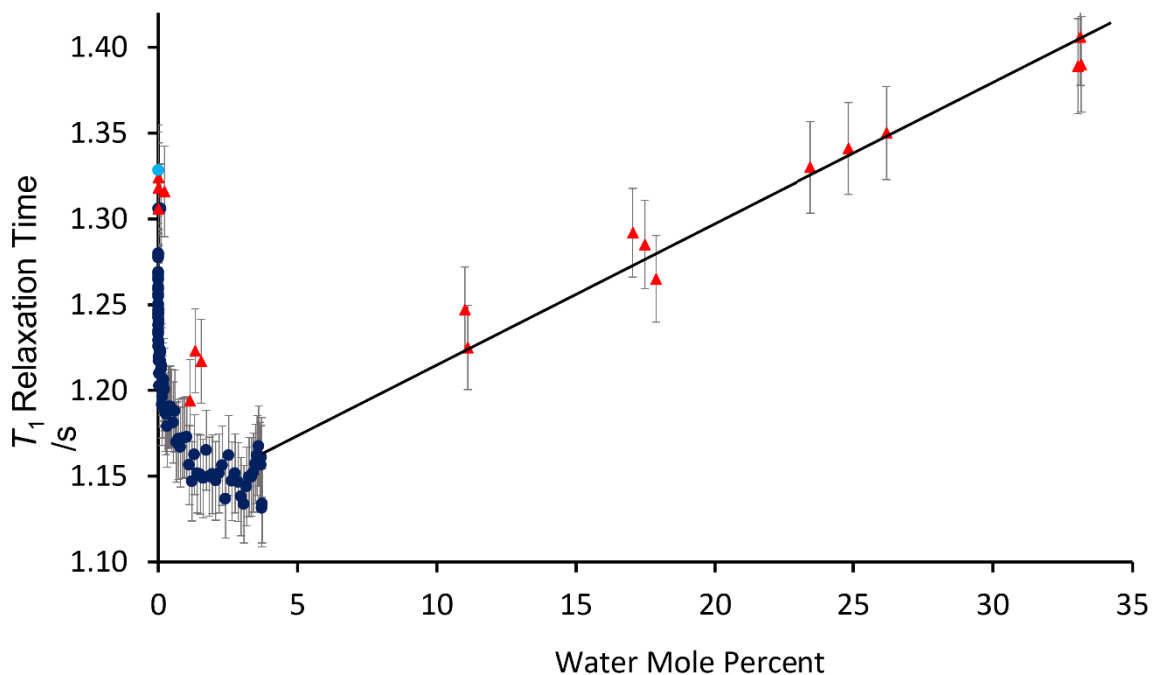


Figure 3.11: A plot of ^{19}F T_1 relaxation time of 0.08 M $\text{Zn}(\text{TfO})_2$ in $\text{C}_2\text{C}_{11}\text{imTfO}$ against water mol% with data from bulk measurements (triangles), and an average of the relaxation time map at $t = 0$ (light blue circle) and averages across the relaxation time map at $t = 33.3$ h (dark blue circles). Error bars correspond to the standard deviation of the measurement.

3.4.2 Discussion

The bulk T_1 relaxation times obtained in Figure 3.8 suggest a complex relationship with water content. Samples at lower water ratios proved difficult and costly to prepare and so an *in situ* T_1 relaxation time imaging water ingress experiment was performed. Using a standard SR experiment, the SNR was insufficient to enable the differentiation between the T_1 relaxation time at different water contents (Figure 3.9). However, summing echo images enabled noise reduction without an increase in experiment time and, when combined with horizontal averaging, sufficiently reduced the noise in the data to establish a change in T_1

relaxation time across the sample. When plotted against Gaussian water ingress, the relationship between T_1 relaxation time water ingress became clear (Figure 3.11).

It is evident that the relationship between T_1 relaxation time and water content at low-water content is non-linear. Closer inspection of the low-water content region shows two regimes: regime 1, up to 0.06 mol%, and regime 2, from 0.06 mol% to 3.0 mol%, in addition to the higher water content linear regime 3, above 3.0 mol%. The different regimes can be explained by an examination of the intermolecular interactions in the IL. The literature has previously established that upon the introduction of water, the intermolecular bonds between the cationic and the anionic species are disrupted and replaced with interactions with water.¹⁸ The change in interaction was supported by the relationship between T_1 relaxation time and water content established here. As T_1 relaxation time is correlated with molecular rotation, it can be interpreted that the initial reduction in relaxation time initially observed upon water ingress, regime 1, is caused by water molecules inserting into pockets in the pre-existing lattice structure of the IL. The pockets would restrict the rotation of the CF_3 group on the triflate anion and cause a reduction in the T_1 relaxation time. The water strongly interacts with the zinc and $\text{C}_2\text{C}_1\text{im}$ ions to generate the species shown in Figure 3.1b and disrupt the IL matrix, causing a release in the restriction of the CF_3 group and thus an increase in the T_1 relaxation time.

Regime 2, from 0.06 – 3.0 mol%, is the transfer between the restricted and unrestricted rotation of the CF_3 groups and thus has a lower rate of change in T_1 relaxation time than either regime 1 or 3.

3.5 Conclusion

In conclusion, the effects of signal averaging, SR experiments, IR experiments, and summing echo images have been characterised using different concentrations of aqueous CuSO_4 . This methodology has enabled sufficient reduction in SNR to establish the relationship between T_1 relaxation time and water content at low amounts of water in the 0.08 M $\text{Zn}(\text{TfO})_2$ in $\text{C}_2\text{C}_{1\text{imTfO}}$ IL. The average T_1 relaxation time across the sample of the T_1 relaxation time map with the largest SNR at the longest time point was used in combination with a simulated Gaussian profile of water ingress to plot the trend of T_1 relaxation time against water ingress. From the trend of T_1 relaxation time against water ingress, the speciation changes in the IL with respect to water were established. The relaxation time data support the speciation suggested in current literature.

Furthermore, the T_1 relaxation time data show that there is a region where both the species observed before and after water addition (Figure 3.1a and b) are present simultaneously, suggesting that the water first inserts into pockets in the IL lattice whilst interacting with the ionic species. Further water insertion causes the disruption and rearrangement of the intermolecular interactions, resulting in the increase in T_1 relaxation

time. The understanding of intermolecular interactions is vital to creating an optimum IL electrolyte for ZIBs and for zinc electroplating.

The methods developed in this chapter are more broadly applicable to studying concentration gradients in solution where the change in concentration corresponds to a change in T_1 relaxation time. Furthermore, summing the echo images provides a more rapid quantitative measurement of T_1 relaxation time when using MRI. For example, summing the echo images may be used to investigate the change in concentration of a charge carrier with unfavourable MRI properties during electrochemistry, the potential for which is demonstrated in Chapter 6, or in *operando* MRI of ZIBs using $\text{Zn}(\text{TfO})_2$ in $\text{C}_2\text{C}_1\text{imTfO}$.

3.6 References

1. C. P. Grey and J. M. Tarascon, *Nat. Mater.*, 2016, 16, 45-56.
2. N. Yabuuchi, K. Kubota, M. Dahbi and S. Komaba, *Chem. Rev.*, 2014, 114, 11636-11682.
3. H. Sun, G. Zhu, X. Xu, M. Liao, Y. Y. Li, M. Angell, M. Gu, Y. Zhu, W. H. Hung, J. Li, Y. Kuang, Y. Meng, M. C. Lin, H. Peng and H. Dai, *Nat. Commun.*, 2019, 10, 3302.
4. M. C. Lin, M. Gong, B. Lu, Y. Wu, D. Y. Wang, M. Guan, M. Angell, C. Chen, J. Yang, B. J. Hwang and H. Dai, *Nature*, 2015, 520, 325-328.
5. N. Jayaprakash, S. K. Das and L. A. Archer, *Chem. Commun.*, 2011, 47, 12610-12612.

6. S. Huang, F. Wan, S. Bi, J. Zhu, Z. Niu and J. Chen, *Angew. Chem. Int. Ed.*, 2019, 58, 4313-4317.
7. **M. Galiński, A. Lewandowski and I. Stępnia**k, *Electrochim. Acta*, 2006, 51, 5567-5580.
8. A. P. Abbott, G. Frisch and K. S. Ryder, *Annu. Rev. Mater. Res.*, 2013, 43, 335-358.
9. Z. Liu, S. Z. E. Abedin and F. Endres, *Electrochim. Acta*, 2013, 89, 635-643.
10. A. P. Abbott and K. J. McKenzie, *Phys. Chem. Chem. Phys.*, 2006, 8, 4265-4279.
11. K. R. Seddon, A. Stark and M.-J. Torres, *Pure Appl. Chem.*, 2000, 72, 2275-2287.
12. A. A. Niazi, B. D. Rabideau and A. E. Ismail, *J. Phys. Chem. B*, 2013, 117, 1378-1388.
13. A. M. O'Mahony, D. S. Silvester, L. Aldous, C. Hardacre and R. G. Compton, *J. Chem. Eng. Data*, 2008, 53, 2884-2891.
14. Z. Liu, S. Zein El Abedin, N. Borisenko and F. Endres, *ChemElectroChem*, 2015, 2, 1159-1163.
15. Z. Liu, N. Borisenko, S. Zein El Abedin and F. Endres, *J. Solid State Electrochem.*, 2014, 18, 2581-2587.
16. T. Cui, A. Lahiri, T. Carstens, N. Borisenko, G. Pulletikurthi, C. Kuhl and F. Endres, *J. Phys. Chem. C*, 2016, 120, 9341-9349.
17. Z. Liu, S. Z. El Abedin and F. Endres, *ChemPhysChem*, 2015, 16, 970-977.
18. Z. Liu, S. Z. El Abedin and F. Endres, *Phys. Chem. Chem. Phys.*, 2015, 17, 15945-15952.
19. Z. Liu, G. Pulletikurthi, A. Lahiri, T. Cui and F. Endres, *Dalton Trans.*, 2016, 45, 8089-8098.
20. K. Schöffski and D. Stroh, in *Encyclopedia of Analytical Chemistry*, John Wiley & Sons Ltd, New York, 2016, pp. 14289-14301.
21. A. García-Mendoza and J. C. Aguilar, *Electrochim. Acta*, 2015, 182, 238-246.

22. K. Saihara, Y. Yoshimura, S. Ohta and A. Shimizu, *Sci. Rep.*, 2015, 5, 10619.
23. M. M. Britton, *Chem. Soc. Rev.*, 2010, 39, 4036-4043.
24. M. M. Britton, *ChemPhysChem*, 2014, 15, 1731-1736.
25. M. M. Britton, P. M. Bayley, P. C. Howlett, A. J. Davenport and M. Forsyth, *J. Phys. Chem. Lett.*, 2013, 4, 3019-3023.
26. S. Chandrashekar, N. M. Trease, H. J. Chang, L. S. Du, C. P. Grey and A. Jerschow, *Nat. Mater.*, 2012, 11, 311-315.
27. S. A. Krachkovskiy, J. D. Bazak, P. Werhun, B. J. Balcom, I. C. Halalay and G. R. Goward, *J. Am. Chem. Soc.*, 2016, 138, 7992-7999.
28. S. Klamor, K. Zick, T. Oerther, F. M. Schappacher, M. Winter and G. Brunklaus, *Phys. Chem. Chem. Phys.*, 2015, 17, 4458-4465.
29. M. Klett, M. Giesecke, A. Nyman, F. Hallberg, R. W. Lindstrom, G. Lindbergh and I. Furo, *J. Am. Chem. Soc.*, 2012, 134, 14654-14657.
30. J. M. Bray, A. J. Davenport, K. S. Ryder and M. M. Britton, *Angew. Chem. Int. Ed.*, 2016, 55, 9394-9397.
31. K. J. Chang and H. Jara, *Appl. Radiol.*, 2005, 34, 34-42.
32. I. Kazour, S. D. Serai, S. A. Xanthakos and R. J. Fleck, *Abdom. Radiol.*, 2018, 43, 2679-2685.
33. X. Tang, F. Cai, D. X. Ding, L. L. Zhang, X. Y. Cai and Q. Fang, *Brain. Res. Bull.*, 2018, 140, 176-189.
34. S. Weingärtner, M. Akcakaya, S. Berg, K. V. Kissinger, W. J. Manning and R. Nezafat, *J. Cardiovasc. Magn. Reson.*, 2013, 15.
35. K. Chow, J. A. Flewitt, J. D. Green, J. J. Pagano, M. G. Friedrich and R. B. Thompson, *Magn. Reson. Med.*, 2014, 71, 2082-2095.
36. D. R. Messroghli, A. Radjenovic, S. Kozerke, D. M. Higgins, M. U. Sivananthan and J. P. Ridgway, *Magn Reson Med*, 2004, 52, 141-146.

37. S. K. Piechnik, V. M. Ferreira, E. Dall'Armellina, L. E. Cochlin, A. Greiser, S. Neubauer and M. D. Robson, *J. Cardiovasc. Magn. Reson.*, 2010, 12, 69.
38. S. Roujol, S. Weingärtner, M. Foppa, K. Chow, K. Kawaji, L. H. Ngo, P. Kellman, W. J. Manning, R. B. Thompson and R. Nezafat, *Radiology*, 2014, 272, 683-689.
39. S. E. Shore, J. P. Ansermet, C. P. Slichter and J. H. Sinfelt, *Phys. Rev. Lett.*, 1987, 58, 953-956.
40. S. E. Barrett, D. J. Durand, C. H. Pennington, C. P. Slichter, T. A. Friedmann, J. P. Rice and D. M. Ginsberg, *Phys. Rev. B Condens. Matter*, 1990, 41, 6283-6296.
41. E. W. Randall, T. G. Nunes, G. Guillot and P. R. Bodart, *Solid State Nucl. Magn. Reson.*, 1999, 14, 165-172.
42. E. W. Randall, A. A. Samoilenko and R. Fu, *Solid State Nucl. Magn. Reson.*, 1999, 14, 173-179.
43. D. G. Gillies, B. Newling and E. W. Randall, *J. Magn. Reson.*, 2001, 151, 235-241.
44. S. J. Riederer, S. T. Bobman, J. N. Lee, F. Farzaneh and H. Z. Wang, *J. Comput. Assist. Tomogr.*, 1986, 10, 103-110.
45. *Prospa*, Magritek, Wellington, New Zealand.
46. *Kaleidagraph*, Synergy Software, Reading, Pennsylvania, 4.0 edn., 2006.
47. J. Hennig, A. Nauerth and H. Friedburg, *Magn. Reson. Med.*, 1986, 3, 823-833.
48. T. Claridge, *High-Resolution NMR Techniques in Organic Chemistry*, 3 edn., 2016.

4 Magnetic Resonance Imaging of Sodium Ion Batteries

4.1 Introduction

This chapter is based on 'Magnetic Resonance Microscopy.

Instrumentation and Applications in Engineering, Life Science and Energy Research, Chapter 18' and '*Operando* visualisation of battery chemistry in a sodium ion battery by ^{23}Na magnetic resonance imaging'.^{1, 2}

The ever-increasing use of portable electronic devices and electric vehicles is fuelling a significant increase in research into energy storage. The interest is also driving the development of novel battery chemistries, which go beyond the current market leader – lithium ion batteries (LIBs).³ As such, sodium ion batteries (NIBs) are a promising new energy storage solution, owing to their lower cost and greater sustainability.⁴ However, NIBs face many similar problems to LIBs with the potential to form dendrites, particularly when a sodium metal electrode is used, and the formation of an optimum solid-electrolyte interphase (SEI) layer. Furthermore, the use of a hard carbon electrode adds additional complications to the sodium incorporation mechanism into the electrode and so further investigation is required.

Operando ^{23}Na nuclear magnetic resonance (NMR) spectroscopy has provided insight into the sodiation mechanism in sodium metal cells with

a hard carbon electrode in combination with pair distribution function (PDF) analysis.⁵ Stratford *et al.*⁵ observed the formation of a peak in the ²³Na NMR spectrum at **−40 ppm** during sodiation below 0.8 V, near the end of the sloping voltage region. The peak continued to grow and shift to 760 ppm during the low voltage electrochemistry, with the reverse occurring during desodiation.⁵ The increase in peak chemical shift is due to the increase in Knight shift⁶ as this species becomes more metallic, therefore it is referred to as quasimetallic. Further observations of the quasimetallic peak in *ex situ* spectra were dependent on the time taken between the execution of the electrochemistry and *ex situ* sample preparation, suggesting that a reaction occurs between the electrolyte and the quasimetallic species, resulting in cell discharge.⁵ When combined with PDF analysis, it was found that the quasimetallic sodium formed when sodium pooled in the hard carbon electrode and formed particles less than 10 Å in size, hence these particles are referred to as quasimetallic nanoparticles.⁵ As the focus was on the sodium insertion mechanism into hard carbon, no investigation was performed on the sodium metal electrode during this study.

The growth of sodium metal dendrites and the development of the SEI has been explored using ²³Na magnetic resonance imaging (MRI) and NMR spectroscopy. Xiang *et al.*⁷ performed *in situ* ²³Na chemical shift MRI (CSI) of sodium metal cells with a copper electrode where the sodium was

deposited and stripped on the copper electrode. The MR images showed the growth of sodium metal dendrites on the copper electrode over 15 charge cycles. Furthermore, the chemical shift of the sodium metal changes from ~ 1125 ppm for the bulk sodium metal electrode to a range of 1110-1150 ppm with the dendrite growth.⁷ The spread in chemical shift was also observed in the *operando* ^{23}Na NMR spectroscopy of the sodium metal. *Ex-situ* ^{23}Na magic angle spinning (MAS) NMR and spectral deconvolution were performed to establish changes in the SEI in the sodium dendrites and showed the presence of NaH and NaF, from reference spectra, in addition to several organic and inorganic components.⁷ This work demonstrates how ^{23}Na MRI and NMR spectroscopy can be combined to give spatially-resolved quantitative chemical information on sodium battery chemistry.

This chapter will explore the use of *operando* ^{23}Na MRI and NMR spectroscopy with three-dimensional (3D) ^1H MRI to study dendrite growth in a sodium metal cell and the evolution of sodium species in a sodium ion full cell.

4.2 Experimental

Data for the sodium metal cell with five separators were acquired by Dr Joshua Bray. All data for the sodium metal cell with two separators were acquired by Dr Joshua Bray and Claire Doswell. Sodium metal cells were assembled by Dr Joshua Bray. Sodium full cells were assembled by Dr Lin Chen. Data for the sodium full cell were collected by Claire Doswell, Dr Galina Pavlovskaya and Dr Melanie Britton. Spectral deconvolution for all cells, analysis, and electrochemistry for the sodium full cells were performed by Claire Doswell.

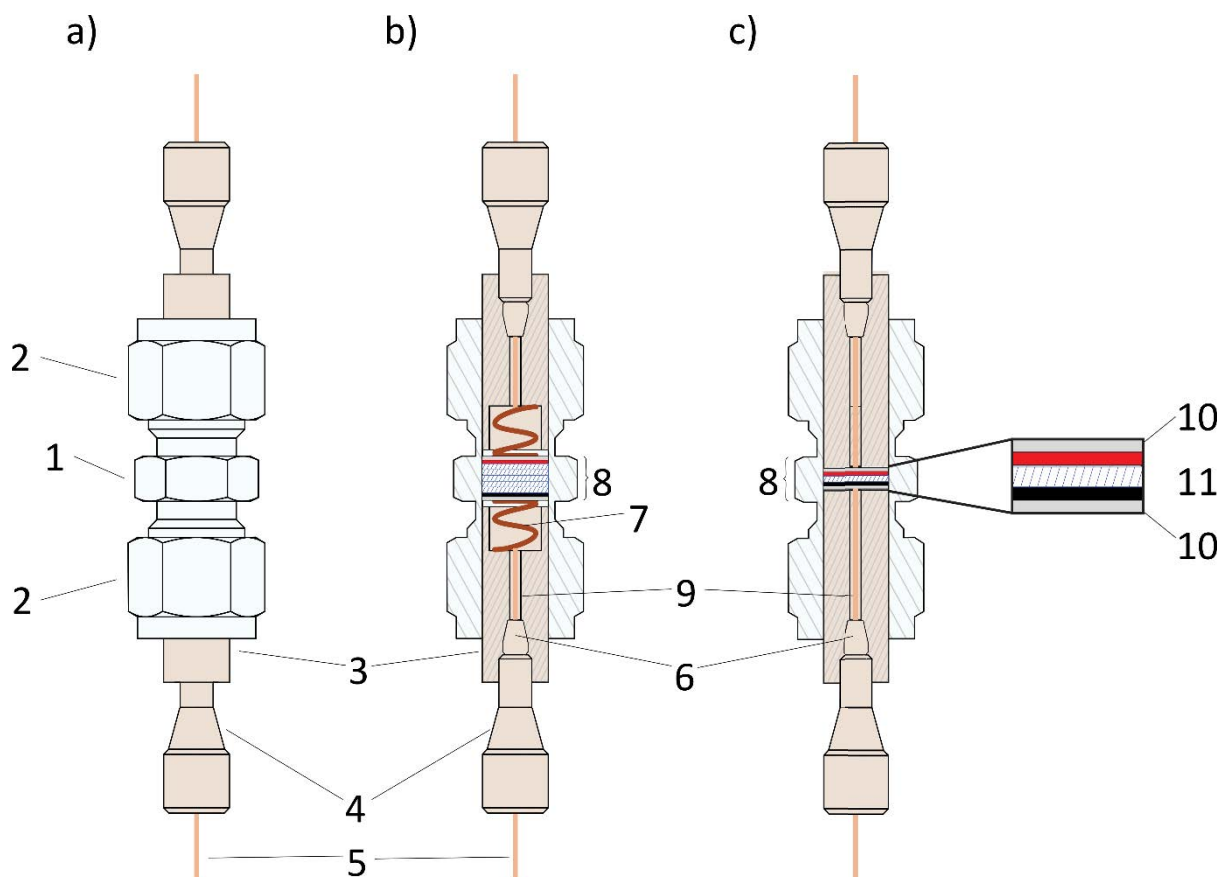


Figure 4.5: Exterior a) and cutaway of the sodium metal b) and full cell c) Swagelok cells with an expansion of the electrode and separator stack. Components are: 1. 3/8" PTFE Swagelok union, 2. PTFE Swagelok nut and ferrule assembly, 3. Custom PEEK rod, 4. 1/16" PEEK HPLC nut, 5. Insulated copper wire, 6. 1/16" PEEK HPLC ferrule, 7. Brass springs, 8. Electrode and separator stack 9. Copper wire with PTFE sheath, 10.

Aluminium current collectors, 11. Expansion of the electrode and separator stack.

The operando cell employed in this work was based on a Swagelok® union (i.d. 3/8" = 9.5 mm) shown in Figure 4.5, which is made from polytetrafluoroethylene (PTFE). The commercial Swagelok® components are made from PTFE and the centre of the union has been milled to maintain the diameter throughout the length of the Swagelok® union.

The electrode contact is made using copper wire threaded through purpose-built polyether ether ketone (PEEK) rods to ensure firm and even electrode contact and cell compression. In the metal cell experiments, the rods contain a recess in which a brass spring (Small-Order Springs & Pressings, Ltd., UK) is positioned to provide cell compression. The copper **wire is secured in position by 1/16" PEEK** high pressure liquid chromatography (HPLC) nuts and ferrules (i.d. 1/16" = 1.6 mm, VICI®) which compress a PTFE sheath fitted to the wire to ensure airtightness.

Details of material synthesis and preparation can be found in reference 12. Sodium metal cells were constructed in an argon-filled glove box (MBraun, H₂O < 0.5 ppm, O₂ < 0.5 ppm) using a sodium metal (1 mm thick, sodium ingot, 99.8% metals basis, Alfa Aesar) CE and hard carbon WE, separated by either five or two Whatman GF/B glass microfibre separators with 1 M NaPF₆ (Alfa Aesar, 99+%) in 1:1 ethylene carbonate (EC, anhydrous 99%, Sigma Aldrich): dimethyl carbonate (DMC, 99.9+%,

Sigma Aldrich) with aluminium current collectors (Alfa Aesar, 99.9% purity) on either side (Figure 4.5b). To ensure compression across the electrode stack, brass springs were used; however, these were not used in the full cell configuration, which comprised a $\text{NaNi}_{1/3}\text{Fe}_{1/3}\text{Mn}_{1/12}\text{Sn}_{1/12}\text{O}_2$ (NaNFMSO) cathode and a hard carbon anode, separated by one Whatman GF/B glass microfibre separator with 1 M NaPF_6 in 1:1 w/v EC: diethyl carbonate (DEC) (Fluorochem) with aluminium current collectors on either side (Figure 4.5c), and assembled in a dry room (dew point of $-50\text{ }^\circ\text{C}$).

Electrochemical experiments on both sodium metal cell and full cells were performed using a two-electrode configuration on an Ivium Octostat 5000. To minimise noise in the MR data while cycling cells within the MRI magnet, both shielding and low-pass filtering were used as described previously.⁸ For the sodium metal cell, an initial charge-discharge (formation) cycle was performed at 30 mA g^{-1} outside the magnet prior to MR imaging. The second charge cycle, performed at 20 mA g^{-1} , was executed with the cell inside the magnet. Galvanostatic plating at 150 mA g^{-1} for 137 min was then used to plate sodium metal onto the hard carbon WE. Plating was continued at up to 600 mA g^{-1} for 210 min. For the sodium-ion full cell, a formation cycle was performed at 30 mA g^{-1} inside the magnet during the acquisition of *operando* ^{23}Na NMR

spectra every 33 min. A charge cycle was also performed outside the magnet at 86 mA g⁻¹ before the collection of *in situ* ²³Na NMR spectra.

All MR data were acquired on a Bruker 9.4 T spectrometer equipped with either 25 mm ²³Na or ¹H single resonance RF coils or a ¹H/²³Na dual resonance RF coil. The cell was positioned in a WB40 microimaging probe using a universal specimen pot with holes drilled through the lid and bottom, to enable wires to connect to the potentiostat.

²³Na NMR spectra were acquired separately for electrolytic and metallic ²³Na environments, using pulse-acquire or spin echo sequences, at 105.8561019 MHz and 105.9757449 MHz, respectively. The large frequency difference, between metallic and electrolytic ²³Na, is the result of the Knight shift,⁹ and allows selective acquisition of either environment. Spectra were acquired with 1024 points, 2048 averages, a spectral width of 50 kHz and a repetition time $T_R = 0.1$ s and processed with zero-filling to 4096 points. ²³Na NMR spectra, covering the full spectral range (0 – 1200 ppm), were acquired using a spin echo sequence, with a spectral width of 250 kHz, a transmitter frequency of 105.9130825 MHz (positioned between the electrolyte and metallic signal), collecting 512 points, 32768 averages and a repetition time $T_R = 0.05$ s. Short excitation and refocusing pulse durations were used, 2 μ s and 4 μ s respectively, to enable the excitation of a sufficiently broad frequency range. Spectra

were Fourier transformed with zero-filling to 2048 points and line broadening of 1800 Hz, and baseline correction.

Spectral fitting was performed using DM Fit software¹⁰ using a combination of Lorentzian and Gaussian functions as described in Chapter 2.1.1.2. A minimum number of peaks were selected to enable the spectrum to be adequately fitted. Data for all spectral deconvolutions can be found in Appendix 2.

²³Na images of the electrolyte, in a pristine metal cell, were acquired using a gradient echo sequence with read encoding along the vertical (z) axis of the cell and phase encoding across the horizontal axis of the cell. Images were acquired with 1024 averages and a spectral width of 200 kHz, 256 read and 16 phase points with a field-of-view (FOV) of 59 × 19.5 mm. Data were Fourier transformed using a sine bell squared filter and zero-filled to 512 × 64 points which resulted in voxels of 115 μm × 305 μm. ²³Na images of sodium metal, in a pristine metal cell, were acquired using a spin echo sequence, with the same orientation as the electrolytic images. The images were acquired with 1024 averages, a spectral width of 200 kHz and 256 read and 16 phase points with a FOV of 59 × 16.9 mm. Data were Fourier transformed using a sine bell squared filter and zero-filled to 512 × 64 points which resulted in voxels of 115 μm × 264 μm. ²³Na images of the full cell were acquired using a spin

echo pulse sequence with the same orientation as the sodium metal cells. Images were acquired with 2048 averages and a spectral width of 50 kHz, 64 read and 16 phase points with a FOV of 26.9×94.2 mm. Data were Fourier transformed using a sine bell squared filter and zero-filled to 256×64 points which resulted in voxels of $105 \mu\text{m} \times 1472 \mu\text{m}$.

3D ^1H MR images, of the electrolyte in the sodium metal cell, were acquired using a multi-slice multi- (spin) echo sequence with horizontal frequency encoding, 15 mm isotropic FOV, with a $117 \mu\text{m} \times 117 \mu\text{m} \times 469 \mu\text{m}$ voxel size and a 1.0 s repetition time T_R . Zero-filling in the y direction was used during processing to produce 3D images with isotropic voxels.

Negative images, to enable observation of sodium microstructures, were produced from the ^1H 3D MRI data, by only displaying voxels below a threshold intensity, which was set to 7.4% of the maximum image intensity. Application of the threshold enabled regions to be identified where the electrolyte was below the level of detection and either absent or depleted (compared to the pristine cell) following the formation of metallic sodium microstructures within the separator. All images were analysed using *Prospa*.¹¹

4.3 Results and Discussion

4.3.1 Distribution and Evolution of Sodium Species in a Sodium Metal Cell

Figure 4.2a shows a ^{23}Na NMR spectrum where different electrolyte locations were observed as two peaks, one corresponding to the sodium within the separator (blue) and the other from sodium in the electrolyte that was between the PEEK rod and the Swagelok casing (grey). Figure 2b shows a spectrum of the sodium metal, with one environment as expected.

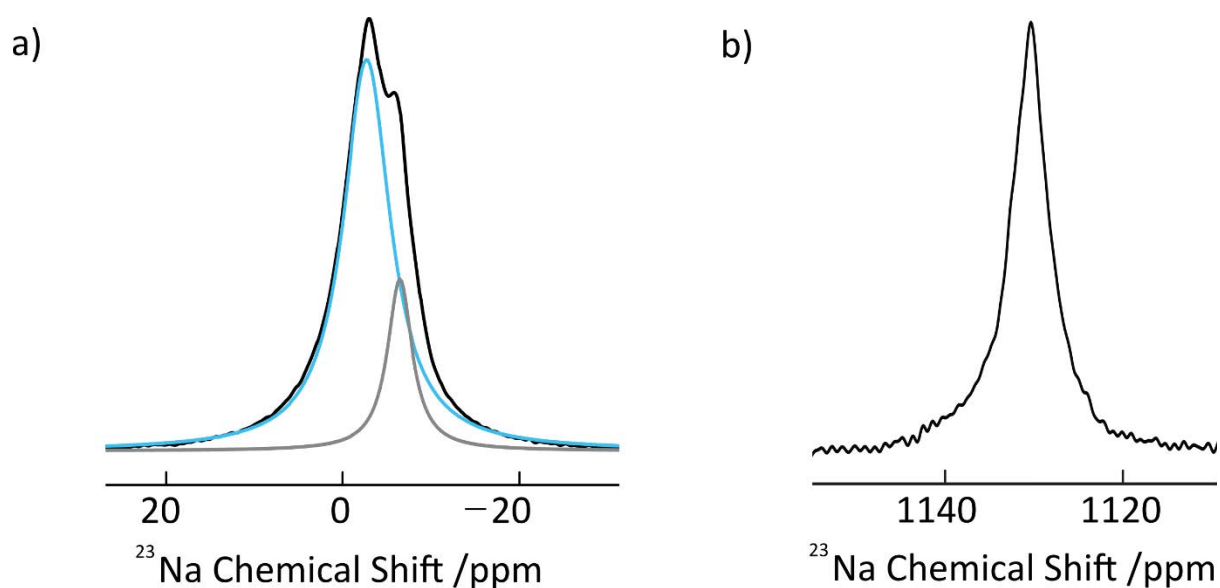


Figure 4.2: ^{23}Na NMR spectra of sodium in the 1 M NaPF_6 in EC/DMC electrolyte a) and metallic sodium b) for a pristine sodium metal cell. Two peaks are observed for the sodium electrolyte (a), arising from electrolyte inside the stack of five separators (0 ppm, blue) and outside the electrode stack (-5 ppm, grey).

In Figure 4.3, 2D ^{23}Na MR images for the electrolytic (blue) and metallic (red) sodium are shown. The signal intensity for the electrolytic sodium was higher in the centre of the cell than on the outer edges, which is due

to the greater signal arising from the large slice thickness that encompassed the cylindrical cell. The signal from the sodium metal appears as two narrow strips of signal, which is because of the skin depth penetration of the RF.¹²

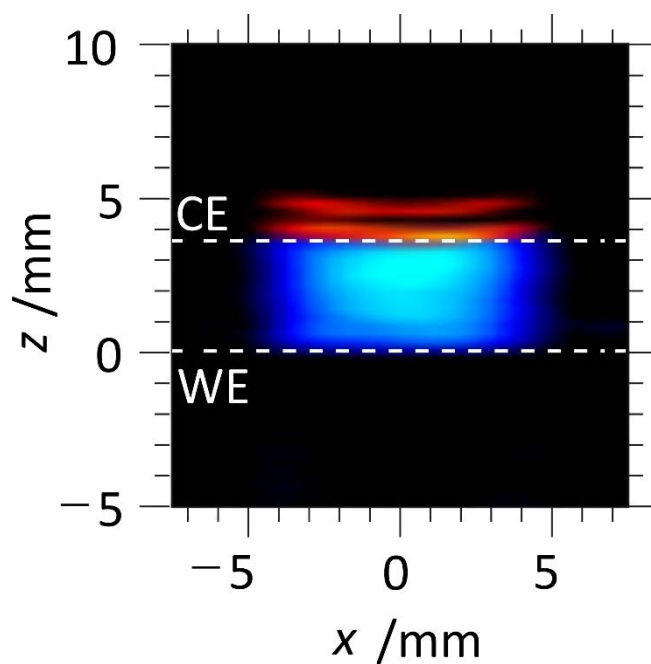


Figure 4.3: 2D ^{23}Na MR images of sodium in the 1 M NaPF_6 in EC/DMC electrolyte (blue) and sodium metal (red) in a pristine sodium metal cell containing five separators.

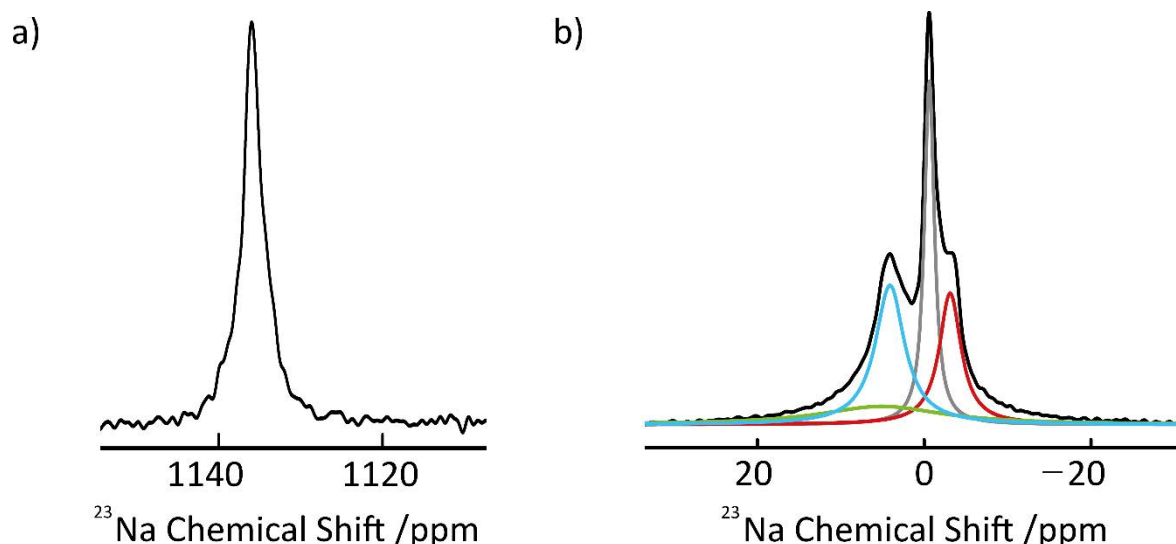


Figure 4.4: ^{23}Na NMR spectra of the sodium metal a) and sodium in the 1 M NaPF_6 in EC/DMC electrolyte b) showing the electrolyte inside the separator (0 ppm, blue), outside of the separator stack (-5 ppm, grey), sodium in the vicinity of the hard carbon working electrode (-7 ppm, red) and sodium with reduced mobility (1 ppm, green) of a sodium metal cell after a formation cycle has been performed.

^{23}Na NMR spectra were acquired for the sodium metal cell, after a formation cycle, and shown in Figure 4.4. No change was observed in the spectrum for metallic sodium, however, in the spectrum for the electrolyte, there were two new environments: one downfield (-7 ppm) believed to arise from sodium in the vicinity of the hard carbon electrode (red), and the other (1 ppm) believed to arise from sodium with reduced mobility (green), for instance the sodium in the SEI.

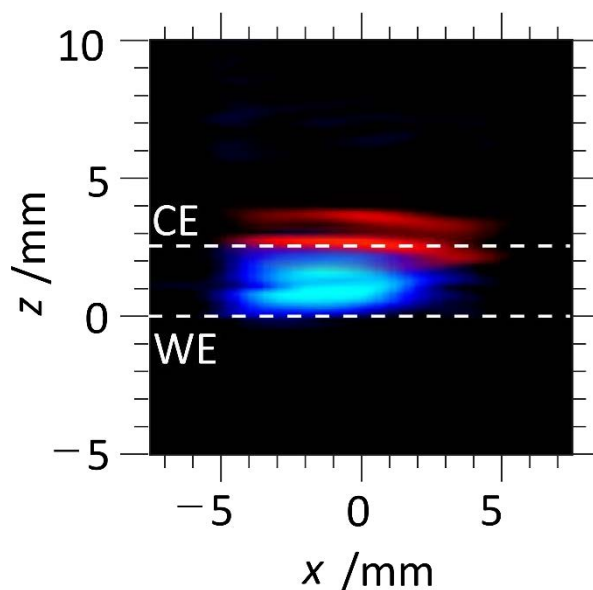


Figure 4.5: 2D ^{23}Na MR images of the sodium in the 1 M NaPF_6 in EC/DMC electrolyte (blue) and sodium metal (red) in a sodium metal cell with two separators after a formation cycle has been performed.

In Figure 4.5, ^{23}Na 2D MR images of the sodium metal (red) and sodium in the electrolyte (blue), for a sodium metal cell following a formation cycle, are presented. The images indicated that the distribution of sodium in the electrolyte was not homogenous in this cell. It is not clear what the origins of the inhomogeneity were, but they could be a consequence of cell assembly, uneven compression across the electrodes leading to inhomogeneity in the cell chemistry, or heterogeneous degradation of the electrolyte. However, observation of such factors is essential to assist with the interpretation of electrochemical behaviour for a cell.

4.3.2 Distribution and Evolution of Sodium Species in a Sodium Full Cell

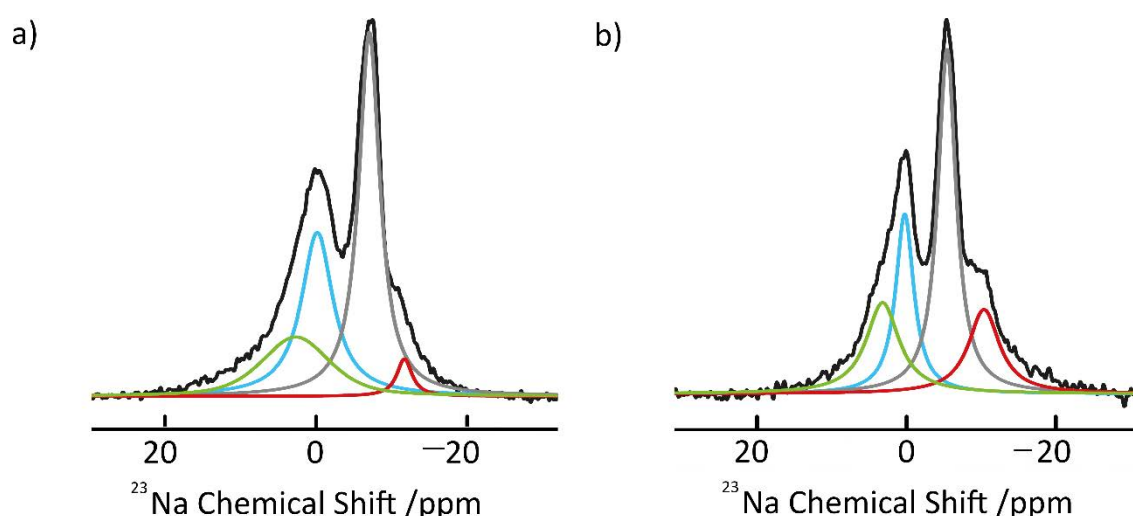


Figure 4.6: ^{23}Na NMR spectra of sodium in the 1 M NaPF_6 in EC/DEC electrolyte in a full cell, containing a single separator before a) and after b) the formation cycle showing sodium in the electrolyte outside the electrode stack (-5 ppm, grey) and inside the separator (0 ppm, blue), sodium in the vicinity of the hard carbon electrode (-13 ppm, red) and sodium with reduced mobility (7 ppm, green).

Whilst the sodium metal cell enabled the exploration of different sodium environments in the electrolyte, it was not representative of a battery that would be produced commercially due to the issues surrounding the use of metal electrodes discussed in Chapter 1.1.1 and 1.2.1. Hence full cells were investigated, which did not contain metallic sodium CEs, enabling observation of the formation of metallic sodium during charge cycling. Figure 4.6 shows ^{23}Na NMR spectra of the electrolyte, within a full cell, before and after a formation cycle. From the spectra, four sodium environments in the electrolyte were observed following peak fitting: signal from sodium in the electrolyte inside the separator stack (blue),

sodium in the electrolyte outside the separator stack (grey), sodium in the vicinity of the hard carbon (red) and sodium with reduced mobility (green). The peaks are believed to arise from sodium within the SEI, or other degradation of the electrolyte upon contact with the electrode.

There is a difference in the range of sodium species observed in full and metal cells prior to the formation cycle. In the metal cell, only one sodium environment was observed within the electrode stack (Figure 4.4b).

However, in the full cell (Figure 4.6a), at least three distinct environments were observed in the electrolytic sodium. It is possible that the differences were because of the changes in electrode materials used.

However, it may have been that an increase in compression in the full cell, at the time of assembly, promoted reaction between the sodium electrolyte and electrodes, giving rise to these additional sodium environments.

Following the formation cycle in the full cell (Figure 4.6b), a similar range of sodium environments was observed. The peak at -13 ppm, associated with sodium in the vicinity of the hard carbon, increased in intensity which could be due to irreversible incorporation of sodium into the hard carbon. Additionally, the width and Gaussian weighting of the peak at 7 ppm decreased which may reflect a change in the range of sodium environments.

4.3.3 Metallic Sodium Formation in a Sodium Metal Cell

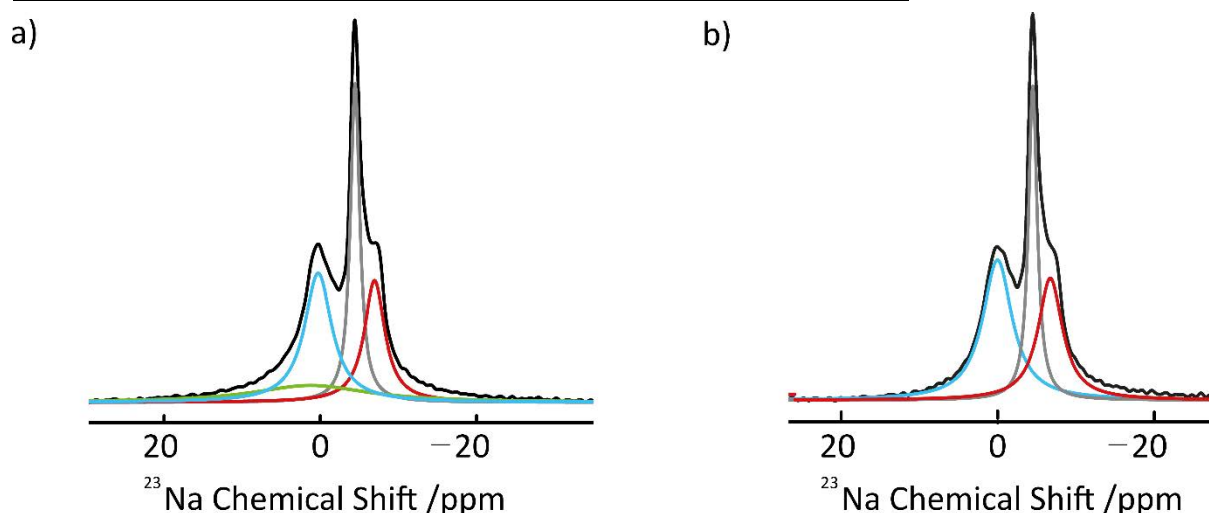


Figure 4.7: ^{23}Na NMR spectra of the sodium in the 1 M NaPF_6 in EC/DMC electrolyte after the formation cycle a) and after the formation of dendrites b) in a sodium metal cell. Peaks are observed for electrolyte inside the separator (0 ppm, blue), electrolyte outside the separator stack (-5 ppm, grey), and reacted sodium in the vicinity of the hard carbon working electrode (-7 ppm, red). However, the peak for sodium with reduced mobility (1 ppm, green) is only observed in the cell prior to dendrite formation.

The formation of sodium dendrites is an area of interest in NIBs and was investigated in the sodium metal cell, during galvanostatic plating. Figure 4.8 shows ^{23}Na NMR spectra of the electrolyte following the formation cycle (Figure 4.7a) and after galvanostatic plating (Figure 4.7b). Three peaks were observed in both spectra that were from sodium in the electrolyte outside the electrode-separator stack (grey), sodium electrolyte in the separator (blue) and reacted sodium in the vicinity of the hard carbon electrode (red).

After the growth of dendrites, the peak from sodium with reduced mobility (green) disappeared below the level of detection, suggesting that

it was replaced by the formation of dendrites. ^{23}Na NMR spectra of metallic sodium (Figure 4.8) show a range of sodium environments corresponding to the sodium metal electrode (red) and new metallic sodium environments. The additional environments are believed to be associated with sodium microstructures, or dendrites. The chemical shifts for the new metallic sodium microstructures were sensitive to the orientation with respect to B_0 . The peak at 1141 ppm was believed to arise from sodium microstructures at 0° to the B_0 field (pink and green), which were growing perpendicular to the sodium CE. However, there were additional peaks (1129–1125 ppm), at a lower chemical shift to the sodium CE (1131 ppm, red), which could arise from microstructures growing at different orientations to the WE, or from pitting on the CE, at **an angle close to 90° to B_0** (blue and orange).

As galvanostatic plating continued, the peak at 1141 ppm increased in intensity, and was greater than the sodium CE. The increase in intensity was due to the higher surface area expected on the dendritic sodium, compared to the sodium CE. Furthermore, the number of peaks above 1131 ppm increased, suggesting a greater range of orientations for these metallic surfaces, as the dendrites grow. However, a similar evolution was not observed for the sodium environments with lower chemical shift to the sodium CE, which do not increase significantly in intensity, possibly

further supporting the supposition that these peaks arise from pitting on the CE, as sodium is removed from the electrode.

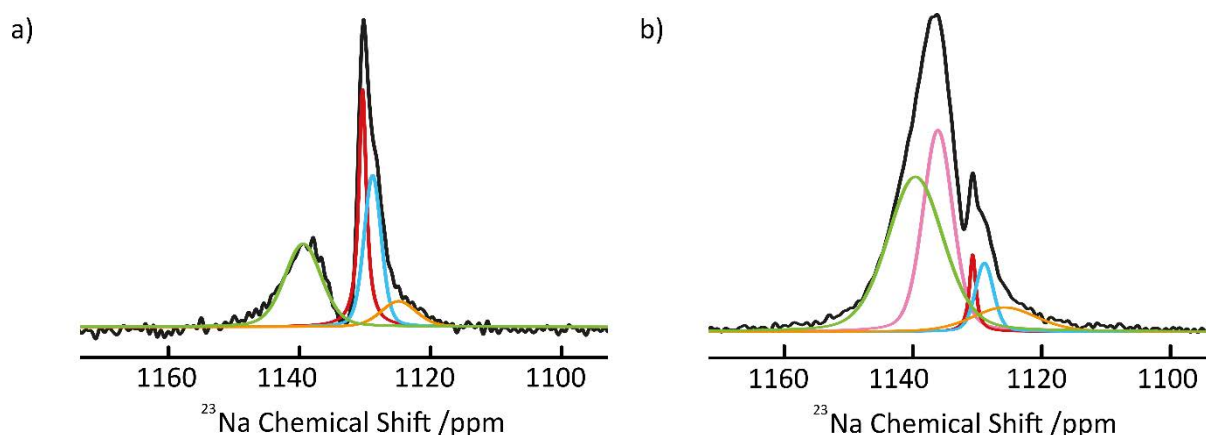


Figure 4.8: ^{23}Na NMR spectra of the sodium metal before a) and after b) the growth of dendrites in a sodium metal cell showing the signal from the sodium metal electrode (1131 ppm, red), sodium microstructures at 90° to the B_0 field (1136 ppm, 1141 ppm, green and pink) and sodium plated on the hard carbon electrode or pitted on the sodium metal electrode at 0° to the B_0 field (1129 ppm, 1126 ppm, blue and orange).

The formation of sodium dendrites was observed in the ^{23}Na MR images of sodium metal (red) and electrolyte (blue) in Figure 4.9. The additional sodium environment, believed to arise from sodium dendrites on the hard carbon, was observed on the surface of the WE. The signal intensity for the metallic dendritic sodium appears to be greater than that of the CE, due to the greater surface area for these microstructures compared to the CE, which agreed with the ^{23}Na NMR spectra (Figure 4.8). Unfortunately, the images were unable to reveal the structure of the dendrites and it was not possible to visualise in 3D, because of the low SNR and high line widths for the ^{23}Na signal. However, by using ^1H MRI of the EC/DMC

electrolyte it was possible to visualise the shape and location of the dendrites (Figure 4.9b).

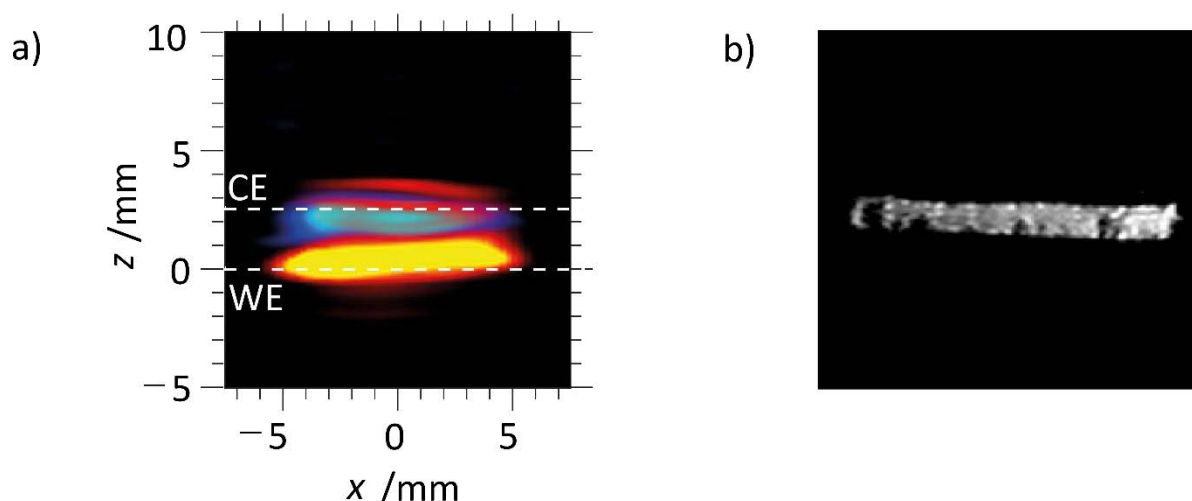


Figure 4.9: a) 2D ^{23}Na MR images of the sodium in the 1 M NaPF_6 in EC/DMC electrolyte (blue) and sodium metal (red) in a sodium metal cell after dendrites have formed. b) Selected slice from a 3D ^1H MR image of showing the location of the 1 M NaPF_6 in EC/DMC electrolyte in the sodium metal cell after the formation of dendrites.

Using the ^1H MR images of the electrolyte, it was possible to generate negative images, which indicated the regions where the electrolyte was below the limit of detection because it was not present or had been displaced by the growth of sodium dendrites. Figure 4.10 shows images of the surface of the hard carbon electrode of the pristine cell and after dendrite growth generated using the ^1H 3D electrolyte images and correlate to the large signal intensity seen on the WE in Figure 4.9a. The dendrites were not uniformly distributed across the electrode, with larger structures observed on the left side of the image (Figure 4.10b). Furthermore, they appeared to have rounded structures, which was

supported by the variety of peaks observed in the metallic ^{23}Na NMR spectrum after dendrite growth (Figure 4.8b).

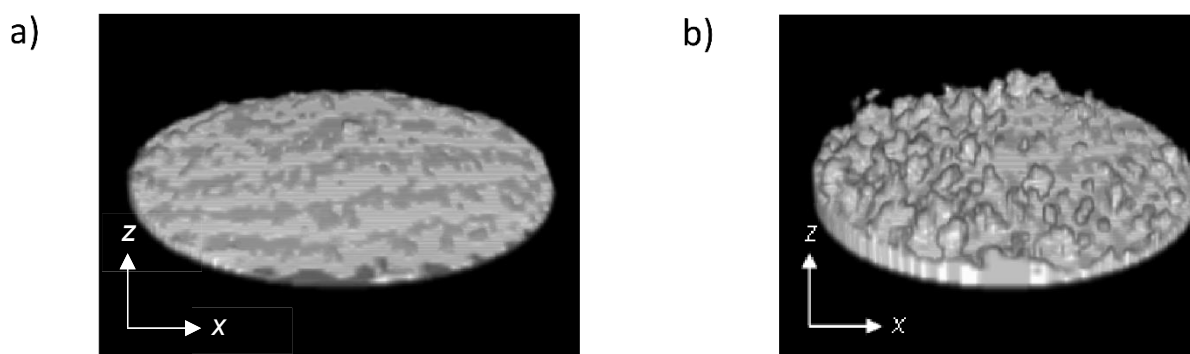


Figure 4.10: Negative images of the surface of the hard carbon WE of a sodium metal cell before a) and after b) the growth of dendrites. Generated using the regions where the signal intensity in a 3D ^1H image of the 1 M NaPF_6 in EC/DMC electrolyte falls below the limit of detection.

4.3.4 Metallic Sodium Formation in a Sodium Full Cell

While sodium metal cells are commonly used in *operando* studies of battery chemistry and dominate *operando* NMR and MRI studies of LIBs and NIBs, the presence of the sodium CE can give rise to increased internal resistance in the cell, as well as mask the development of new metallic sodium environments during charge cycling. By moving to a full cell configuration, it was possible to prevent both of the issues. Figure 4.11 shows *operando* ^{23}Na NMR spectra, and corresponding electrochemistry, during the formation cycle of a full cell. Prior to the formation cycle, the pristine cell displayed only a single electrolytic environment, as expected. As the formation cycle proceeded, a peak developed below 0 ppm and was intermittently observed from 0.5–3 h

and after 4 h. The peak indicated the presence of sodium which had inserted within the hard carbon or SEI formation. Formation of quasimetallic nanoparticles was observed for the first time in a sodium full cell as a signal that develops out of the electrolytic signal during the potential plateau, after 2.5 h of charging. The quasimetallic peak shifted further upfield and increased in peak width as the cell continued to charge. The increased chemical shift suggested that the nanoparticles were becoming larger and more metallic as more sodium was incorporated within the hard carbon electrode. Figure 4.12 shows selected ^{23}Na NMR spectra that were acquired during the formation cycle of a sodium full cell. Figure 4.12a shows multiple environments in the region associated with the electrolyte signal; these are sodium in the vicinity of the hard carbon electrode (red, green), such as in the SEI or intercalated sodium, and initial formation of quasimetallic nanoparticles (orange). Figure 4.12b shows the development of the quasimetallic species which has moved further upfield.

After 2 h of charging, at the potential plateau around 2.5 V, a metallic signal (pink) was observed in the spectra at over 1000 ppm (Figure 4.13). The development of metallic sodium has not been previously reported in the literature, but has been hypothesised.¹³ The majority of *operando* studies employ sodium metal CEs which have a large signal from the sodium CE; this signal would obscure any small increase in signal in the

metallic region of the spectrum. Hence the new metallic species may have been present in previous studies but not observed. As the full cell progressed in the formation cycle, the intensity of the metallic peak initially decreases in intensity before shifting further upfield and disappearing at the end of the potential plateau.

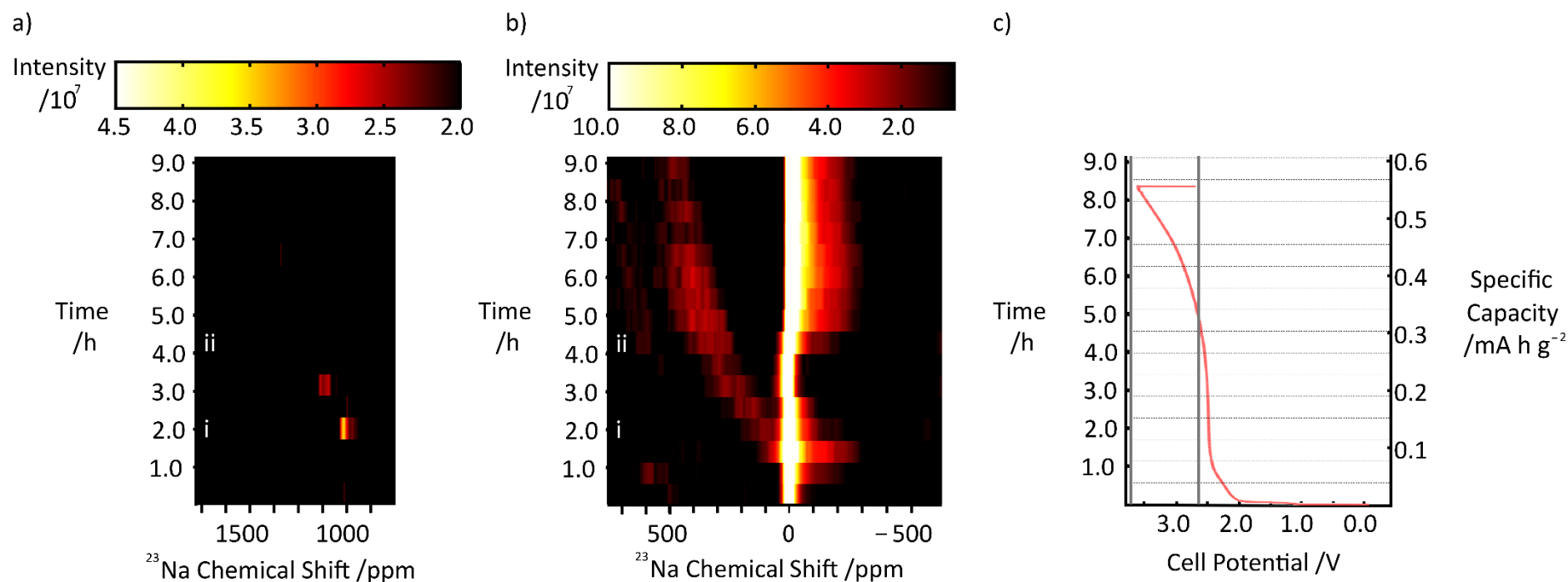


Figure 4.11: ^{23}Na NMR spectra acquired in *operando* during a formation cycle at 30 mA g^{-1} of a sodium-ion full cell showing the formation of a metallic species and the evolution of quasimetallic species showing the metallic a), and electrolytic b) regions of the NMR spectrum and the corresponding electrochemistry c). Labelled spectra i and ii are shown in Figure 12 a and b respectively.

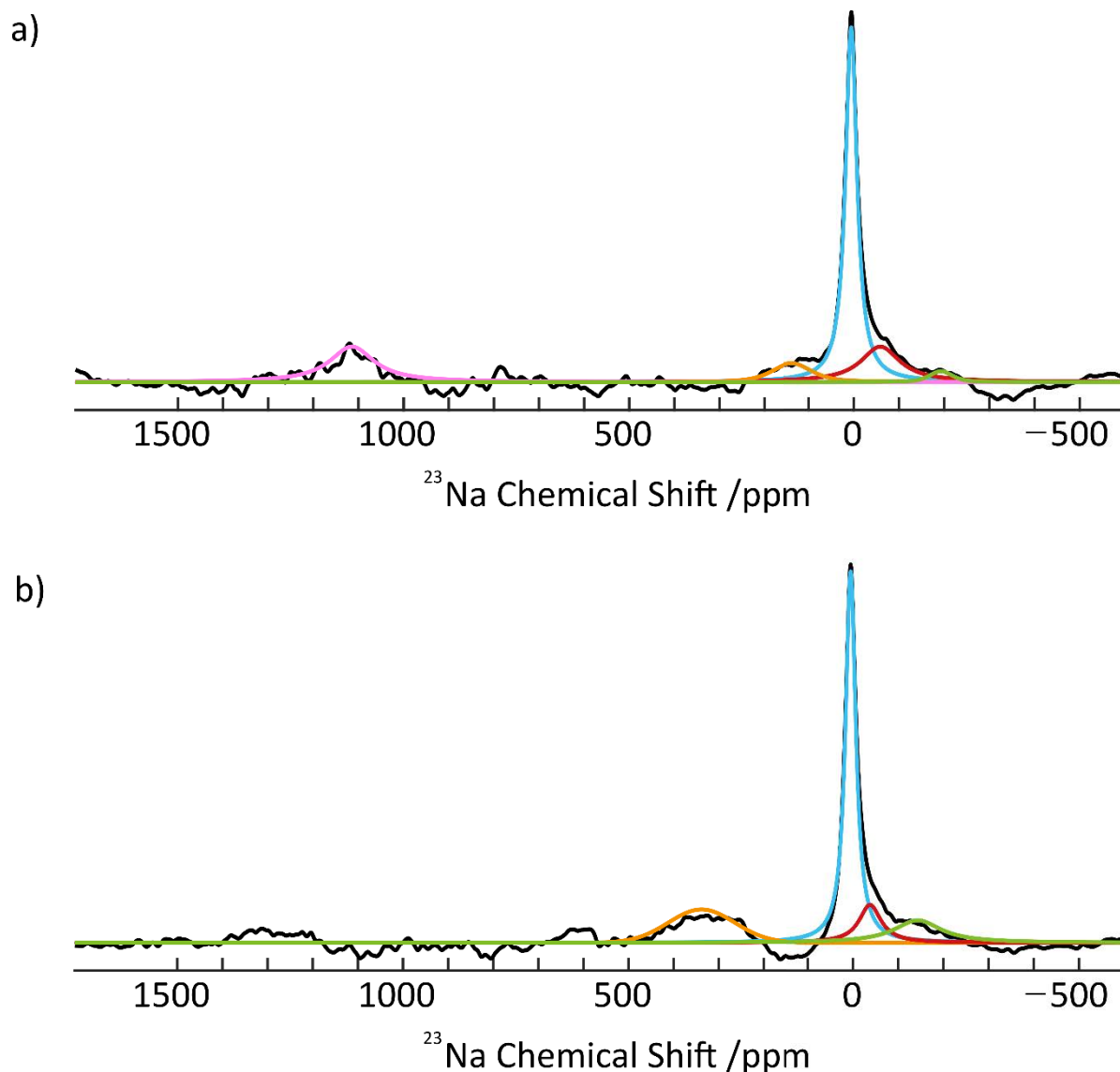


Figure 4.12: ^{23}Na NMR spectra covering the full spectral range acquired *operando* during the formation cycle of a sodium-ion full cell showing the formation of a metallic signal (pink) at low electrochemical potential with the electrolyte (blue) and species in the vicinity of the hard carbon electrode or SEI (red and green) (Figure 4.11 spectrum i) a) and subsequent quasimetallic species (orange) (Figure 4.11 spectrum ii) b).

Late in the charge cycle, a range of environments above 1300 ppm were observed (Figure 4.13). The peaks were low intensity, and around the level of the noise. Above 1300 ppm is a high chemical shift for sodium

environment, however, the peaks were responsive to phase angle changes during spectral processing like the other metallic peaks seen. Furthermore, there has been evidence in the literature of sodium species at high chemical shifts as insulated sodium clathrate structures observed by Gryko *et al.*¹⁴ The sodium clathrate species were within silicon and it is suggested that the large shift was due to paramagnetic effects related to isolated sodium atoms within the clathrate structures. In the sodium full cell, as more sodium began to incorporate into the hard carbon structure, some sodium may have occupied small isolated pores making the sodium environment an insulated cage-like structure as described by Gryko *et al.*¹⁴ The small amount of sodium existing in this insulated species would account for the low signal intensity. The presence of small, insulated sodium cages has never been observed or theorised in NIBs.

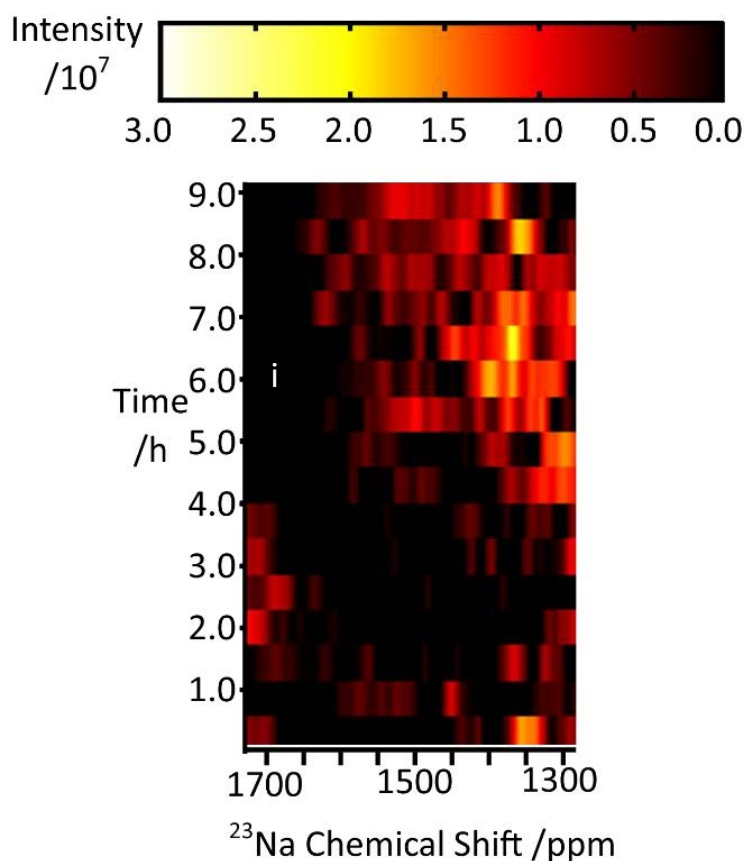


Figure 4.13: Time series of ^{23}Na NMR spectra, shown between 1300 and 1700 ppm, acquired in *operando* during a formation cycle at 30 mA g^{-1} of a sodium-ion full cell showing the formation of species with a high chemical shift. Labelled spectrum i is shown in Figure 14.

Additional information about the evolution of sodium species at higher charge rates was interpreted from analysis of the ^{23}Na NMR spectra shown in Figure 4.15. In contrast to Figure 4.11, the spectra show no development of a quasimetallic signal emerging from the electrolyte signal throughout the charge cycle. Furthermore, there was an increase in the intensity of the environments observed in the metallic region of the spectrum ($>1000 \text{ ppm}$, Figure 4.15a). The predominant signal emerged at $\sim 2.5 \text{ h}$ and was less intense in the following spectrum but reappeared at 3.5 h . The emergence of this metallic signal is significantly later in the

charge cycle of the battery in comparison to the cell charged at 30 mA h g⁻¹ and above the voltage plateau at 2.6 V. However, the environment appeared at ~ 2.5 h after the beginning of the charge as observed in the slower charge rate. The appearance of this metallic signal around the same time after the start of the charge cycle at both fast and slow charge rates could suggest that the metallic environment is related to the transport kinetics of sodium through the hard carbon. Since the sodium requires time to diffuse into the structure it could take a defined amount of time for the metallic species to form. Alternatively, the environment may have been different to what was observed at the lower charge rate and caused by sodium plating onto the hard carbon electrode.

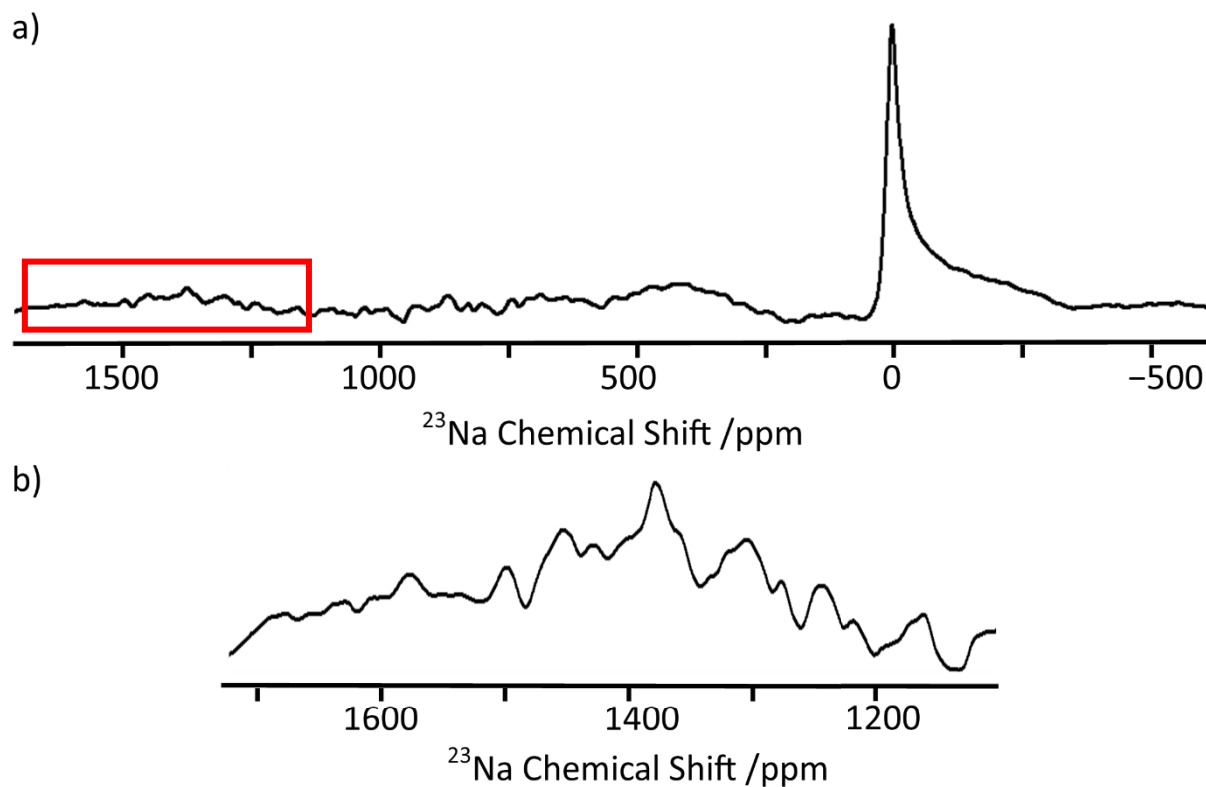


Figure 4.14: ^{23}Na NMR spectrum, from $-550 - 1700$ ppm, acquired in *operando* during the formation cycle of a sodium ion full cell showing the formation of a range of environments with high chemical shift, a). A magnification for the region of interest highlighted in a), between $1200 - 1700$ ppm is provided in b).

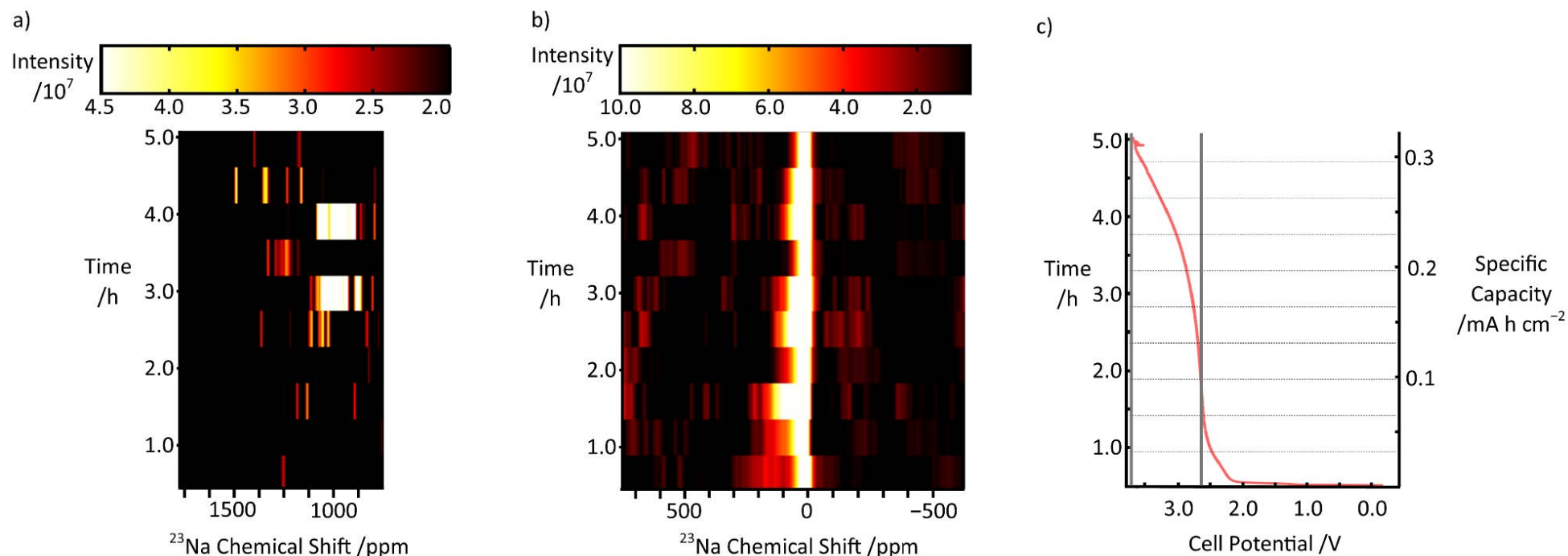


Figure 4.15: ^{23}Na NMR spectra acquired in *operando* during a formation cycle at 60 mA g^{-1} of a sodium-ion full cell showing the formation of a metallic species showing the metallic a), and electrolytic b) regions of the NMR spectrum and the corresponding electrochemistry c).

4.4 Conclusion

This chapter presents information acquired from sodium batteries using off-the-shelf MRI equipment. It was possible to detect multiple sodium species using ^{23}Na NMR spectroscopy before, during, and after cycling batteries. Differences in the sodium species present before charging in sodium metal and full cells could be due to differences in the hard carbon used or cell compression. The electrolyte outside of the electrode stack was not electroactive and comprised a large amount of the sodium signal observed in the ^{23}Na NMR spectra. Future cell designs should aim to minimise the excess electrolyte in addition to providing even compression across the battery.

The formation of metallic dendrites was observed using ^{23}Na MRI, and their distribution and shape in 3D confirmed using ^1H MRI. To reduce potential issues with cell internal resistance and possible masking of smaller metallic signals, a full cell configuration was used. Quasimetallic nanoparticles were formed during the formation cycle of a full cell and their development monitored *in operando* using ^{23}Na NMR spectroscopy. Additionally, a metallic species was detected that formed during the formation cycle. The metallic species may not have been observed in the sodium metal electrodes as the signal from the metal may obscure new metallic environments formed during cycling. Further investigations into

the nature of the metallic species observed during the formation cycle should be conducted.

Furthermore, quasimetallic nanoparticle formation was not observed at the higher charge rate; however, an increase in signal in the metallic region at high chemical shift was present toward the end of the charge cycle. The increase in metallic signal at the end of the charge cycle at the higher charge rate may be due to a kinetic limitation in the formation of quasimetallic nanoparticles, and thus the sodium instead plated onto the surface of the hard carbon electrode, although further investigation is required. Additionally, optimisation of the SNR, for example by increasing the sample filling factor in the coil and reducing the requirement for the sample holder is required to enable observation of the full range of sodium species present during cell cycling.

The *operando* MRI and NMR techniques used in this chapter are widely applicable to other electrochemical systems. The indirect MRI methods used can be applied to nuclei without favourable NMR properties for MRI, such as ^{27}Al , enabling investigation into a greater range of electrochemically active elements. Furthermore, the development of MRI for use on NMR active nuclei with rapid relaxation times allows for direct observation of a broad range of nuclei *in operando* to investigate electrochemical behaviour and changes in distribution and speciation.

4.5 References

1. C. L. Doswell, G. E. Pavlovskaya, T. Meersmann and M. M. Britton, in *Magnetic Resonance Microscopy. Instrumentation and Applications in Engineering, Life Science and Energy Research*, eds. S. Haber-Pohlmeier, B. Blumich and L. Ciobanu, John Wiley & Sons, Weinheim, 2021, ch. 18.
2. J. M. Bray, C. L. Doswell, G. E. Pavlovskaya, L. Chen, B. Kishore, H. Au, H. Alptekin, E. Kendrick, M. M. Titirici, T. Meersmann and M. M. Britton, *Nat. Commun.*, 2020, 11, 2083.
3. C. P. Grey and J. M. Tarascon, *Nat. Mater.*, 2016, 16, 45-56.
4. J. Y. Hwang, S. T. Myung and Y. K. Sun, *Chem. Soc. Rev.*, 2017, 46, 3529-3614.
5. J. M. Stratford, P. K. Allan, O. Pecher, P. A. Chater and C. P. Grey, *Chem. Commun.*, 2016, 52, 12430-12433.
6. W. D. Knight, *Phys. Rev.*, 1949, 76, 1259-1260.
7. Y. Xiang, G. Zheng, Z. Liang, Y. Jin, X. Liu, S. Chen, K. Zhou, J. Zhu, M. Lin, H. He, J. Wan, S. Yu, G. Zhong, R. Fu, Y. Li and Y. Yang, *Nat. Nanotechnol.*, 2020, 15, 883-890.
8. J. M. Bray, A. J. Davenport, K. S. Ryder and M. M. Britton, *Angew. Chem. Int. Ed.*, 2016, 55, 9394-9397.
9. P. M. Bayley, N. M. Trease and C. P. Grey, *J. Am. Chem. Soc.*, 2016, 138, 1955-1961.
10. D. Massiot, F. Fayon, M. Capron, I. King, S. Le Calvé, B. Alonso, J. - O. Durand, B. Bujoli, Z. Gan and G. Hoatson, *Magn. Reson. Chem.*, 2002, 40, 70-76.
11. *Prospa*, Magritek, Wellington, New Zealand.
12. A. J. Ilott, S. Chandrashekar, A. Klockner, H. J. Chang, N. M. Trease, C. P. Grey, L. Greengard and A. Jerschow, *J. Magn. Reson.*, 2014, 245, 143-149.
13. R. Dugas, A. Ponrouch, G. Gachot, R. David, M. R. Palacin and J. M. Tarascon, *J. Electrochem. Soc.*, 2016, 163, A2333-A2339.

14. J. Gryko, P. F. McMillan and O. F. Sankey, *Phys. Rev. B Condens. Matter*, 1996, 54, 3037-3039.

5 Magnetic Resonance Studies on a Lithium Metal Cell

5.1 Introduction

Magnetic resonance (MR) methods have been used during the previous two decades to investigate intercalation mechanisms and the chemistry of lithium ion batteries (LIBs).^{1, 2} Most of the prior work on using nuclear magnetic resonance (NMR) to study LIBs has centred on establishing NMR spectroscopy techniques for monitoring intercalation, solid-electrolyte interphase (SEI) growth, or dendrite and mossy microstructure formation.

Initial studies applying NMR spectroscopy to LIBs used ^7Li spectroscopy on lithium metal cells with disordered carbon anodes to follow the evolution of lithium environments during intercalation into the disordered carbon structure, and establishing that intercalation compounds could be identified from their chemical shift and lineshape.^{3, 4} Investigations into lithium metal and graphite cells and the assignment of resonances to specific graphite intercalation compounds has been performed by Letellier *et al.* using *in situ* ^7Li NMR.⁵ The assignment of NMR peaks to specific intercalation compounds was confirmed by Lorie Lopez *et al.*⁶ using derivative operando (dOp) NMR where signals that remain constant over time are removed from the spectrum, making it easier to establish what is changing in the spectra over time. The NMR environments for intercalation compounds mostly have a ^7Li NMR chemical shift greater than that of the electrolyte, assigned at 0 ppm by convention,⁶ and the

chemical shift moves further upfield as the lithium concentration in the carbon increases. Chemical shifts below that of the electrolyte have been assigned to LiC_{72} and precursors to LiC_{72} .⁶ Other resonances below 0 ppm have been assigned to lithium in the SEI near the carbon electrode,^{3, 6} LiF on the lithium metal electrode,⁷ and lithium in the electrolyte.^{6, 7}

The chemical shift of metallic lithium is significantly higher than lithium in the electrolyte due to the Knight shift,⁸ around 250 ppm. Furthermore, lithium microstructures will have a different chemical shift due to their orientation with respect to B_0 . Trease *et al.* suggest that microstructure formations with a chemical shift lower than 270 ppm are not dendrites but mossy structures that are closer in orientation with respect to B_0 to the electrode surface, with dendrites having a chemical shift above 270 ppm.⁹ However, the explicit assignment of lithium microstructure morphologies based on chemical shift has been disputed, with the suggestion that microstructures with different morphologies produce the same chemical shift due to the average orientation of deposits being perpendicular to the bulk electrode surface.¹⁰

Recently, investigations have begun into lithium ion full cells. Using $\text{LiNi}_{0.8}\text{Mn}_{0.1}\text{Co}_{0.1}\text{O}_2$ (NMC811) as a cathode and graphite as an anode, Märker *et al.* used *operando* ^7Li NMR spectroscopy to investigate chemical reactions and intercalation occurring at both the graphite and NMC

electrodes.¹¹ They observed peaks, at dilute stages of lithium intercalation, as an upfield shoulder on the electrolyte peak, followed by, at more dense stages of intercalation, peaks between 0–15 ppm and 40–50 ppm.^{3–6} Furthermore, lithium metal deposition was observed on the graphite electrode when the battery was cycled at -5°C .

^7Li magnetic resonance imaging (MRI) of the electrolyte can provide quantitative information on charge carrier distribution,^{12, 13} and when combined with ^{19}F MRI, Li^+ transference and mass transport numbers can be calculated.¹⁴ Both direct and indirect MRI have been used to spatially locate dendrites and microstructures in LIBs as described in Chapter 1.1.1.^{15, 16} Direct ^7Li imaging of dendrites using chemical shift imaging has been used to demonstrate the spatial location and relative contributions of signal from the microstructure growth and metal electrode.¹⁵ Furthermore, three-dimensional (3D) ^7Li MRI can provide useful information on microstructure growth within lithium metal cells. Due to the rapid relaxation time of lithium, higher resolution images to show the morphology in more detail are not possible using direct ^7Li MRI. Instead, indirect imaging, of the signal from the ^1H in the electrolyte, can be used to generate a 3D negative image of the microstructures in high resolution.¹⁶

This chapter will explore the use of *operando* ^7Li NMR spectroscopy, ^7Li one-dimensional (1D) MRI, 3D ^1H MRI, and spectral deconvolution in monitoring the lithiation of a lithium metal cell containing argon bubbles.

5.2 Experimental

The lithium metal cell was assembled by Dr Pooja Kumari.

The *operando* cell employed in this work was based on a Swagelok® union (i.d. 3/8" = 9.5 mm) as described in Chapter 4.

Lithium metal cells were constructed in an argon-filled glove box (MBraun, $\text{H}_2\text{O} < 0.5$ ppm, $\text{O}_2 < 0.5$ ppm) using a lithium metal (99.9%, 0.5 mm thick, Goodfellow Cambridge Ltd.) counter electrode (CE) and graphite (commercial, ATME Power) working electrode (WE), separated by one Whatman GF/B glass microfibre separator with 1.2 M LiPF_6 in 3:7 ethylene carbonate (EC):ethyl methyl carbonate (EMC) (Soulbrain, PuriEL) with an aluminium (Alfa Aesar, 99.9% purity) current collector on the graphite side and copper (Harrison and Harrison, 99.9% purity, 9 mm diameter) current collector on the lithium metal side. Aluminium and lithium disks were **cut with a brass cork borer (Sigma Aldrich, 3/16 ")**. Electrochemical experiments were performed using a two-electrode configuration on a Biologic VSP potentiostat. The formation cycle was performed at 10.5 mA g^{-1} inside the magnet during the acquisition of

operando ^7Li NMR spectra, 1D electrolyte and 1D metal profiles for the first 6.3 h and ^7Li full spectra every 8 min thereafter.

All MR data were acquired on a Bruker 7 T spectrometer equipped with either a ^7Li linear transmit/receive (LTR) or ^1H quadrature transmit/receive (QTR) RF coil. The cell was positioned in a WB40 microimaging probe using a universal specimen pot with holes drilled through the lid and bottom to enable wires to connect to the potentiostat.

^7Li NMR spectra, covering a spectral range of -85 – 340 ppm, were acquired using a spin echo sequence, with a spectral width of 50 kHz, a transmitter frequency of 116.6570217 MHz (positioned between the electrolyte and metallic signal), collecting 16384 points, 1024 averages and a repetition time $T_R = 0.23$ s optimised for signal-to-noise ratio (SNR), corresponding to approximately 80% signal relaxation. The repetition time was calculated using equation 5.1 where S_n is the normalised signal intensity (0.8), τ is the repetition time, and T_1 is the estimated T_1 relaxation time (0.14 s).

$$S_n = 1 - e^{\frac{-\tau}{T_1}} \quad \text{Equation 5.1}$$

Spectral fitting was performed using DM Fit software¹⁷ using a combination of Lorentzian and Gaussian functions as described in Chapter

2.1.1.2. Fitting results for all spectral deconvolutions can be found in Appendix 3.

^7Li 1D profiles of the electrolyte and metallic lithium, in a pristine metal cell, were acquired using a spin echo sequence at 116.6423504 MHz and 116.6716931 MHz for the electrolyte and metal respectively. *Read* encoding was performed along the vertical (*z*) axis of the cell. Profiles were acquired with 8192 averages and a spectral width of 100 kHz, 128 *read* points with a field-of-view (FOV) of 25 mm resulting in pixels of 195 μm . Data were Fourier transformed using an exponential filter.

3D ^1H MR images of the electrolyte were acquired using a multi-slice multi- (spin) echo sequence with horizontal frequency encoding, a spectral width of 100 kHz, 32 signal averages, a $15 \times 16 \times 20$ mm FOV, with a $117 \mu\text{m} \times 500 \mu\text{m} \times 78 \mu\text{m}$ voxel size, a repetition time $T_R = 1.0$ s and an echo time $T_E = 3.5$ s. All images were processed using *Prospa*.¹⁸

5.3 Results and Discussion

5.3.1 Pristine Cell Before Cycling

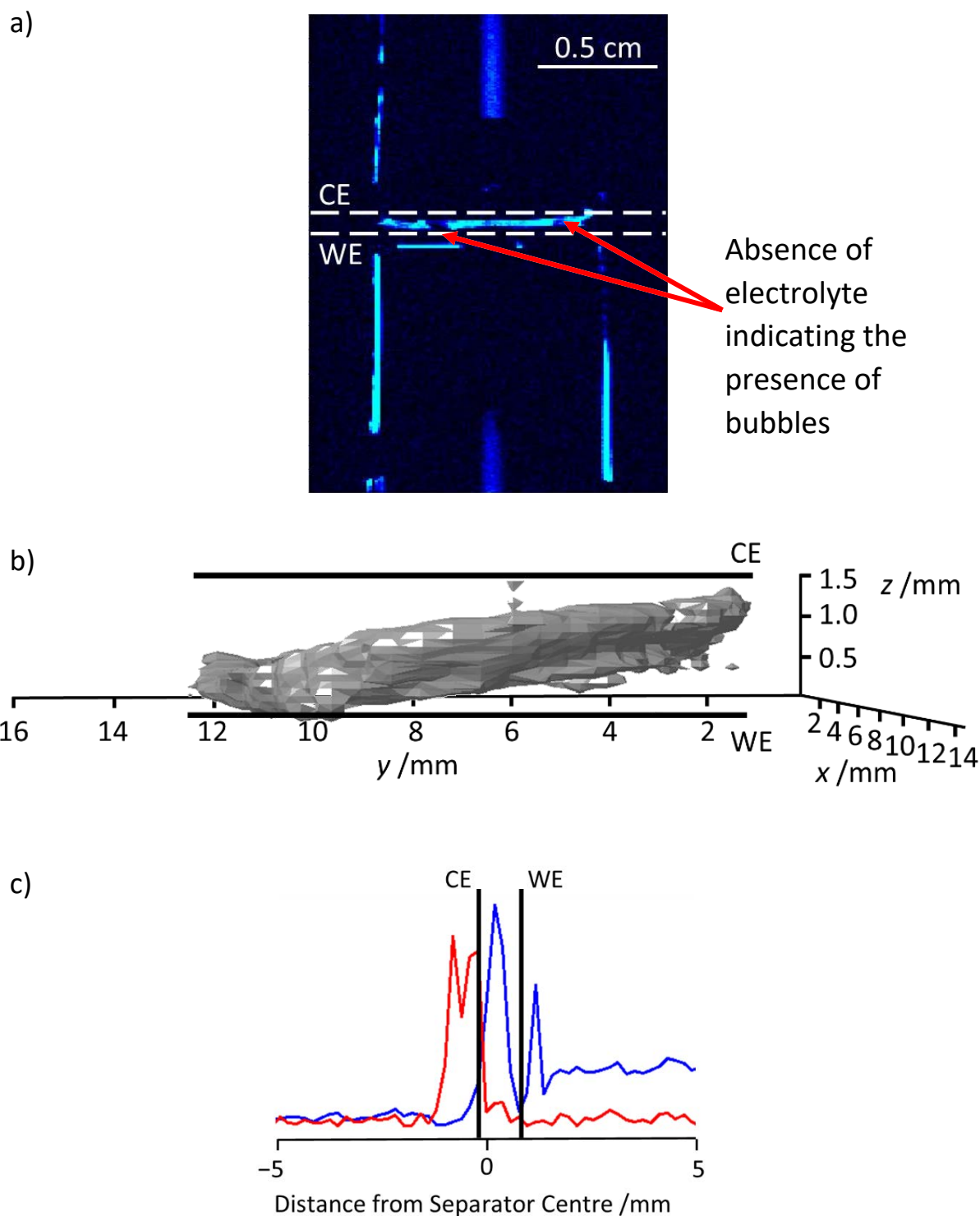


Figure 5.1: ^1H images of 1.2 M LiPF_6 in 3:7 EC/EMC a) a two-dimensional slice of the electrolyte showing regions where the electrolyte is absent in the separator and b) a 3D image of the electrolyte in the separator showing the angle of the separator in the cell, and c) 1D ^7Li profiles of the

lithium in the electrolyte (blue) and the lithium metal electrode (red) before charge cycling. Locations of the lithium metal CE and graphite WE are indicated.

Figure 5.1a and b show ^1H images of the distribution of the electrolyte within the cell in the separator before charge cycling. In the pristine cell, there were a few large argon bubbles in the separator and the electrolyte was distributed throughout the Swagelok cell between the polyether ethyl ketone (PEEK) rod and polytetrafluoroethylene (PTFE) union, seen on the right and left sides of the image (Figure 5.1a). Further signal intensity was observed in the top centre of the image in Figure 5.1a, from electrolyte in the centre of the PEEK rod and surrounding the copper wire. The electrolyte outside the separator was observed in the ^7Li 1D profile of the electrolyte (Figure 5.1c) where the electrolyte was predominantly below the separator region.

The separator was not perpendicular to the B_0 field and was at a slanted angle (Figure 5.1b), suggesting that the lithium metal and graphite electrodes were also at an angle not perpendicular to B_0 . It was possible that the angle of the metal electrode may obscure any metallic features that developed on the electrode during the electrochemistry. The metallic region of the ^7Li spectrum for this cell (Figure 5.2b) showed that there was only one environment present although the peak shape was not perfectly Lorentzian, indicating that the metal electrode was not correctly

aligned. The 1D ^7Li profiles acquired before lithiation (Figure 5.1c) show one region of intensity for the lithium metal electrode, as expected.

The ^7Li NMR spectrum of the cell before any charge cycling showed a multitude of environments by deconvolution (Figure 5.2b), corresponding to the lithium in the electrolyte outside the separator region (grey), the lithium in the electrolyte within the separator (red), lithium species that have reacted and were near the electrodes (blue), for example in the SEI and LiF, the lithium that was in close proximity to the graphite electrode (green), and lithium that had begun to incorporate into the carbon structure (orange).

Some of the reacted lithium species (blue) have larger peak widths than the lithium in the electrolyte both inside and outside the separator region, suggesting that these lithium species were in a more spatially restricted environment, which corresponds with that of solid LiF or SEI on the electrodes.⁷ The peaks **at -0.1 and -0.2 ppm** have a narrow linewidth, and may correspond to lithium that had reacted with the carbon electrode to form either precursor species to LiC_{72} or LiC_{72} itself.⁶

Most of the lithium species in the vicinity of the graphite electrode (green) have similar peak widths, 5–18 Hz, to the lithium in the electrolyte,

18 Hz, which suggests that these are mobile species, corresponding with lithium close to, but not reacted with, the carbon surface; although, the peak at 1.25 ppm was broader than the other environments. Therefore, the lithium in the environment at 1.25 ppm was more restricted than the other lithium in proximity to the electrode. The environment at 1.25 ppm may have been lithium that was contained within the pores in the uneven surface of the carbon electrode since, whilst graphite itself is a flat carbon structure, the surface of the manufactured electrode material was not perfectly smooth. The environments at a higher chemical shift, at 6-8 ppm, can be correlated to environments previously reported in the literature as LiC_{27} at 6.75 ppm and $\text{Li}_{0.63}\text{C}_6$ at 7.75 ppm.^{3, 5, 6} The incorporation of lithium into the carbon may have occurred at the surface of the electrode in the time between cell assembly and spectrum acquisition.

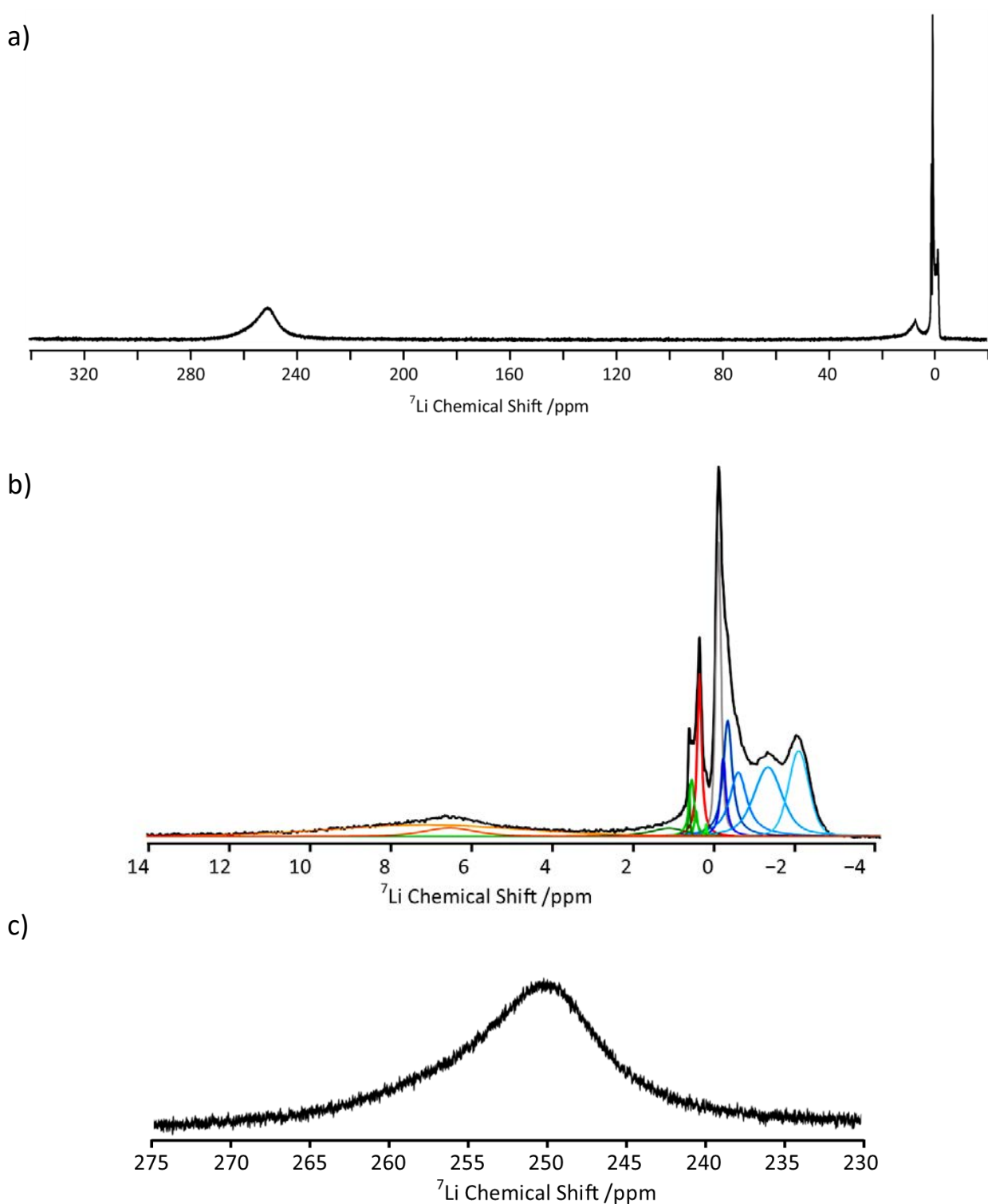


Figure 5.2: ^7Li full spectrum before cycling (Figure 5.3, spectrum i) a), with b) the lithium electrolyte region showing the lithium in the electrolyte outside the separator (grey), lithium inside the separator (red), reacted lithium species in the vicinity of the electrodes (blue), lithium in the vicinity of the carbon electrode (green), lithium species incorporated into the carbon (orange), and c) lithium metal signal.

5.3.2 Formation Cycle

To investigate the development of the lithium species during a formation cycle, ^7Li full spectra were acquired *in operando* (Figure 5.3). The signal corresponding to the lithium in the electrolyte, at 0 ppm, maintains intensity throughout the charge cycle. However, the signal at 7 ppm moves to a higher chemical shift as the graphite begins to lithiate but starts to disappear after 7.8 h, approximately corresponding with the plateau observed in the electrochemistry (Figure 5.3b). The upfield shift of the signal starting at 7 ppm has been shown in the literature to be increased lithiation of the graphite electrode. In the literature, the signal corresponding to lithiated carbon will begin to shift upfield to between 40–50 ppm during graphite lithiation, however that does not occur here. The lack of signal from 40–50 ppm may be due to the presence of the argon bubbles, as electrochemistry has been shown to be enhanced at the corona of a bubble.¹⁹ The bubble corona may also act as a nucleation site for microstructural growth or electrode pitting.

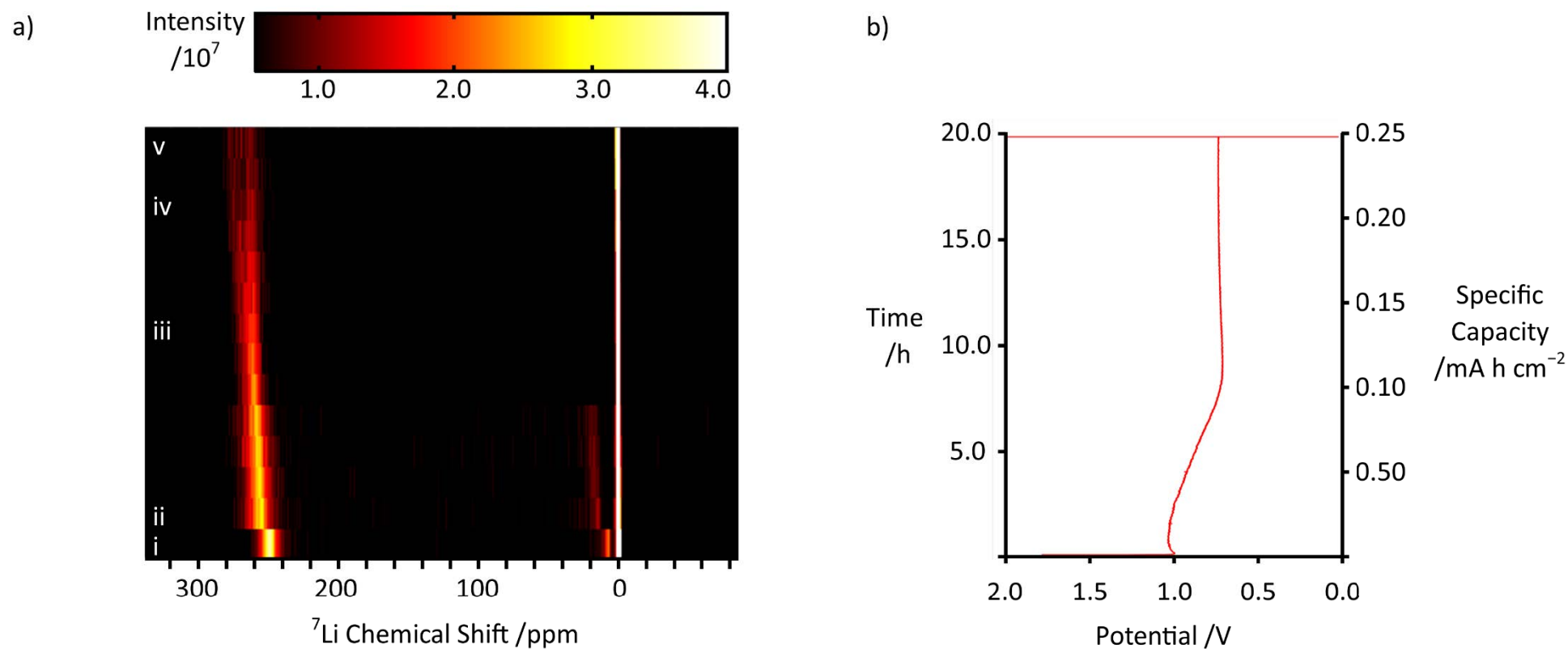


Figure 5.3: Selected ^{7}Li NMR spectra acquired in *operando* during a formation cycle at 10.5 mA g^{-1} of a lithium metal cell showing the development of a species in the vicinity of the electrolyte and the evolution of the metal species. Labelled spectra (i-v) on a) are shown in Figures 5.2, and 5.4–5.8. Electrochemistry is shown in b).

At the beginning of lithiation, the environment corresponding to lithiated carbon shifted upfield to 14 ppm, which has been shown to be LiC_{18} in the literature (Figure 5.4a).⁶ After the lithiation had begun, one environment upfield of 2 ppm was present, as opposed to the two that were present before lithiation, as only the broad signal remained. Additionally, there was little change to the peaks corresponding to the environments in the vicinity of the carbon (0–2 ppm, green). Furthermore, **the species at –0.2 ppm** had disappeared, supporting its assignment as a precursor species to LiC_{72} , as more lithium was intercalating into the carbon electrode and becoming LiC_{72} . Furthermore, **the peak at –0.1 ppm** had increased in intensity, suggesting that it could be assigned to LiC_{72} .

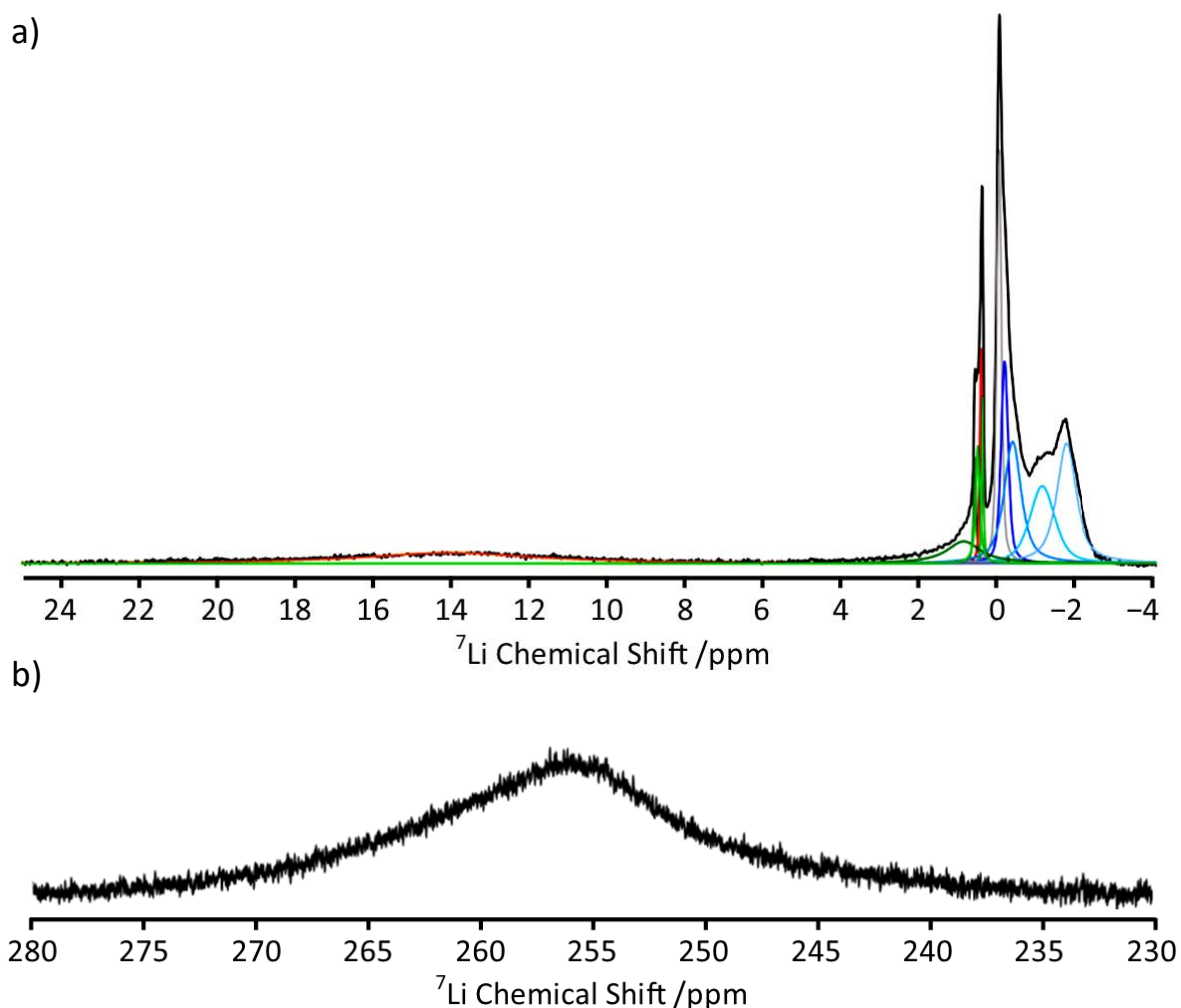
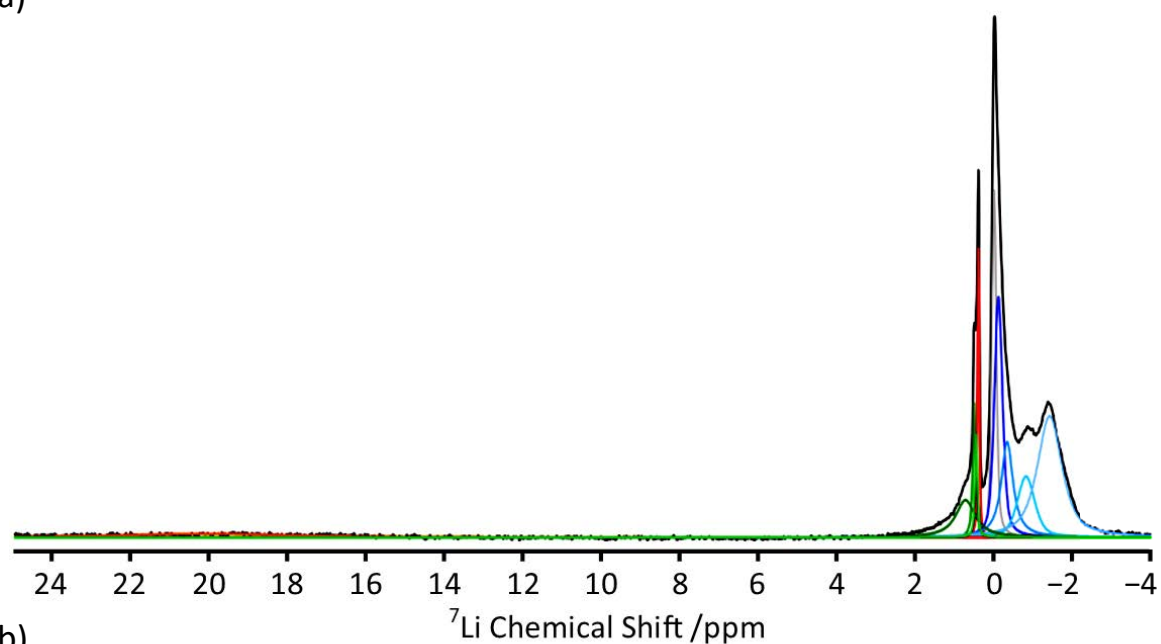


Figure 5.4: ^7Li spectrum at the start of cycling (Figure 5.3, spectrum ii), showing a) the lithium in the electrolyte outside the separator (grey), lithium inside the separator (red), reacted lithium species in the vicinity of the electrodes (blue), lithium in the vicinity of the carbon electrode (green), lithium species incorporated into the carbon (orange), and b) lithium metal.

After 9 h of lithiation the signal from the lithium in the carbon structure had shifted upfield to 20 ppm (Figure 5.5a). The upfield shift indicated an increase in the concentration of lithium in the carbon.⁶ The peak at -0.1 ppm for LiC_{72} had increased in intensity. Furthermore, the peaks at -0.4 and -0.8 ppm, attributed to lithium in the SEI, have decreased in

intensity, perhaps indicating that some lithium was not trapped in the SEI and was able to move through the structure and intercalate into the carbon.

a)



b)

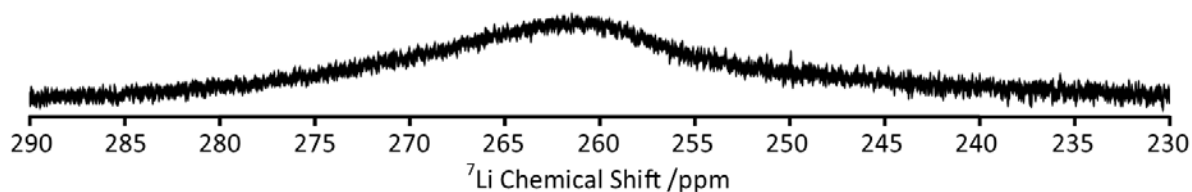


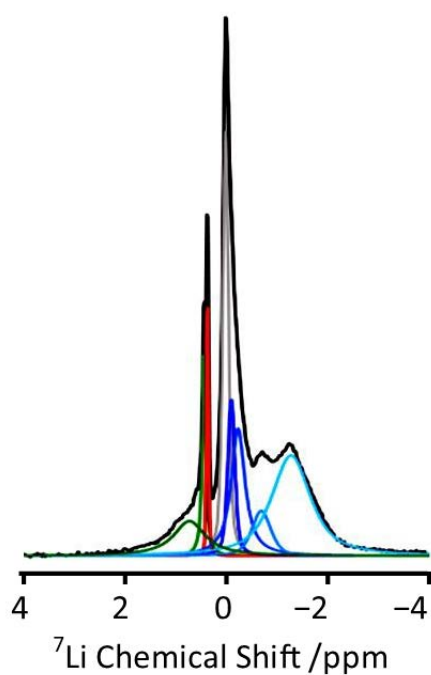
Figure 5.5: ${}^7\text{Li}$ spectrum after 9 h of cycling (Figure 5.3, spectrum iii), showing a) the lithium in the electrolyte outside the separator (grey), lithium inside the separator (red), reacted lithium species in the vicinity of the electrodes (blue), lithium in the vicinity of the carbon electrode (green), lithium species incorporated into the carbon (orange), and b) lithium metal.

Toward the end of the charge cycle, 15 h, in the ${}^7\text{Li}$ spectrum in Figure 5.6a, the peak at 20 ppm corresponding to higher concentrations of

lithium in carbon was no longer present and the distribution of environments relating to lithium in the vicinity of the carbon electrode had decreased. Additionally, the metallic environment ~ 250 ppm developed a shoulder at ~ 280 ppm after ~ 11 h, corresponding to the formation of metallic structures at 0° to the B_0 field, perpendicular to the lithium metal electrode. The development of the shoulder on the metallic peak suggested that there were pits forming on the lithium metal electrode. Another assignment of the new peak at ~ 280 ppm could be dendrite formation, as the dendrites would also form at 0° to B_0 ; however, this was unlikely as it is difficult to form dendrites during a formation cycle.

The pit peak increased in intensity but remains at a constant chemical shift as the lithiation continued (Figure 5.7) suggesting an increasing pit depth but no change in the orientation. There were no further changes to most of the environments corresponding to lithium near the carbon electrode. However, the increase in intensity of the peak **at -1.7 ppm** could be due to an increase in the amount of SEI, because pits in the metallic electrode would expose additional surface area to be passivated.

a)



b)

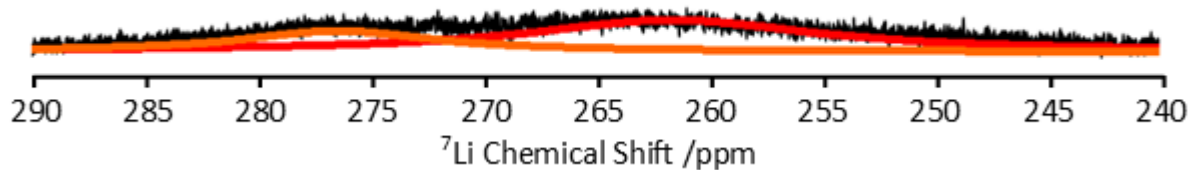
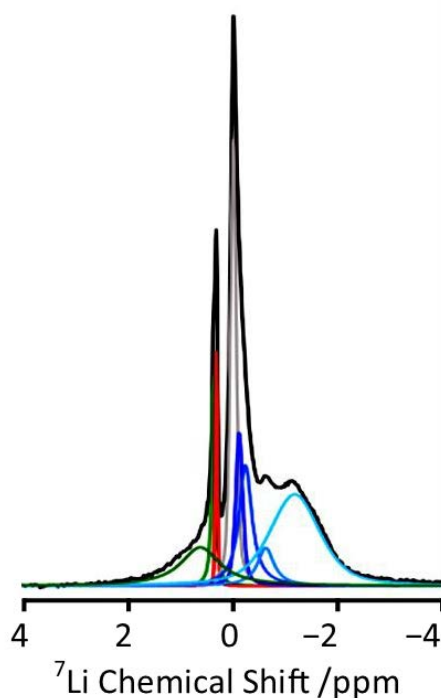


Figure 5.6: ^7Li spectrum after 15 h cycling (Figure 5.3, spectrum iv), showing a) the lithium in the electrolyte outside the separator (grey), lithium inside the separator (red), reacted lithium species in the vicinity of the electrodes (blue), lithium in the vicinity of the carbon electrode (green), lithium species incorporated into the carbon (orange), and b) lithium metal (red) lithium at 0° to \mathbf{B}_0 (orange).

a)



b)

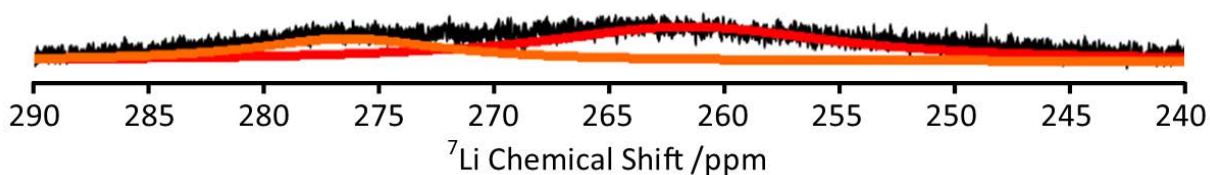


Figure 5.7: ^7Li spectrum after 18 h cycling (Figure 5.3, spectrum v), showing a) the lithium in the electrolyte outside the separator (grey), lithium inside the separator (red), reacted lithium species in the vicinity of the electrodes (blue), lithium in the vicinity of the carbon electrode (green), lithium species incorporated into the carbon (orange), and b) lithium metal (red) and lithium at 0° to \mathbf{B}_0 (orange).

Figure 5.8 shows 1D profiles of the lithium in the metal (red) and the electrolyte (blue) at the start, during, and the end of the charge cycle. As the lithiation of the carbon electrode progressed, the lithium electrode distribution changed as more of the intensity moved toward the carbon electrode. The change in intensity distribution could be indicative of pitting on the lithium metal electrode surface; as more surface area was

exposed on the surface of the electrode there would be an increase in the signal from the lithium metal due to the skin depth penetration of the RF. The penetration depth of the RF is also why there appeared to be two regions of intensity for the lithium metal electrode after lithiation. There was only one region of intensity for the lithium metal electrode at the start of the cycle (Figure 5.8a) due to the orientation of the electrode not being perfectly aligned to B_0 , resulting in 'blurring' of the ^7Li 1D profile of the metal electrode. Upon completion of the battery cycle (Figure 5.8c), the lithium metal signal distribution had changed, correlating with the formation of an additional metallic environment at 280 ppm and suggesting the species was at 0° to B_0 .

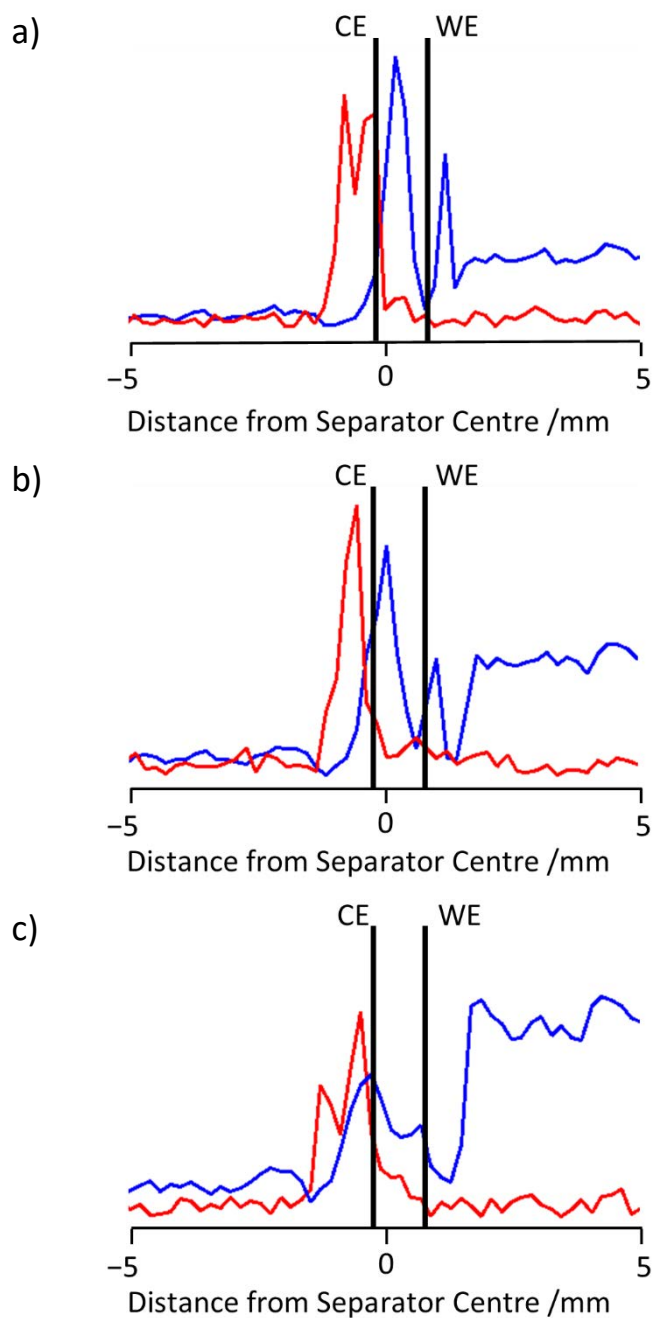


Figure 5.8: 1D ^7Li profiles of the lithium in the electrolyte, 1.2 M LiPF_6 in 3:7 EC/EMC, (blue) and the lithium metal electrode (red) at a) the start of, b) during, and c) after cycling.

The intensity of the signal from lithium metal within the separator was larger than the intensity from the lithium metal electrode in Figure 5.8c.

However, the frequency range per pixel was 758 Hz and the difference in frequency between the bulk metal electrode peak and the peak corresponding to lithium at 0° to B_0 was 1400 Hz; hence, it is likely that there was a misregistration of this signal by approximately two pixels. Obtaining a 3D image of the pitting using a negative image of a ^1H image of the electrolyte was not possible due to the presence of bubbles in the cell.

5.4 Conclusion

This chapter shows the evolution of lithium species in a lithium metal cell during a charge cycle where pitting occurred on the lithium metal electrode. The electrolyte in the cell was visualised using 3D ^1H MRI and showed that bubbles were present within the separator and the electrode stack was not aligned with B_0 . Furthermore, the electrolyte that was outside the electrode and separator stack was not electroactive and shown in the 1D ^7Li profiles to be below the separator. Identification of individual lithium species from the ^7Li spectra was performed using deconvolution and approximate spectral assignments are presented.

Species were broadly grouped as metallic, higher concentrations of lithium in carbon, low concentrations of lithium in carbon, lithium in the vicinity of the carbon electrode, lithium in the SEI, and lithium in the electrolyte. Throughout the lithiation of the cell the species at low

chemical shift evolved, with the cycle culminating in the formation of pits on the lithium metal surface and a short circuit of the cell. 3D imaging of the pits on the lithium electrode was not possible due to the SNR of direct ^7Li imaging and the presence of bubbles in the cell, which inhibited the use of indirect ^1H imaging of the electrolyte to create a negative image of the electrode surface. 1D ^7Li metal profiles showed an increase in signal due to the increase in surface area caused by pitting. The formation of pits was supported by the development of a peak at 276 ppm, corresponding to lithium metal at 0° to B_0 .

The electrochemistry of the cell showed no deviations from the expected lithiation profile of a lithium metal cell, with no indication of dendrite formation. It is possible that the presence of bubbles enhanced the rate of lithium aggregation at their corona and provided an initiation site for increased lithium stripping, resulting in pitting of the metal electrode. The ability of MRI to quickly detect bubble formation within the cell may be crucial to cell function and the prevention of dendrite formation or electrode pitting. Further work is required to establish whether the electrode pitting was due to the presence of bubbles by comparison with an equivalent LIB without bubbles in the separator.

Using the methods originally introduced in Chapter 4, this chapter applies the *operando* NMR and MRI methods developed on sodium ion batteries

thus illustrating their versatility in application to *operando* measurements of different NMR active nuclei. Furthermore, the issue surrounding bubble formation in custom batteries for NMR and MRI experiments is not uncommon, yet the influence of bubbles in these systems is seldom discussed. Here, the suggestion that the bubbles are not a benign entity and may cause pitting, and the removal of bubbles altogether, warrants further investigation.

5.5 References

1. R. E. Gerald II, R. J. Klinger, G. Sandí, C. S. Johnson, L. G. Scanlon and J. W. Rathke, *J. Power Sources*, 2000, 89, 237-243.
2. R. E. Gerald, J. Sanchez, C. S. Johnson, R. J. Klingler and J. W. Rathke, *J. Phys. Condens. Matter*, 2001, 13, 8269-8285.
3. F. Chevallier, M. Letellier, M. Morcette, J.-M. Tarascon, E. Frackowiak, J.-N. Rouzaud and F. Béguin, *Electrochem. Solid-State Lett.*, 2003, 6, A225-A228.
4. M. Letellier, F. Chevallier, C. Clinard, E. Frackowiak, J.-N. Rouzaud, F. Béguin, M. Morcrette and J.-M. Tarascon, *J. Chem. Phys.*, 2003, 118, 6038-6045.
5. M. Letellier, F. Chevallier and F. Béguin, *J. Phys. Chem. Solids*, 2006, 67, 1228-1232.
6. J. L. Lorie Lopez, P. J. Grandinetti and A. C. Co, *J. Mater. Chem. A*, 2018, 6, 231-243.
7. M. A. Hope, B. L. D. Rinkel, A. B. Gunnarsdottir, K. Marker, S. Menkin, S. Paul, I. V. Sergeyev and C. P. Grey, *Nat. Commun.*, 2020, 11, 2224.
8. W. D. Knight, *Phys. Rev.*, 1949, 76, 1259-1260.

9. H. J. Chang, N. M. Trease, A. J. Illott, D. Zeng, L.-S. Du, A. Jerschow and C. P. Grey, *J. Phys. Chem. C*, 2015, 119, 16443-16451.
10. V. Kupers, M. Kolek, P. Bieker, M. Winter and G. Brunklaus, *Phys. Chem. Chem. Phys.*, 2019, 21, 26084-26094.
11. K. Marker, C. Xu and C. P. Grey, *J. Am. Chem. Soc.*, 2020, 142, 17447-17456.
12. S. Klamor, K. Zick, T. Oerther, F. M. Schappacher, M. Winter and G. Brunklaus, *Phys. Chem. Chem. Phys.*, 2015, 17, 4458-4465.
13. J. D. Bazak, S. A. Krachkovskiy and G. R. Goward, *J. Phys. Chem. C*, 2017, 121, 20704-20713.
14. S. A. Krachkovskiy, J. D. Bazak, P. Werhun, B. J. Balcom, I. C. Halalay and G. R. Goward, *J. Am. Chem. Soc.*, 2016, 138, 7992-7999.
15. S. Chandrashekar, N. M. Trease, H. J. Chang, L. S. Du, C. P. Grey and A. Jerschow, *Nat. Mater.*, 2012, 11, 311-315.
16. A. J. Illott, M. Mohammadi, H. J. Chang, C. P. Grey and A. Jerschow, *Proc. Natl. Acad. Sci. U. S. A.*, 2016, 113, 10779-10784.
17. D. Massiot, F. Fayon, M. Capron, I. King, S. Le Calvé, B. Alonso, J.-O. Durand, B. Bujoli, Z. Gan and G. Hoatson, *Magn. Reson. Chem.*, 2002, 40, 70-76.
18. *Prospa*, Magritek, Wellington, New Zealand.
19. Y. B. Vogel, C. W. Evans, M. Belotti, L. Xu, I. C. Russell, L. J. Yu, A. K. K. Fung, N. S. Hill, N. Darwish, V. R. Goncales, M. L. Coote, K. Swaminathan Iyer and S. Ciampi, *Nat. Commun.*, 2020, 11, 6323.

6 Magnetic Resonance Investigations of Aluminium Battery Electrolytes

6.1 Introduction

Aluminium ion batteries (AIBs) are a promising alternative to lithium ion batteries due to their higher theoretical volumetric capacities, 2042 mA h cm⁻¹ for lithium and 8056 mA h cm⁻¹ for aluminium, and three electron redox reaction.¹ AIBs rely on electroplating aluminium rather than on intercalation, as discussed in Chapter 1.2.3. However, the formation of aluminium hydroxides from aluminium metal with water electrolytes, forming aluminium hydroxides, poses an issue for the development of commercial AIBs.

Common organic electrolytes used for lithium ion batteries (LIBs) do not work for AIBs due to the inability to plate aluminium.¹ Early electrolytes that could plate aluminium operated at high temperature, 100-160 °C, and were eutectic mixtures of AlCl₃-KCl-NaCl known as a molten salt electrolyte.^{2, 3} These high temperature batteries used an aluminium anode and chlorine cathode and operated by reducing chlorine. Efforts were made to reduce the operating temperature to 107 °C by changing the molten salt to AlCl₃-NaCl, although improved results were obtained at 270 °C, and the chloride cathode replaced with FeS₂.⁴ However, the operating temperature of the rechargeable cells remained an issue.

Ionic liquid (IL) electrolytes have been suggested as an option to reduce the operating temperature of AIBs.⁵ One such type of IL is the family of imidazolium chloride ILs, with the formula $C_xC_y\text{imCl}$, where x and y correspond to the lengths of the alcohol chains on the imidazolium ring. Commonly used imidazolium chloride ILs are 1-ethyl-3-methylimidazolium chloride ($C_2C_1\text{imCl}$) and 1-butyl-3-methylimidazolium chloride ($C_4C_1\text{imCl}$).^{6, 7} When combined with AlCl_3 , these ILs form various ionic AlCl_3 species dependent upon the concentration of AlCl_3 in the IL. The electrochemically active dimer species ($[\text{Al}_2\text{Cl}_7]^-$) is only present in Lewis acidic ILs with a molar ratio of IL to AlCl_3 above 1:1; below 1:1, only the monomeric $[\text{AlCl}_4]^-$ is present in the system and so electroplating cannot occur.^{1, 8, 9} These ILs are able to plate dense aluminium deposits which is promising for reducing dendrite growth in AIBs.¹⁰ However, ILs are viscous and have reduced conductivity, which is undesirable in a battery;¹¹ hence the addition of water may be advantageous.¹²

Studies have been performed to identify the nature of water in an IL. It has been shown that the water is present in imidazolium ILs initially in water pockets.¹² Furthermore, diffusion of water within the IL may not be directly correlated with viscosity.¹³ The addition of water is likely to change the aluminium species present in the system which may render the IL unable to perform the necessary electroplating. However, there is an example of electroplating performed in $C_2C_1\text{imCl}:\text{AlCl}_3$ with a molar

ratio of 1:1.5 under ambient conditions¹⁴ although limited materials characterisation was provided by this report, hence it is difficult to determine how much water was present in the electrolyte used.

An alternative to using costly IL electrolytes is to use an aqueous electrolyte.^{15, 16} However, aqueous electrolytes form aluminium hydroxide species that ultimately result in battery failure. The issue of electrode degradation may be solved with the introduction of an intermediate material between the aluminium electrode and the electrolyte, such as proposed in the 'aluminium anode, lid, film, air cathode' (ALFA) cell by Mori in 2013.¹⁵ The rechargeable aluminium-air battery uses aluminium metal coated with an aluminium ion conductor as an anode, a saltwater electrolyte, and an air cathode. There have since been improvements to the ALFA design such as refinements of the air cathode,^{17, 18} the introduction of an aluminium ion conductor coating on the anode,¹⁹ electrolyte buffering,²⁰ and the suppression of hydroxide formation using hydrophobic additives such as petroleum jelly combined with a deep eutectic solvent.²¹

The speciation of aluminium in aqueous systems is dependent upon the concentration of aluminium and the pH of the system.^{22, 23} As the saltwater electrolyte is acidic, it is unlikely that any polymeric aluminium hydroxide species are present,²³ which corresponds with the suggestions

by Mori of charge carriers in the system.²⁴ However, the charge-carrying species in the ALFA battery system were not thoroughly investigated and the exact mechanism of electroplating was not described.

This chapter will investigate the aluminium species present in $C_4C_1\text{imCl}:\text{AlCl}_3$ electrolytes with the molar ratio of aluminium greater than one, and in the saltwater electrolyte used by Mori with different concentrations of AlCl_3 using ^{27}Al NMR spectroscopy. Analysis of interactions with the imidazolium, using evidence from ^1H NMR spectroscopy, for the IL system will be presented. The ^1H T_1 and T_2 relaxation times for both IL and aqueous electrolytes are evaluated for suitability in terms of their NMR relaxation time contrast for MRI visualisation of electrochemistry in the aluminium IL battery and ALFA cell.

6.2 Experimental

Data acquisition, relaxation time analysis, NMR spectral deconvolution and sample preparation for the AlCl_3 in saltwater (10% w/w NaCl in water) system were performed by MSc student Colombe Ténières.

AlCl_3 (99% extra pure, Acros Organics) was added to 1-butyl-3-methylimidazolium chloride (95%, Sigma Aldrich) over a 15 min period

with vigorous stirring. The resulting clear yellow liquid was stirred for a further 15 min. The sample was then transferred into a vial and stored in an atmospheric desiccator over silica gel.

AlCl_3 (99% extra pure, Acros Organics) was added to a 10% w/w NaCl (99%, Sigma Aldrich) solution in ultra pure H_2O (MilliQ, $18.2 \text{ M}\Omega \text{ cm}^{-1}$). AlCl_3 concentrations of 0.5–500 mM were prepared by serial dilution.

NMR data were acquired on a Bruker AVANCE III HD spectrometer equipped with a 7 T vertical wide-bore superconducting magnet, using a Bruker diff30 probe equipped with either a 10 mm ^1H or 10 mm ^{27}Al coil. The RF pulses were calibrated for each sample, **10–21 μs at 12.5 W for ^1H , 38–60 μs at 60 W for ^{27}Al** . Data were acquired at a temperature of $298 \pm 0.3 \text{ K}$, which was maintained by the water-cooled gradient coils of the diff30 probe. ^1H and ^{27}Al T_1 NMR relaxation data were collected using an inversion recovery (IR) pulse sequence. IR experiments were performed with a minimum of seven time points logarithmically spaced from $5 \times 10^{-6} \text{ s}$ to $5 T_1$ and a repetition time $T_R > 5 T_1$. ^1H T_2 relaxation times were measured using a Carr-Purcell-Meiboom-Gill experiments (CPMG) pulse sequence performed with nine logarithmically spaced echo steps between 0.004–2048 s with $T_E = 2 \text{ ms}$. ^1H diffusion data were collected using a pulsed gradient stimulated echo (PGSTE) pulse sequence with 16 logarithmically spaced gradient steps up to 300 G m^{-1} , $\Delta = 0.06 \text{ s}$

or 0.08 s and $\delta = 0.002$ s. Data were analysed using *Prospa*²⁵ and the integrals of signal intensity fit using *KaleidaGraph*.²⁶ ²⁷Al NMR spectra for AlCl₃ in saltwater were acquired with 32k points, 2 averages, a spectral width of 10000 Hz, and zero-filled to 130k prior to deconvolution. ²⁷Al spectra were referenced to [AlCl₄]⁻ at 103 ppm. Spectral deconvolution was performed using DM Fit software²⁷ using a combination of Lorentzian and Gaussian functions as described in Chapter 2.1.1.2. Data for all spectral deconvolutions can be found in Appendix 4.

MR images for the ¹H T_1 relaxation time map of the water in AlCl₃ in saltwater (10% w/w NaCl in water) were acquired using a WB40 microimaging probe equipped with a ¹H quadrature transmit/receive (QTR) coil at a temperature of 239 ± 0.3 K, which was maintained by the water-cooled micro2.5 gradient coils. A 1 mm slice thickness was used with a 64×64 pixel matrix resulting in an isotropic pixel size of $313 \mu\text{m} \times 313 \mu\text{m}$. Images were acquired using a RARE pulse sequence.²⁸ Saturation recovery (SR) experiments were performed with a repetition time ranged logarithmically from 55 ms to $5 T_1$, 16 echo images and an echo time $T_E = 3$ ms. T_1 maps were generated by summing the echo images as described in Chapter 3 using *Prospa*.²⁵

6.3 Results and Discussion

6.3.1 $C_4C_1imCl:AlCl_3$ Ionic Liquid Electrolyte

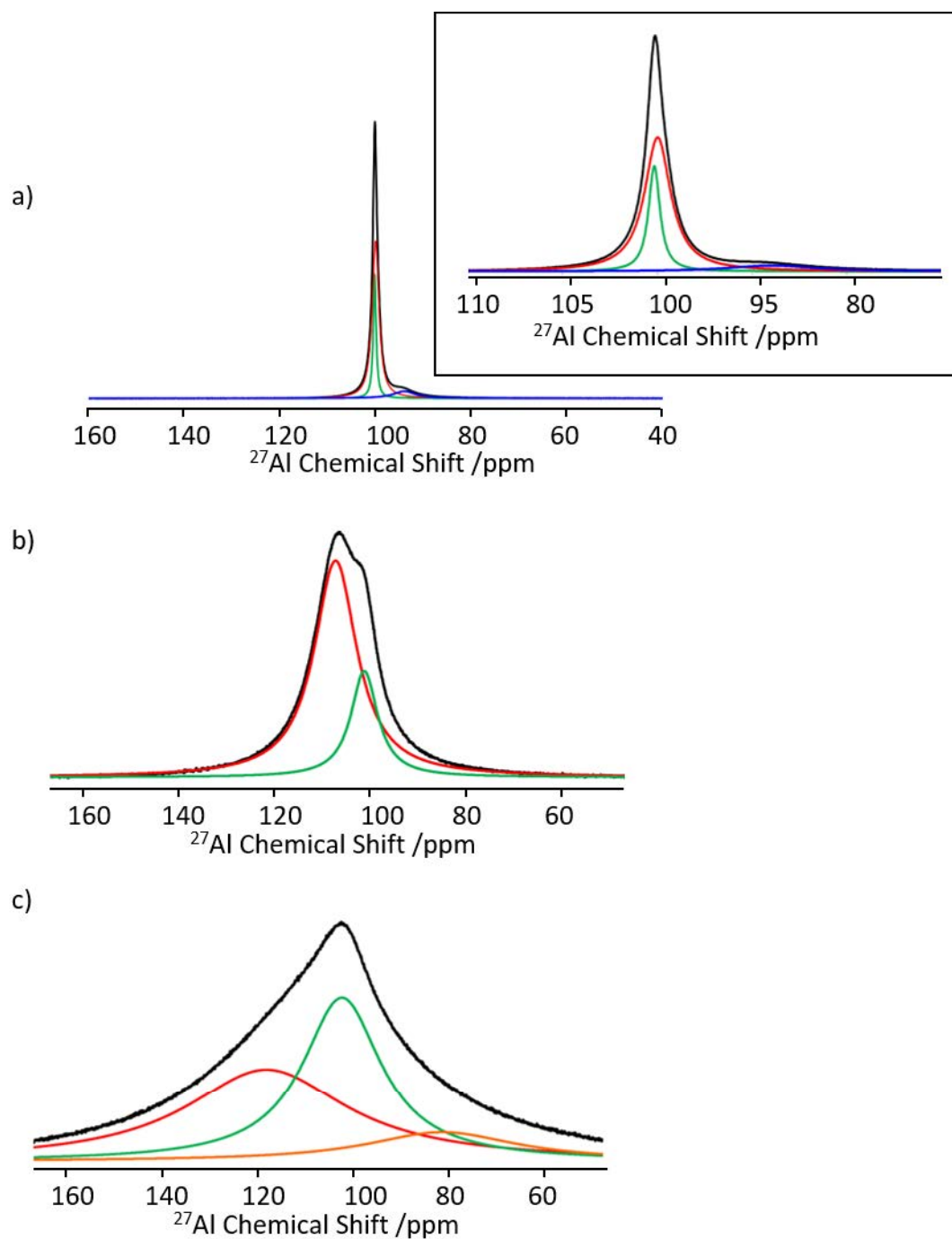


Figure 6.1: ^{27}Al NMR spectra for a) 1:1.1, b) 1:1.2, and c) 1:1.8 molar ratio of $AlCl_3$ in $C_4C_1imCl:AlCl_3$. Showing $AlCl_{4-n}(OH)_n$ (red), $[AlCl_4]^-$ (green), $[Al_2Cl_7]^-$ (blue), and $[Al(OH)_4]^-$ (orange).

Figure 6.1 shows ^{27}Al NMR spectra of $C_4C_1imCl:AlCl_3$ at different ratios of $AlCl_3$. There was a significant difference between the spectra of 1:1.1 and

1:1.8 both in the chemical shift of the environments, and their peak widths. Since the samples contained water, evidenced by the peak for H-9 in the ^1H spectra (Figure 6.4), they are not directly comparable to previous studies, such as by Ferrara *et al.*²⁹ The water in the IL was absorbed from the atmosphere during sample preparation as it was not conducted in a dry environment.

The symmetry of the ligands surrounding the metal influences the chemical shift of the ^{27}Al NMR signal.³⁰ It is known that tetrahedral aluminium species have a chemical shift of approximately 100 ppm, and aluminium species with octahedral symmetry are at 0 ppm with respect to $\text{Al}(\text{H}_2\text{O})_6$.³⁰ There was no signal around 0 ppm, so it can be assumed that all aluminium species above the level of detection are four coordinate with tetrahedral symmetry.

Peak linewidths can be used to infer the symmetry surrounding the aluminium ion due to its quadrupolar relaxation.³⁰ The symmetric $[\text{AlCl}_4]^-$ ion was expected to have a narrower linewidth than corresponding hydroxide species, $\text{AlCl}_{4-n}(\text{OH})_n$, up until $[\text{Al}(\text{OH})_4]^-$ which appears at 79 ppm.³¹ Furthermore, the peak corresponding to $[\text{AlCl}_4]^-$ would not shift with respect to AlCl_3 addition (Figure 6.2); hence, the peak at 103 ppm is assigned to $[\text{AlCl}_4]^-$, shown in Figure 6.1 (green). The NMR signal that shifts upfield from 103 ppm to 120 ppm could be ascribed to $[\text{AlH}_x\text{Cl}_{x-1}]^-$

as previously observed in the literature;³² however, due to the presence of water in the system, the presence of a hydride is unlikely as a hydride species would react immediately with the water.

The upfield environment (Figure 6.1, red) has been observed by Ferrara *et al.*²⁹ and was assigned $\text{AlCl}_{4-n}(\text{OH})_n$. The assignment is further supported in the literature, as peaks around 110 ppm have been attributed to aluminium hydrolysis products.³³ The peak at 97 ppm was assigned to $[\text{Al}_2\text{Cl}_7]^-$, shown as the blue line in Figure 6.1a, as previously described in the literature.²⁹ The peak for $[\text{Al}_2\text{Cl}_7]^-$ is only detectable in the sample with an AlCl_3 ratio of 1.1; this may be due to an increase in exchange between $[\text{AlCl}_4]^-$ and $[\text{Al}_2\text{Cl}_7]^-$ as more AlCl_3 is added. Fast exchange would result in the apparent disappearance of the $[\text{Al}_2\text{Cl}_7]^-$ peak. Alternatively, the equilibrium between the aluminium environments may increasingly favour formation of the hydroxide species over the dimer as more AlCl_3 is added, resulting in a reduction of the amount of $[\text{Al}_2\text{Cl}_7]^-$ present in the sample.

The relative amounts of $[\text{AlCl}_4]^-$ and $\text{AlCl}_{4-n}(\text{OH})_n$ remain constant across the range of AlCl_3 concentrations examined and the peak widths increase with increasing AlCl_3 concentration. As the diffusion coefficient of the cation in the IL did not change with respect to AlCl_3 content, it can be assumed that the viscosities of the liquids were comparable. Hence, the

increase in linewidth of peaks in the ^{27}Al NMR spectra has been attributed to the change in quadrupolar relaxation in the literature;²⁹ the increase in peak linewidth may also be due to an increase in exchange between the different aluminium species present in the sample, such as $[\text{AlCl}_4]^-$ and $\text{AlCl}_{4-n}(\text{OH})_n$. Moreover, whilst the chemical shift of $[\text{AlCl}_4]^-$ remained constant, the $\text{AlCl}_{4-n}(\text{OH})_n$ peak shifted further upfield which may suggest an increase in the number of hydroxide groups on the aluminium. At a molar ratio of 1:1.8 $\text{C}_4\text{C}_1\text{imCl}:\text{AlCl}_3$ an environment at 83 ppm is observed, shown as the orange line in Figure 6.1c; this is assigned to $[\text{Al}(\text{OH})_4]^-$ from the literature³¹ and may not have been present in spectra of samples with a lower AlCl_3 ratio as its quantity may have been below the level of detection.

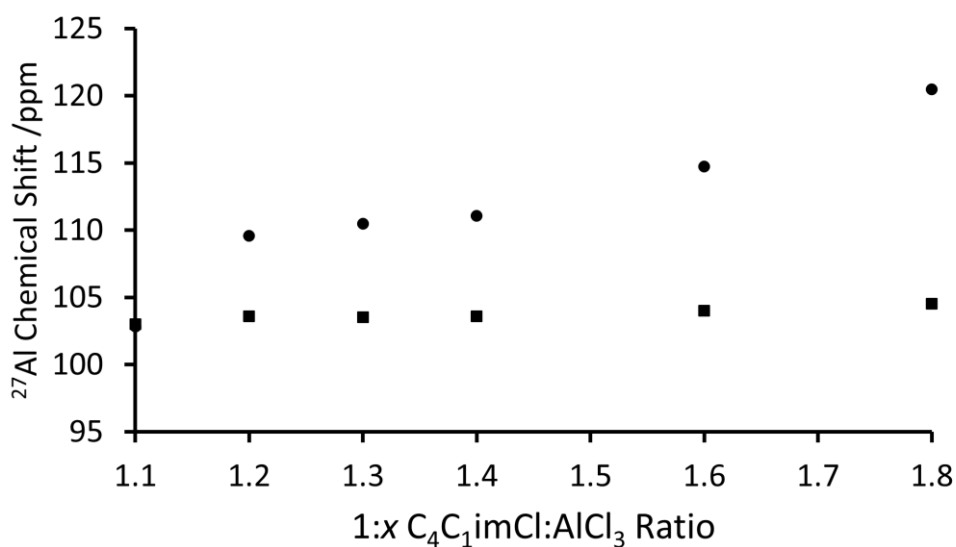


Figure 6.2: ^{27}Al Chemical shift of $[\text{AlCl}_4]^-$ (circles) and $[\text{AlCl}_3(\text{OH})]^-$ (squares) peaks as a function of $\text{C}_4\text{C}_1\text{imCl}:\text{AlCl}_3$ ratio.

^{27}Al T_1 and T_2 NMR relaxation times, for samples with an AlCl_3 molar ratio above 1.1, were found to be on the order of 10s of microseconds; for example $T_1 = 23\ \mu\text{s}$, $T_2 = 14\ \mu\text{s}$ and $3\ \mu\text{s}$ for an AlCl_3 molar ratio of 1.3, which agreed with literature reports of ^{27}Al relaxation time measurements in ILs.³⁴ Although, due to the length of the 90° pulse, $41.5\ \mu\text{s}$, there is likely to be a large error in the measurement of the T_1 relaxation time (Figure 6.3). A graph of all NMR relaxation times with respect to AlCl_3 concentration can be found in Appendix 4. The relaxation times are too short for RARE imaging using ^{27}Al , so direct detection of the aluminium species using MRI was unlikely, therefore indirect detection using ^1H MRI was explored.

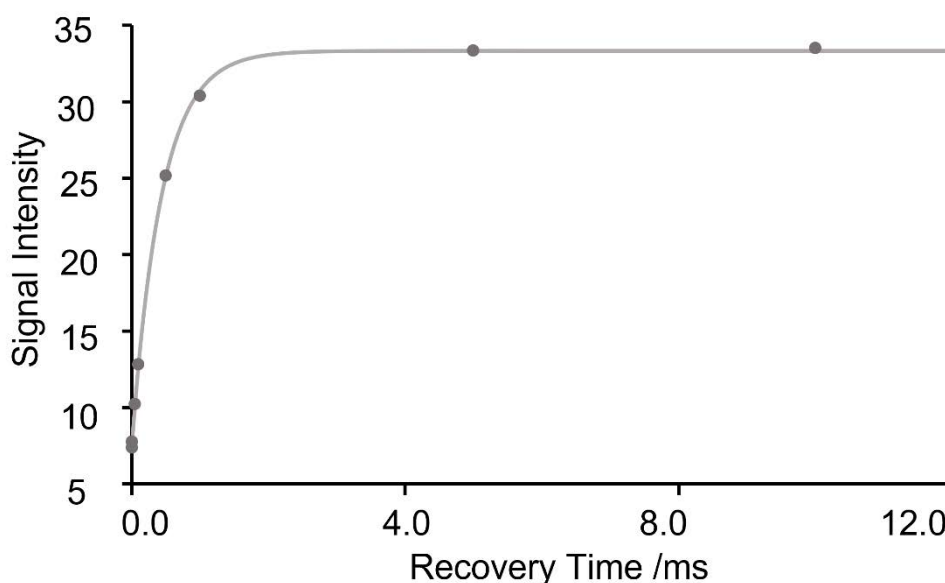


Figure 6.3: ^{27}Al NMR T_1 relaxation time graph of signal intensity versus inversion time for 1:1.2 $\text{C}_4\text{C}_1\text{imCl}:\text{AlCl}_3$ showing the data points in dark grey and fitted data in light grey.

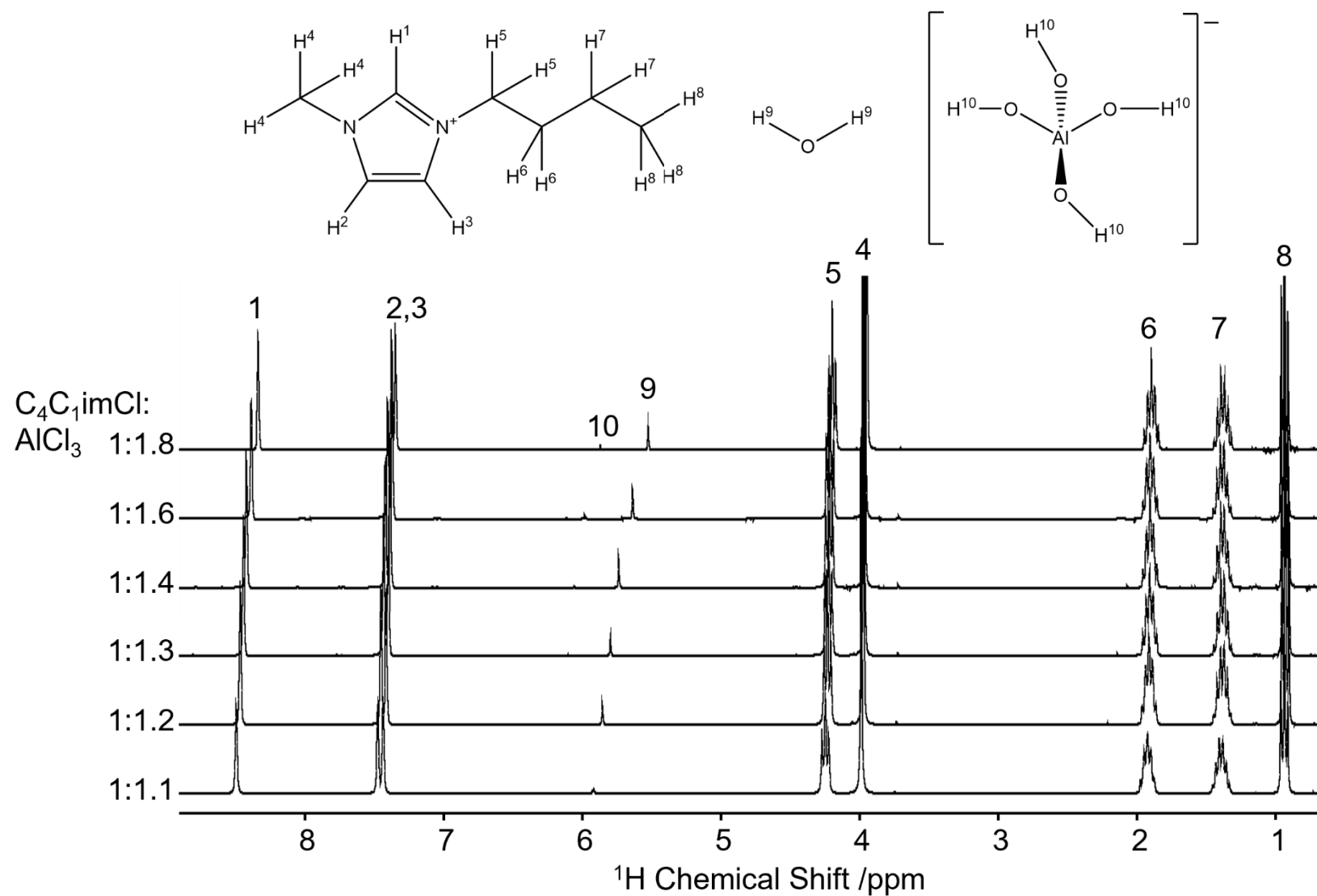


Figure 6.4: ¹H NMR spectra and proton assignments for mixtures of C₄C₁imCl and AlCl₃ as a function of AlCl₃ ratio.

The changes in the ^1H NMR spectra with respect to AlCl_3 concentration are significantly less than those observed in the ^{27}Al NMR spectra (Figure 6.4). Chemical shifts of the ^1H peaks decreased with respect to AlCl_3 concentration until 0.5 mole fraction, at which point the rate of change in chemical shift decreased.⁵ The changes in ^1H chemical shift described in the literature are in the opposite direction to what was observed in the ^1H NMR spectra (Figure 6.5). The multiplets below 2 ppm, assigned to H-6, H-7, and H-8, showed no changes with increased AlCl_3 content. However, H-4 and H-5, showed downfield shifts.

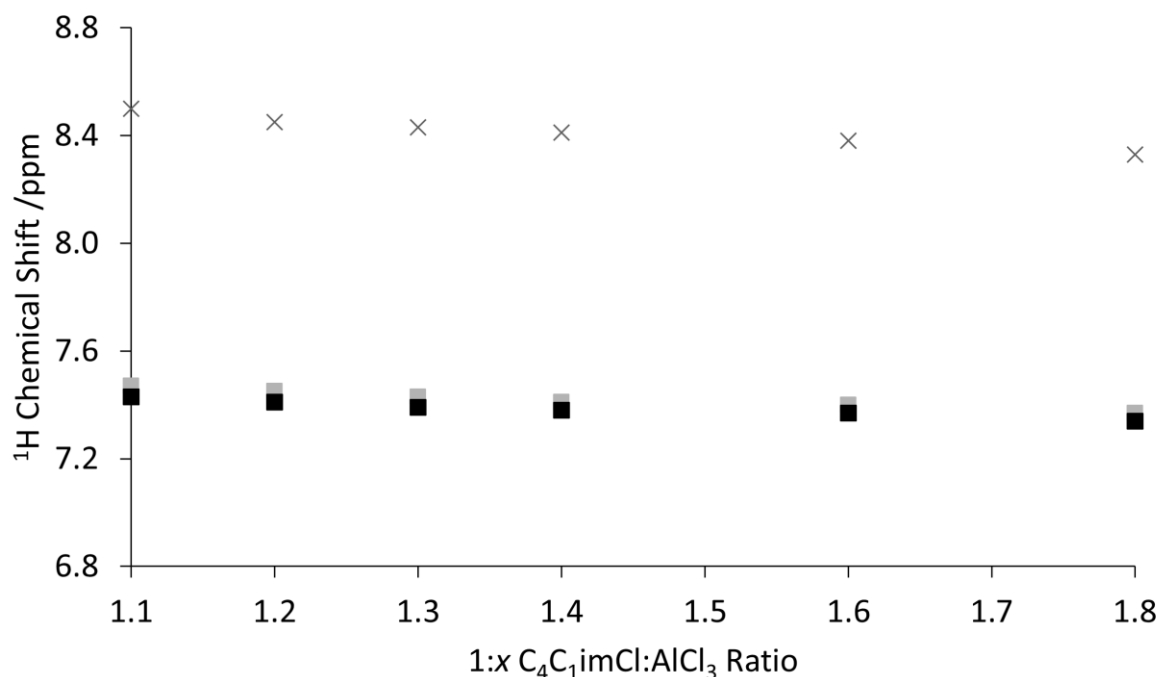


Figure 6.5: ^1H Chemical shift of H-1 (crosses), H-2 (grey squares), and H-3 (black squares) as a function of $\text{C}_4\text{C}_1\text{imCl}:\text{AlCl}_3$ ratio.

Larger changes in chemical shift are observed for H-1, H-2, and H-3, which was expected as these hydrogens were expected to be hydrogen bonded to AlCl_3 and water. Figure 6.5 shows the downward trend in chemical shift of H-1, H-2, and H-3 with respect to increasing AlCl_3

concentration suggesting that as the content of AlCl_3 increased, the average hydrogen bonding strength around these hydrogens decreased. The decrease in hydrogen bond strength may be due to an increase in competitiveness of the Cl^- in hydrogen bonding compared with water, due to the relative electronegativity of the Cl^- and water molecules.

H-9 and H-10 showed a downfield shift with respect to AlCl_3 ratio (Figure 6.6). The downfield shift further supports an increase in the amount of hydrogen bonds formed with Cl^- with increasing AlCl_3 content. Moreover, the integral of H-10 increased as more AlCl_3 was added, although the total amount of water in the system remained relatively constant, with no environment present at a ratio of $\text{C}_2\text{C}_1\text{imCl}:\text{AlCl}_3$ of 1:1.1 to a clearly visible environment at 1:1.8. Hence, as the intensity of the H-10 peak increases with respect to AlCl_3 content, it was assigned to $[\text{Al}(\text{OH})_4]^-$, and not the water in the pockets of the IL lattice. The increase in chemical shift of H-10 in comparison to bulk water was caused by the interaction with the Al^{3+} . The assignment of H-10 to $[\text{Al}(\text{OH})_4]^-$ also correlates with the ^{27}Al NMR spectra (Figure 6.1) as there is no peak for $[\text{Al}(\text{OH})_4]^-$ at a ratio of 1:1.1 (Figure 6.1a) but a peak for $[\text{Al}(\text{OH})_4]^-$ is present in the ^{27}Al NMR spectrum at a ratio of 1:1.8 $\text{C}_2\text{C}_1\text{imCl}:\text{AlCl}_3$ (Figure 6.1c).

^1H diffusion coefficients for all imidazolium environments remained constant at $3.7 \pm 0.3 \times 10^{-11} \text{ m}^2 \text{ s}^{-1}$ across all AlCl_3 concentrations,

suggesting insignificant changes in viscosity. All diffusion coefficients can be found in Appendix 4. However, H-9 and H-10, that are not part of the imidazolium, had a lower diffusion coefficient, $2.2 \pm 0.4 \times 10^{-11} \text{ m}^2 \text{ s}^{-1}$. The lower diffusion coefficients of H-9 and H-10 supports the literature observation that water is confined to pockets at low concentration, resulting in restricted movement of water and hydrated species.¹³

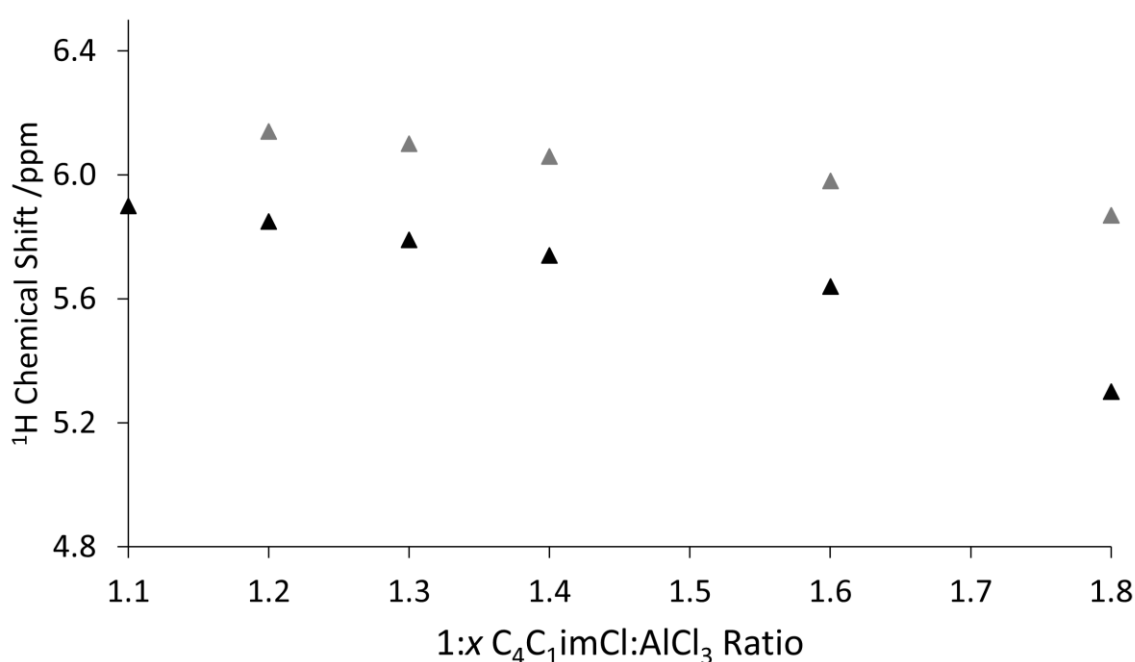


Figure 6.6: ¹H Chemical shift of H-9 (black) and H-10 (grey), associated with the spectra in Figure 6.4, as a function of C₄C₁imCl:AlCl₃ ratio.

Using information from ²⁷Al and ¹H spectroscopy and the literature on hydrogen bonding in imidazolium chloride ILs,^{12, 35, 36} the molecular speciation in Figure 6.7 has been proposed. At a low AlCl₃ ratio (Figure 6.7a), there was sufficient water in the system to enable interaction between the water and imidazolium. Furthermore, the previously proposed exchange between [AlCl₄]⁻ and [Al₂Cl₇]⁻ appears to

be sufficiently slow to enable the observation of a peak corresponding to $[\text{Al}_2\text{Cl}_7]^-$ in the ^{27}Al NMR spectrum. As the AlCl_3 ratio increases, the amount of $[\text{Al}(\text{OH})_4]^-$ increases; this is because the oxygen in the water molecule has a higher affinity for interaction with the Al^{3+} than for hydrogen bonding with the imidazolium ion. The increase in $\text{AlCl}_{4-n}(\text{OH})_n$ species was evidenced in the ^{27}Al spectra, with $[\text{Al}(\text{OH})_4]^-$ above the level of detection at an IL to AlCl_3 ratio of 1:1.8. The increase in $\text{AlCl}_{4-n}(\text{OH})_n$ species results in a reduction of the amount of water available to hydrogen bond with the imidazolium, causing the overall downfield chemical shift of these environments and the speciation shown in Figure 6.7b.

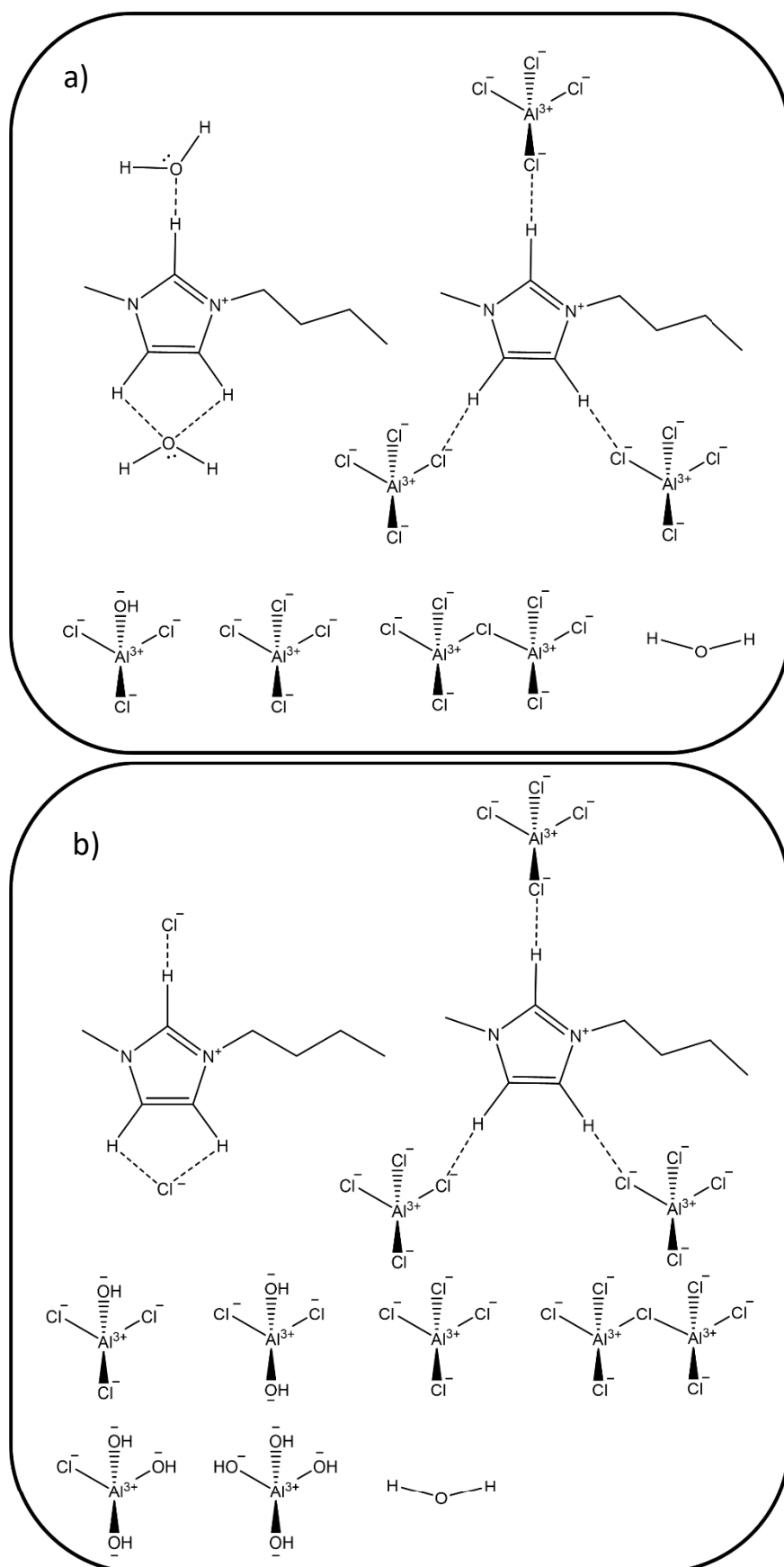


Figure 6.7: Speciation diagrams of $C_4C_1imCl:AlCl_3$ at a) 1:1.1 and b) 1:1.8 molar ratio of $AlCl_3$

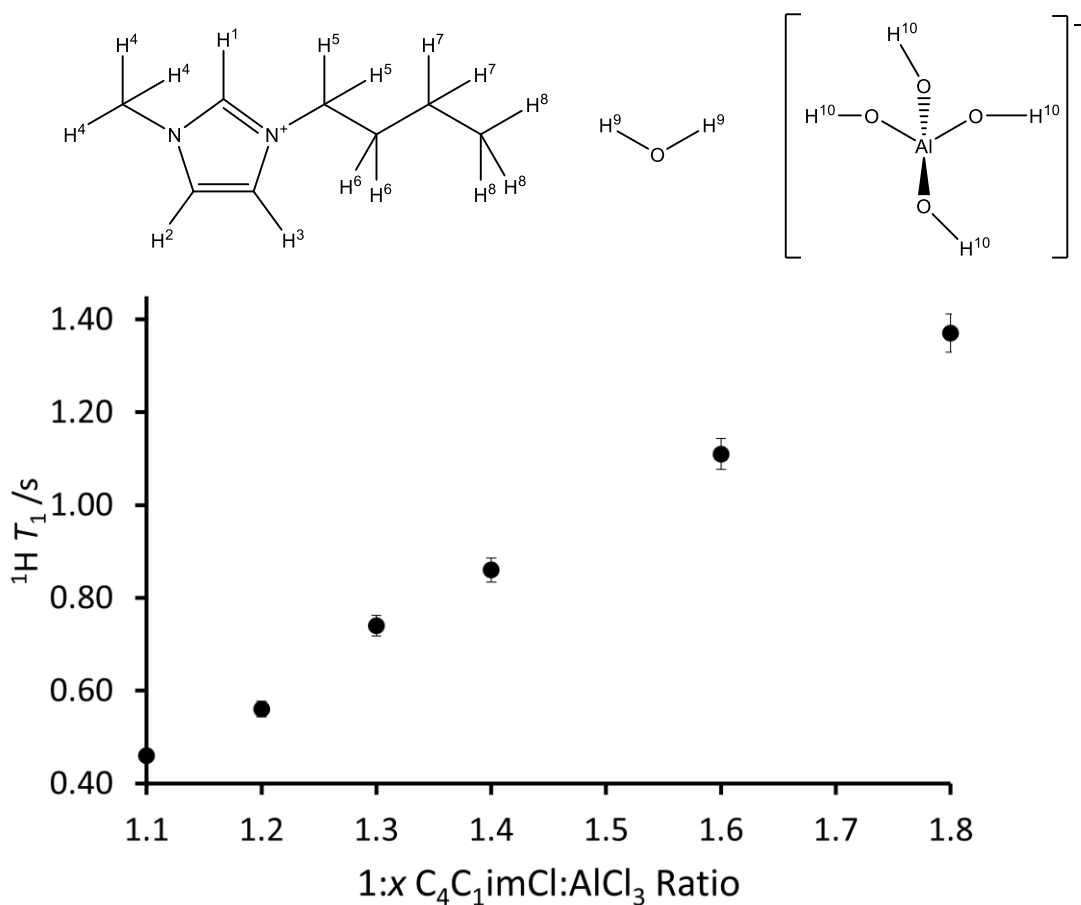


Figure 6.8: ^1H T_1 relaxation time of H-2 and H-3 as a function of $\text{C}_4\text{C}_1\text{imCl}:\text{AlCl}_3$ ratio. Inset of $\text{C}_2\text{C}_1\text{im}^+$, H_2O , and $[\text{Al}(\text{OH})_4]^-$ with labelled ^1H environments.

The ^1H T_1 NMR relaxation times of all imidazolium protons increase with respect to AlCl_3 ratio (Figure 6.8). As the change in relaxation times was linear with respect to AlCl_3 concentration, and the diffusion coefficients for all samples were $3.7 \pm 0.3 \times 10^{-11} \text{ m}^2 \text{ s}^{-1}$, it can be assumed that this is related to a change in the interaction with the different aluminium species and not change in sample viscosity. The ^1H T_2 relaxation times did not all increase linearly with AlCl_3 concentration (Figure 6.9) although the overall T_2 relaxation time of the molecule changed linearly with respect to AlCl_3 concentration. The increase in T_2 relaxation time suggested that the AlCl_3

was either increasing the molecular tumbling rate or facilitating an increase in exchange. As the ^1H on the imidazolium are unable to exchange, it must therefore be that the aluminium species present in the sample facilitate faster relaxation of the ^1H in the IL.

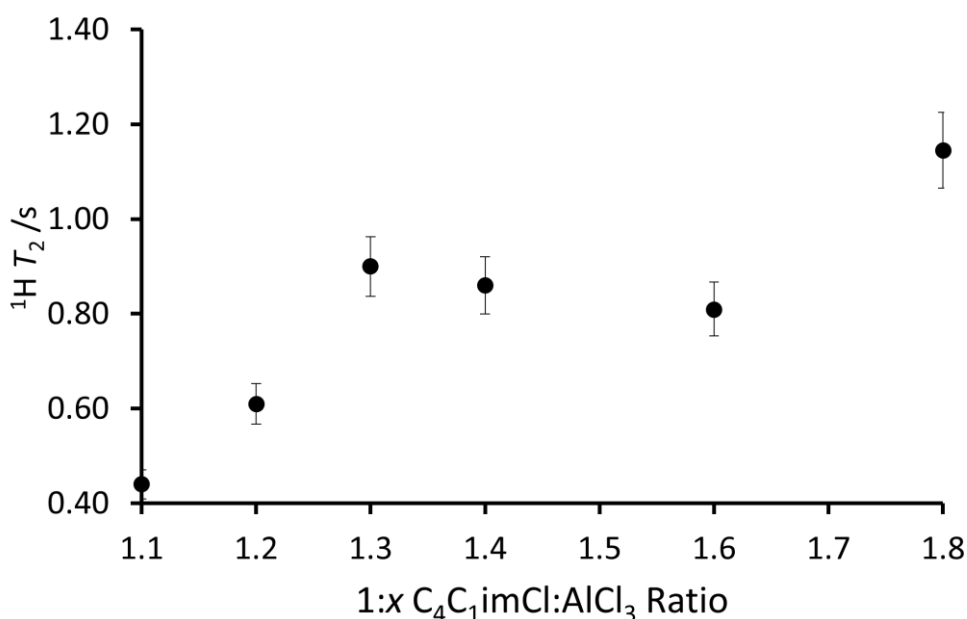


Figure 6.9: $^1\text{H } T_2$ relaxation time of H-2 and H-3 as a function of C₄C₁imCl:AlCl₃ ratio.

As the ^{27}Al NMR relaxation times of the aluminium species in this IL inhibited the use of direct detection of aluminium concentration, ^1H NMR relaxation time mapping could be used. The linear increase of T_1 relaxation time at ratios of C₄C₁imCl:AlCl₃ of 1:1.1–1:1.8 make T_1 relaxation time a promising contrast method for MRI of this IL. Furthermore, the T_2 relaxation time changes linearly with respect to AlCl₃ concentration and so may also be suitable for MRI contrast. Both $^1\text{H } T_1$ and T_2 relaxation times change over a suitable range to enable the

differentiation of a range of aluminium concentrations that may be found in an AIB with a $C_4C_1\text{imCl}:\text{AlCl}_3$ electrolyte.

6.3.2 AlCl_3 in Saltwater Electrolyte

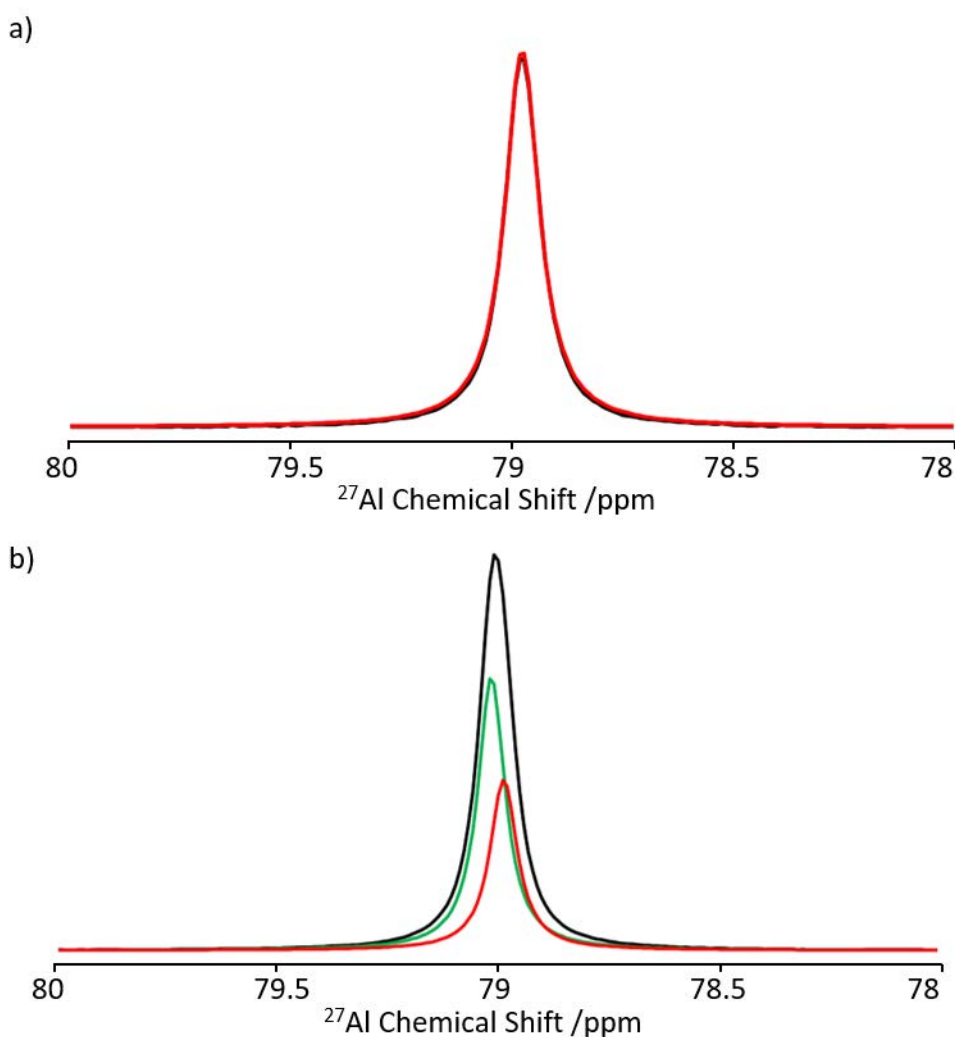


Figure 6.10: ^{27}Al NMR spectra for a) 100 mM and b) 500 mM AlCl_3 in saltwater (10% NaCl w/w). Showing $[\text{Al}(\text{OH})_4]^-$ (red) and $\text{AlCl}_{4-n}(\text{OH})_n$ (green).

Deconvoluted ^{27}Al NMR spectra for 100 mM and 500 mM AlCl_3 in saltwater (10% NaCl w/w) are shown in Figure 6.10. All spectra were referenced with respect to $[\text{Al}(\text{OH})_4]^-$ at 79 ppm. At 100 mM AlCl_3 there was only one environment, corresponding to $[\text{Al}(\text{OH})_4]^-$. There was no $[\text{Al}(\text{OH})_6]^{4-}$ peak, expected at around 0 ppm, in the spectrum which may have been because the NaCl altered the equilibrium of aluminium hydroxide species by making the electrolyte more acidic. Furthermore, there was no peak at

103 ppm associated with $[\text{AlCl}_4]^-$. As the AlCl_3 concentration increased, a second aluminium environment was present in the spectrum (Figure 6.10b). Due to its similar chemical shift and peak width as the peak corresponding to $[\text{Al}(\text{OH})_4]^-$, the environment above 79 ppm, was assigned to a similar tetrahedrally coordinated aluminium hydroxide species. The new peak may have been $\text{AlCl}_{4-n}(\text{OH})_n$ which has been proposed to exist.¹⁷ The exact species present were not determined from the chemical shift and the pH of the system was unknown. The proposed range of species is shown in Figure 6.11. Data for AlCl_3 concentrations lower than 100 mM showed no signal in the ^{27}Al NMR spectra due to the species being below the level of detection.

The ^{27}Al NMR relaxation times were on the order of 10s of milliseconds, for example 49 ms for T_1 and 11 ms for T_2 relaxation time for 200 mM AlCl_3 in saltwater. A graph of all relaxation times can be found in Appendix 4. These relaxation times were too fast to enable imaging using a RARE pulse sequence, so indirect detections using ^1H NMR relaxation time was explored.

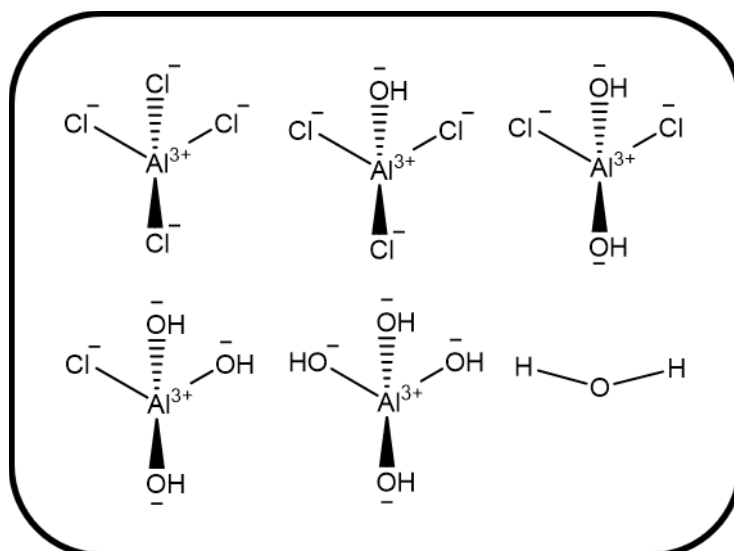


Figure 6.11: Suggested speciation in AlCl_3 in saltwater.

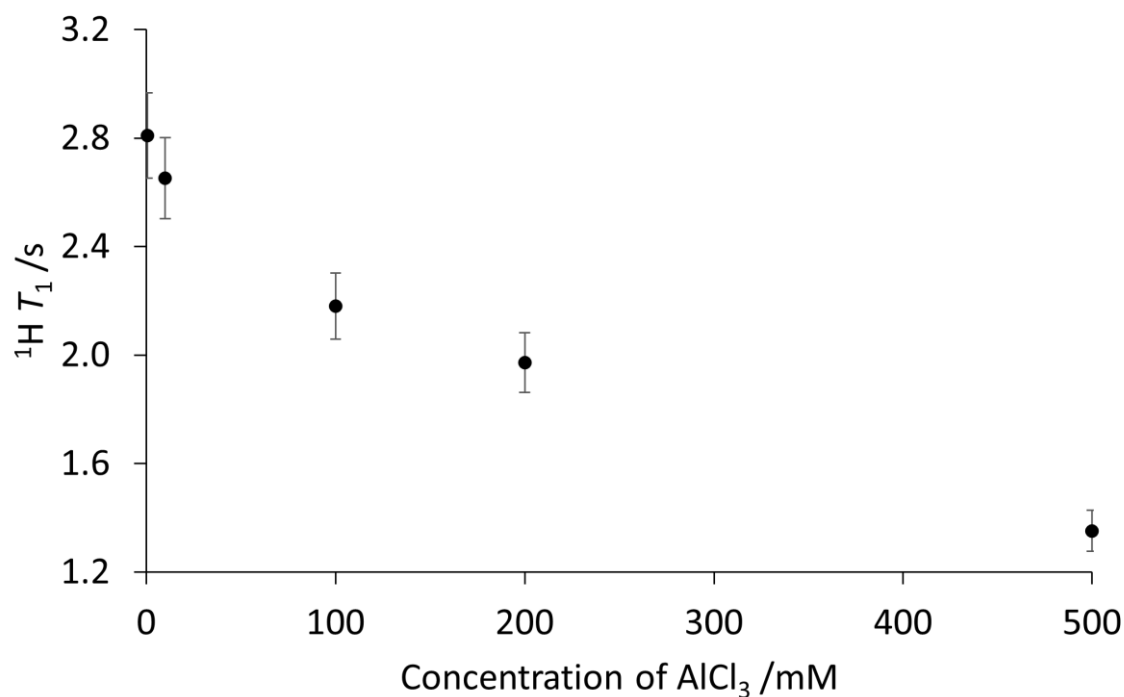


Figure 6.12: $^1\text{H } T_1$ NMR relaxation time of water in the AlCl_3 in saltwater as a function of AlCl_3 concentration in saltwater.

There was only a single peak in the ^1H NMR spectrum of AlCl_3 in saltwater, and its relaxation times did not vary linearly with AlCl_3 concentration. The $^1\text{H } T_1$ NMR relaxation time showed a large range of relaxation times with respect to AlCl_3 concentration (Figure 6.12). The T_2

relaxation time showed a significant change as AlCl_3 was added (Figure 6.13). A rapid decrease in the T_2 relaxation time from 0.5–10 mM AlCl_3 suggested a change in speciation which may have been accompanied by an increase in exchange between environments. The amount of aluminium hydroxide at low AlCl_3 concentration was low, and so the bulk T_2 relaxation time was unlikely to be influenced by any aluminium hydroxide species. However, at higher AlCl_3 concentrations more exchange would occur between the aluminium species, resulting in a reduction in the T_2 relaxation time. Above 100 mM AlCl_3 , the T_2 relaxation time did not vary significantly.

To visualise the changes in aluminium concentration in the electrolyte of an ALFA cell, ^1H NMR relaxation time contrast was used as the ^{27}Al NMR relaxation times were too short for RARE imaging. The larger range of T_1 values over the range of aluminium concentrations studied supports the use of ^1H T_1 relaxation time as MRI contrast for *in situ* or *operando* imaging studies. The rapid decrease in T_2 relaxation time between 0.05 mM AlCl_3 and 5 mM AlCl_3 would make it difficult to differentiate between higher concentrations of AlCl_3 and so would provide poor MRI contrast.

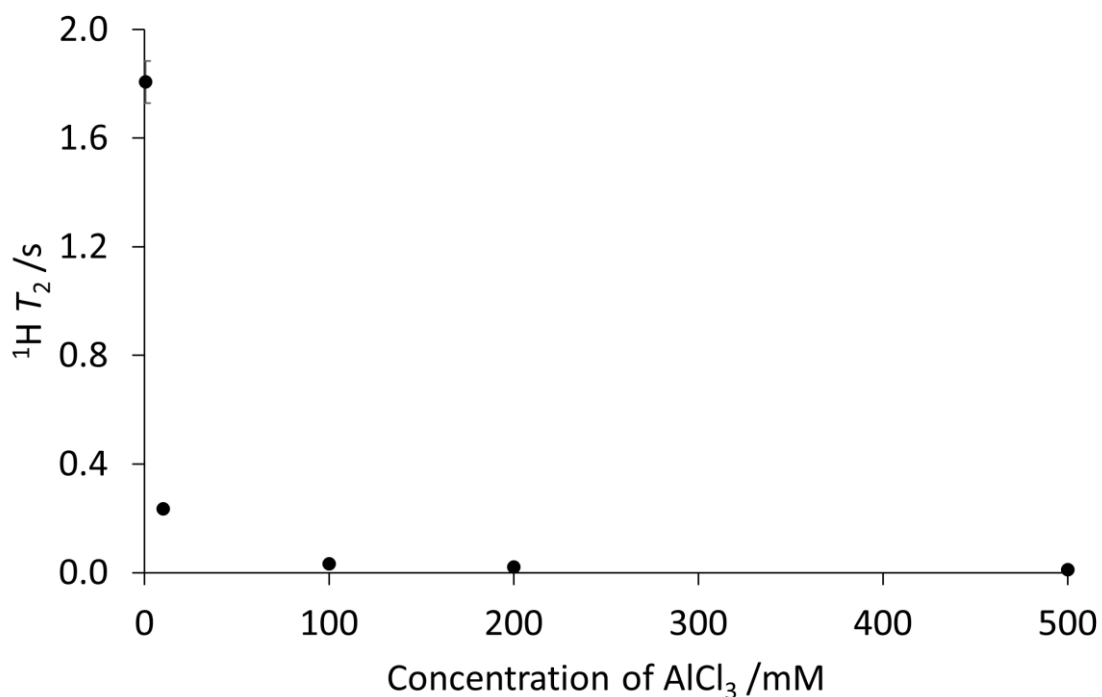


Figure 6.13: ^1H T_2 relaxation time as a function of AlCl_3 concentration in saltwater.

To investigate the efficacy of ^1H T_1 relaxation time as contrast in MRI, a ^1H T_1 relaxation time map was acquired for the same range of AlCl_3 concentrations as used in the NMR spectroscopy experiments, applying the echo summation methodology developed in Chapter 3. In Figure 6.14, the T_1 contrast showed the different AlCl_3 concentrations clearly and so would be appropriate for use in imaging an aluminium hydroxide battery *in operando*.

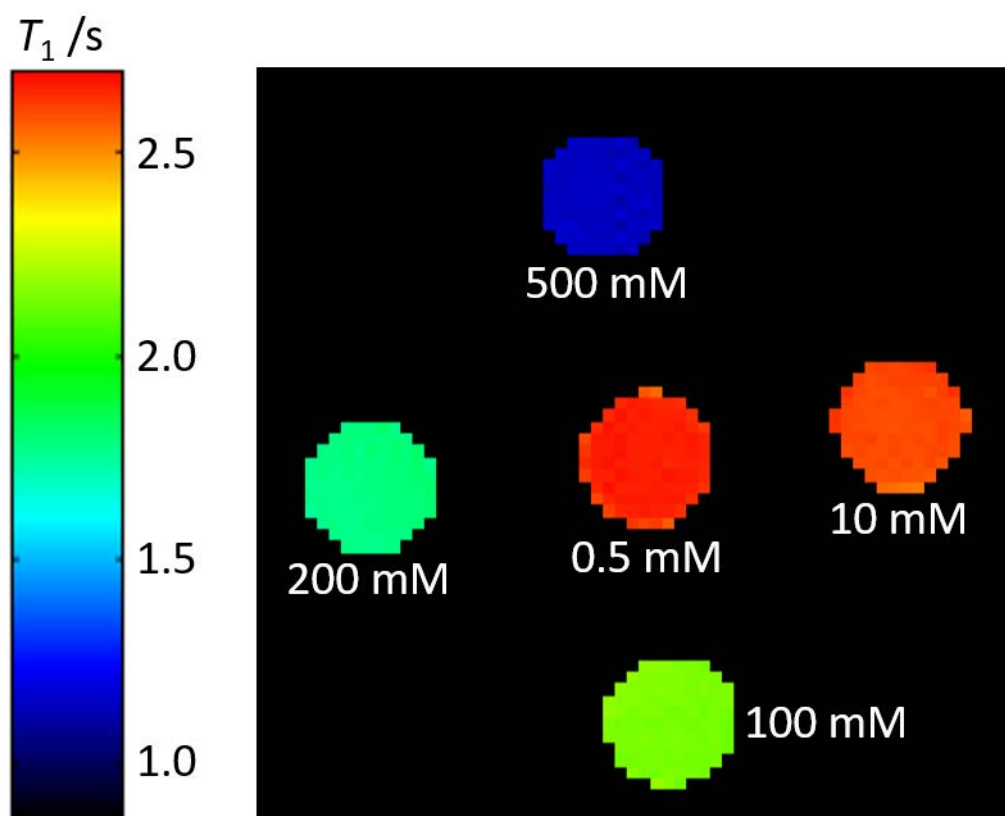


Figure 6.14: ^1H T_1 MR relaxation time map of a phantom containing a range of concentrations of AlCl_3 in saltwater.

6.4 Conclusion

In conclusion, the speciation in $\text{C}_4\text{C}_1\text{imCl}:\text{AlCl}_3$ changed with the addition of AlCl_3 , whilst the water concentration remained constant. The ^{27}Al spectra showed an increase in linewidth of both $[\text{AlCl}_4]^-$ and $\text{AlCl}_{4-n}(\text{OH})_n$ environments with respect to AlCl_3 which may correspond with an increase in exchange between the aluminium species in the sample in addition to an increase in quadrupolar relaxation rate. Only the sample with the lowest AlCl_3 ratio showed a peak for the electroactive $[\text{Al}_2\text{Cl}_7]^-$ species, which may have been due to reduced exchange at an IL to AlCl_3 ratio of 1:1.1. The ^{27}Al relaxation times were on the order of 10 ms, too fast to accurately measure using an IR or CPMG pulse sequence, and the

measurement of the linewidth was impacted by the SNR of the acquisition.

The ^1H spectra showed small downfield shifts to peaks typically involved in hydrogen bonding, suggesting that the average hydrogen bond strength became weaker as AlCl_3 was added to the system. Hence, it is hypothesised that as AlCl_3 was added to the system, the water preferentially interacted with the Al^{3+} , creating more $[\text{Al}(\text{OH})_4]^-$ and AlCl_4^- species, resulting in fewer water hydrogen bonds to the imidazolium, with the imidazolium hydrogen bonding to the Cl^- instead. Furthering the understanding of intermolecular interactions in this system may aid in the development of improved non-aqueous electrolytes for AIBs.

Overall, the changes in ^1H T_1 and T_2 relaxation times were appropriate to provide contrast in MRI of $\text{C}_4\text{C}_1\text{imCl}:\text{AlCl}_3$. Further investigation into the possibility of electroplating in $\text{C}_4\text{C}_1\text{imCl}:\text{AlCl}_3$ and identification of the electroactive species using *operando* ^{27}Al NMR spectroscopy should be performed in addition to *operando* ^1H T_1 relaxation time mapping to observe the aluminium electroplating in real-time.

In the case of AlCl_3 in saltwater, it was unlikely that the species present change once the AlCl_3 was added into the system, although the distribution of the species was likely to vary. The appearance of a second environment in the ^{27}Al spectrum at 200 mM AlCl_3 was likely due to this species now being present above the level of detection. There was no $[\text{Al}(\text{OH})_6]^{3-}$ in AlCl_3 in saltwater due to the presence of NaCl , and so it was suggested that the species are $\text{AlCl}_{4-n}(\text{OH})_n$ and $[\text{Al}(\text{OH})_4]^-$, although a more exact composition cannot be suggested with the data available. Knowledge of the speciation in AlCl_3 in saltwater is an important step in understanding the redox reactions in an ALFA cell. The ^{27}Al relaxation times were on the order of 50 ms for AlCl_3 in saltwater, and so were not able to be effectively measured by IR or CPMG experiments.

The ^1H spectra showed only one peak, however the relaxation times changed with respect to AlCl_3 concentration. The T_1 relaxation time across 0.5–100 mM AlCl_3 showed a decrease with increasing AlCl_3 concentration that would be appropriate for use as contrast in MRI. The T_2 relaxation time dropped rapidly after the addition of >0.5 mM AlCl_3 , suggesting that this is related to the exchange of the ^1H between the species present as the concentration of the aluminium species increased. Additionally, the T_2 relaxation time showed little variation above 100 mM AlCl_3 and so would provide poor MRI contrast in this region. Therefore, the electroactive

species may be identifiable using *operando* ^{27}Al NMR spectroscopy and the battery chemistry spatially resolved using *operando* ^1H T_1 mapping.

This chapter demonstrates a potential use of the quantitative T_1 imaging methodology developed in Chapter 1, with different concentrations of AlCl_3 in saltwater showing a different ^1H T_1 relaxation time using both NMR spectroscopy and MRI. The use of NMR relaxation time and chemical shift to establish speciation and intermolecular interactions is applicable to all NMR active nuclei with measurable relaxation times, with a limitation in measuring T_1 relaxation time when the NMR pulse lengths are comparable to the T_1 relaxation time. Overall, the insight into molecular speciation and intermolecular interactions aids in the understanding of electrochemical systems, and thus leads to the development of improved battery electrolytes.

6.5 References

1. S. K. Das, S. Mahapatra and H. Lahan, *J. Mater. Chem. A*, 2017, 5, 6347-6367.
2. G. L. Holleck, *J. Electrochem. Soc.*, 1972, 119, 1158-1161.
3. G. L. Holleck and J. Giner, *J. Electrochem. Soc.*, 1972, 119, 1161-1166.
4. N. Koura, *J. Electrochem. Soc.*, 1980, 127, 1529-1531.
5. A. A. Fannin Jr, L. A. King, J. A. Levisky and J. S. Wilkes, *J. Am. Chem. Soc.*, 1984, 88, 2609-2614.
6. A. Bakkar and V. Neubert, *Electrochim. Acta*, 2013, 103, 211-218.

7. Q. Wang, Q. Zhang, X. Lu and S. Zhang, *Ionics*, 2017, 23, 2449-2455.
8. N. Jayaprakash, S. K. Das and L. A. Archer, *Chem. Commun.*, 2011, 47, 12610-12612.
9. P. K. Lai and M. Skyllas-Kazacos, *J. Electroanal. Chem.*, 1988, 248, 431-440.
10. T. Jiang, M. J. Chollier Brym, G. Dubé, A. Lasia and G. M. Brisard, *Surf. Coat. Technol.*, 2006, 201, 1-9.
11. Y. Zheng, K. Dong, Q. Wang, J. Zhang and X. Lu, *J. Chem. Eng. Data*, 2012, 58, 32-42.
12. A. A. Niazi, B. D. Rabideau and A. E. Ismail, *J. Phys. Chem. B*, 2013, 117, 1378-1388.
13. S. S. Bystrov, V. V. Matveev, A. V. Egorov, Y. S. Chernyshev, V. A. Konovalov, V. Balevicius and V. I. Chizhik, *J. Phys. Chem. B*, 2019, 123, 9187-9197.
14. R. Revel, T. Audichon and S. Gonzalez, *J. Power Sources*, 2014, 272, 415-421.
15. R. Mori, *RSC Adv.*, 2013, 3, 11547-11551.
16. J. R. González, F. Nacimiento, M. Cabello, R. Alcántara, P. Lavela and J. L. Tirado, *RSC Adv.*, 2016, 6, 62157-62164.
17. R. Mori, *RSC Adv.*, 2014, 4, 1982-1987.
18. R. Mori, *RSC Adv.*, 2017, 7, 6389-6395.
19. R. Mori, *J. Electron. Mater.*, 2016, 45, 3375-3382.
20. R. Mori, *RSC Adv.*, 2014, 4, 30346-30351.
21. R. Mori, *Phys. Chem. Chem. Phys.*, 2018, 20, 29983-29988.
22. P. Canizares, F. Martínez, C. Jiménez, J. Lobato and M. A. Rodrigo, *Ind. Eng. Chem. Res.*, 2006, 45, 8745-8756.
23. C. Wanga, Z. Hana, P. Wangb, N. C. T. Laoa and P. Hong, *Bullitin of the Chemical Society of Ethiopia*, 2008, 22, 155-164.
24. R. Mori, *J. Appl. Electrochem.*, 2015, 45, 821-829.
25. *Prosopa*, Magritek, Wellington, New Zealand.

26. *Kaleidagraph*, Synergy Software, Reading, Pennsylvania, 4.0 edn., 2006.
27. D. Massiot, F. Fayon, M. Capron, I. King, S. Le Calvé, B. Alonso, J. - O. Durand, B. Bujoli, Z. Gan and G. Hoatson, *Magn. Reson. Chem.*, 2002, 40, 70-76.
28. J. Hennig, A. Nauerth and H. Friedburg, *Magn. Reson. Med.*, 1986, 3, 823-833.
29. C. Ferrara, V. Dall'Asta, V. Berbenni, E. Quartarone and P. Mustarelli, *J. Phys. Chem. C*, 2017, 26607-26614.
30. M. Haouas, F. Taulelle and C. Martineau, *Prog. Nucl. Magn. Reson. Spectrosc.*, 2016, 94-95, 11-36.
31. **Z. Černý, J. Macháček, J. Fusek, B. Čásenský, O. Kříž and D. G. Tuck**, *Inorganica Chim. Acta*, 2000, 300-302, 556-564.
32. M. C. Lefebvre and B. E. Conway, *J. Electroanal. Chem.*, 1998, 448, 217-227.
33. T. Rodopoulos, L. Smith, M. D. Horne and T. Ruther, *Chem.*, 2010, 16, 3815-3826.
34. C. E. Keller and W. R. Carper, *J. Magn. Reson. A*, 1994, 110, 125-129.
35. P. A. Hunt, B. Kirchner and T. Welton, *Chem.*, 2006, 12, 6762-6775.
36. O. Gorlova, S. M. Craig and M. A. Johnson, *J. Chem. Phys.*, 2017, 147, 231101.

7 Conclusions and Further Work

This thesis is focused on the development of magnetic resonance methods to improve the signal-to-noise ratio (SNR) of nuclear magnetic resonance (NMR) relaxation time mapping, investigate battery function *in operando*, and study molecular speciation in electrolytes using off-the-shelf magnetic resonance imaging (MRI) equipment. The methods presented have been developed using multiple nuclei, including nuclei with low gyromagnetic ratios and rapid NMR relaxation times, enabling the application of these methods across multiple chemistries.

Quantitative T_1 imaging methods using echo image summation were tested to enable the optimisation of T_1 relaxation time mapping to generate NMR relaxation time data with an improved SNR without an increase in experiment time. Echo image summation was applied to imaging water ingress into the ionic liquid (IL) 0.08M $\text{Zn}(\text{TfO})_2$ in 1-ethyl-3-methylimidazolium triflate ($\text{C}_2\text{C}_1\text{imTfO}$). The increase in SNR enabled the interpretation of speciation changes of the IL with respect to water concentration at low water mol% that support current literature. It was established that by summing the echo images obtained at each recovery time, the SNR of the resulting ^{19}F T_1 relaxation time map can be improved to show water ingress into 0.08M $\text{Zn}(\text{TfO})_2$ in $\text{C}_2\text{C}_1\text{imTfO}$ from the atmosphere over time. The echo summation methodology could be further applied to imaging nuclei where the SNR is low without increasing

the experiment time. The decrease in acquisition time allows for an increase in temporal resolution when performing *in situ* or *operando* experiments whilst maintaining the SNR.

Operando ^{23}Na NMR spectroscopy and spectral deconvolution were performed on both sodium metal and sodium full cells for the first time. The evolution of sodium species in the electrolyte region of the spectrum, ~ 0 ppm, showed the development of sodium environments in the vicinity of the hard carbon and potential solid electrolyte interphase (SEI) formation. Quasimetallic species were observed, in addition to a metallic species that develops at a low potential,¹ at a slow charge rate; however, the quasimetallic and metallic species were not observed at a higher charge rate, suggesting that the formation of these species may be kinetically limited. To further explore the nature of the quasimetallic nanoparticles and metallic species formed at the slower cell cycle rate, ^{23}Na NMR experiments with a reduced spectral width may provide further information on the metallic species, in addition to imaging using X-ray micro computed tomography (micro-CT) to investigate the quasimetallic and metallic species as they are unable to be imaged using MRI. Furthermore, optimisation of cell assembly to limit the excess electrolyte surrounding the electrode-electrolyte stack should be conducted.

One-dimensional (1D) *operando* ^7Li MRI, NMR spectroscopy, and spectral deconvolution were performed on a lithium metal cell containing bubbles in the electrolyte for the first time. The use of ^1H MRI to confirm the presence of bubbles in the cell may be crucial to predicting early cell failure. The presence of bubbles in the electrolyte was established using three-dimensional (3D) ^1H MRI, in addition to the cell orientation not being perpendicular to B_0 . Deconvolution of the ^7Li spectra show the evolution of lithium in the carbon, in the SEI, and in the vicinity of the carbon during the formation cycle. Furthermore, a second metallic environment was observed at a higher chemical shift than the initial lithium metal from the electrode, attributed to pitting on the lithium electrode. It is suggested that the electrode pitting may be initiated due to the presence of bubbles in the electrolyte near the electrode that may accelerate the electrochemistry. Comparison of these results with those from a cell without bubbles is necessary to confirm the hypothesis.

The speciation and hydrogen bonding between the imidazolium, water, and AlCl_3 in 1-butyl-3-methylimidazolium chloride ($\text{C}_4\text{C}_1\text{imCl}$) IL with AlCl_3 and water was investigated using ^{27}Al and ^1H NMR spectroscopy. The ^{27}Al NMR spectra show a sudden change in speciation between aluminium chloride ratios of 1.1 and 1.2, with a gradual increase in line width of the NMR peaks in ratios of above 1.2. The species present are assigned to $[\text{AlCl}_4]^-$ (103 ppm), $[\text{Al}_2\text{Cl}_7]^-$ (97 ppm), $[\text{Al}(\text{OH})_4]^-$ (79 ppm), and

$\text{AlCl}_{4-n}(\text{OH})_n$ (103–120 ppm). The increase in line with for the $[\text{AlCl}_4]^-$ and $\text{AlCl}_{4-n}(\text{OH})_n$ species was hypothesised to be caused by an increase in quadrupolar relaxation, in addition to exchange between the aluminium species. The rapid relaxation times of the aluminium species, on the order of microseconds, make them poor candidates for direct detection using MRI. The ^1H NMR spectra showed downfield shifts of the environments associated with hydrogen bonding in the IL as the AlCl_3 ratio increases. The downfield shift suggests an increase in the hydrogen bonding with Cl^- . The ^1H T_1 and T_2 relaxation times increased with respect to AlCl_3 ratio and provided sufficient variation for indirect detection of the aluminium species.

An investigation of the speciation in the AlCl_3 in saltwater (10% NaCl w/w in water) electrolyte used in the aluminium anode, lid, film, air cathode (ALFA) cell was conducted using ^{27}Al and ^1H NMR spectroscopy. The ^{27}Al NMR spectra show two aluminium peaks above 200 mM AlCl_3 ; only one aluminium species is observed below 200 mM AlCl_3 . The second species may have been present in all samples but was only above the level of detection in samples above 200 mM AlCl_3 . The NMR peaks are assigned to $\text{AlCl}_{4-n}(\text{OH})_n$ and $[\text{Al}(\text{OH})_4]^-$ with further assignment not possible using the current data. The ^{27}Al T_1 and T_2 relaxation times were on the order of 10^{-2} s which made direct imaging of the electroactive species infeasible. The ^1H spectra contained only one signal and the T_1 and T_2 relaxation

times were sensitive to AlCl_3 concentration. The ^1H T_1 relaxation time was inversely proportional to AlCl_3 concentration. The variation across the measured concentration range was appropriate for use in indirect detection of aluminium species. However, the T_2 relaxation time showed an exponential decrease as the AlCl_3 concentration increased, with little variation above 100 mM AlCl_3 and hence would not provide sufficient contrast to identify aluminium concentrations above this level.

This work has established MRI and NMR spectroscopy methodologies that can be applied to electrochemical systems using either direct or indirect detection. Further NMR spectroscopy studies are required to establish the nature of the novel sodium species observed in the slow formation cycle of the full cell and the influence of bubbles on the evolution of lithium species in the metal cell. Additionally, MRI experiments using ^1H relaxation time as indirect charge carrier detection in the $\text{C}_4\text{C}_{1\text{im}}\text{Cl}:\text{AlCl}_3$ system with water and of the ALFA cell to spatially resolve electroplating in these systems may provide insight on the electroplating mechanism. The techniques developed can be used across a range of nuclei and demonstrate how MRI and NMR measurements can be used to study chemistry *in operando*. Further development in MR methodologies to improve the detection of species with fast NMR relaxation times, or that exist for shorter time periods, would be beneficial to the understanding of different battery chemistries.

The methods in this thesis, whilst often demonstrated in isolation, are complimentary to one another. The measurements to establish relationships between NMR relaxation times and electroactive species concentrations, shown in Chapter 6, can be directly used with the quantitative T_1 relaxation time imaging, demonstrated in Chapter 1. Furthermore, the NMR spectroscopy performed at equilibrium in Chapter 6 can be performed *in operando*, such as in Chapters 4 and 5, to monitor speciation change during electrochemistry. The use of the methods in combination provides a thorough, holistic understanding of electrochemistry in a system for nuclei with varying NMR properties.

7.1 References

1. J. M. Bray, C. L. Doswell, G. E. Pavlovskaya, L. Chen, B. Kishore, H. Au, H. Alptekin, E. Kendrick, M. M. Titirici, T. Meersmann and M. M. Britton, *Nat. Commun.*, 2020, 11, 2083.

Appendices:

Appendix 1:

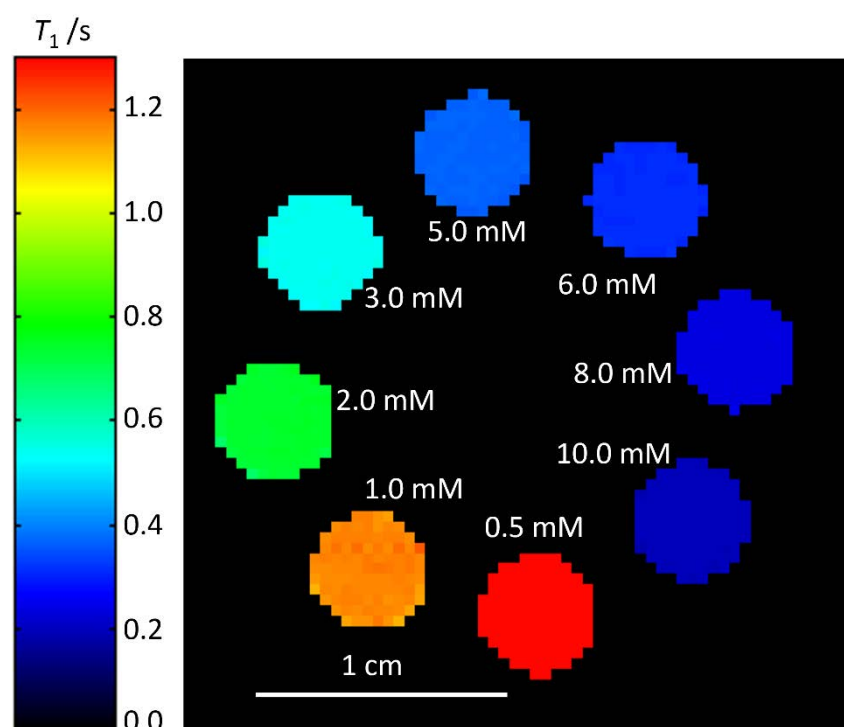


Figure A1.1: A ^1H T_1 magnetic resonance (MR) relaxation time map of a phantom of aqueous CuSO_4 over a range of concentrations acquired using inversion recovery (IR) methodology with 2 signal averages, a rapid acquisition with relaxation enhancement (RARE) factor of 1, and 1 echo image.

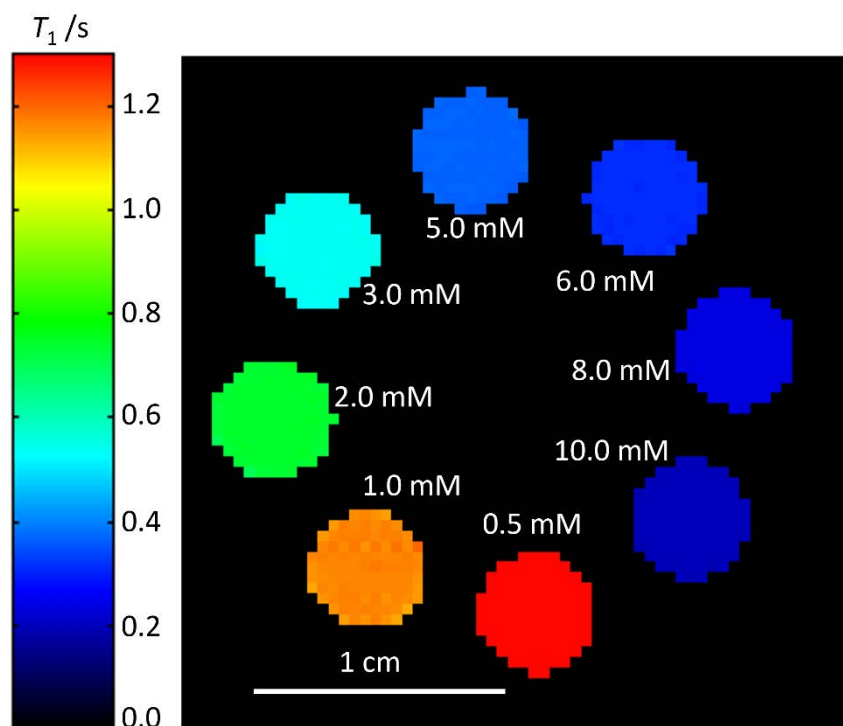


Figure A1.2: A ^1H T_1 MR relaxation time map of a phantom of aqueous CuSO_4 over a range of concentrations acquired using IR methodology with 2 signal averages, a RARE factor of 1, and 2 summed echo images.

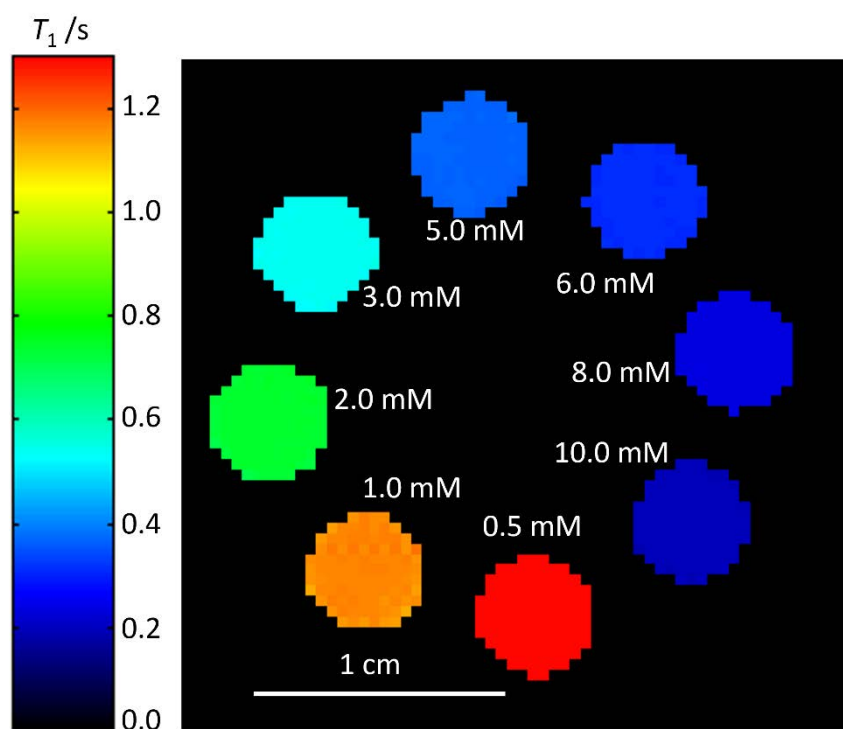


Figure A1.3: A ^1H T_1 MR relaxation time map of a phantom of aqueous CuSO_4 over a range of concentrations acquired using IR methodology with 2 signal averages, a RARE factor of 1, and 4 summed echo images.

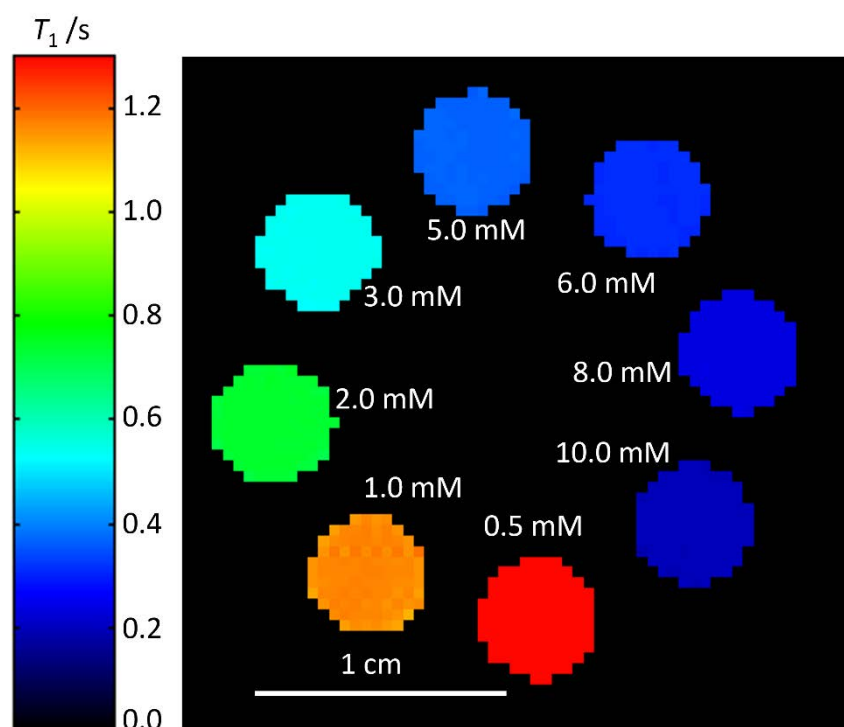


Figure A1.4: A ^1H T_1 MR relaxation time map of a phantom of aqueous CuSO_4 over a range of concentrations acquired using IR methodology with 2 signal averages, a RARE factor of 1, and 8 summed echo images.

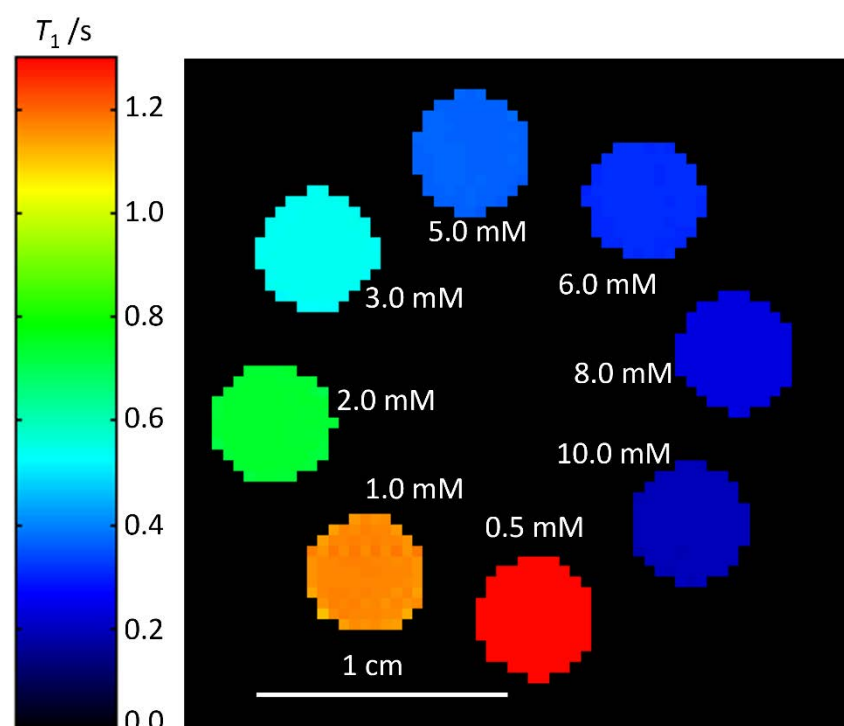


Figure A1.5: A ^1H T_1 MR relaxation time map of a phantom of aqueous CuSO_4 over a range of concentrations acquired using IR methodology with 2 signal averages, a RARE factor of 1, and 16 summed echo images.

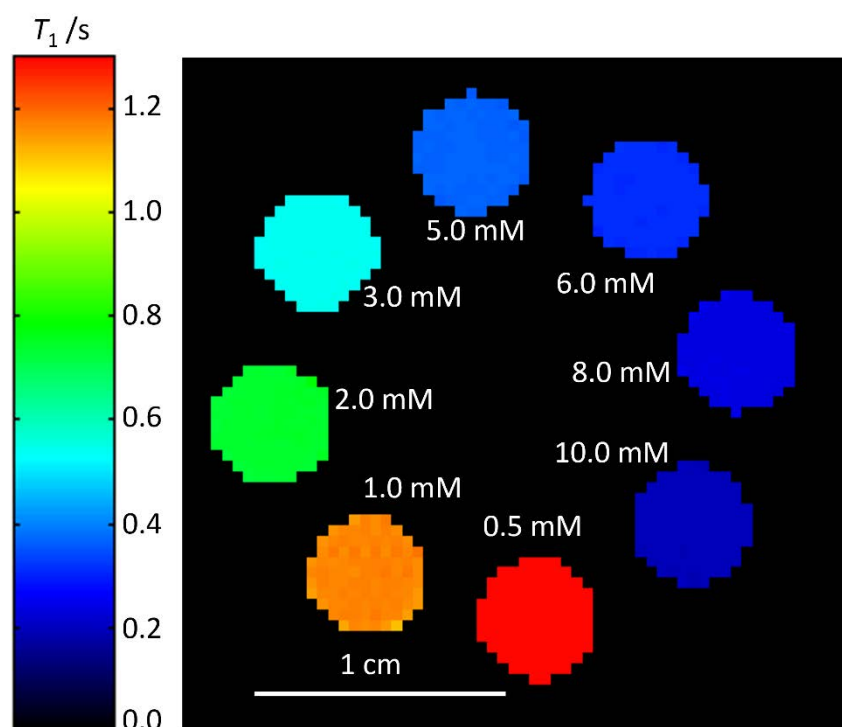


Figure A1.6: A ^1H T_1 MR relaxation time map of a phantom of aqueous CuSO_4 over a range of concentrations acquired using IR methodology with 4 signal averages, a RARE factor of 1 and 1 echo image.

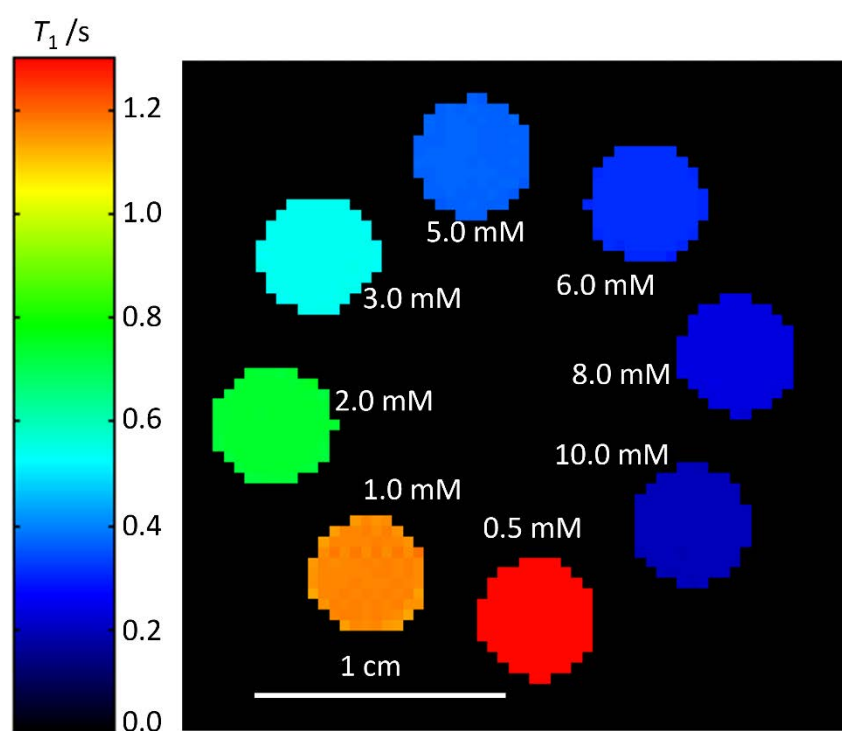


Figure A1.7: A ^1H T_1 MR relaxation time map of a phantom of aqueous CuSO_4 over a range of concentrations acquired using IR methodology with 4 signal averages, a RARE factor of 1, and 2 summed echo images.

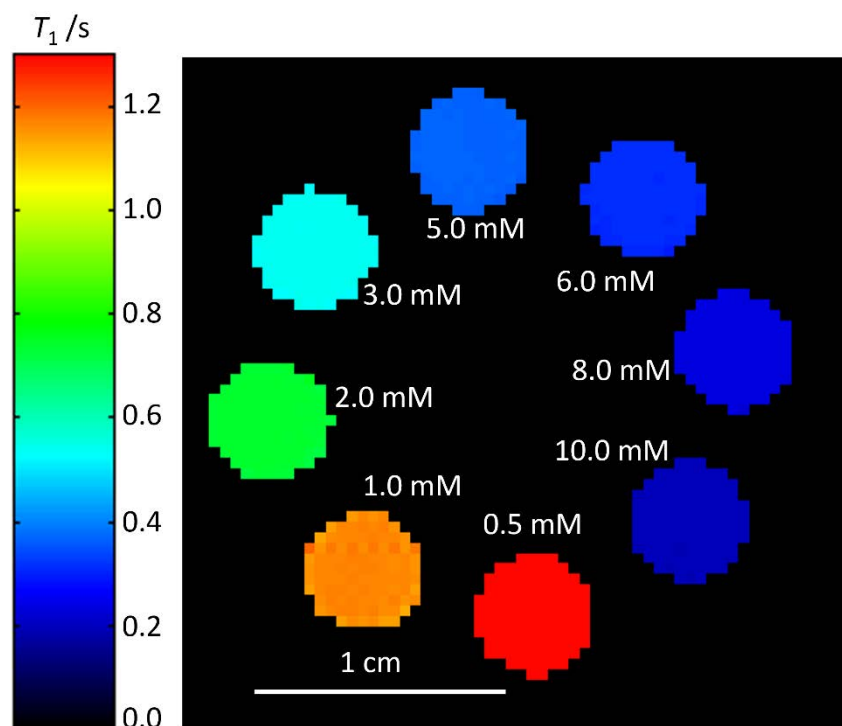


Figure A1.8: A ^1H T_1 MR relaxation time map of a phantom of aqueous CuSO_4 over a range of concentrations acquired using IR methodology with 4 signal averages, a RARE factor of 1 and 4 summed echo images.

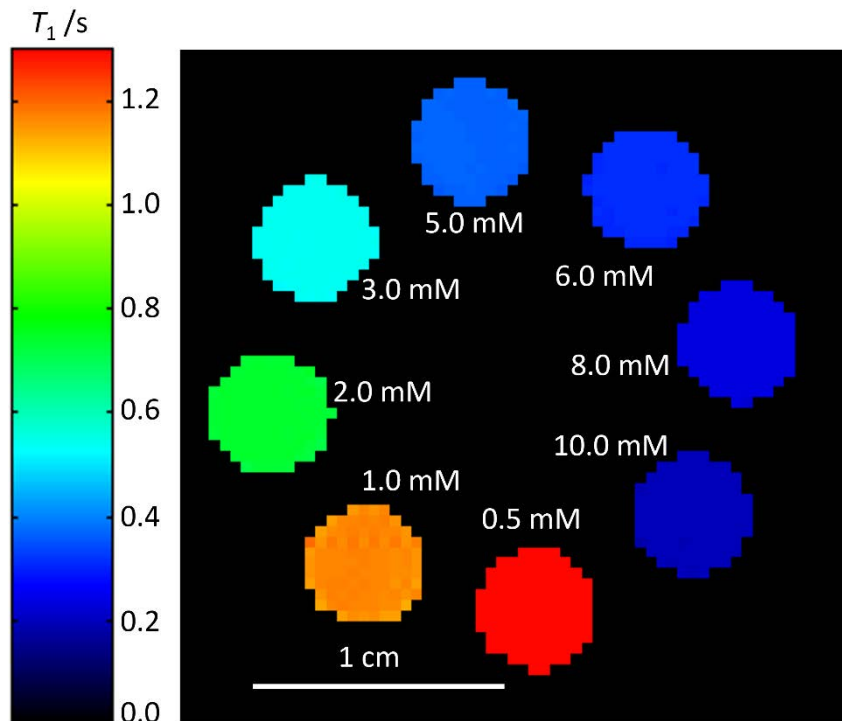


Figure A1.9: A ^1H T_1 MR relaxation time map of a phantom of aqueous CuSO_4 over a range of concentrations acquired using IR methodology with 4 signal averages, a RARE factor of 1, and 8 summed echo images.

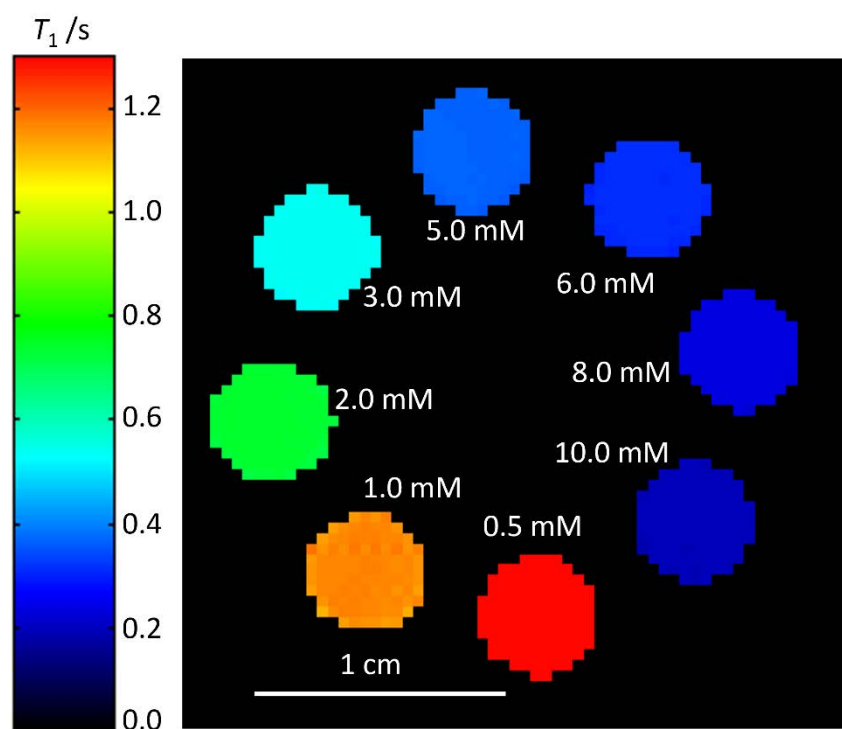


Figure A1.10: A ^1H T_1 MR relaxation time map of a phantom of aqueous CuSO_4 over a range of concentrations acquired using IR methodology with 4 signal averages, a RARE factor of 1 and 16 summed echo images.

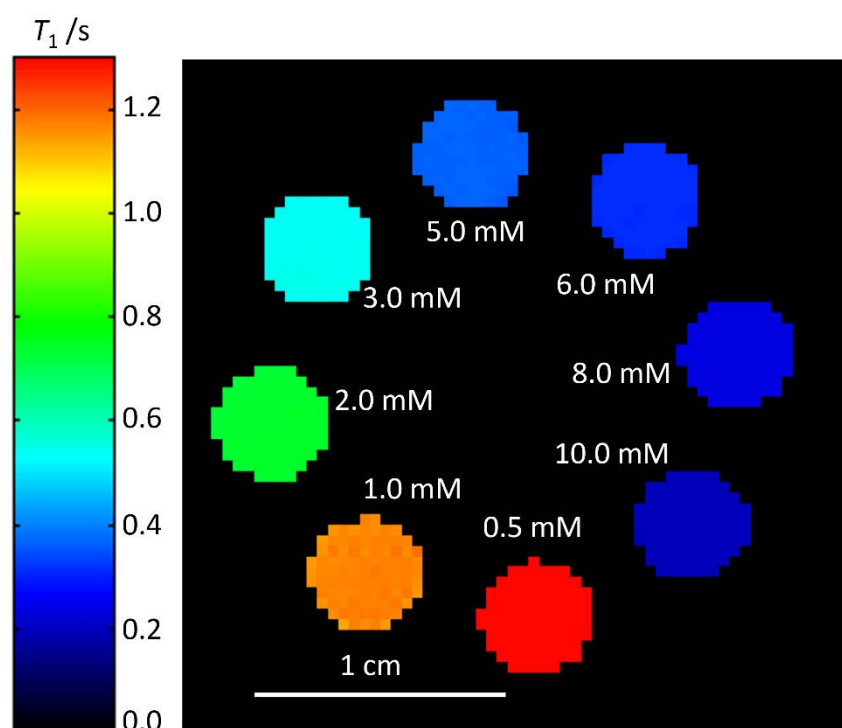


Figure A1.11: A ^1H T_1 MR relaxation time map of a phantom of aqueous CuSO_4 over a range of concentrations acquired using IR methodology with 8 signal averages, a RARE factor of 1, and 1 echo image.

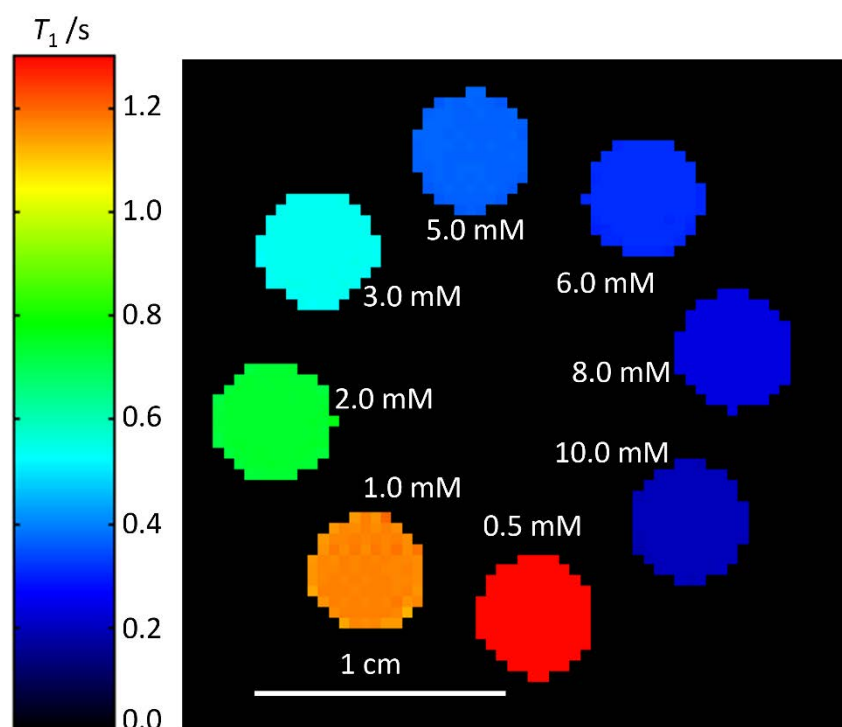


Figure A1.12: A ^1H T_1 MR relaxation time map of a phantom of aqueous CuSO_4 over a range of concentrations acquired using IR methodology with 8 signal averages, a RARE factor of 1, and 2 summed echo images.

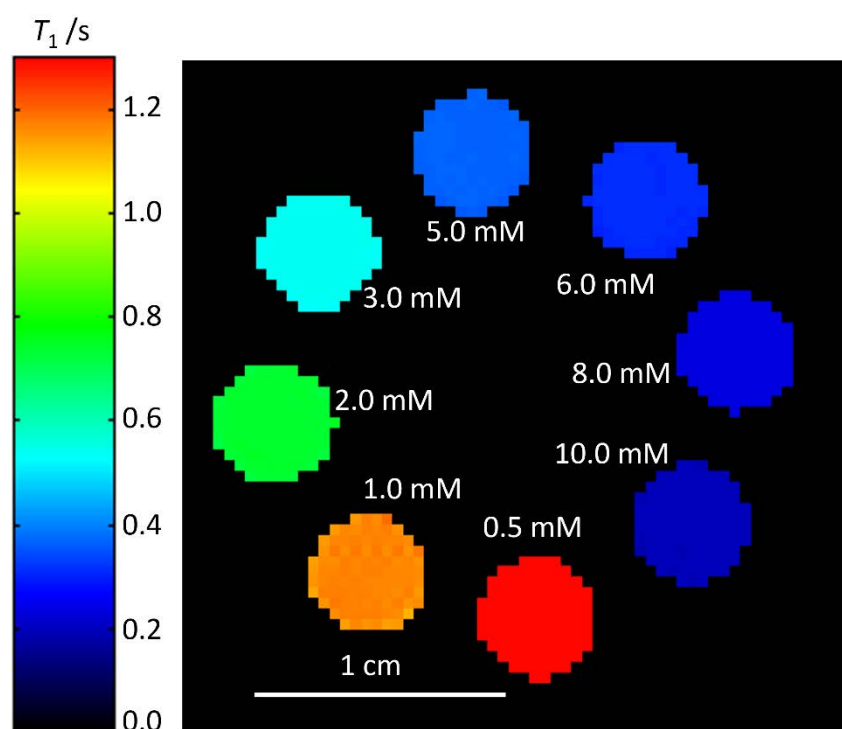


Figure A1.13: A ^1H T_1 MR relaxation time map of a phantom of aqueous CuSO_4 over a range of concentrations acquired using IR methodology with 8 signal averages, a RARE factor of 1, and 4 summed echo images.

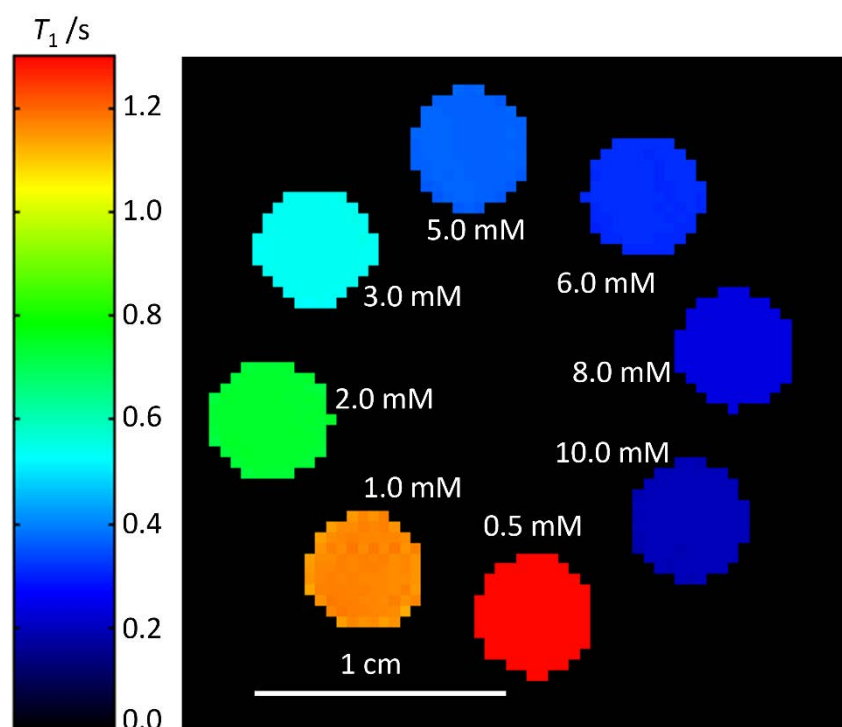


Figure A1.14: A ^1H T_1 MR relaxation time map of a phantom of aqueous CuSO_4 over a range of concentrations acquired using IR methodology with 8 signal averages, a RARE factor of 1, and 8 summed echo images.

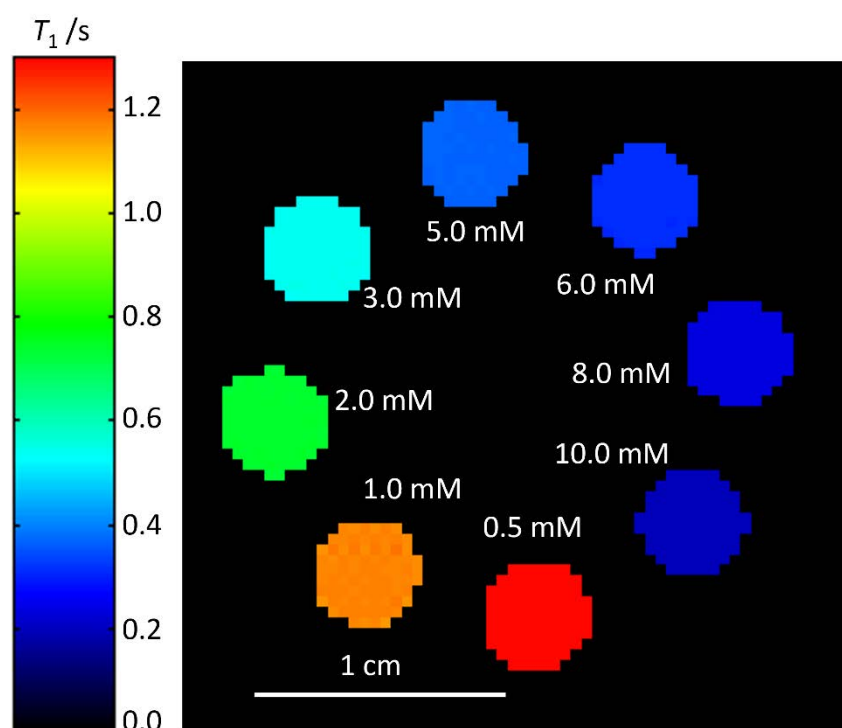


Figure A1.15: A ^1H T_1 MR relaxation time map of a phantom of aqueous CuSO_4 over a range of concentrations acquired using IR methodology with 8 signal averages, a RARE factor of 1, and 16 summed echo images.

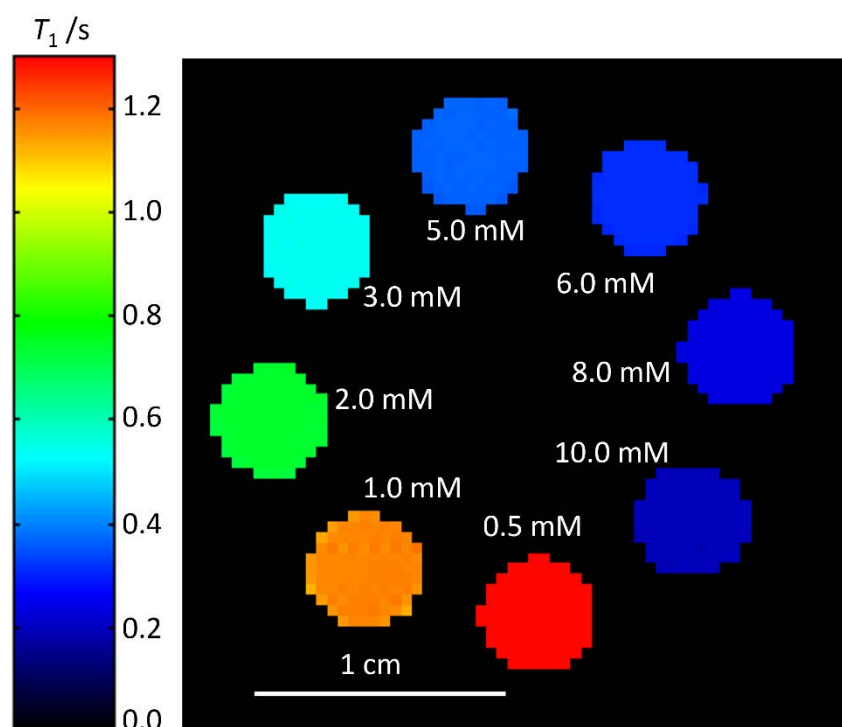


Figure A1.16: A ^1H T_1 MR relaxation time map of a phantom of aqueous CuSO_4 over a range of concentrations acquired using IR methodology with 16 signal averages, a RARE factor of 1, and 1 echo image.

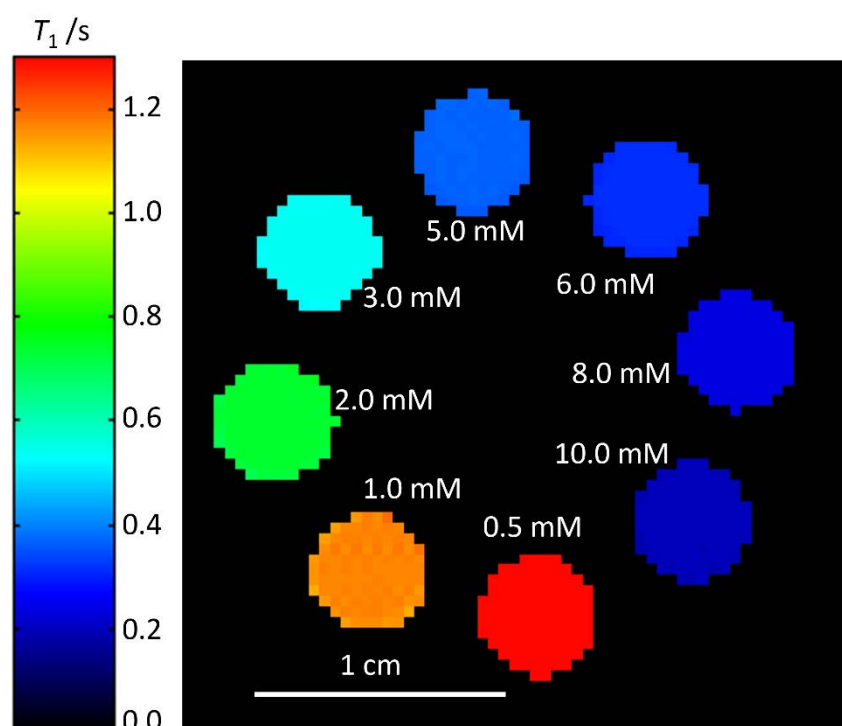


Figure A1.17: A ^1H T_1 MR relaxation time map of a phantom of aqueous CuSO_4 over a range of concentrations acquired using IR methodology with 16 signal averages, a RARE factor of 1, and 2 summed echo images.

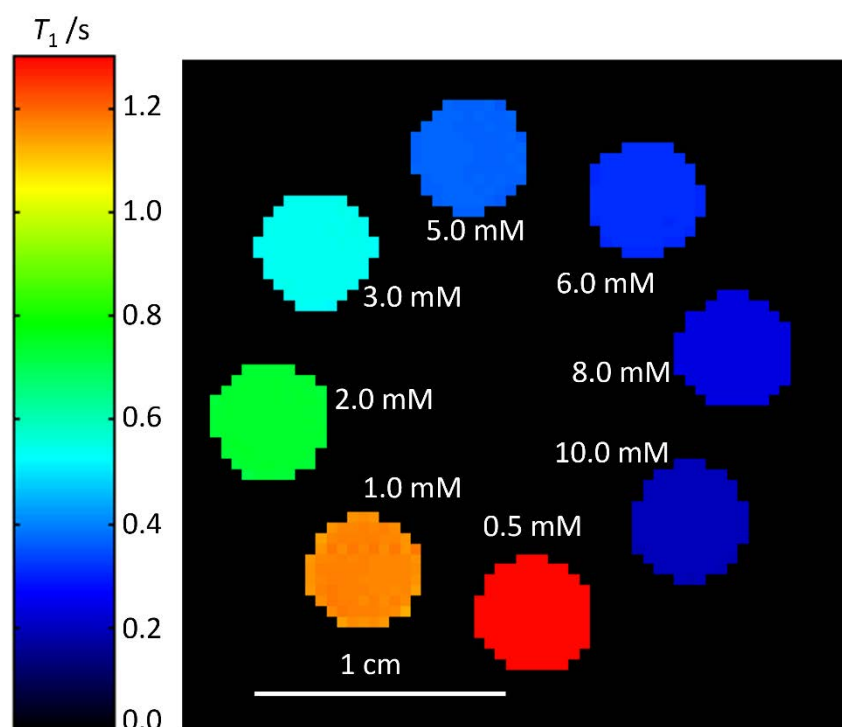


Figure A1.18: A ^1H T_1 MR relaxation time map of a phantom of aqueous CuSO_4 over a range of concentrations acquired using IR methodology with 16 signal averages, a RARE factor of 1, and 4 summed echo images.

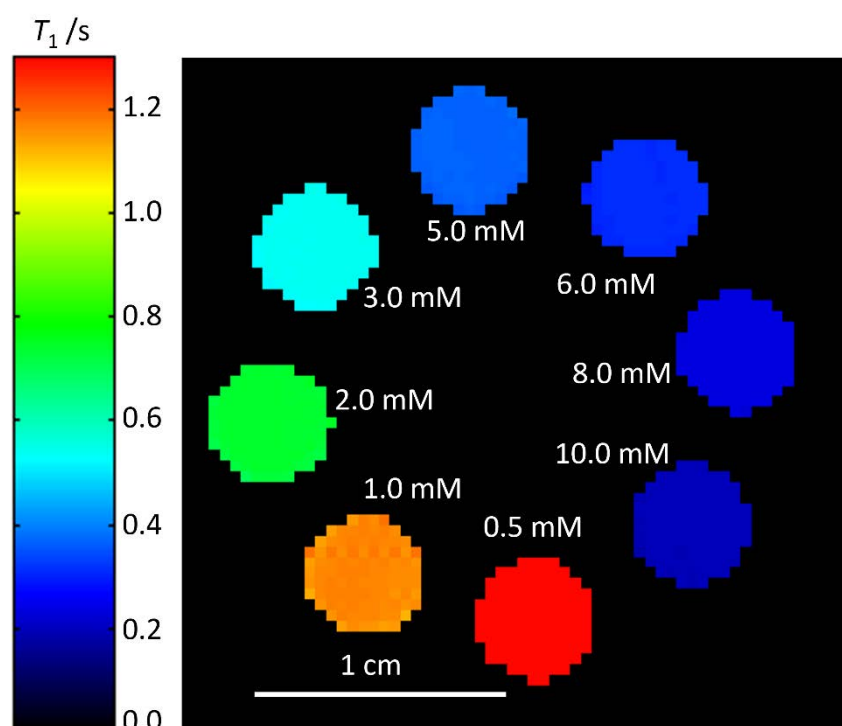


Figure A1.19: A ^1H T_1 MR relaxation time map of a phantom of aqueous CuSO_4 over a range of concentrations acquired using IR methodology with 16 signal averages, a RARE factor of 1, and 8 summed echo images.

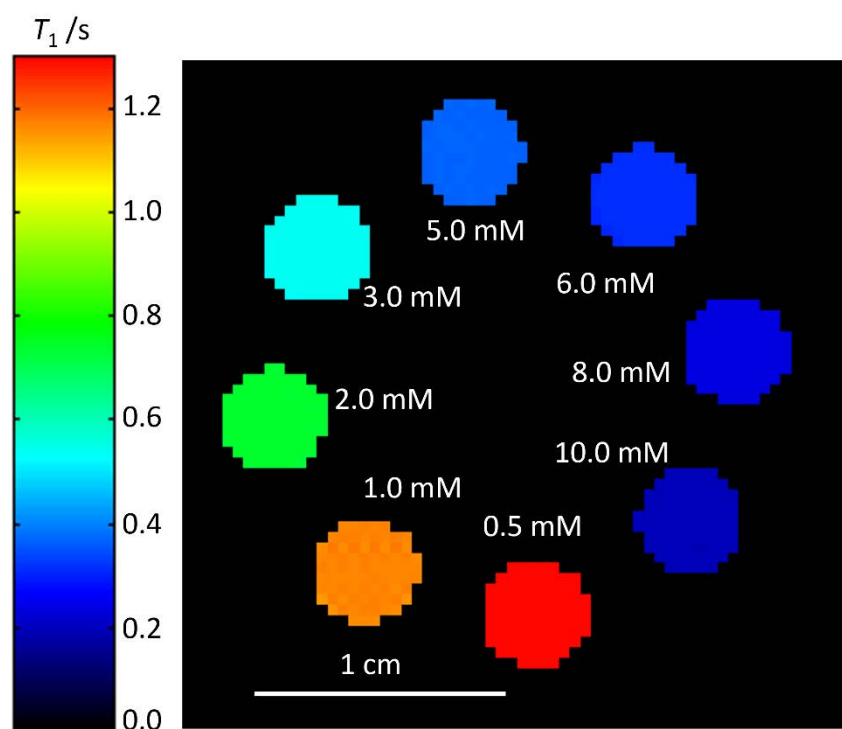


Figure A1.20: A ^1H T_1 MR relaxation time map of a phantom of aqueous CuSO_4 over a range of concentrations acquired using IR methodology with 16 signal averages, a RARE factor of 1, and 16 summed echo images.

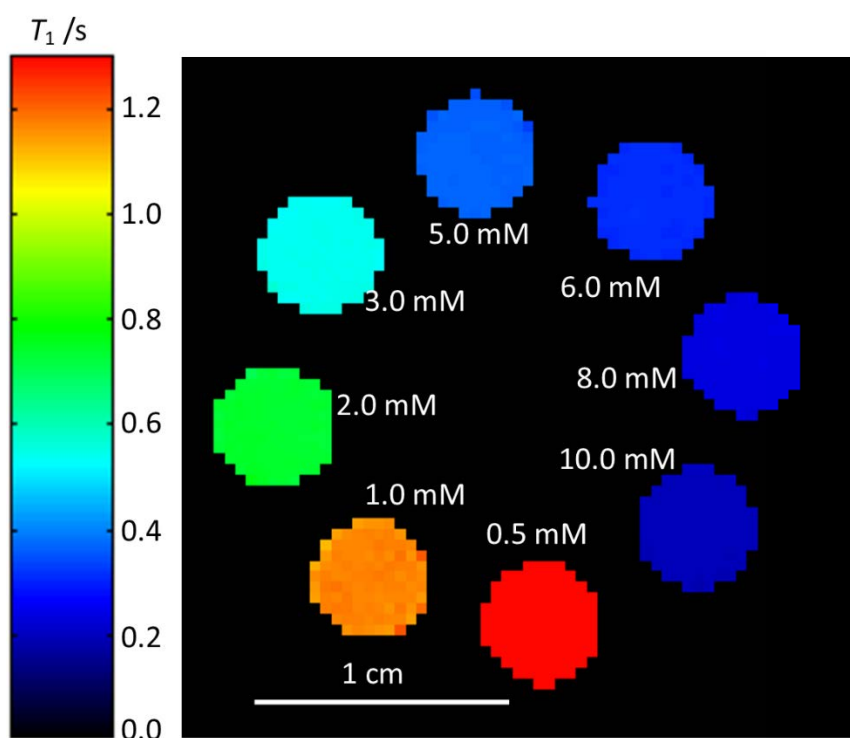


Figure A1.21: A ^1H T_1 MR relaxation time map of a phantom of aqueous CuSO_4 over a range of concentrations acquired using IR methodology with 2 signal averages, a RARE factor of 4, and 1 echo image.

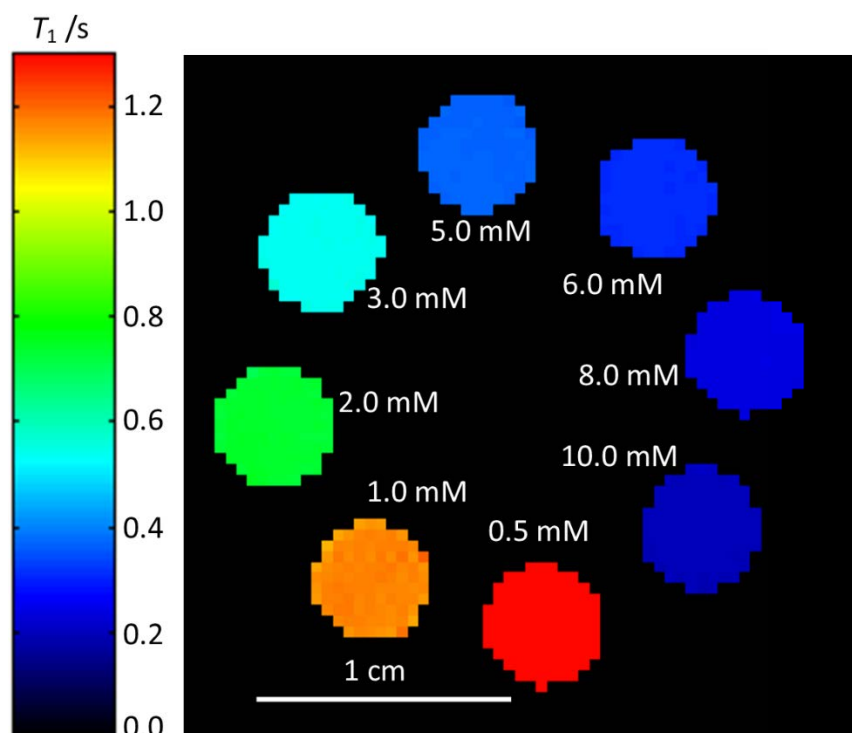


Figure A1.22: A ^1H T_1 MR relaxation time map of a phantom of aqueous CuSO_4 over a range of concentrations acquired using IR methodology with 2 signal averages, a RARE factor of 4, and 2 summed echo images.

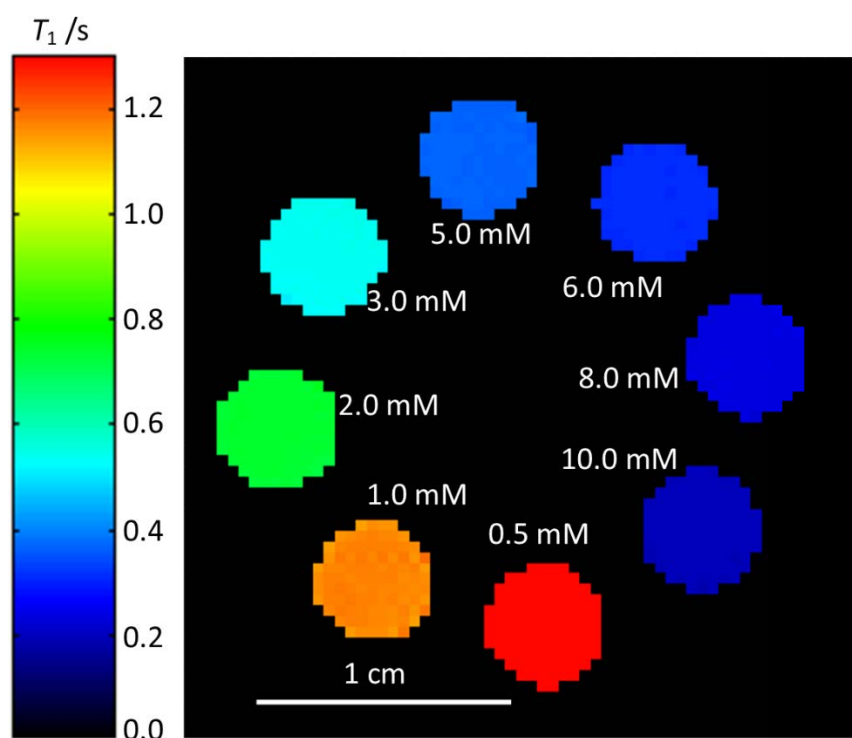


Figure A1.23: A ^1H T_1 MR relaxation time map of a phantom of aqueous CuSO_4 over a range of concentrations acquired using IR methodology with 2 signal averages, a RARE factor of 4, and 4 summed echo images.

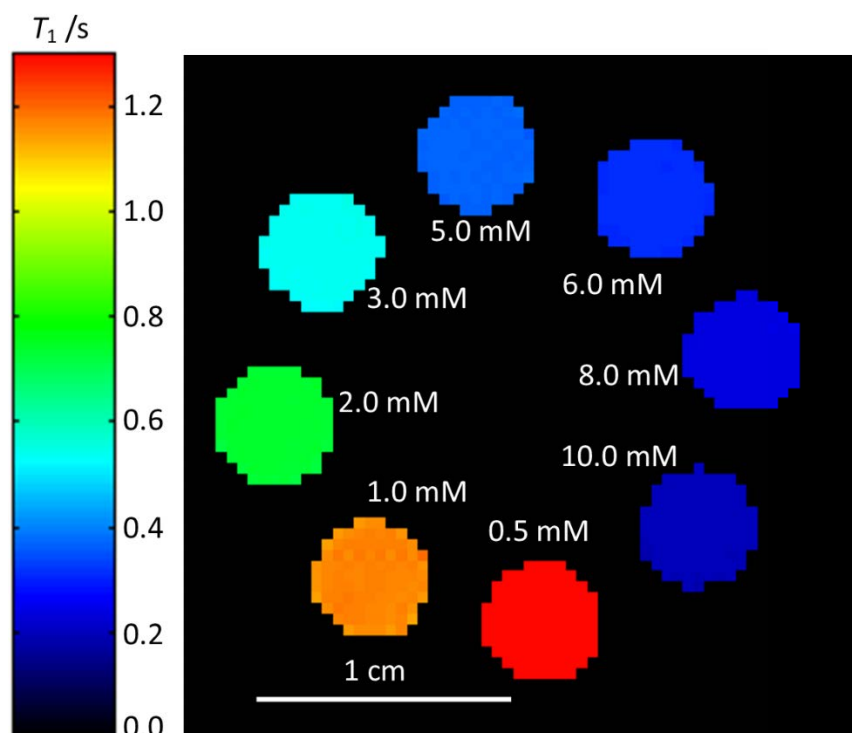


Figure A1.24: A ^1H T_1 MR relaxation time map of a phantom of aqueous CuSO_4 over a range of concentrations acquired using IR methodology with 2 signal averages, a RARE factor of 4, and 8 summed echo images.

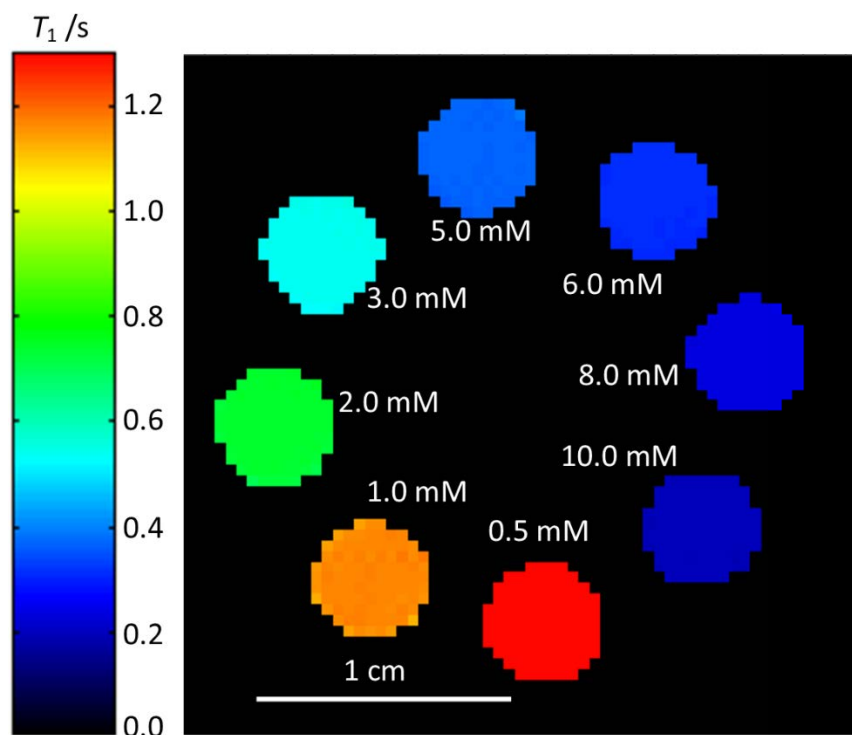


Figure A1.25: A ^1H T_1 MR relaxation time map of a phantom of aqueous CuSO_4 over a range of concentrations acquired using IR methodology with 2 signal averages, a RARE factor of 4, and 16 summed echo images.

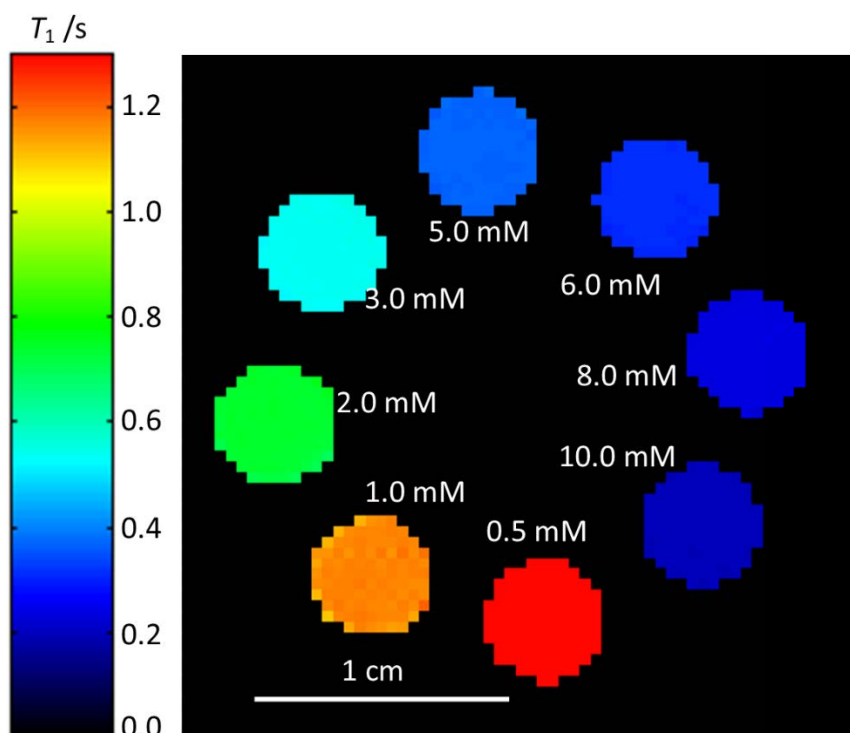


Figure A1.26: A ^1H T_1 MR relaxation time map of a phantom of aqueous CuSO_4 over a range of concentrations acquired using IR methodology with 4 signal averages, a RARE factor of 4, and 1 echo image.

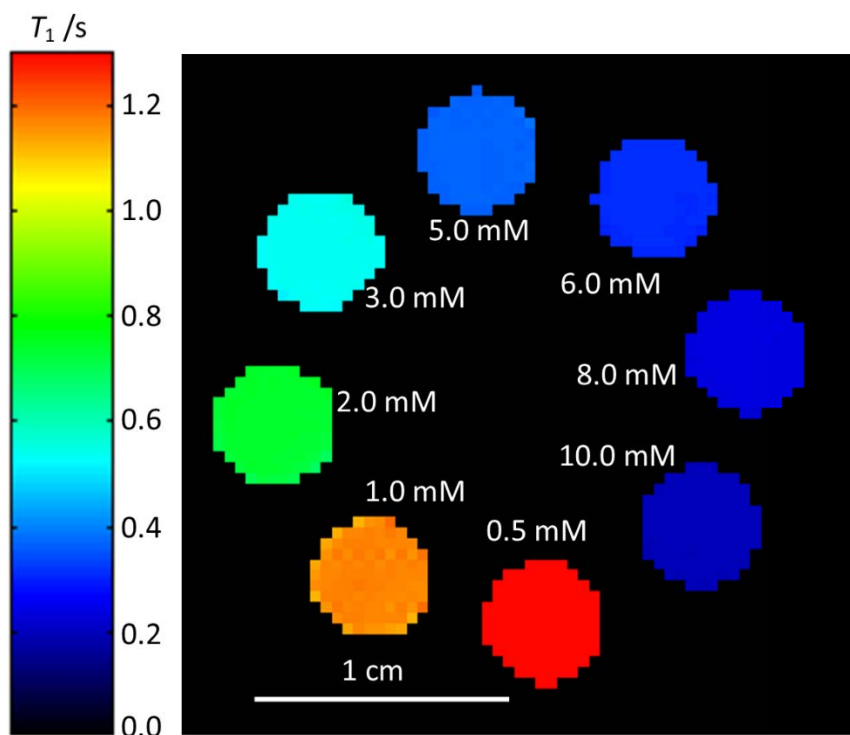


Figure A1.27: A ^1H T_1 MR relaxation time map of a phantom of aqueous CuSO_4 over a range of concentrations acquired using IR methodology with 4 signal averages, a RARE factor of 4, and 2 summed echo images.

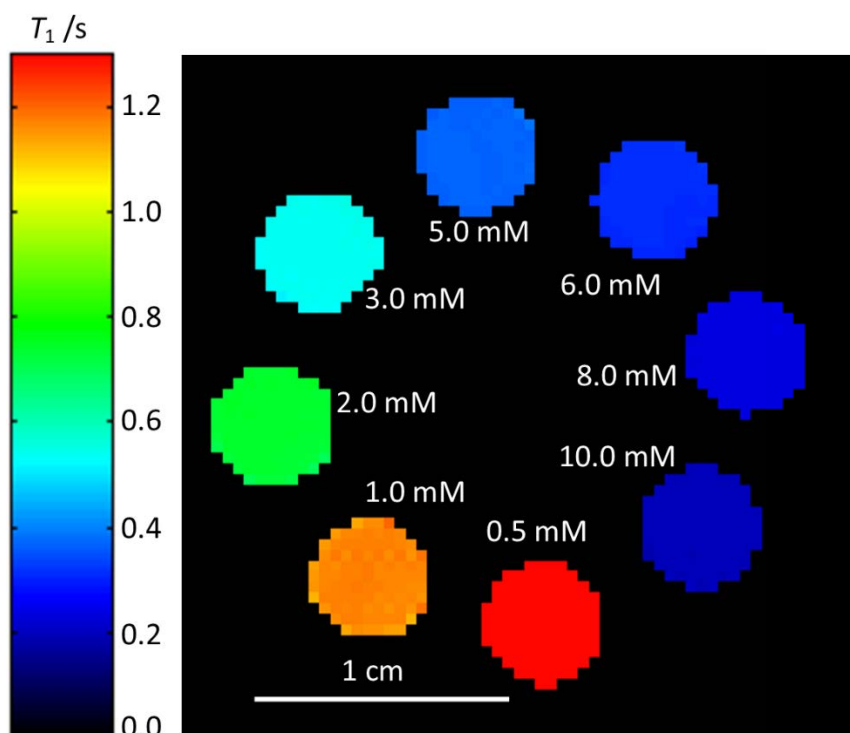


Figure A1.28: A ^1H T_1 MR relaxation time map of a phantom of aqueous CuSO_4 over a range of concentrations acquired using IR methodology with 4 signal averages, a RARE factor of 4, and 4 summed echo images.

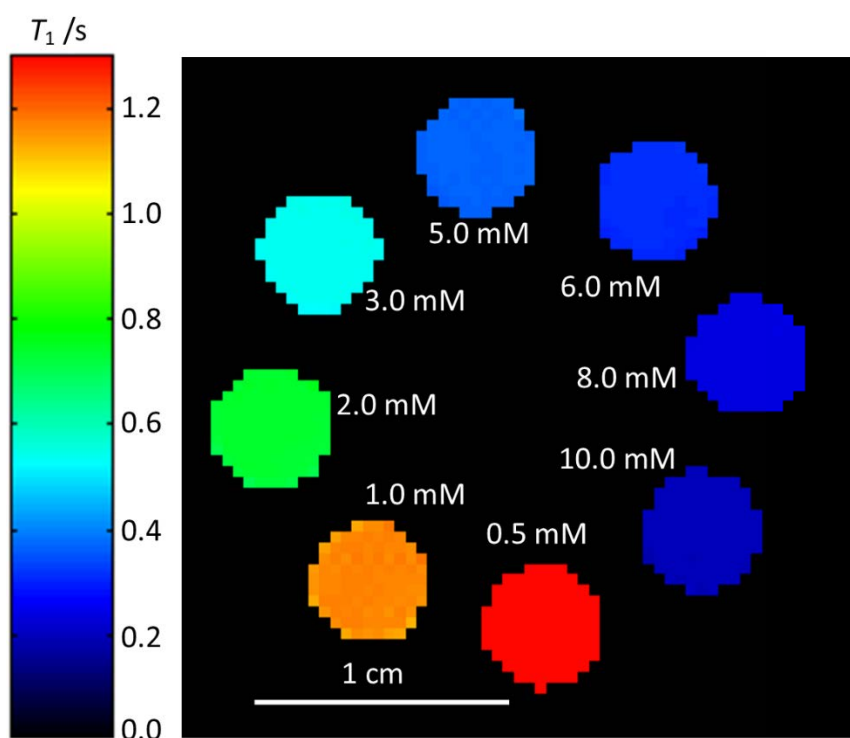


Figure A1.29: A ^1H T_1 MR relaxation time map of a phantom of aqueous CuSO_4 over a range of concentrations acquired using IR methodology with 4 signal averages, a RARE factor of 4, and 8 summed echo images.

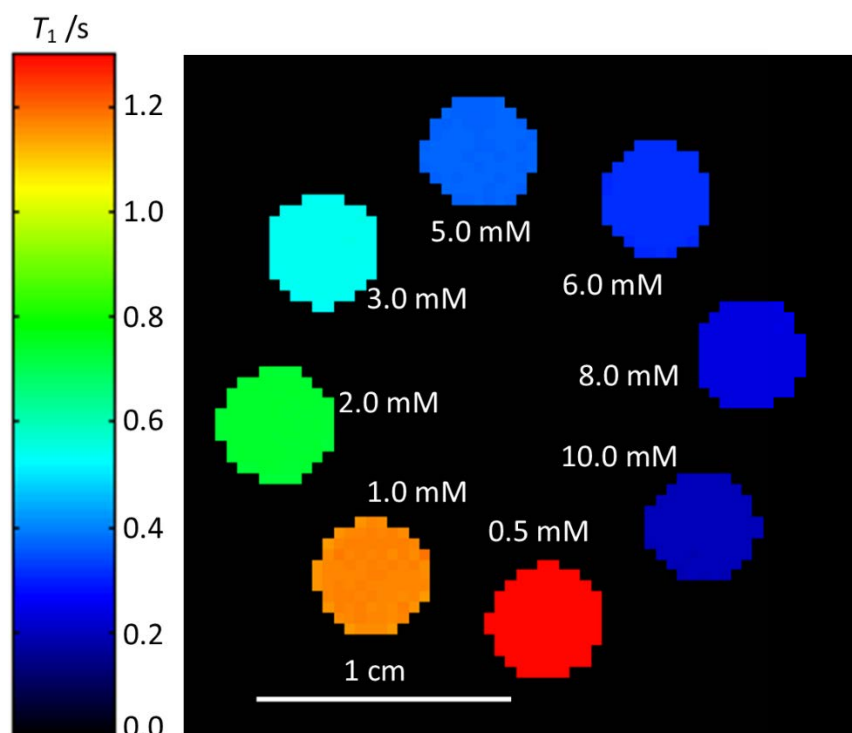


Figure A1.30: A ^1H T_1 MR relaxation time map of a phantom of aqueous CuSO_4 over a range of concentrations acquired using IR methodology with 4 signal averages, a RARE factor of 4, and 16 summed echo images.

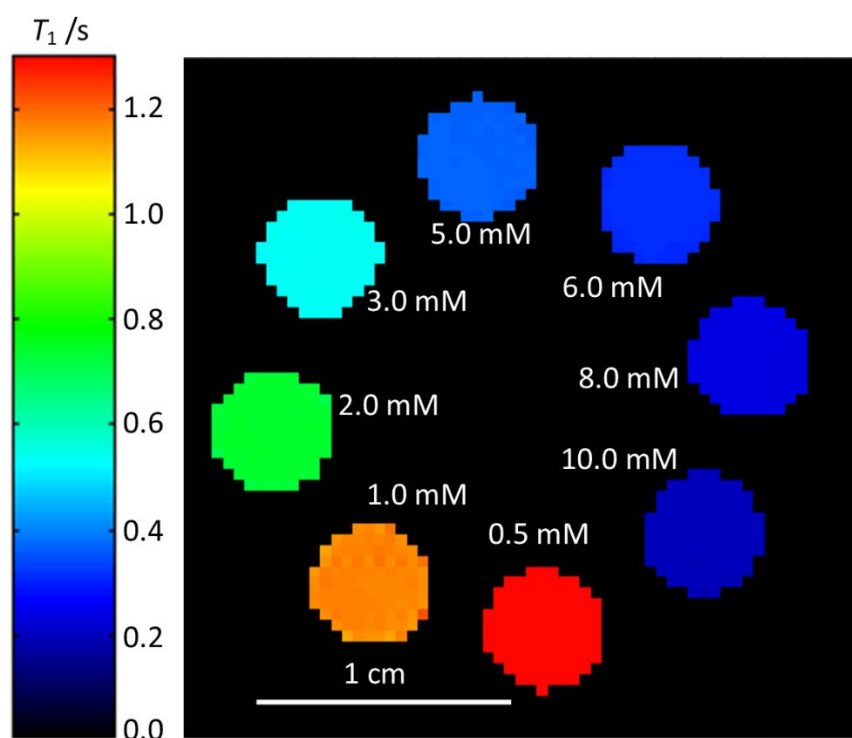


Figure A1.31: A ^1H T_1 MR relaxation time map of a phantom of aqueous CuSO_4 over a range of concentrations acquired using IR methodology with 8 signal averages, a RARE factor of 4, and 1 echo image.

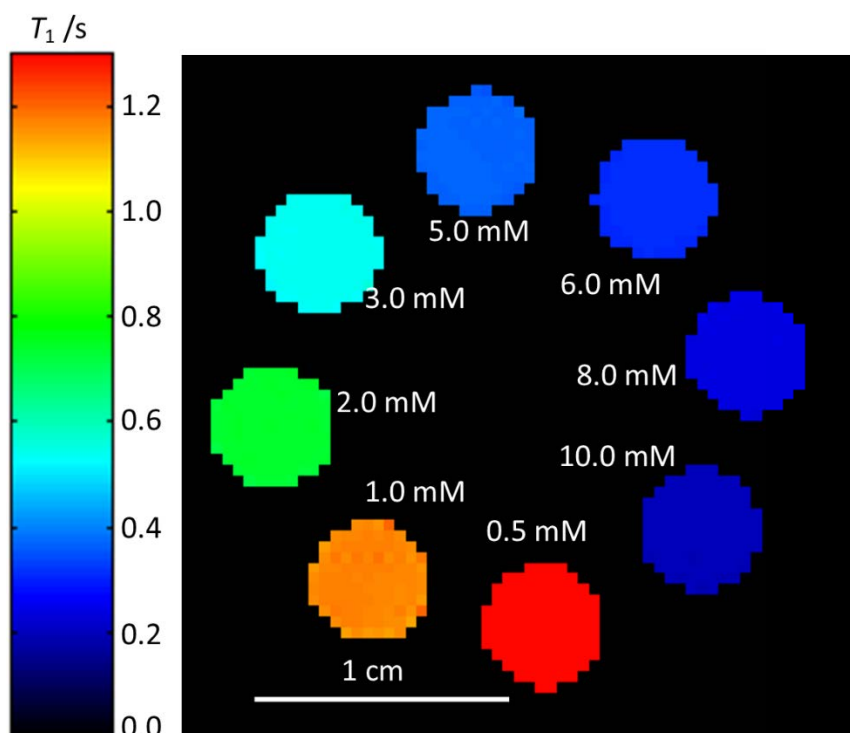


Figure A1.31: A ^1H T_1 MR relaxation time map of a phantom of aqueous CuSO_4 over a range of concentrations acquired using IR methodology with 8 signal averages, a RARE factor of 4, and 2 summed echo images.

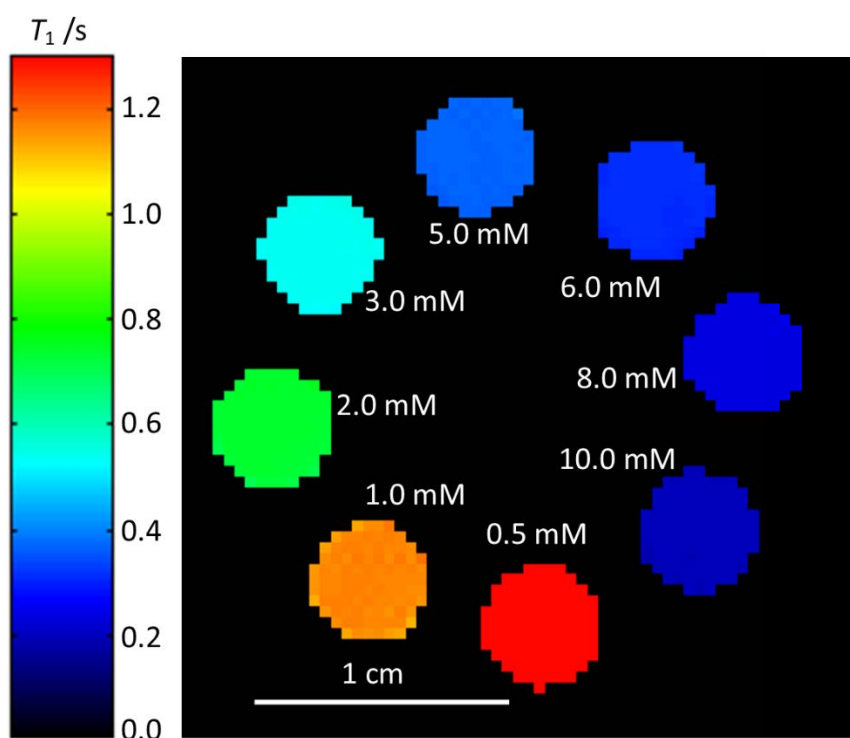


Figure A1.32: A ^1H T_1 MR relaxation time map of a phantom of aqueous CuSO_4 over a range of concentrations acquired using IR methodology with 8 signal averages, a RARE factor of 4, and 4 summed echo images.

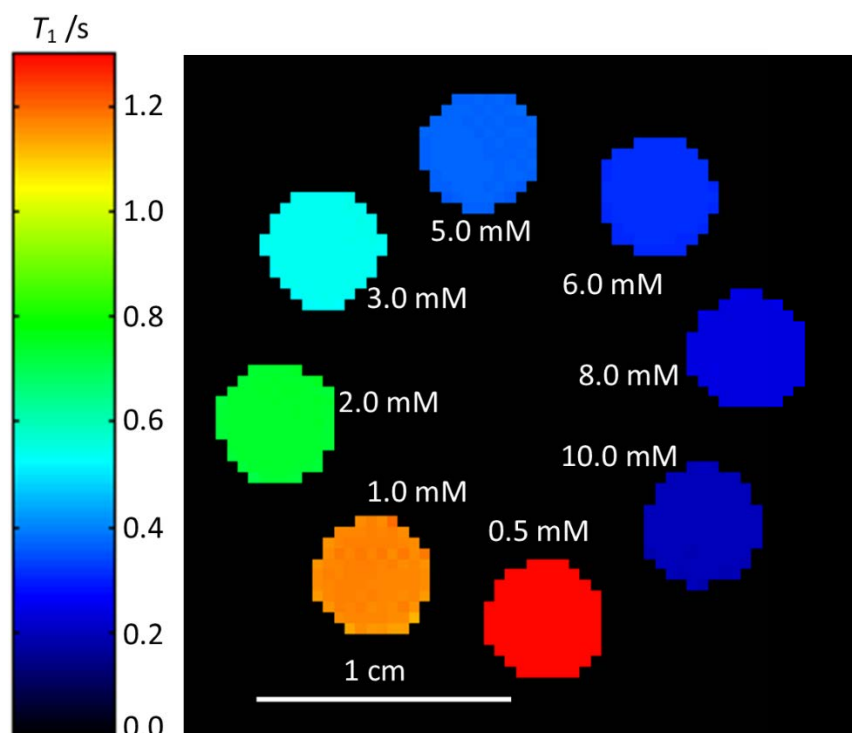


Figure A1.33: A ^1H T_1 MR relaxation time map of a phantom of aqueous CuSO_4 over a range of concentrations acquired using IR methodology with 8 signal averages, a RARE factor of 4, and 8 summed echo images.

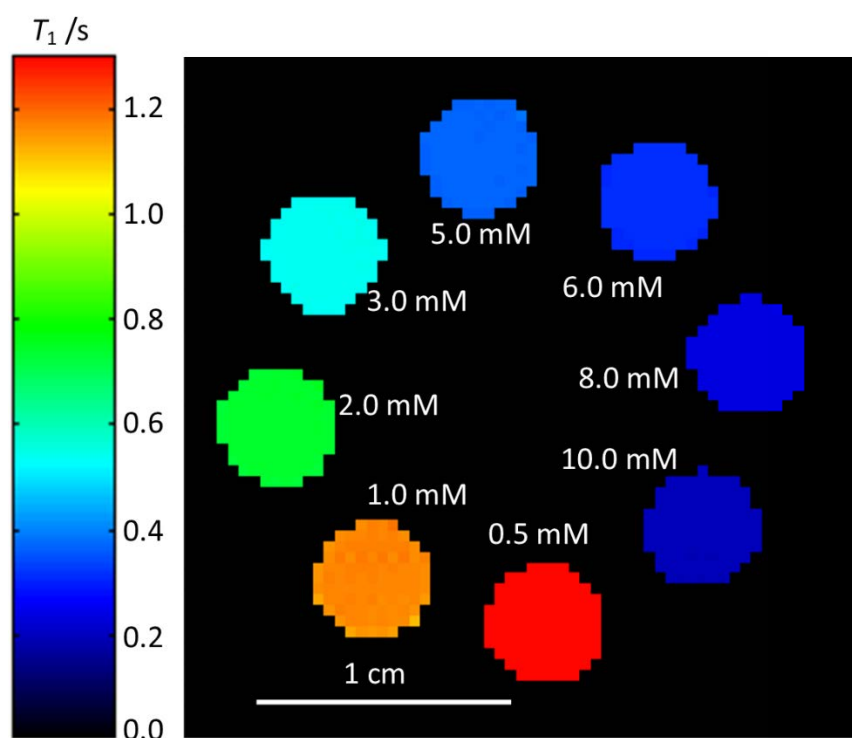


Figure A1.34: A ^1H T_1 MR relaxation time map of a phantom of aqueous CuSO_4 over a range of concentrations acquired using IR methodology with 8 signal averages, a RARE factor of 4, and 16 summed echo images.

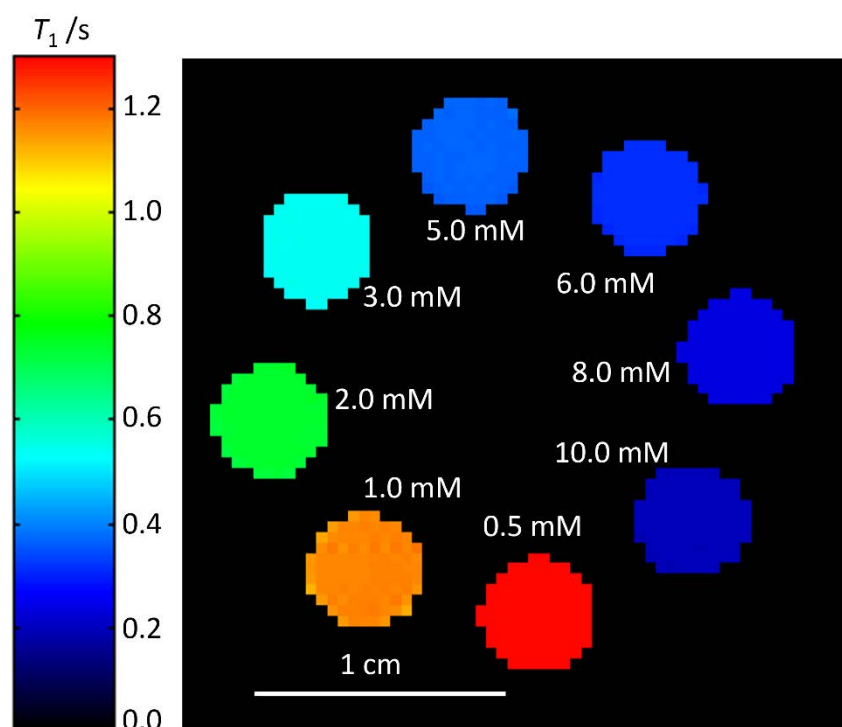


Figure A1.35: A ^1H T_1 MR relaxation time map of a phantom of aqueous CuSO_4 over a range of concentrations acquired using IR methodology with 16 signal averages, a RARE factor of 4, and 1 echo image.

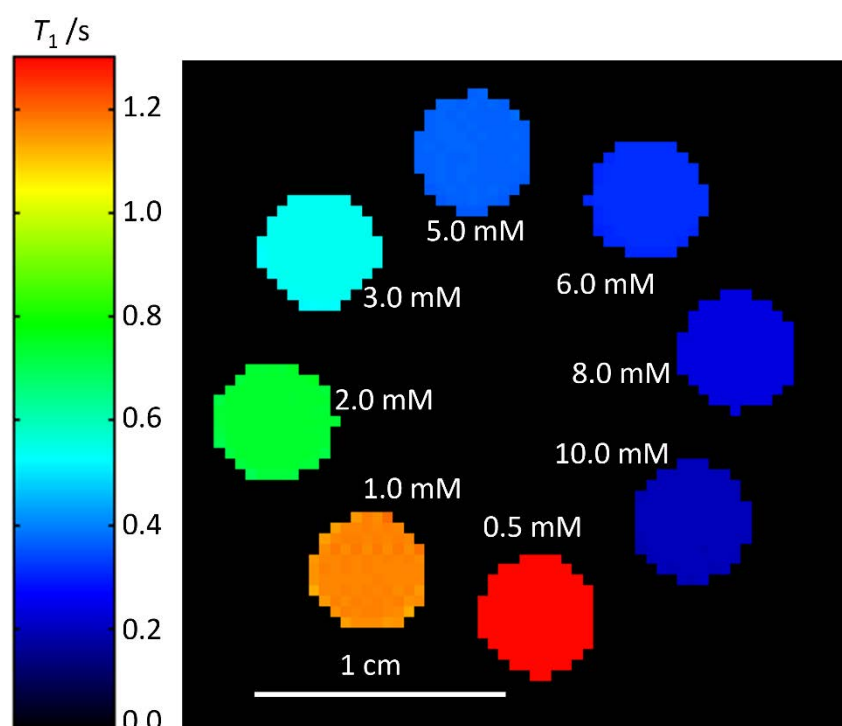


Figure A1.36: A ^1H T_1 MR relaxation time map of a phantom of aqueous CuSO_4 over a range of concentrations acquired using IR methodology with 16 signal averages, a RARE factor of 4, and 2 summed echo images.

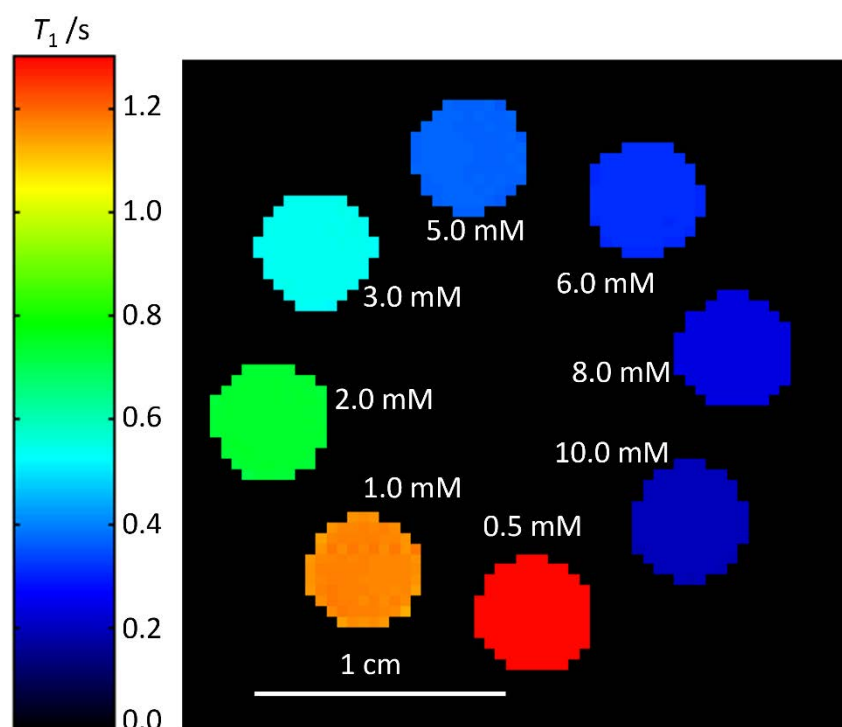


Figure A1.37: A ^1H T_1 MR relaxation time map of a phantom of aqueous CuSO_4 over a range of concentrations acquired using IR methodology with 16 signal averages, a RARE factor of 4, and 4 summed echo images.

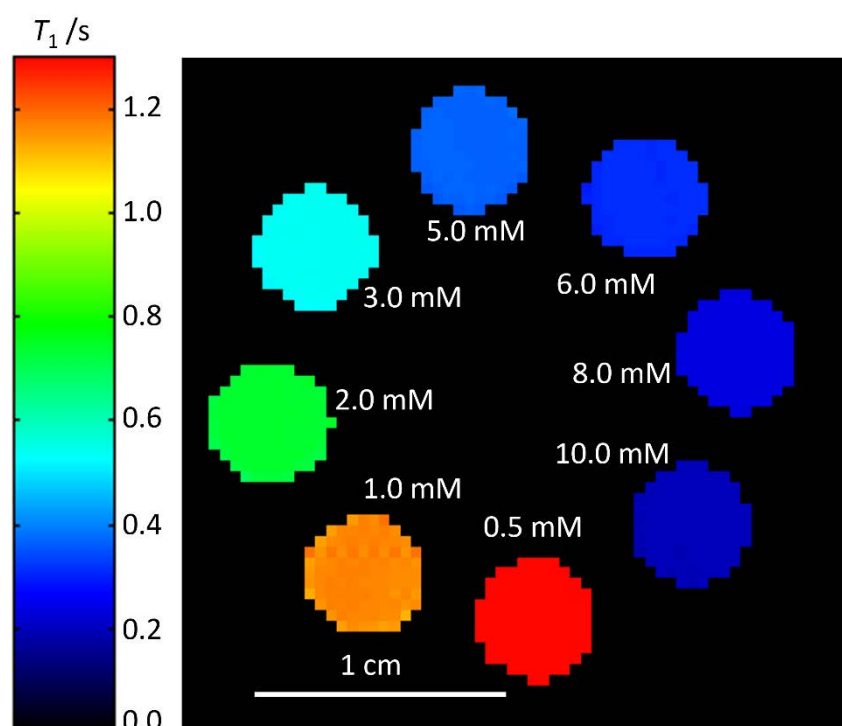


Figure A1.38: A ^1H T_1 MR relaxation time map of a phantom of aqueous CuSO_4 over a range of concentrations acquired using IR methodology with 16 signal averages, a RARE factor of 4, and 8 summed echo images.

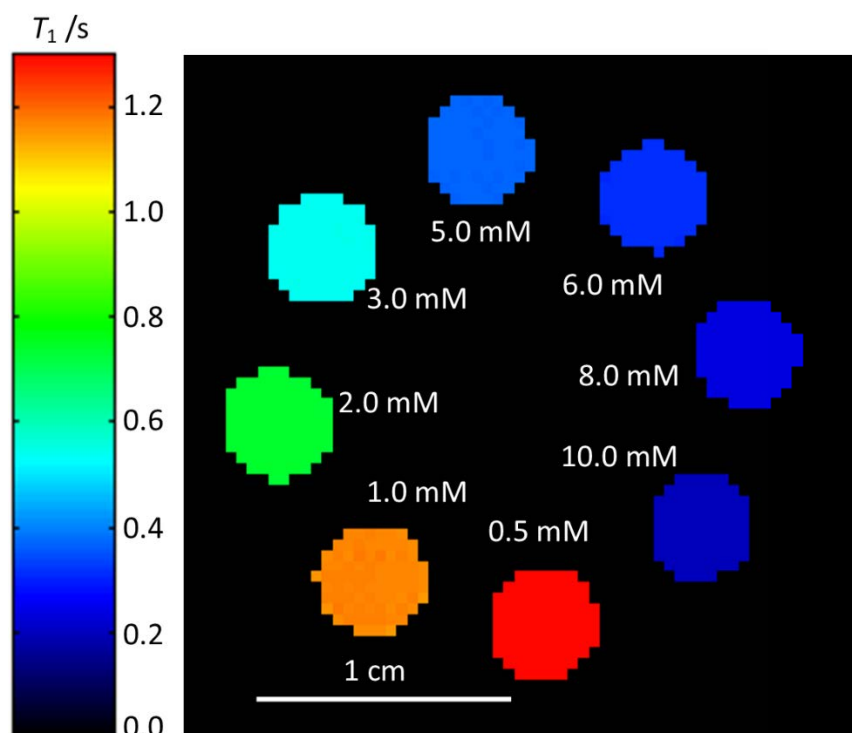


Figure A1.39: A ^1H T_1 MR relaxation time map of a phantom of aqueous CuSO_4 over a range of concentrations acquired using IR methodology with 16 signal averages, a RARE factor of 4, and 16 summed echo images.

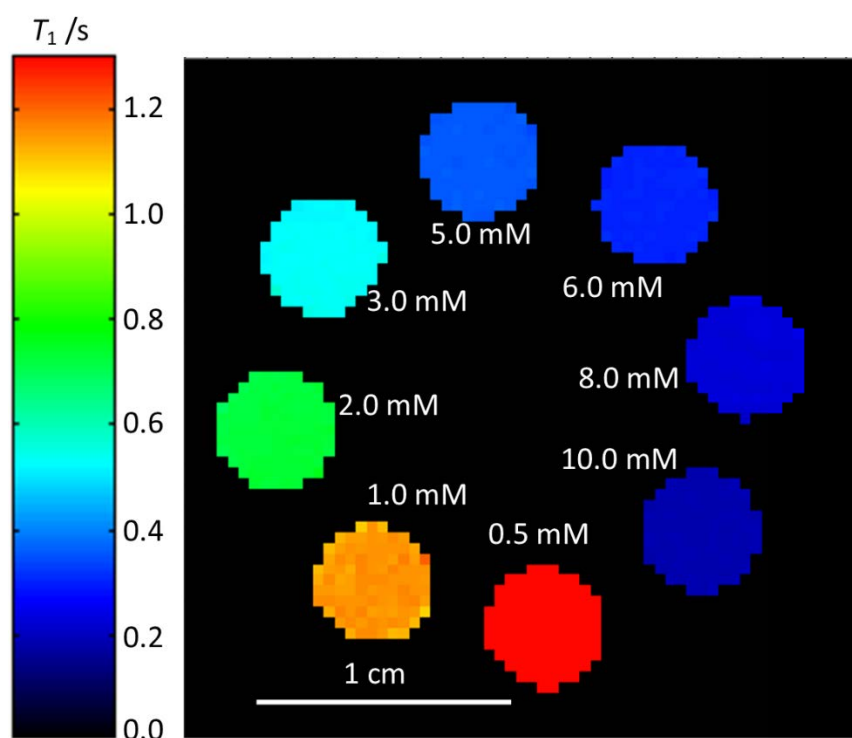


Figure A1.40: A ^1H T_1 MR relaxation time map of a phantom of aqueous CuSO_4 over a range of concentrations acquired using saturation recovery (SR) methodology with 2 signal averages, a RARE factor of 1, and 1 echo image.

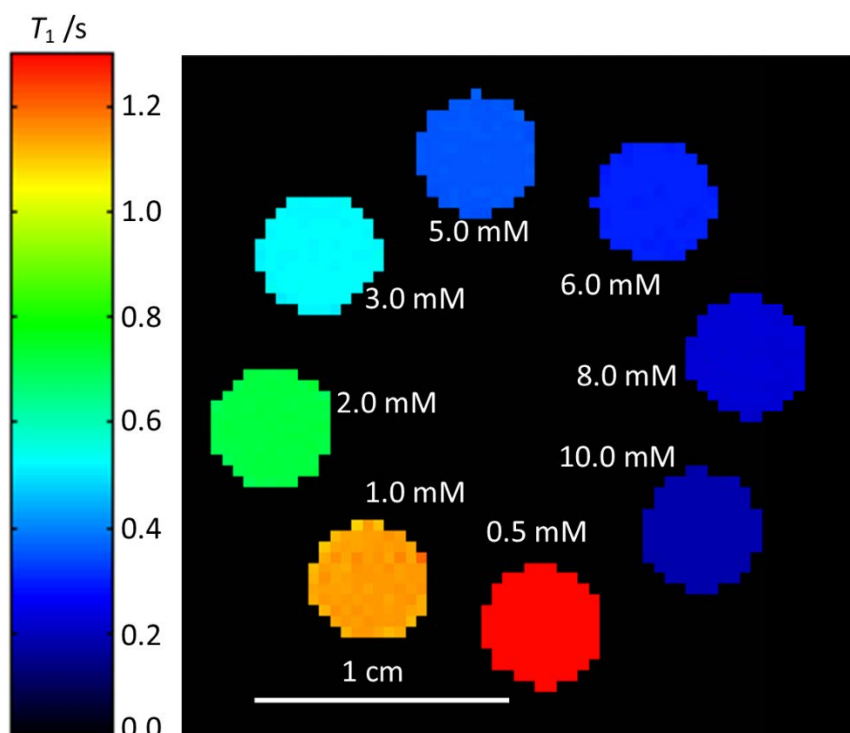


Figure A1.41: A ^1H T_1 MR relaxation time map of a phantom of aqueous CuSO_4 over a range of concentrations acquired using SR methodology with 2 signal averages, a RARE factor of 1, and 2 summed echo images.

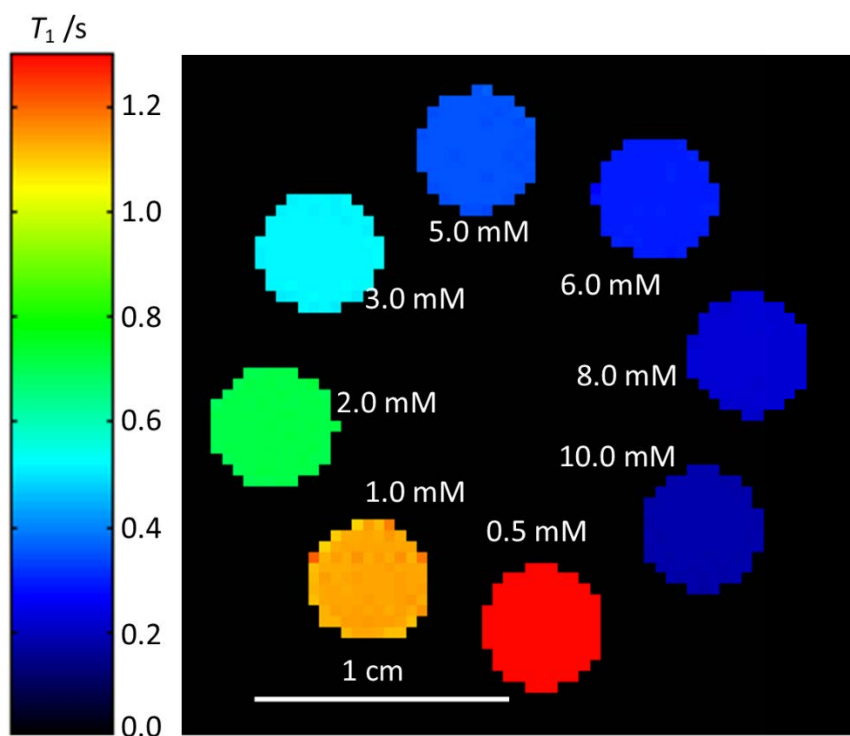


Figure A1.42: A ^1H T_1 MR relaxation time map of a phantom of aqueous CuSO_4 over a range of concentrations acquired using SR methodology with 2 signal averages, a RARE factor of 1, and 4 summed echo images.

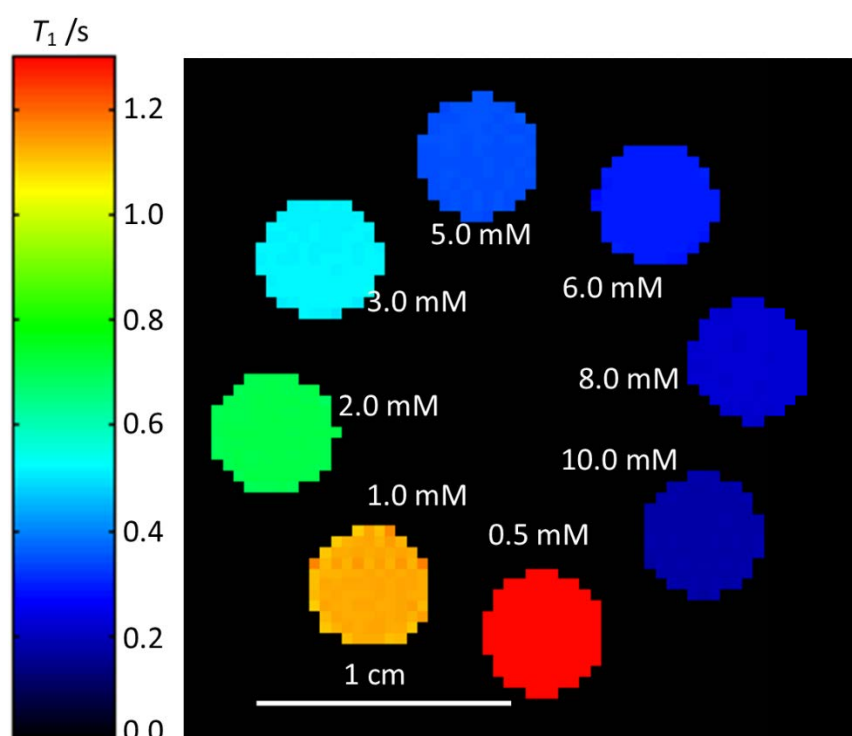


Figure A1.43: A ^1H T_1 MR relaxation time map of a phantom of aqueous CuSO_4 over a range of concentrations acquired using SR methodology with 2 signal averages, a RARE factor of 1, and 8 summed echo images.

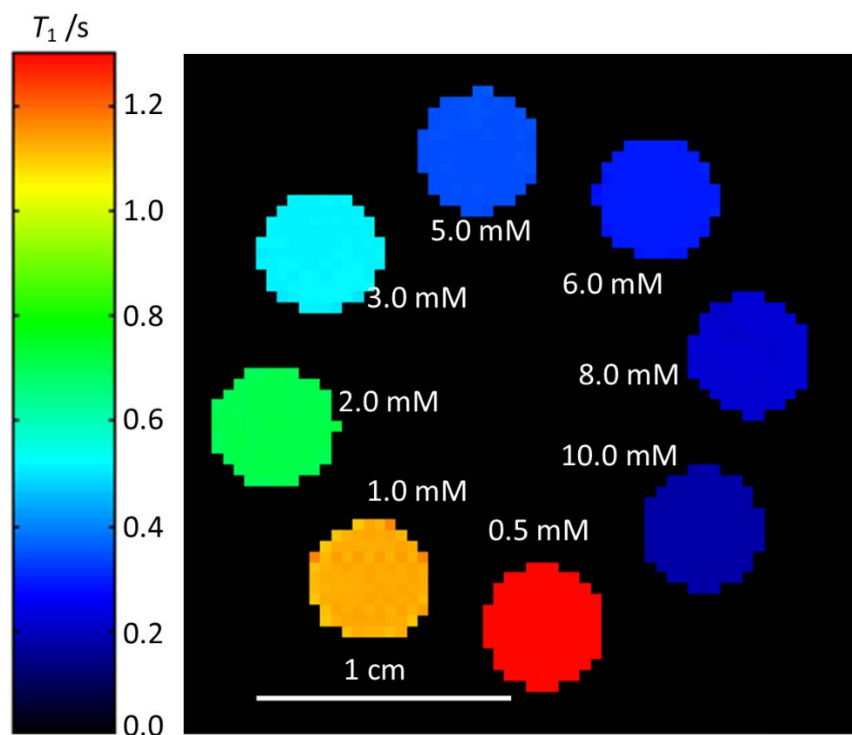


Figure A1.44: A ^1H T_1 MR relaxation time map of a phantom of aqueous CuSO_4 over a range of concentrations acquired using SR methodology with 2 signal averages, a RARE factor of 1, and 16 summed echo images.

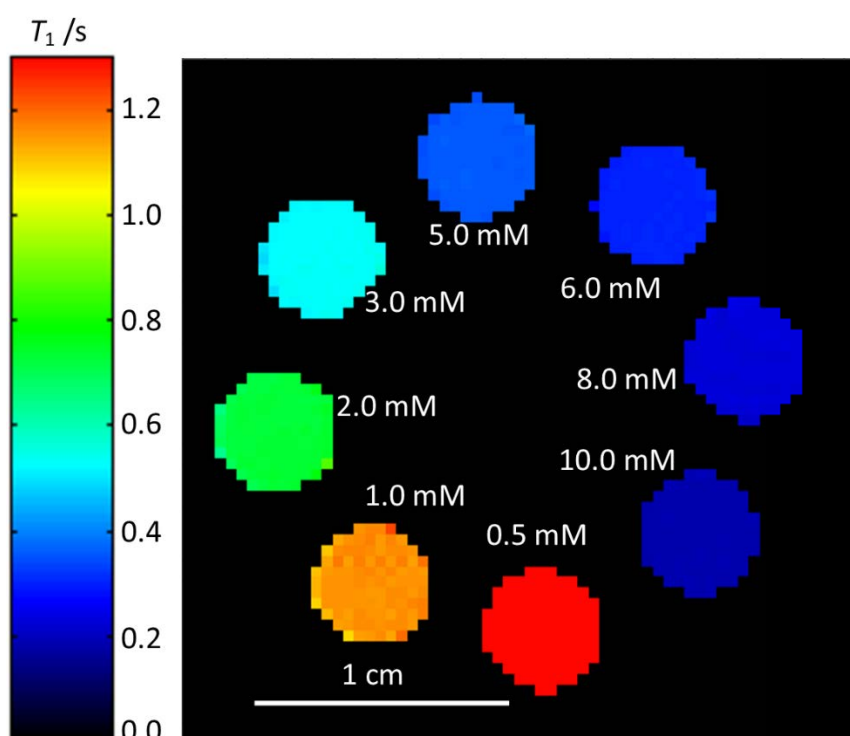


Figure A1.45: A ^1H T_1 MR relaxation time map of a phantom of aqueous CuSO_4 over a range of concentrations acquired using SR methodology with 4 signal averages, a RARE factor of 1, and 1 echo image.

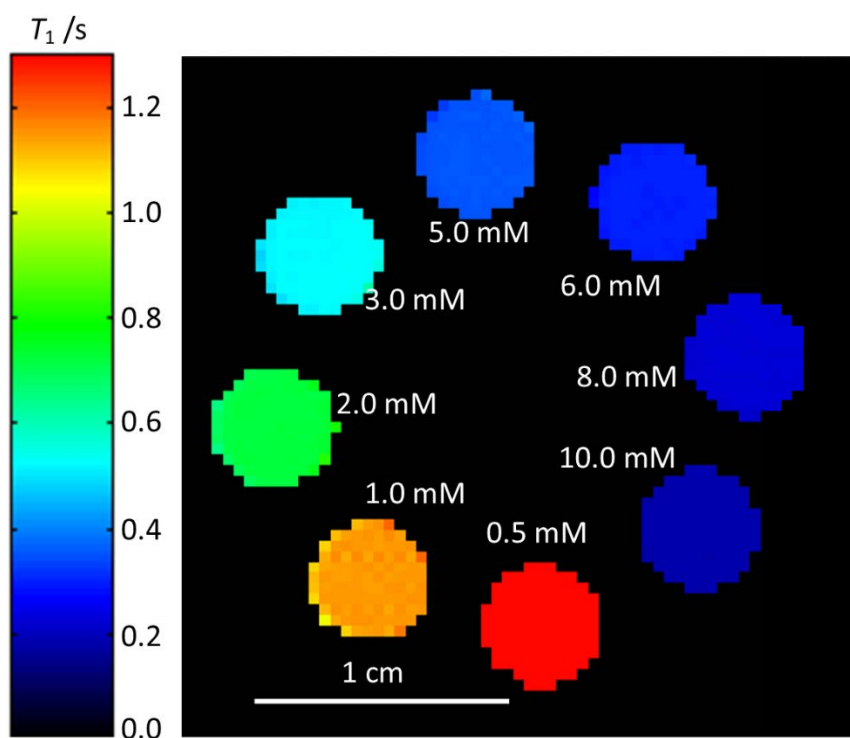


Figure A1.46: A ^1H T_1 MR relaxation time map of a phantom of aqueous CuSO_4 over a range of concentrations acquired using SR methodology with 4 signal averages, a RARE factor of 1, and 2 summed echo images.

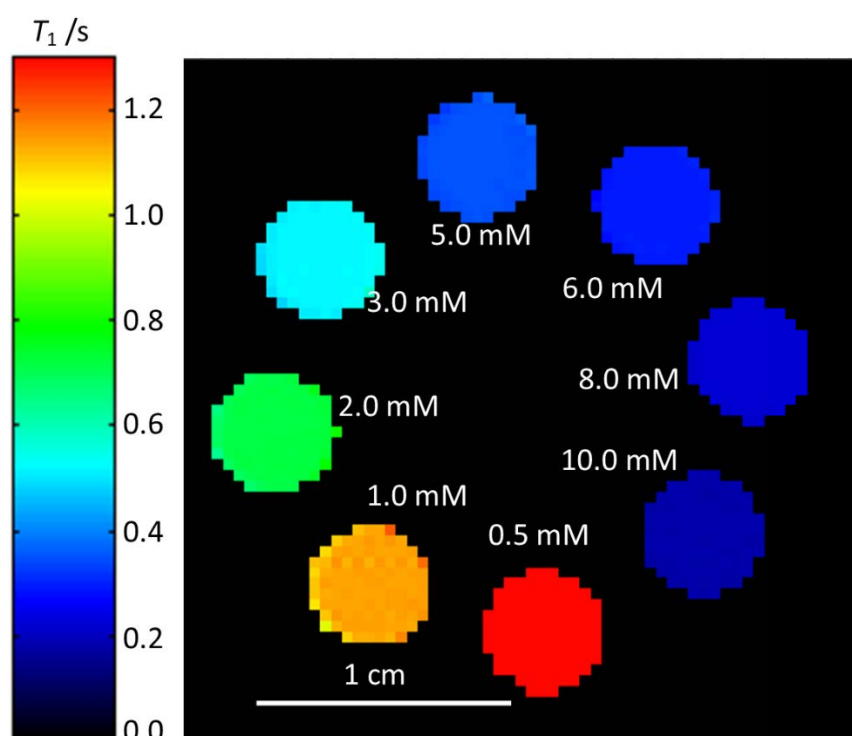


Figure A1.47: A ^1H T_1 MR relaxation time map of a phantom of aqueous CuSO_4 over a range of concentrations acquired using SR methodology with 4 signal averages, a RARE factor of 1, and 4 summed echo images.

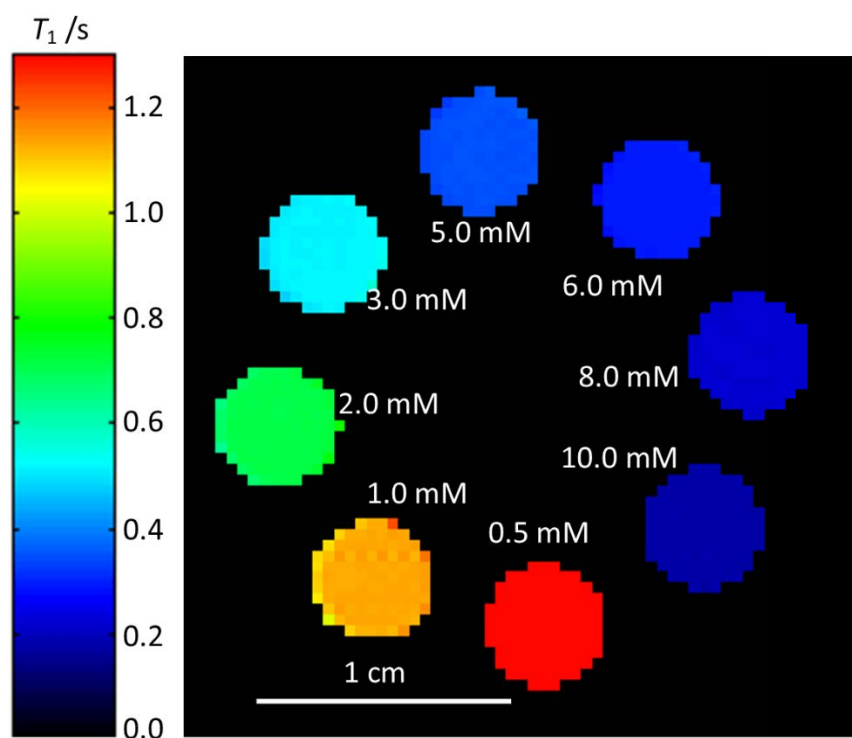


Figure A1.48: A ^1H T_1 MR relaxation time map of a phantom of aqueous CuSO_4 over a range of concentrations acquired using SR methodology with 4 signal averages, a RARE factor of 1, and 8 summed echo images.

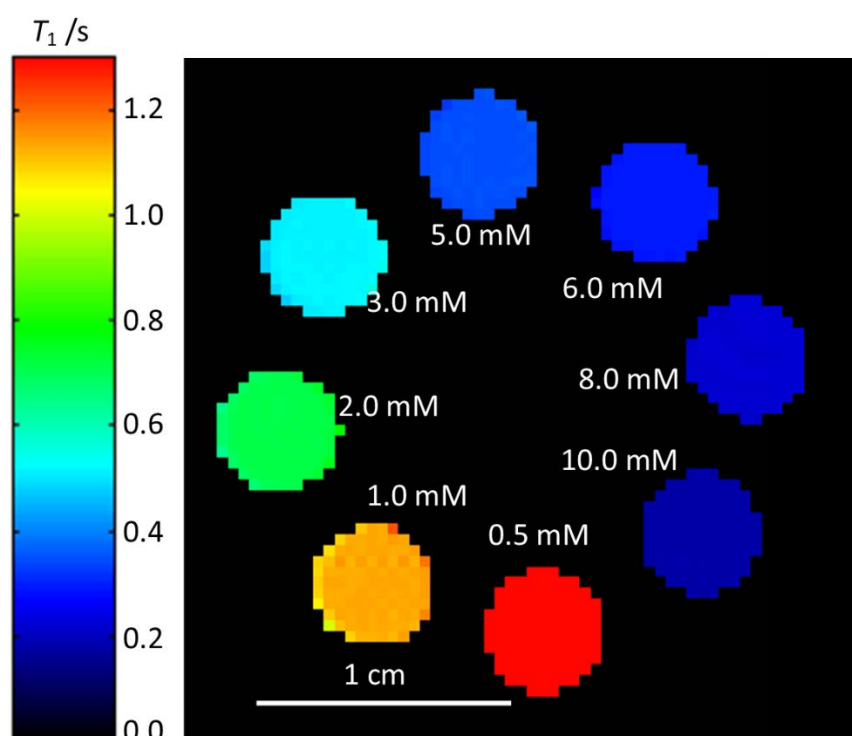


Figure A1.49: A ^1H T_1 MR relaxation time map of a phantom of aqueous CuSO_4 over a range of concentrations acquired using SR methodology with 4 signal averages, a RARE factor of 1, and 16 summed echo images.

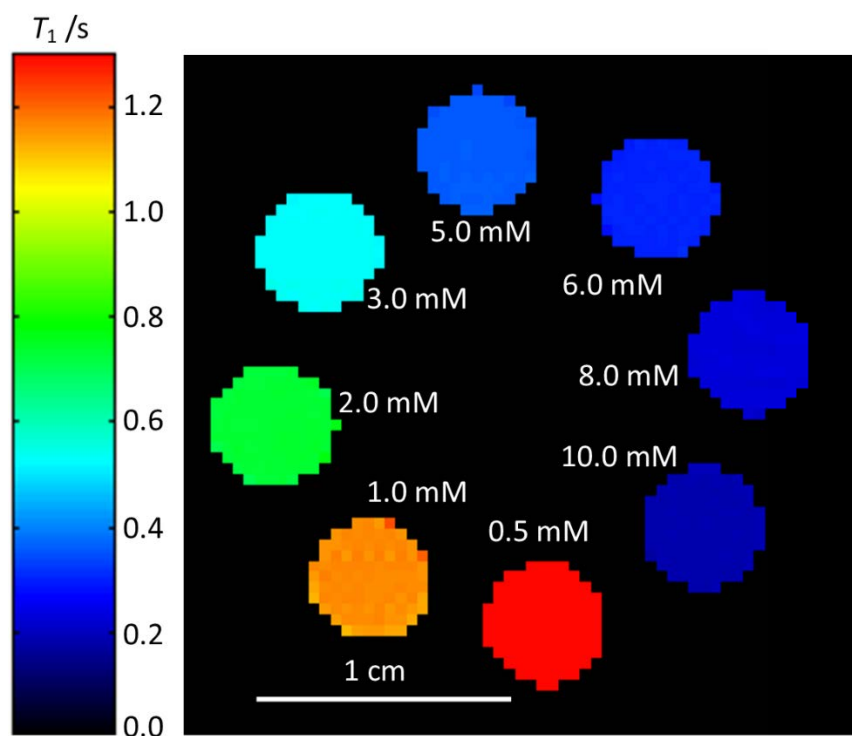


Figure A1.50: A ^1H T_1 MR relaxation time map of a phantom of aqueous CuSO_4 over a range of concentrations acquired using SR methodology with 8 signal averages, a RARE factor of 1, and 1 echo image.

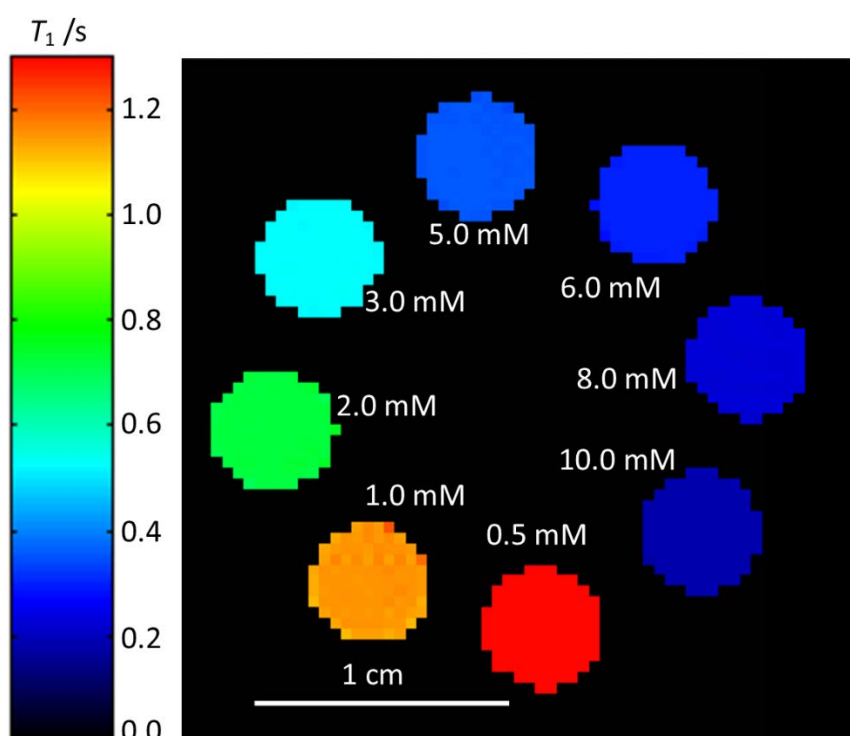


Figure A1.51: A ^1H T_1 MR relaxation time map of a phantom of aqueous CuSO_4 over a range of concentrations acquired using SR methodology with 8 signal averages, a RARE factor of 1, and 2 summed echo images.

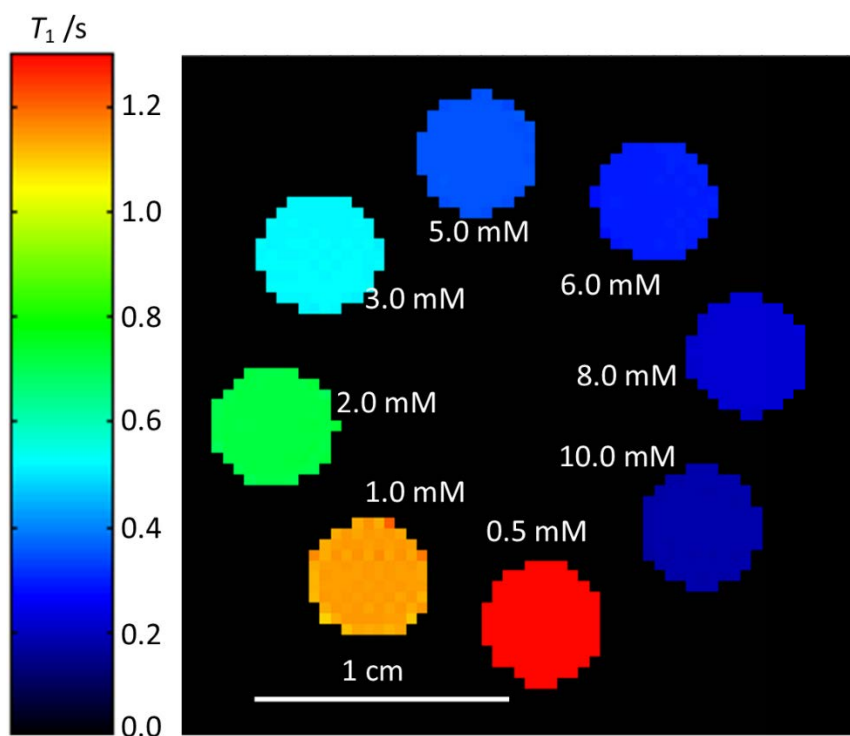


Figure A1.52: A ^1H T_1 MR relaxation time map of a phantom of aqueous CuSO_4 over a range of concentrations acquired using SR methodology with 8 signal averages, a RARE factor of 1, and 4 summed echo images.

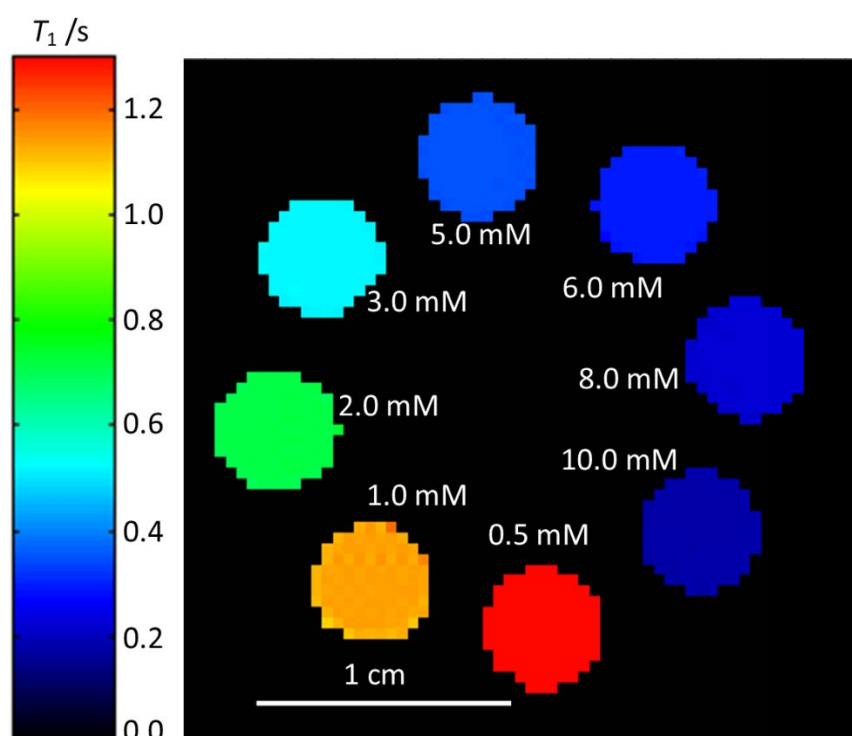


Figure A1.53: A ^1H T_1 MR relaxation time map of a phantom of aqueous CuSO_4 over a range of concentrations acquired using SR methodology with 8 signal averages, a RARE factor of 1, and 8 summed echo images.

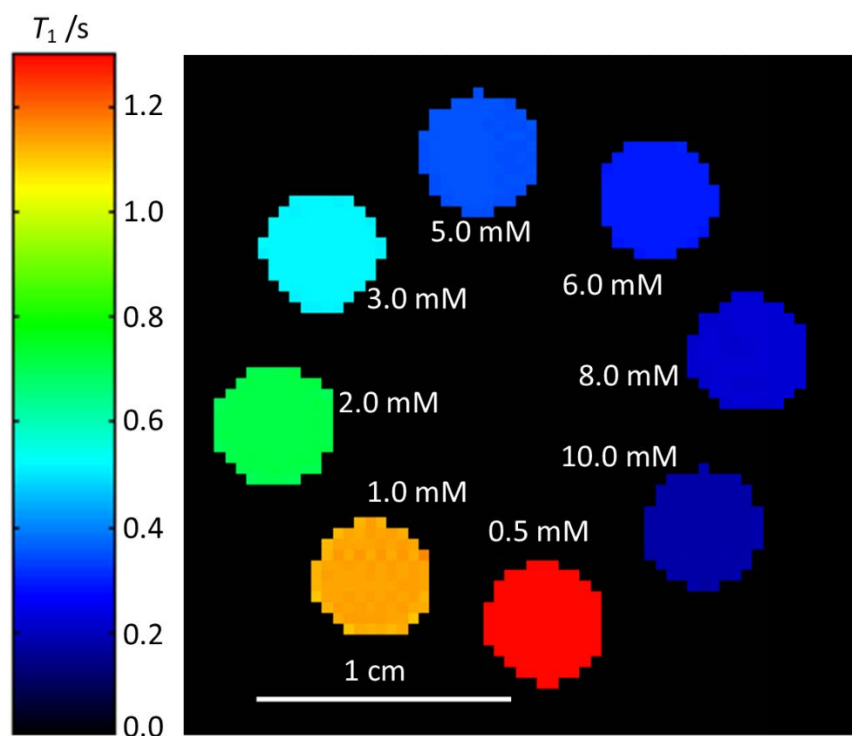


Figure A1.54: A ^1H T_1 MR relaxation time map of a phantom of aqueous CuSO_4 over a range of concentrations acquired using SR methodology with 8 signal averages, a RARE factor of 1, and 16 summed echo images.

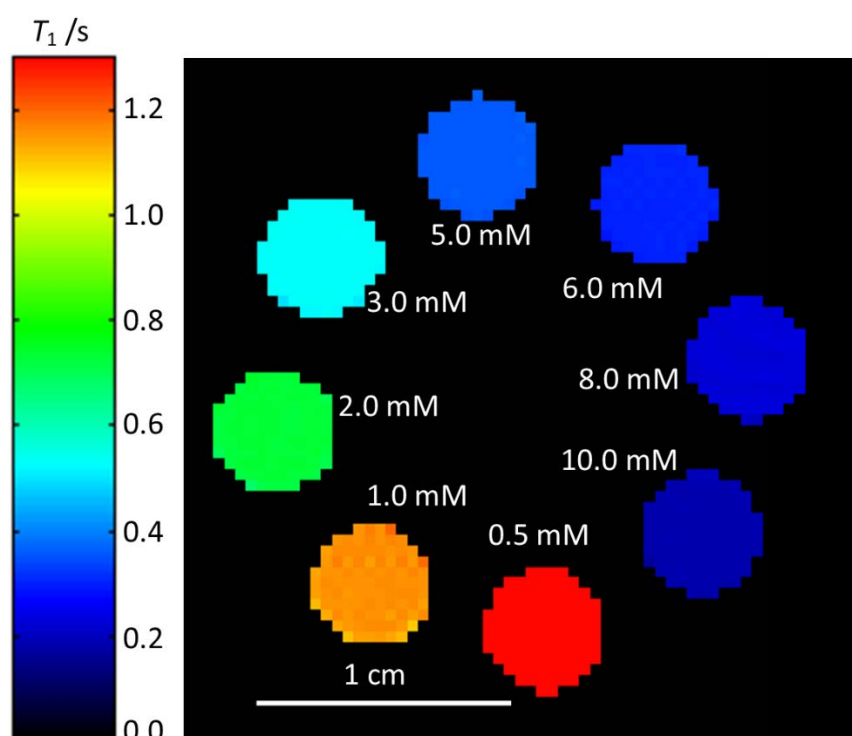


Figure A1.55: A ^1H T_1 MR relaxation time map of a phantom of aqueous CuSO_4 over a range of concentrations acquired using SR methodology with 16 signal averages, a RARE factor of 1, and 1 echo image.

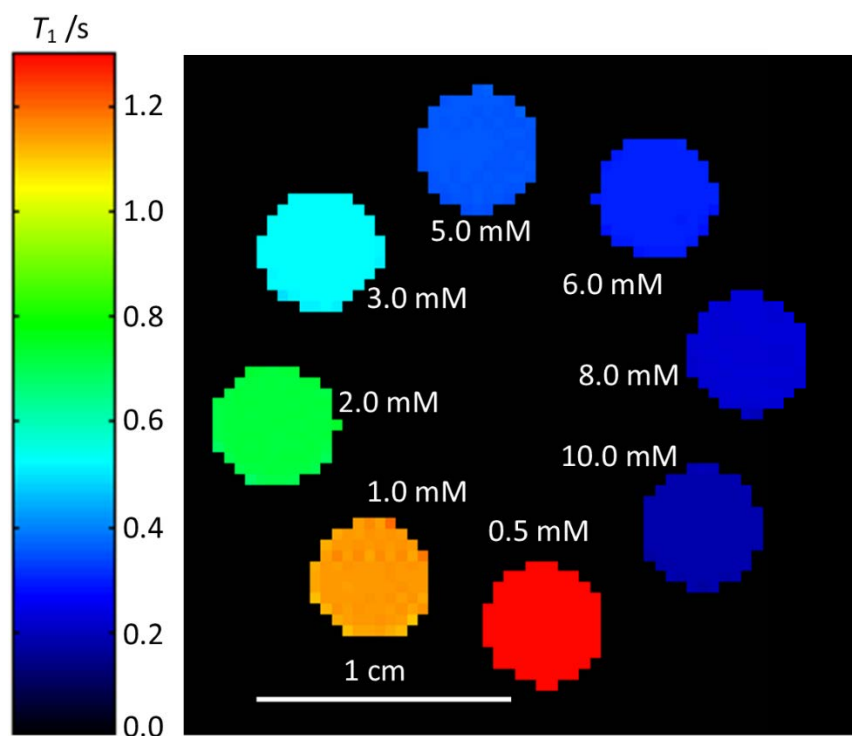


Figure A1.56: A ^1H T_1 MR relaxation time map of a phantom of aqueous CuSO_4 over a range of concentrations acquired using SR methodology with 16 signal averages, a RARE factor of 1, and 2 summed echo images.

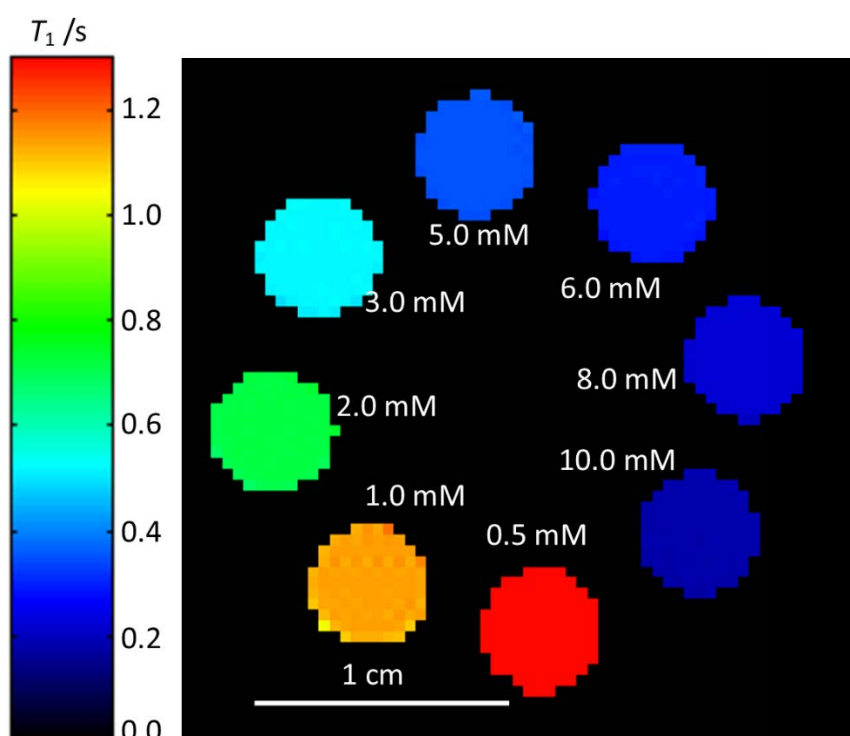


Figure A1.57: A ^1H T_1 MR relaxation time map of a phantom of aqueous CuSO_4 over a range of concentrations acquired using SR methodology with 16 signal averages, a RARE factor of 1, and 4 summed echo images.

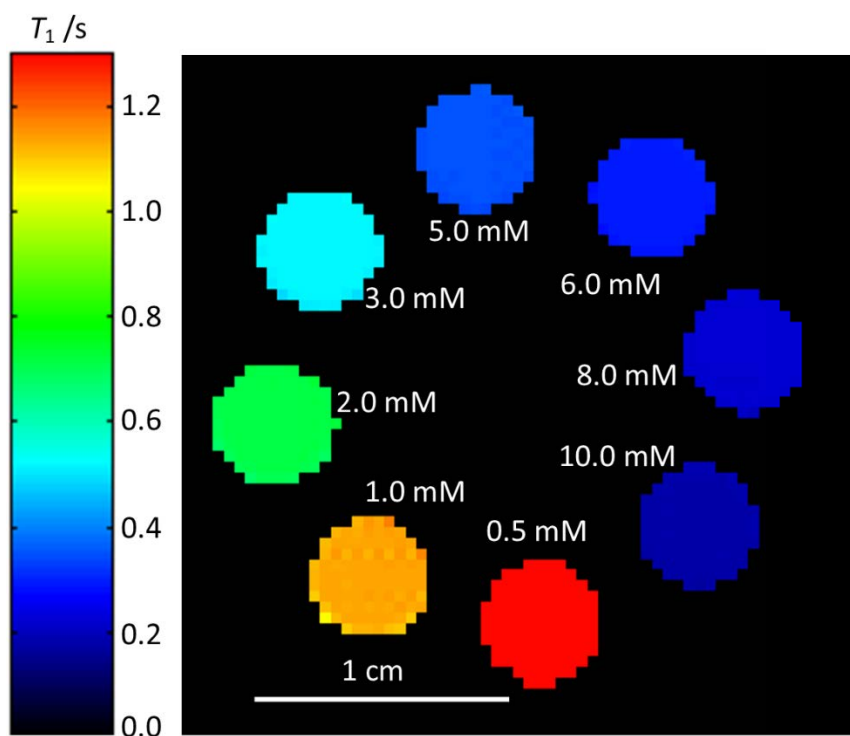


Figure A1.58: A ^1H T_1 MR relaxation time map of a phantom of aqueous CuSO_4 over a range of concentrations acquired using SR methodology with 16 signal averages, a RARE factor of 1, and 8 summed echo images.

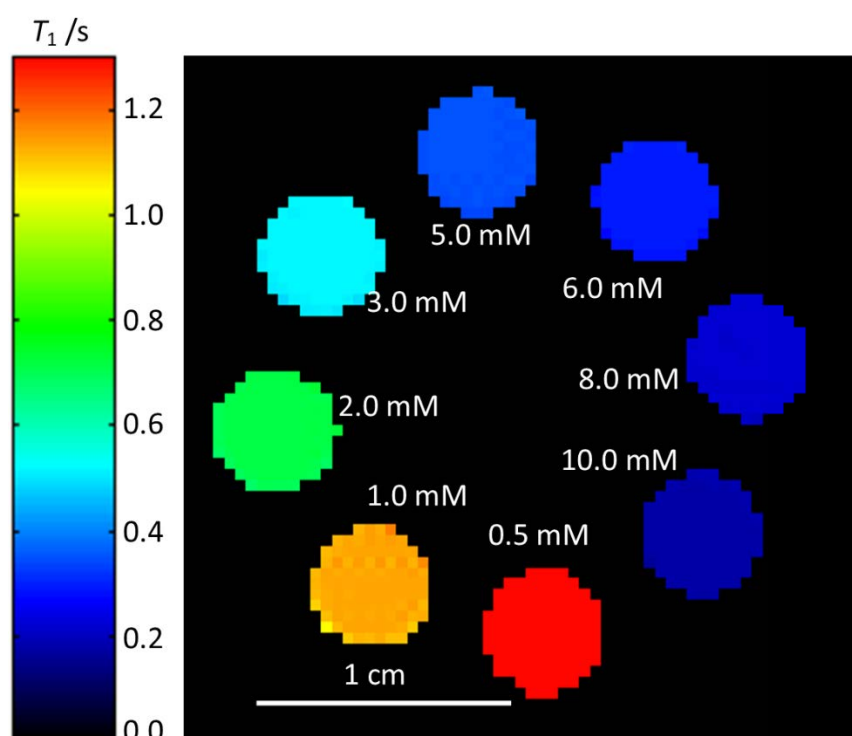


Figure A1.59: A ^1H T_1 MR relaxation time map of a phantom of aqueous CuSO_4 over a range of concentrations acquired using SR methodology with 16 signal averages, a RARE factor of 1, and 16 summed echo images.

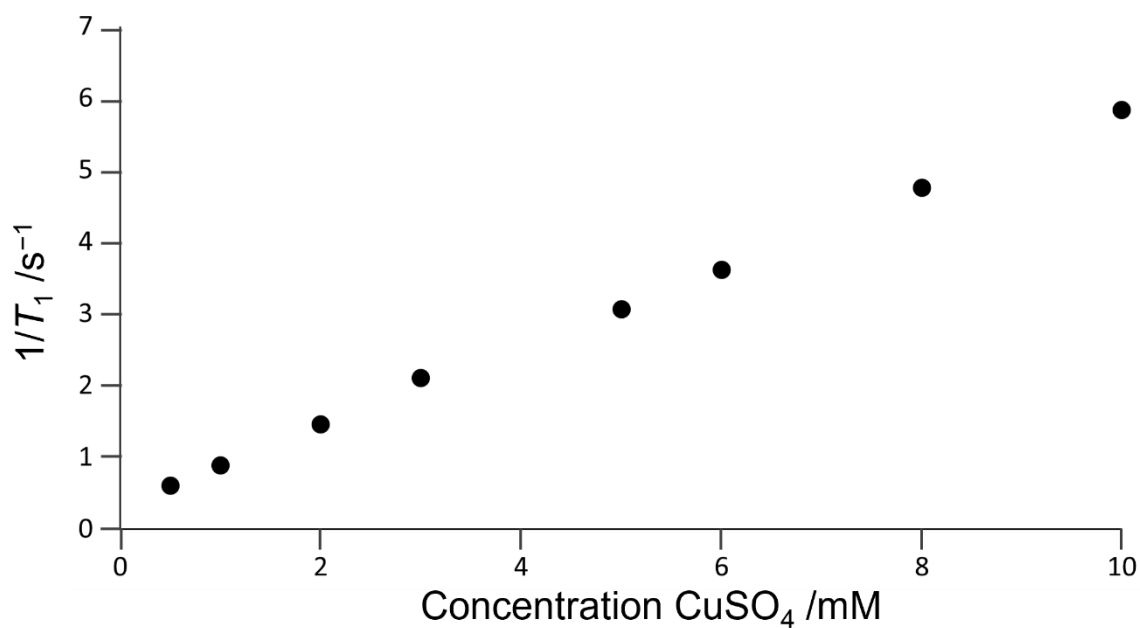


Figure A1.60: Relaxivity graph of CuSO_4 in H_2O obtained using bulk spectroscopy using both IR and SR methods and diff30 and WB40 probes. Error bars are within the markers.

The relationship between $1/T_1$ and CuSO_4 concentration is linear, Figure A1.1. This does not change with respect to acquisition method, saturation recovery (SR) or inversion recovery (IR), when a RARE factor is used, with the number of signal averages used, or the number of echo images summed, Figures A2-A5. The improvement in signal-to-noise ratio (SNR) for 0.5 mM CuSO_4 is shown in Figure A1.6, where the increase in SNR is most pronounced without a RARE factor. This is expected as the echo images will have relatively lower intensity when a RARE factor is used due to the increase in diffusive attenuation of the signal.

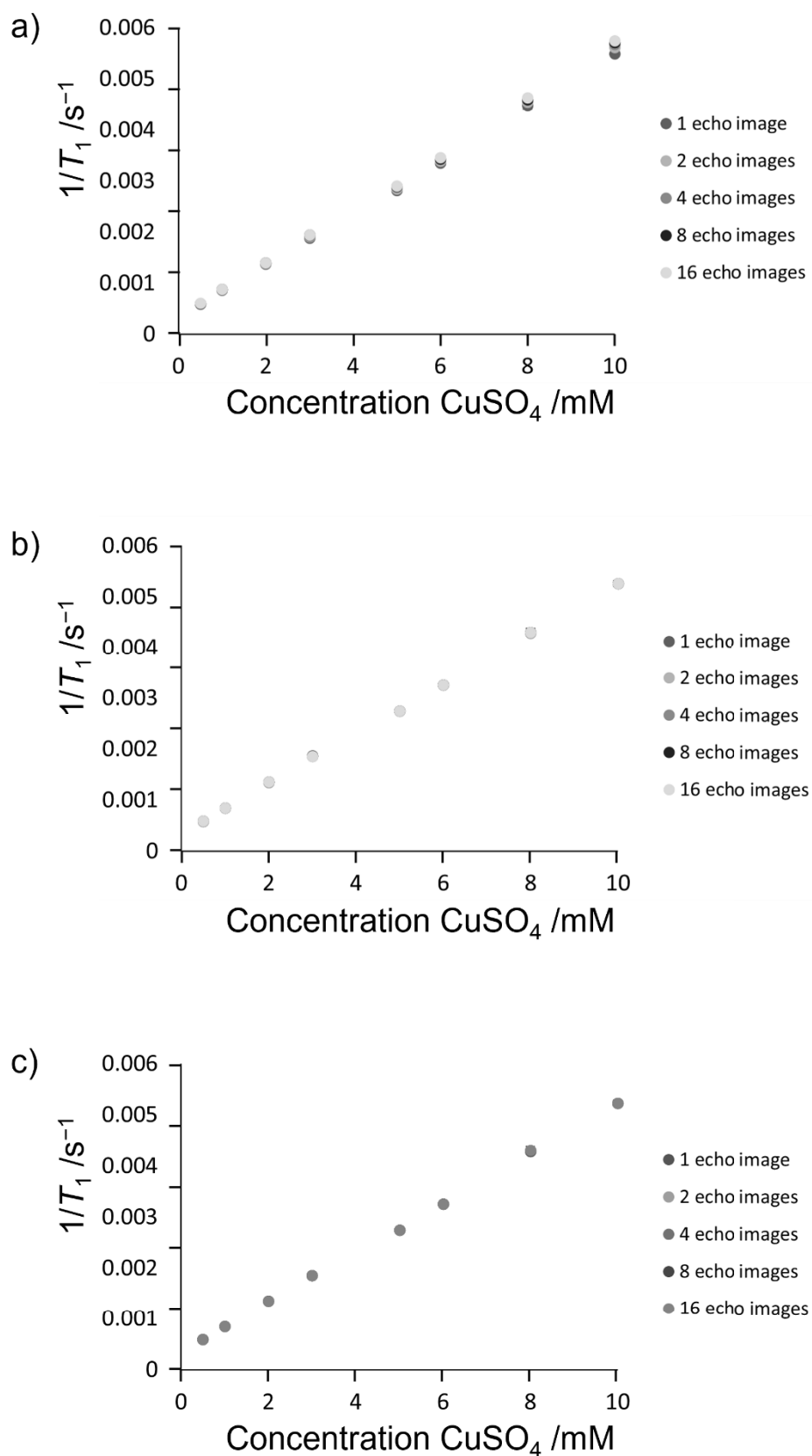


Figure A1.61: Relaxivity graphs for CuSO₄ obtained using 2 signal averages and echo summation methodology and a) SR, b) IR and c) IR with a RARE factor of 4. Number of echoes summed indicated in legend. Error bars are within the markers.

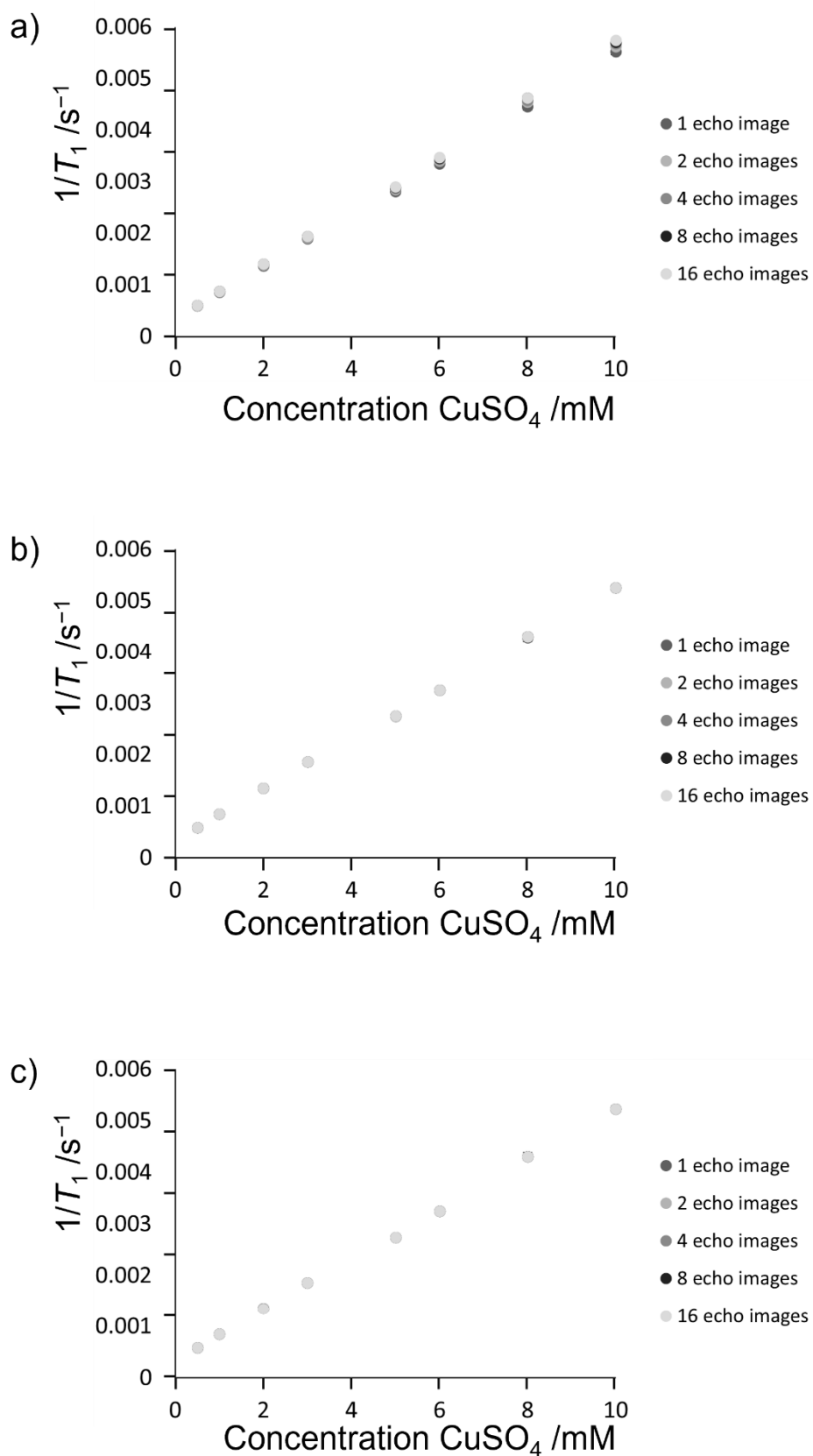


Figure A1.62: Relaxivity graphs for CuSO_4 obtained using 4 signal averages and echo summation methodology and a) SR, b) IR and c) IR with a RARE factor of 4. Number of echoes summed indicated in legend. Error bars are within the markers.

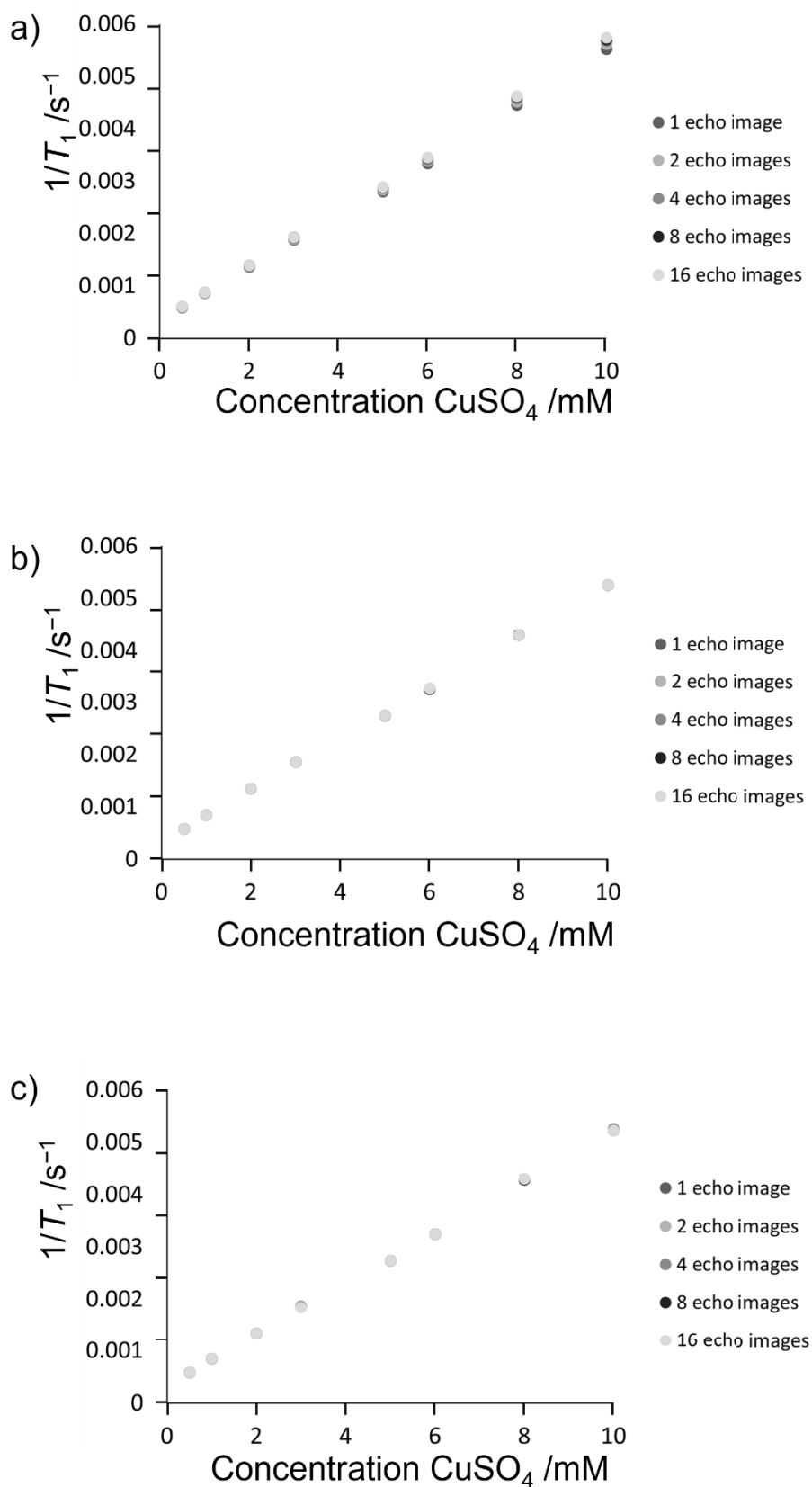


Figure A1.63: Relaxivity graphs for CuSO_4 obtained using 8 signal averages and echo summation methodology and a) SR, b) IR and c) IR with a RARE factor of 4. Number of echoes summed indicated in legend. Error bars are within the markers.

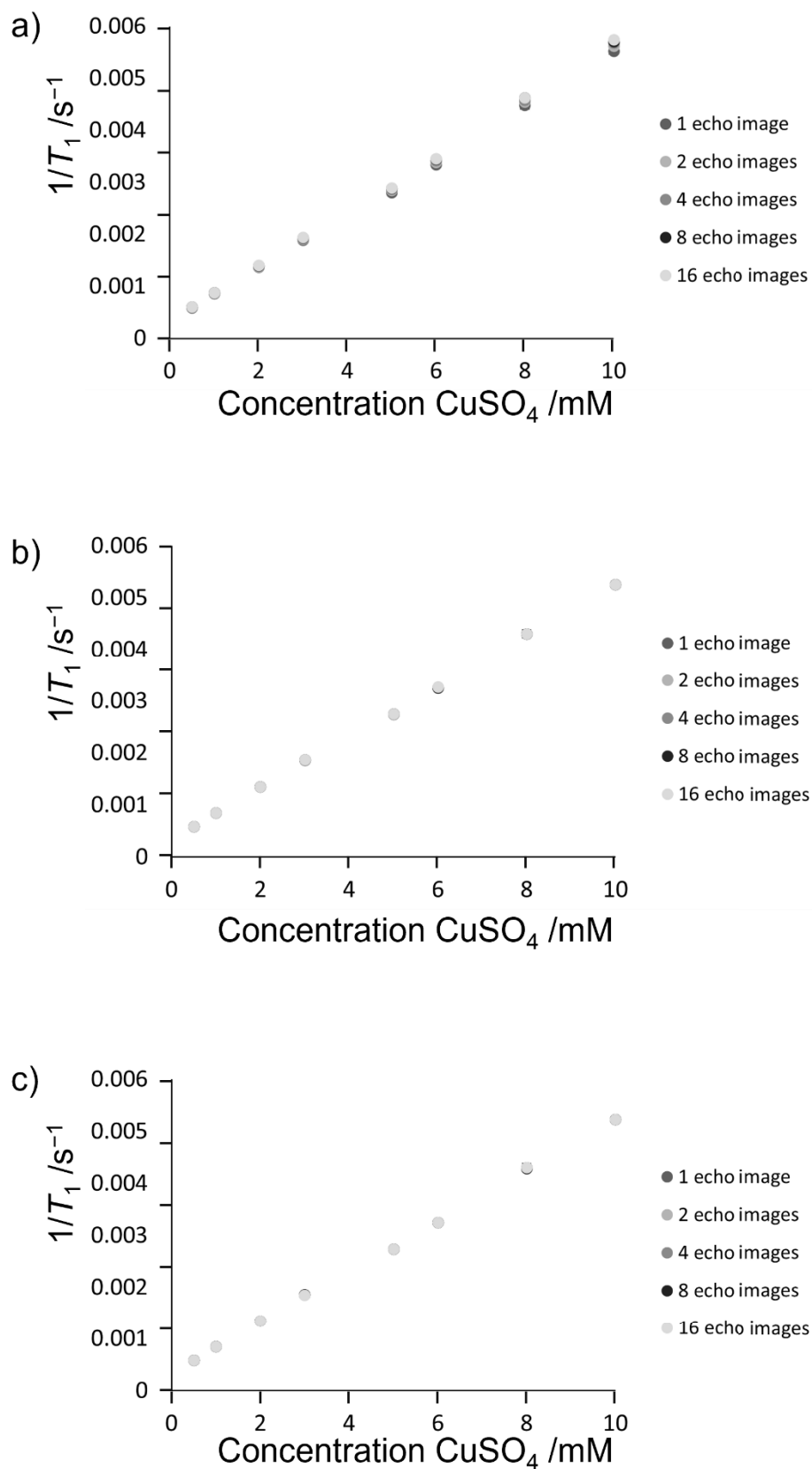


Figure A1.64: Relaxivity graphs for CuSO_4 obtained using 16 signal averages and echo summation methodology and a) SR, b) IR and c) IR with a RARE factor of 4. Number of echoes summed indicated in legend. Error bars are within the markers.

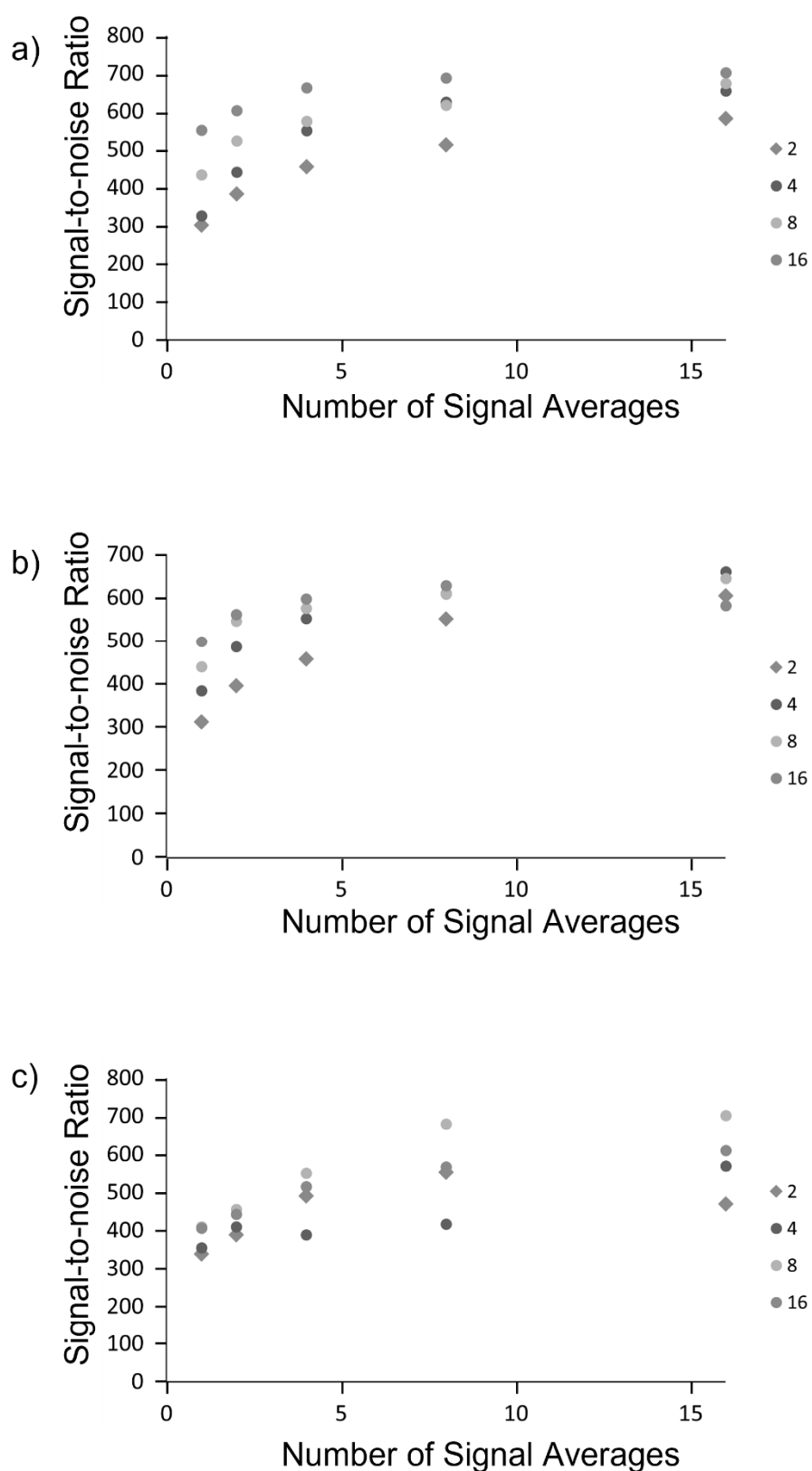


Figure A1.65: Graphs of signal-to-noise ratio obtained for 0.5 mM CuSO₄ in T_1 relaxation time maps using a) SR, b) IR and c) IR with a RARE factor of 4. Number of echoes summed indicated in legend. Error bars are within the markers.

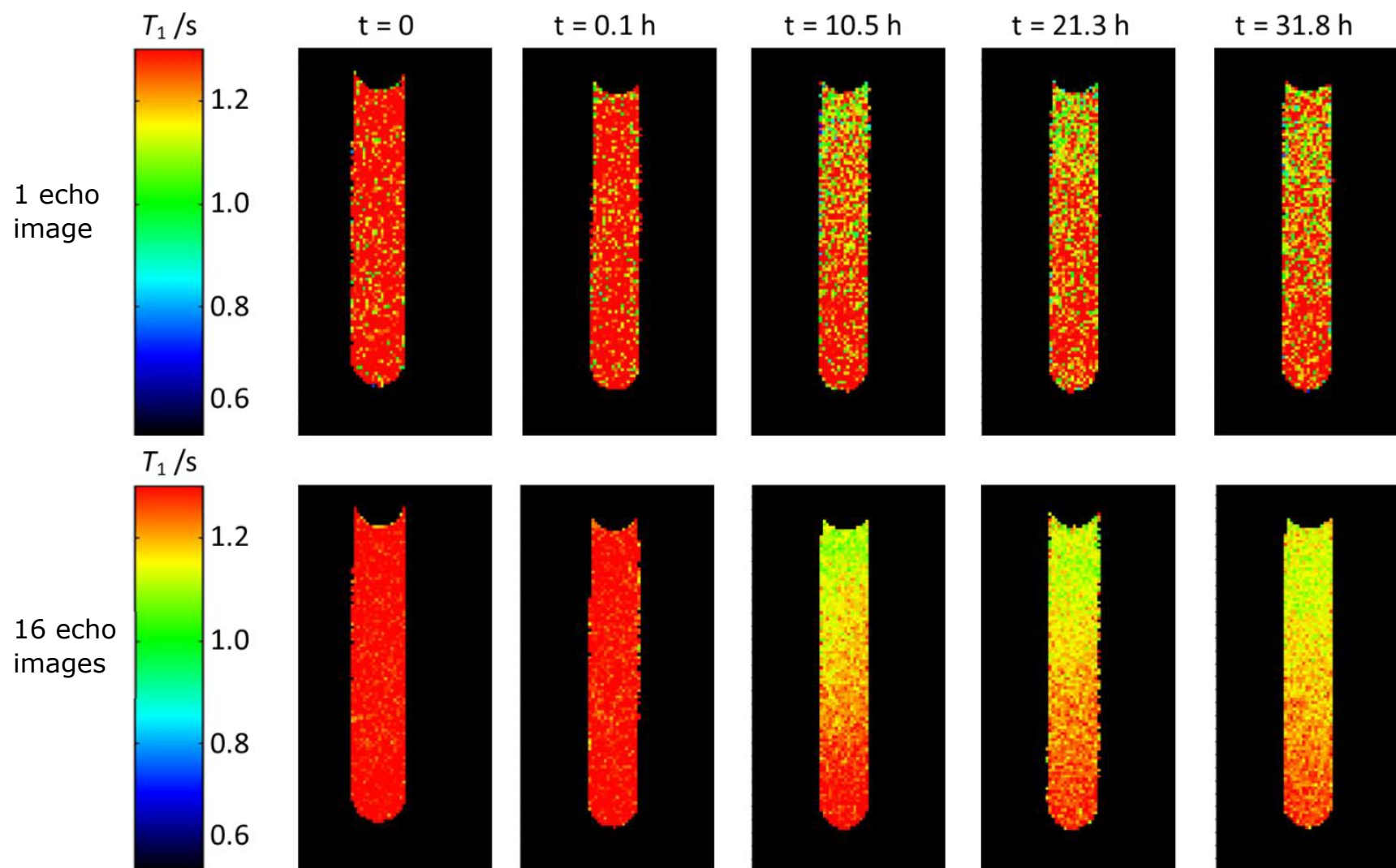


Figure A1.66: ^{19}F T_1 relaxation time maps of 0.08 M $\text{Zn}(\text{TfO})_2 \cdot \text{C}_{22}\text{C}_{18}\text{imTfO}$ at 0 h, 0.1 h, 10.5 h, 21.3 h and 31.8 h of water ingress from the atmosphere obtained using saturation recovery with 2 averages with 1 and 16 echo images summed.

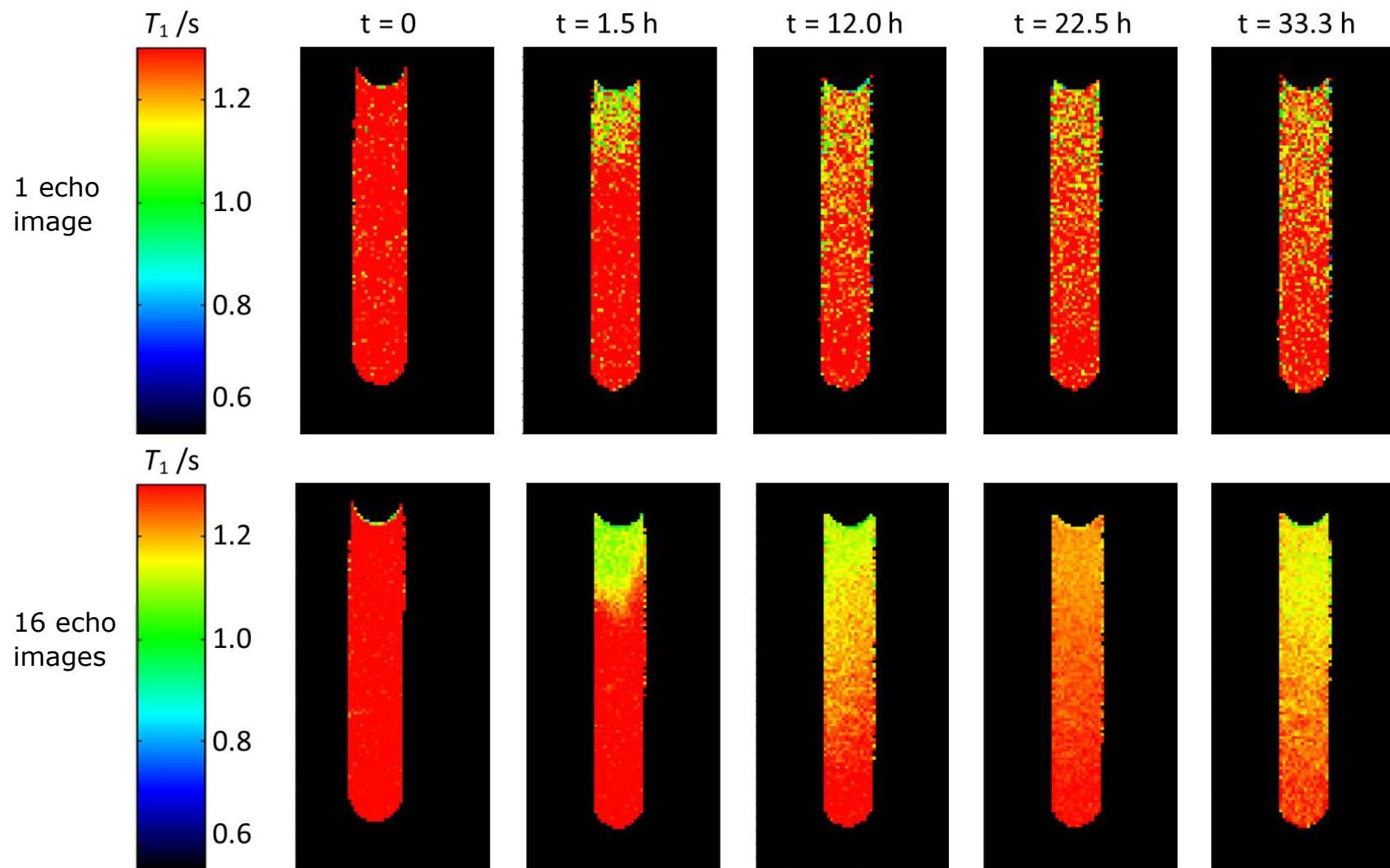


Figure A1.67: ^{19}F T_1 relaxation time maps of 0.08 M $\text{Zn}(\text{TfO})_2 \cdot \text{C}_{22}\text{C}_{11}\text{imTfO}$ at 0 h, 0.1 h, 10.5 h, 21.3 h and 31.8 h of water ingress from the atmosphere obtained using saturation recovery with 4 averages with 1 and 16 echo images summed.

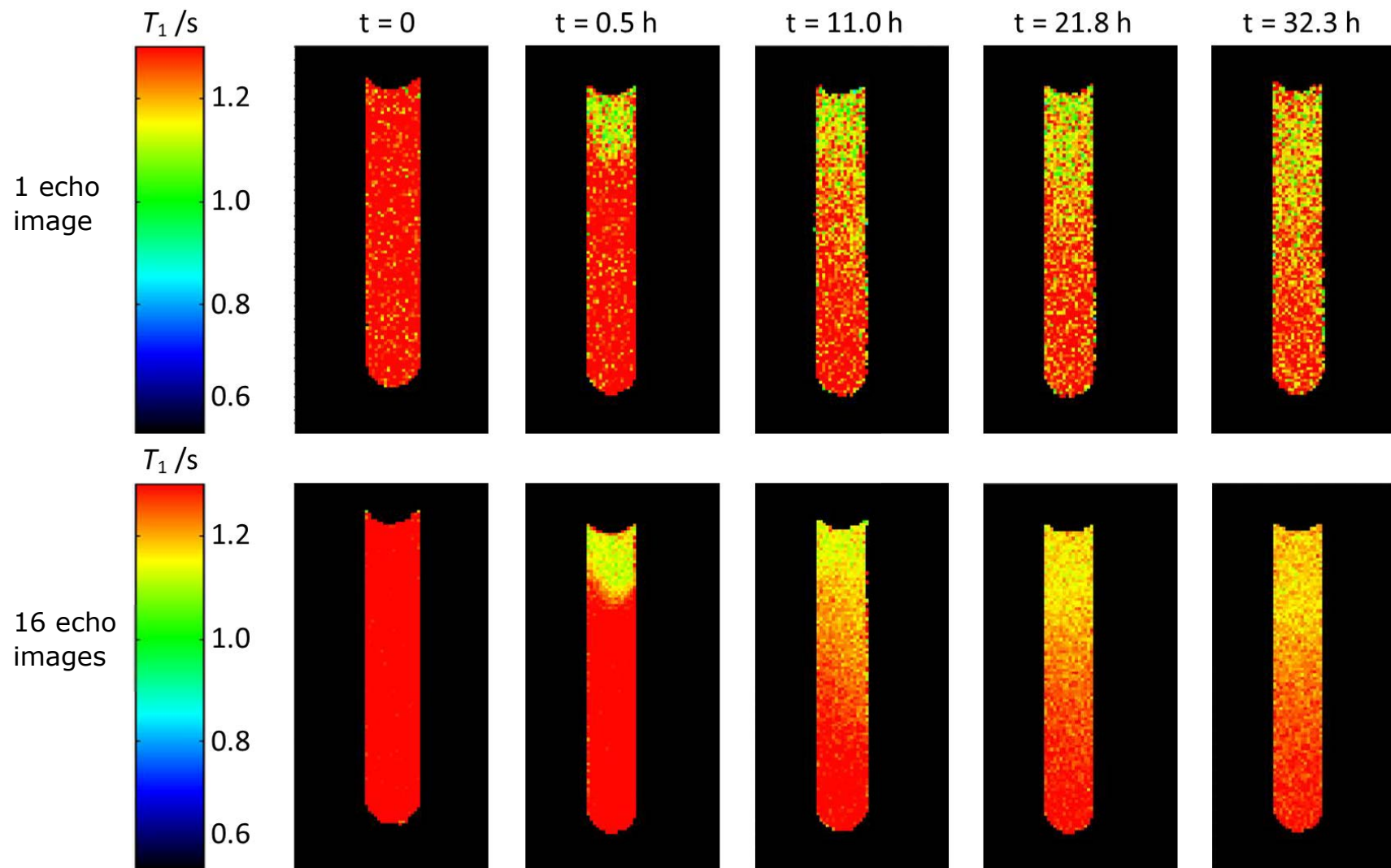


Figure A1.68: ^{19}F T_1 relaxation time maps of 0.08 M $\text{Zn}(\text{TfO})_2 \cdot \text{C}_{22}\text{C}_{11}\text{imTfO}$ at 0 h, 0.1 h, 10.5 h, 21.3 h and 31.8 h of water ingress from the atmosphere obtained using inversion recovery with 2 averages with 1 and 16 echo images summed.

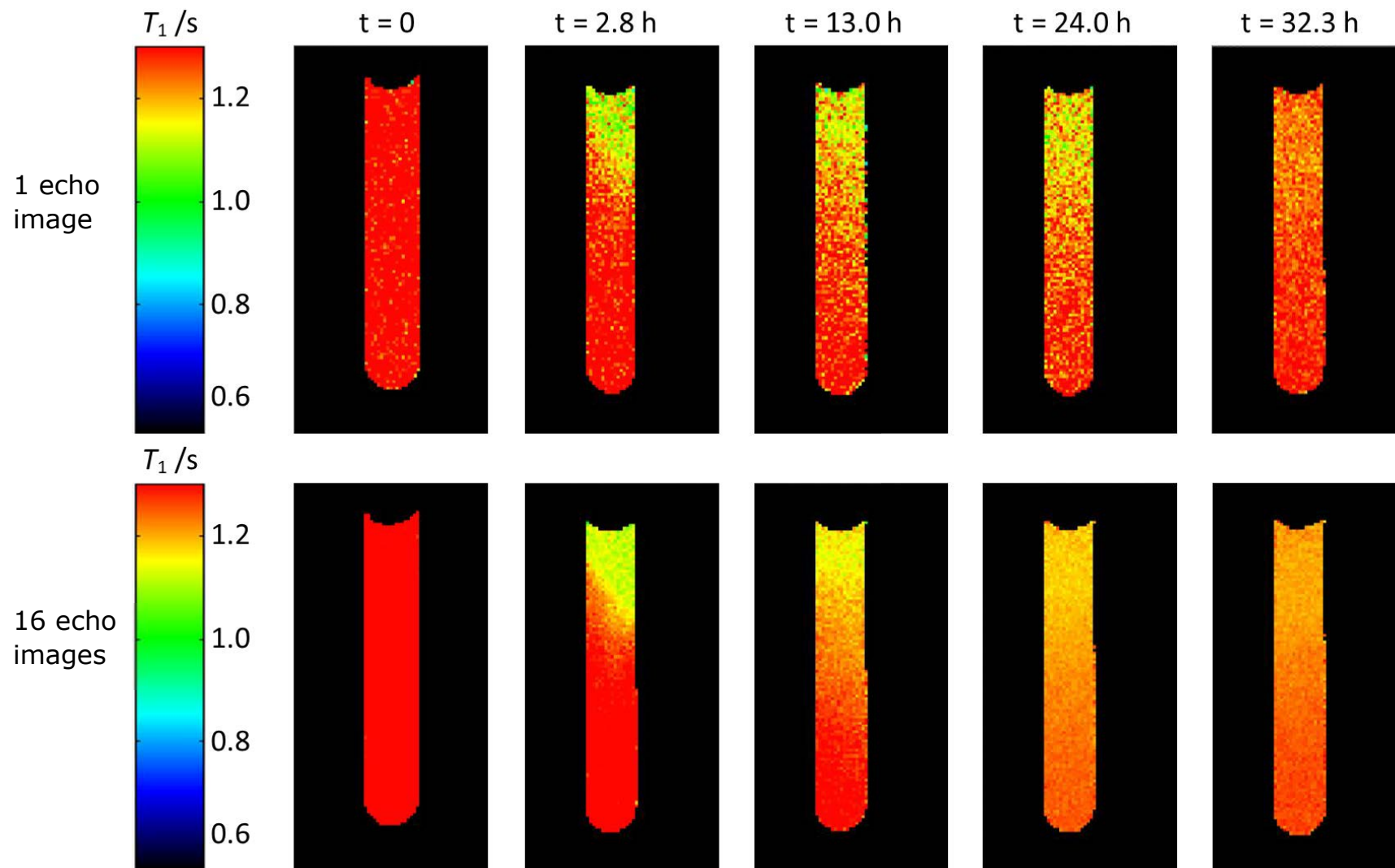


Figure A1.69: ^{19}F T_1 relaxation time maps of 0.08 M $\text{Zn}(\text{TfO})_2 \cdot \text{C}_{22}\text{H}_{45}\text{N}_3\text{O}_4$ at 0 h, 0.1 h, 10.5 h, 21.3 h and 31.8 h of water ingress from the atmosphere obtained using inversion recovery with 4 averages with 1 and 16 echo images summed.

Appendix 2:

Table A2.1: Deconvolution values for electrolytic sodium in ^{23}Na nuclear magnetic resonance (NMR) spectra in sodium metal cell

Peak	After 1 st charge cycle			After 2 nd charge cycle			After discharge at a rate 150 mA g ⁻¹			After discharge at a rate 600 mA g ⁻¹		
	δ /ppm	$\Delta\nu$ /Hz	%	δ /ppm	$\Delta\nu$ /Hz	%	δ /ppm	$\Delta\nu$ /Hz	%	δ /ppm	$\Delta\nu$ /Hz	%
1	-7.0	334	23	-7.0	349	26	-7.0	358	28	-7.0	399	30
2	-5.0	152	27	-5.0	149	30	-5.0	146	32	-5.0	144	28
3	0.0	448	32	0.0	397	24	0.0	421	27	0.0	480	42
4	1.0	1901	18	1.0	2399	20	6.5	1878	12			

Table A2.2: Deconvolution values for metallic sodium in ^{23}Na NMR spectra in sodium metal cell

Peak	After 1st charge cycle			After 2nd charge cycle			After discharge at a rate 150 mA g^{-1}				After discharge at a rate 600 mA g^{-1}			
	δ /ppm	$\Delta\nu$ /Hz	%	δ /ppm	$\Delta\nu$ /Hz	%	δ /ppm	$\Delta\nu$ /Hz	%	Gaussian %	δ /ppm	$\Delta\nu$ /Hz	%	Gaussian %
1	1131	309	100	1131	293	87	1125	703	10	75	1126	1259	9	75
2				1141	1413	13	1129	342	29	0	1129	354	7	75
3							1131	153	27	75	1131	127	4	0
4							1141	736	34	75	1136	585	33	75
5											1140	1091	48	75

Table A2.3: Deconvolution values for *in situ* ^{23}Na NMR spectra in full cell after charging

Peak	After Charge				After 4 Hours				After Discharge		
	δ /ppm	$\Delta\nu$ /Hz	%	Gaussian %	δ /ppm	$\Delta\nu$ /Hz	%	Gaussian %	δ /ppm	$\Delta\nu$ /Hz	%
1	-157	9901	4	50							
2	-49	9529	13	50	-10	3398	7	0			
3	9	3012	67	0	9	2696	64	0	11	3030	100
4	486	16066	16	100	652	22976	29	100			

Table A2.4: Deconvolution values for selected *in operando* ^{23}Na NMR spectra in full cell during the formation cycle

Peak	Pristine Cell			After Charging for 1.5 Hours				After Charging for 4.5 Hours			
	δ /ppm	$\Delta\nu$ /Hz	%	δ /ppm	$\Delta\nu$ /Hz	%	Gaussian %	δ /ppm	$\Delta\nu$ /Hz	%	Gaussian %
1	-7	633	9	-198	6264	3	50	-148	13367	15	0
2	0	293	49	-64	11023	18	0	-43	6205	12	0
3	8	1052	42	0	3239	52	0	0	2889	53	0
4				133	109	8	50	339	18298	20	100
5				1109	12632	20	0				

Appendix 3:

Table A3.1: Deconvolution values for selected *in operando* ^7Li NMR spectra during the formation cycle

Peak	Before cycling			At the start of cycling			After cycling for 9 h			After cycling for 15 h			After cycling for 18 h		
	δ /ppm	$\Delta\nu$ /Hz	%	δ /ppm	$\Delta\nu$ /Hz	%	δ /ppm	$\Delta\nu$ /Hz	%	δ /ppm	$\Delta\nu$ /Hz	%	δ /ppm	$\Delta\nu$ /Hz	%
1	-2.0	69	7	-1.7	70	9									
2	-1.2	97	9	-1.1	88	6	-1.4	14	87	-1.3	107	17	-1.2	132	18
3	-0.5	60	6	-0.4	61	8	-0.8	5	61	-0.7	52	3	-0.6	44	3
4	-0.2	31	6	-0.2	4	0	-0.3	6	42	-0.2	38	9	-0.2	35	7
5	-0.1	19	2	-0.1	25	5	-0.1	9	29	-0.1	19	4	-0.1	19	4
6	0.0	18	7	0.0	16	6	0.0	7	16	0.0	16	10	0.0	16	10
7	0.3	5	0	0.4	6	1	0.4	0	4						
8	0.5	15	4	0.4	10	2	0.4	2	7						
9	0.6	10	0	0.5	14	2	0.5	1	7	0.4	6	2	0.3	6	2
10	0.7	18	2	0.6	8	1	0.5	2	9	0.4	9	3	0.4	9	3
11	0.7	5	0	0.9	123	3	0.7	4	70	0.7	88	5	0.6	105	7
12	1.2	126	2												
13	6.6	173	2												
14	7.2	654	9	14.0	618	7	20.2	3	595						
15	250.7	1111	46	256.5	1231	49	261.9	47	1442	261.1	1479	31	261.6	1799	31
16										273.4	1136	14	276.4	1185	13

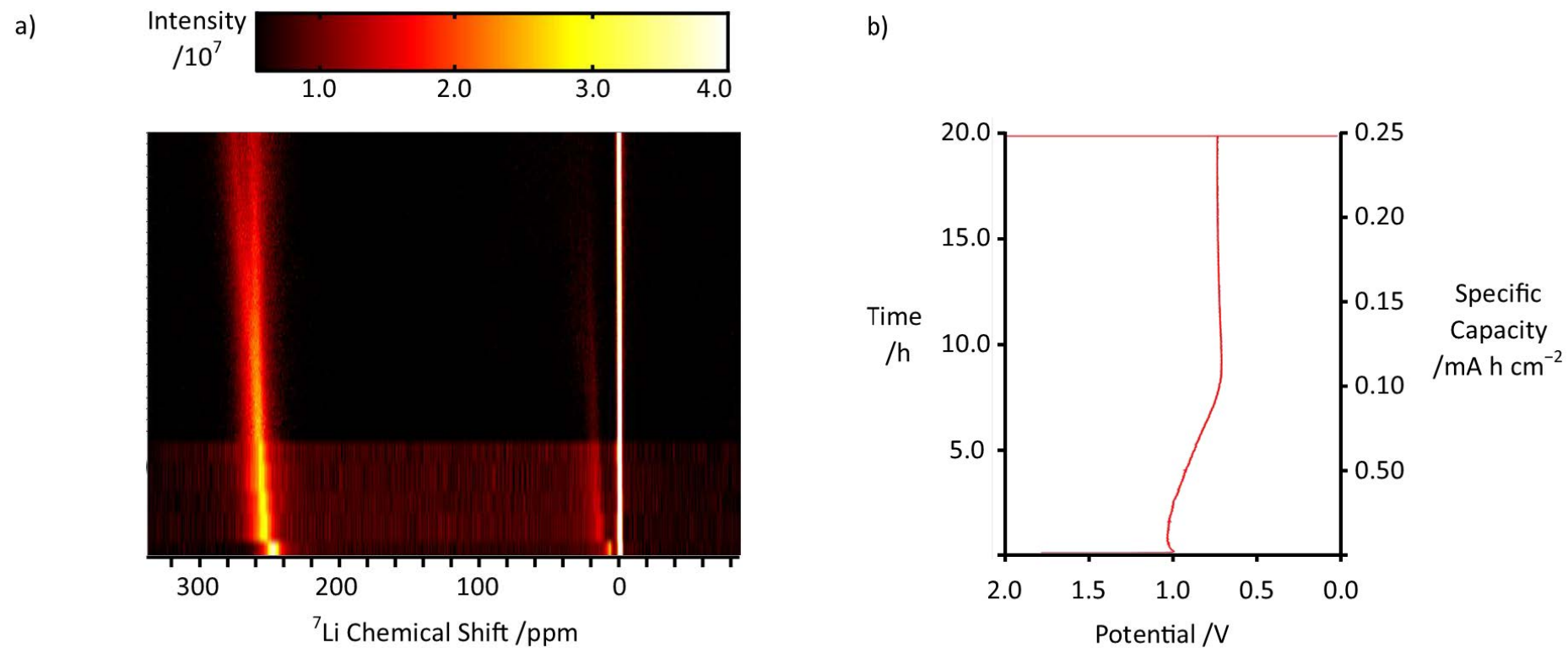


Figure 3.1: ^{7}Li NMR spectra acquired in *operando* during a formation cycle at 10.5 mA g^{-1} of a lithium metal cell showing the development of a species in the vicinity of the electrolyte and the evolution of the metal species.

Appendix 4:

The concentration of Al^{3+} in the electrolyte after cycling the ALFA cell¹ for **20 h was estimated using Faraday's Law** of capacitance, equation 1, where Q is the cell capacity, N_{e-} is the number of electrons transferred in the electrochemical reaction, and F is Faraday's constant, and an assumed anode mass of 0.5 g.

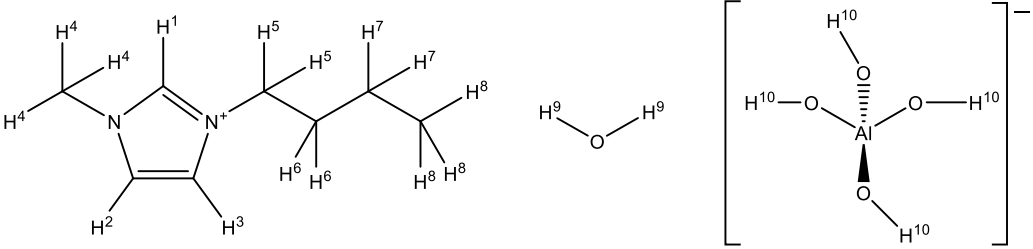
$$N_{Al} = \frac{Q}{N_{e-} \times F}$$

$$\begin{aligned} N_{Al} &= \frac{19.8 \times 3600 \times 10^{-3}}{3 \times 96500} \\ &= 2.46 \times 10^{-4} \text{ mol g}^{-1} \\ &= 1.23 \times 10^{-4} \text{ mol} \end{aligned}$$

Assuming an electrolyte volume of 700 μl

$$\begin{aligned} [Al^{3+}] &= \frac{1.23 \times 10^{-4}}{700 \times 10^{-6}} \\ [Al^{3+}] &= 175.7 \text{ mM} \end{aligned}$$

Table 4.1: ^1H Diffusion coefficients for each environment on $\text{C}_4\text{C}_1\text{im}$.



AlCl_3 ratio	1.1								
H	1	2 and 3	4	5	6	7	8	9	10
Diffusion coefficient / $10^{-11} \text{ m}^2 \text{ s}^{-1}$	3.82	3.82	3.82	3.78	3.81	3.8	3.81	2.3	N/A
AlCl_3 ratio	1.2								
H	1	2 and 3	4	5	6	7	8	9	10
Diffusion coefficient / $10^{-11} \text{ m}^2 \text{ s}^{-1}$	3.76	3.76	3.77	3.75	3.75	3.76	3.76	2.34	2.48
AlCl_3 ratio	1.3								
H	1	2 and 3	4	5	6	7	8	9	10
Diffusion coefficient / $10^{-11} \text{ m}^2 \text{ s}^{-1}$	3.89	3.89	3.9	3.88	3.88	3.88	3.9	2.42	2.2
AlCl_3 ratio	1.4								
H	1	2 and 3	4	5	6	7	8	9	10
Diffusion coefficient / $10^{-11} \text{ m}^2 \text{ s}^{-1}$	3.72	3.71	3.71	3.7	3.71	3.7	3.71	2.36	2.06
AlCl_3 ratio	1.6								
H	1	2 and 3	4	5	6	7	8	9	10
Diffusion coefficient / $10^{-11} \text{ m}^2 \text{ s}^{-1}$	3.74	3.75	3.76	3.73	3.74	3.74	3.75	2.44	2.07
AlCl_3 ratio	1.8								
H	1	2 and 3	4	5	6	7	8	9	10
Diffusion coefficient / $10^{-11} \text{ m}^2 \text{ s}^{-1}$	3.19	3.18	3.2	3.17	3.18	3.18	3.19	2.14	1.85

Table A4.1: Deconvolution values for ^{27}Al NMR spectra at different AlCl_3 ratios in $\text{C}_4\text{C}_1\text{imCl}$

Peak	AlCl_3 ratio 1.1			AlCl_3 ratio 1.2			AlCl_3 ratio 1.3			AlCl_3 ratio 1.4			AlCl_3 ratio 1.6			AlCl_3 ratio 1.8		
	δ /ppm	$\Delta\nu$ /Hz	%	δ /ppm	$\Delta\nu$ /Hz	%	δ /ppm	$\Delta\nu$ /Hz	%	δ /ppm	$\Delta\nu$ /Hz	%	δ /ppm	$\Delta\nu$ /Hz	%	δ /ppm	$\Delta\nu$ /Hz	%
1	96.8	438	10	103.6	529	23	103.5	606	23	103.6	633	23	104.0	938	31	83.3	3015	13
2	102.8	131	67	109.6	846	77	110.5	1743	77	111.1	2352	77	114.7	3028	69	104.5	1588	40
3	103.0	56	23													120.5	3226	46

Table A4.2: Deconvolution values for ^{27}Al NMR spectra at different AlCl_3 concentrations in saltwater

Peak	100 mM AlCl_3			200 mM AlCl_3			500 mM AlCl_3		
	δ /ppm	$\Delta\nu$ /Hz	%	δ /ppm	$\Delta\nu$ /Hz	%	δ /ppm	$\Delta\nu$ /Hz	%
1	79.00	7	100	79.00	6	48	79.00	5	21
2				79.03	5	52	79.04	6	79

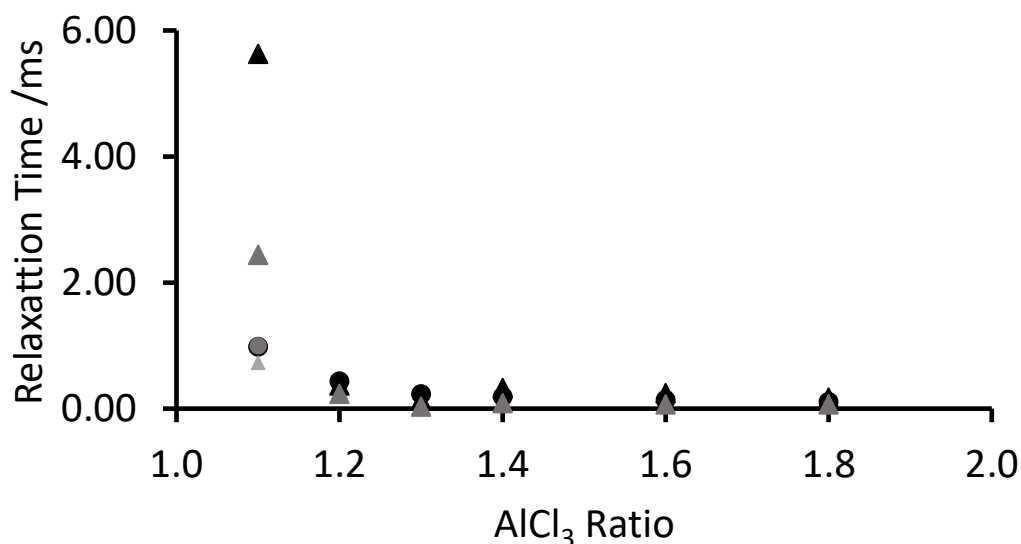


Figure A4.1: ^{27}Al NMR relaxation times of Al in $\text{C}_4\text{C}_1\text{imCl}:\text{AlCl}_3$ as a function of AlCl_3 concentration in $\text{C}_4\text{C}_1\text{imCl}$. Faster T_1 relaxation time (grey circles), slower T_1 relaxation time (black circles), faster T_2 relaxation time (light grey triangles), faster T_2 relaxation time (dark grey triangles), slower T_2 relaxation time (grey circles).

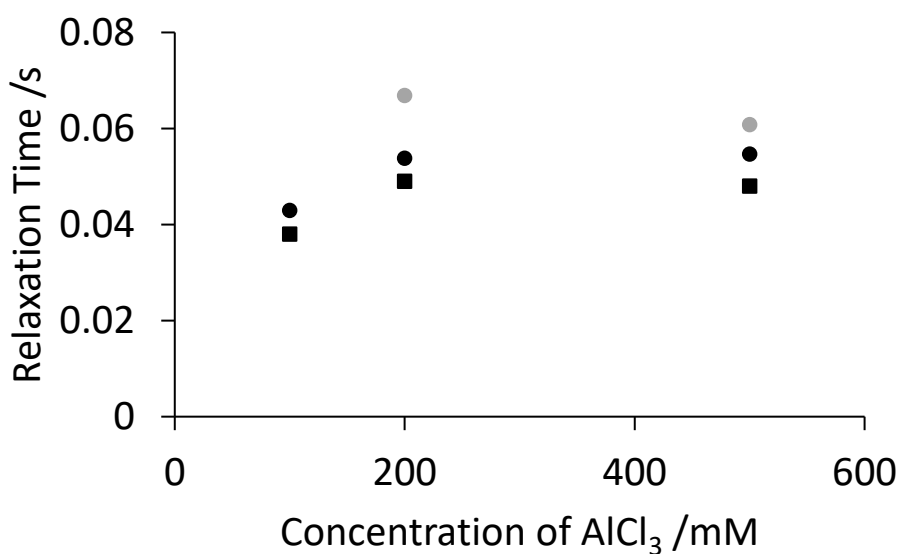


Figure A4.2: ^{27}Al NMR relaxation times of AlCl_3 in the AlCl_3 in saltwater as a function of AlCl_3 concentration in saltwater. T_1 relaxation time (squares), faster T_2^* relaxation time (black circles), slower T_2^* relaxation time (grey circles).

Appendix 4 References:

1. R. Mori, *J. Electron. Mater.*, 2016, 45, 3375-3382.